THE HONG KONG POLYTECHNIC UNIVERSITY
香港理工大學
Pao Yue-kong Library
包玉剛圖書館

Copyright Undertaking

This thesis is protected by copyright, with all rights reserved.

By reading and using the thesis, the reader understands and agrees to the following terms:

1. The reader will abide by the rules and legal ordinances governing copyright regarding the use of the thesis.
2. The reader will use the thesis for the purpose of research or private study only and not for distribution or further reproduction or any other purpose.
3. The reader agrees to indemnify and hold the University harmless from and against any loss, damage, cost, liability or expenses arising from copyright infringement or unauthorized usage.

IMPORTANT

If you have reasons to believe that any materials in this thesis are deemed not suitable to be distributed in this form, or a copyright owner having difficulty with the material being included in our database, please contact lbsys@polyu.edu.hk providing details. The Library will look into your claim and consider taking remedial action upon receipt of the written requests.

Pao Yue-kong Library, The Hong Kong Polytechnic University, Hung Hom, Kowloon, Hong Kong

http://www.lib.polyu.edu.hk

QUANTITATIVE ANALYSIS OF HEMODYNAMIC STATE AND MUSCLE ATROPHY OF RESIDUAL LIMB AFTER TRANS-FEMORAL AMPUTATION

DONG RUIQI

PhD

The Hong Kong Polytechnic University

This programme is jointly offered by The Hong Kong Polytechnic University and Sichuan University

2018

The Hong Kong Polytechnic University

Department of Biomedical Engineering

Sichuan University

College of Architecture and Environment

Quantitative Analysis of Hemodynamic State and Muscle Atrophy of Residual Limb after Trans-femoral Amputation

DONG Ruiqi

A thesis submitted in partial fulfillment of the requirements

for the degree of Doctor of Philosophy

August 2017

CERTIFICATE OF ORIGINALITY

I hereby declare that this thesis is my own work and that, to the best of my knowledge and belief, it reproduces no material previously published or written, nor material that has been accepted for the award of any other degree or diploma, except where due acknowledgement has been made in the text.

___________________________________(Signed)

DONG RUIQI 董瑞琪 (Name of student)

ABSTRACT

Amputation is defined as a destructive surgical procedure that removes the limbs which have lost the physiological function and activity or have endangered the life safety. After the lower limb amputation, no matter what the reason and the level, amputees would face many complex postoperative problems and various potential complications, such as edema, blisters, ulcers and other skin problems, deep tissue injury, muscle atrophy, etc. Among these problems, the most prevalent clinical issue is residual limb (RL) muscle atrophy. Continuous changes of the RL shape and volume caused by muscle atrophy would lead to many negative consequences, especially in patients' rehabilitation, and also greatly increase the expense and time cost for fitting prosthesis. To carry out systematic and thorough investigation on muscle atrophy and other RL problems, the lower limb blood circulation system is a crucial factor from the physiological and biomechanical point of view. It nourishes the entire lower extremity musculoskeletal system while it could be a major cause of amputation. In addition, the emergence of those RL issues usually involves blood circulation disorders, vascular lesions and other angioneurotic issues. In fact, the spatial structure of RL arterial tree has undergone tremendous changes after amputation, and that would inevitably cause the changes of endovascular hemodynamic parameters and lead to high possibility that the blood flow within RL is different from sound limb (SL). Therefore, this thesis launched a comprehensive study focusing on the muscle atrophy and arterial hemodynamic state of thigh RL (trans-femoral level), including the analysis of the correlation between their morphological changes, the flow field comparison and discussion of each main artery based on three kinds of numerical model and calculation method.

Through the case study of 8 unilateral trans-femoral amputees, the morphological indices analysis of muscle atrophy, artery narrowness, and their relationship was carried out. The collected data showed that after trans-femoral amputation, the degree of atrophy of each RL muscle was different: the quadriceps were larger and

the hamstrings were smaller. The change of each main artery of RL was also different: the superficial femoral artery was the largest while the deep femoral artery or medial femoral circumflex artery was the smallest. Meanwhile, the case difference in both muscles and arteries mainly depended on the use of prosthesis. Those subjects not using prostheses showed greater atrophy degree gaps between muscles but smaller stenosis degree gaps between arteries. Based on the blood nourishing relationship, the subjects using prostheses exhibited positive correlation between muscle atrophy and the narrowness of its main blood-supply artery. However, this kind of correlation was not clear in the subjects who did not use prostheses. Thereafter, the Hausdorff distance was applied to quantify the spatial difference of arterial tree in comparing the vessel deformation between two follow-up subjects, and between their SLs and RLs. The results demonstrated that the subject wearing prosthesis presented greater arterial tree deformation in the RL than in the SL, and the bilateral deformation degree gap decrease over time while the subject not using prosthesis showed an opposite result. These phenomena implied that the key impact factor on bilateral arterial tree deformation could be the mobility pattern of the amputee --- prostheses usage. Through these two sections of morphological investigation, the findings suggested that using prostheses not only achieve the functional compensation for RL effectively, but also promote the physiological adjustment of the muscles and arteries in both lower limbs in order to accommodate a new gait and body balance, and facilitate the original bipedal locomotion.

In the hemodynamic study section, this research performed three kinds of numerical simulation method on the bilateral thigh main arteries of Case-1 and Case-2: the steady flow calculation of 3D models, the unsteady flow calculation of 3D-constant resistance (3D-CR) coupling models and 3D- three-element Windkessel (3D-WK) coupling models. The results of the 3D models showed that, under steady flow conditions, there are significant differences in the numerical results and phenomena between the two cases, especially in the value ranges of wall pressure (WP) and wall shear stress (WSS). However, their common findings were that, the arterial tree bifurcation site and the upper half of the deep femoral artery of RL displayed high WP, low WSS and disordered velocity fields that could induce high risk for arterial diseases. By comparing the results of unsteady flow of the 3D-CR models and 3D-WK models with the measured ultrasonic data of Case-1 in a cardiac cycle, it illustrated that the 3D-CR models could achieve a qualitative description of pulse wave propagation, but the 3D-WK models had obvious advantage in the accuracy of numerical results. Therefore, the following summaries were drawn from the 3D-WK models coupling calculation results of Case-1 and Case-2: the WP of bilateral arterial trees were at the highest level during the rapid ejection period; from slow ejection period, larger low shear stress areas (LSSAs) appeared in RL with lower WSS value compared with SL; the velocity field disturbance in the bifurcation segment of RL was more severe than that of SL, and RL displayed more disordered secondary flow directions at the cross sections near the bifurcation site. These results demonstrated that the occurrence of atherosclerosis and other vascular lesions could be greater in RL than in SL, especially in the high-risk zones with LSSAs which located at the arterial tree bifurcation site and the upper half of deep femoral artery. The differences of the two cases were summarized as: Case-1's WSS state in SL was better than that in RL, while Case-2 had similar bilateral WSS situations; Case-2 exhibited larger bilateral LSSAs with lower WSS values than in Case-1. In addition to the same high-risk sites with Case-1, the upper half of lateral femoral circumflex artery in Case-2's both limbs was also susceptible to vascular diseases. From the above findings, amputees without using prosthesis might have greater chance of arterial lesions and larger bilateral high-risk areas than prosthesis users.

The conclusion and main contribution of this thesis are summarized as follows: (1) after trans-femoral amputation, patients using prosthesis showed a positive correlation between RL muscle atrophy and blood-supply artery narrowness, and exhibited a joint adjustment of the spatial structures of bilateral arterial trees during the follow-up period that showed prosthesis usage being a key factor affecting the states of RL muscles and arteries. Thus, it is necessary to consider vascular system and blood flow in the studies focusing on lower RL especially related to prosthesis design; (2) the chance of various arterial lesions was found greater in RL than that in SL, especially in the high WP, low WSS, disordered velocity field zones which located at the arterial tree bifurcation site and the upper half of deep femoral artery but how to reduce the risk of vascular diseases in RL needed further researches; (3) since the range, the distribution and the changes of various hemodynamic parameters in a cardiac cycle were found different between RL and SL, the hemodynamic state of RL deserved more in-depth and meticulous targeted research; (4) compared with prostheses users, amputees without using prosthesis could have greater chance of arterial lesions in both SL and RL; (5) in each phase of a cardiac cycle, the values and distributions of WP, WSS and blood flow velocity were different, thus the qualitative analysis for above single parameter could employ the characteristic velocity in different phases to perform relatively simple steady flow calculation on the 3D model; (6) as for multi-scale coupling calculation, the 3D-CR model should have the function to describe the pulse wave propagation, and the availability to illustrate the qualitative hemodynamic states in a cardiac cycle, but the 3D-WK model could provide obvious advantage in numerical precision, especially in RL. Therefore, according to specific research objectives, the 3D-CR model or 3D-WK model could be selected by considering the measured data, calculation scale and time consuming, etc.

The findings of this thesis, including the descriptions of RL muscle atrophy, artery narrowness and potential vascular lesion areas, together with full discussion on the hemodynamic state of bilateral main arteries and suggestions for the numerical study methodology of lower limb arteries, would provide useful reference data and theoretical support for lower limb amputation researches involving muscle and blood flow situations, and could give some inspirations for various clinical and biomedical studies to eventually promote the comprehensive rehabilitation.

PUBLICATIONS

PAPERS

DONG Ruiqi, WONG M.S. (2015). Research advances in muscle atrophy of lower residual limb: A review. *OA Musculoskeletal Medicine, accepted in January 4, 2015.*

DONG Ruiqi, JIANG Wentao, YAN Fei, ZHENG Tinghui, FAN Yubo. (2015). Numerical Analysis of the Impact of Atherosclerotic Plaque and Different Stents Spacing on Drug Deposition. *Journal of Mechanics in Medicine and Biology*, 15(01), 2015. DOI: https://doi.org/10.1142/S0219519415500116 (SCI)

Dong Ruiqi, Jiang Wentao, Zhang Ming, Leung Aaron, Wong M.S. (2015). Review: hemodynamic studies for lower limb amputation and rehabilitation. *Journal of Mechanics in Medicine and Biology*, 15(04), 2015. DOI: http://dx.doi.org/10.1142/S0219519415300057 (SCI)

Dong RuiQi, Li XiaoLong, Yan Fei, Fan YuBo, Jiang WenTao, Wong M.S. (2016). The Spatial Structure Changes of Thigh Arterial Trees after Transfemoral Amputation: Case Studies. *Journal of Medical Imaging and Health Informatics*, 6(3), 2016: 688-692. (SCI)

Fei Yan, Wentao Jiang, **Ruiqi Dong**, Qingyuan Wang, Yubo Fan, Ming Zhang. (2017). Blood flow and oxygen transport in the descending branch of lateral femoral circumflex arteries: a numerical study. *Journal of Medical and Biological Engineering*, 37(1), 2017: 63-73. (SCI)

李小龙，晏菲，**董瑞琪**，陈宇，蒋文涛，樊瑜波. (2016). 一种表征残肢血管结构变形的参数方法. 医用生物力学，31(1), 2016: 19-23.（中文核心）

Rui-Qi DONG, Wen-Tao JIANG, M.S. WONG, Hong DUAN, Ming ZHANG, Aaron LEUNG. Morphological study of muscle atrophy and arterial shrinkage of trans-femoral residual limb. (Under preparation)

Rui-Qi DONG, Wen-Tao JIANG, M.S. WONG, Hong DUAN, Ming ZHANG, Aaron LEUNG. Multi-scale numerical study of the hemodynamics of thigh arteries after trans-femoral amputation. (Under preparation)

CONFERENCE PRESENTATIONS

董瑞琪，蒋文涛，樊瑜波．(2012). 动脉粥样硬化斑块和不同支架间距对药物沉积量影响的数值分析．海报展示于第十届全国生物力学学术会议暨第十二届全国生物流变学学术会议，10月11-15日，2012年，成都，中国。摘要收录于医用生物力学《第十届全国生物力学学术会议暨第十二届全国生物流变学学术会议论文汇编》，2012年10月，第27卷，增刊。

DONG Ruiqi, JIANG Wentao, FAN Yubo. (2013). Numerical Analysis of the Impact of Atherosclerotic Plaque and Different Stents Spacing on Drug Deposition. Poster presentation at the 6th WACBE World Congress on Bioengineering on August 5-8, 2013, Beijing, China.

Dong Ruiqi, Jiang Wentao, Zhang Ming, Leung Aaron, Wong M.S. (2015). Quantitative analysis of arterial morphological changes and muscle atrophy of residual limb after trans-femoral amputation. Oral presentation at the International Society for Prosthetics and Orthotics (ISPO) World Congress 2015 on June 22-25, 2015, Lyon, France.

Dong Ruiqi, Jiang Wentao, Zhang Ming, Leung Aaron, Wong M.S. (2015). The spatial structure changes of thigh arterial trees after transfemoral amputation. Oral presentation at The 3rd Symposium on Fluid-Structure-Sound Interactions and Control (FSSIC) on July 5-9, 2015, Perth, Western Australia.

Fei YAN, Wentao JIANG, **Ruiqi DONG**, Qingyuan WANG, Yubo FAN, Ming ZHANG. (2015). Numerical study on the effects of blood velocity on oxygen transport in the residuum vasculature. Oral presentation at The 3rd Symposium on Fluid-Structure-Sound Interactions and Control (FSSIC) on July 5-9, 2015, Perth, Western Australia.

RuiQi DONG, M.S. WONG, WenTao JIANG, Ming ZHANG, Aaron LEUNG. (2017). A study on hemodynamic state of residual limb after trans-femoral amputation. Oral presentation at the International Society for Prosthetics and Orthotics (ISPO) World Congress 2017 on May 8-11, 2017, Cape Town, South Africa.

RuiQi DONG, M.S. WONG, WenTao JIANG, Ming ZHANG, Aaron LEUNG. (2017). A Study on Hemodynamic State of Residual Limb after Trans-femoral Amputation. Oral presentation at the 8th WACBE World Congress on Bioengineering on 30 July-2 August, 2017, Hong Kong.

FUNDING

This work was supported by the grants from joint PhD programme with Sichuan University by the Hong Kong Jockey Club, and the National Natural Science Foundation of China (11272224).

ACKNOWLEDGEMENTS

First of all, I would like to sincerely appreciate the Hong Kong Jockey Club for sponsoring the four-year Joint PhD Programme of the Institute of Disaster Management and Reconstruction (IDMR), Sichuan University-The Hong Kong Polytechnic University. This support enabled me to complete my doctoral study under the high quality education of the two universities.

Secondly, I would like to express my deepest gratitude to my chief-supervisors Dr. M.S. WONG and Prof. WenTao JIANG. They gave me the rare opportunities to participate in the project of National Natural Science Foundation of China, and to join the ISPO Hong Kong National Society. They also generously gave me invaluable guidance, trust, support and encouragement during my entire Ph.D. stage. What I have learned from them is not only scientific research ability, but also rigorous and painstaking study spirit. I am also heartfully indebted to my co-supervisors Prof. Ming ZHANG and Dr. Aaron K.L. LEUNG, for their precious guidance and suggestions.

I also owe special thanks to my study fellows, Fei YAN, YongHong Yang, Qian WANG, and all workmates who gave me a lot of help from West China Hospital and the laboratory of biomechanical engineering of Sichuan University. My thanks also extend to my patients for their understanding, support and cooperation to my research.

Last but not least, I would like to thank my beloved parents for their selfless companionship, support and encouragement through all these years. My thanks would also go to my family, my friends, for their concern and help during my Ph.D. phase.

Table of contents

LIST OF TABLES

LIST OF FIGURES

LIST OF ABBREVIATIONS

Abbreviations	Full name
RL	Residual limb
SL	Sound limb
MA	Muscle atrophy
DTI	Deep tissue injury
SART	Sartorius
RF	Rectus femoris
VI	Vastus intermedius
VM	Vastus medialis
VL	Vastus lateralis
GRAC	Gracilis
AM	Adductor magnus
AL	Adductor longus
AB	Adductor brevis
SEMI_T	Semitendinosus
SEMI_M	Semimembranosus
BF	Biceps femoris
CFA	Common femoral artery
SFA	Superficial femoral artery
DFA	Deep femoral artery
LFCA	Lateral femoral circumflex artery
MFCA	Medial femoral circumflex artery
CSA	Cross-sectional area
N-S	Navier-Stokes
FEA	Finite element analysis
CFD	Computational fluid dynamics
CR	Constant resistance
WK	Windkessel

WP	Wall pressure
WSS	Wall shear stress
FV	Flow velocity

CHAPTER 1: LITERATURE REVIEW

1.1 INTRODUCTION

Amputation, a kind of destructive operation, refers to resect the limb that endanger patient's life or has lost the physiological function and activity. The common causes of this surgery are neuropathy, peripheral vascular disease, malignant tumors, severe trauma, congenital anomalies and infections. According to clinical experiences, in developing countries, including China, trauma (mechanical, chemical and traffic accident injuries etc.) is the leading cause of amputation. Whereas in the developed countries, amputation is mainly due to diabetes and its complications, lower extremity arteriosclerosis obliterans, thromboangiitis obliterans and other peripheral vascular occlusive diseases [1-3]. Some of these diseases or lesions would continue to damage the residual limb (RL) after amputation resulting in secondary or even multiple surgeries [4], or producing a high incidence of complications (34.4%) and a 7.0% 30-day mortality rate [5]. The China second national sample survey on disability in 2006 shows that the number of amputees is up to 2 million 260 thousand among the 24 million 120 thousand physical disabled people (Luo Yongzhao & Sun Wei, 2009). Moreover, the 2008 Wenchuan earthquake caused a large number of patients with limb disability, and according to the situation of the earthquake rehabilitation center of West China Hospital, lower limb amputees are in the majority. No matter what the reason and level of amputation are, amputees will face many complex and challengeable postoperative problems and potential complications. For example, due to the friction and pressure of wearing prosthesis would result in the poor skin micro-circulation and subsequent ulcers, blisters, edema, pressure ulcers and other skin problems [6, 7]; the high stress around residual bone end would cause deep soft tissue injury [8]; greatly reduced exercise amount would lead to RL muscle atrophy (MA) [9-11]. These problems pose a threat to the physical and mental health of amputees, and seriously impede their comprehensive rehabilitation. In order to alleviate or avoid the above issues, researchers in various fields have done a lot of studies [12-17] for helping amputees to return to normal life.

In the above-mentioned troubles, the most common clinical phenomenon is RL MA, which would cause the continuous changes of RL shape and volume and give rise to many adverse consequences. For instance, the prosthetic socket loosening would make the increase of friction and local stress concentration [18]; the abnormal gait would result in the acceleration and deterioration of skin problems; patients would reduce their activity (mainly walking) amount due to the pain from wearing prosthesis, that would accordingly result in the loss of muscle strength and joint force which would lead to more abnormal and energy-consuming gait; long-term low exercise quantity could give rise to the degradation of cardiovascular and pulmonary function as well as some complications. In addition, suffering from MA makes patients have to frequently replace the prosthetic socket, which will lead to high expense and time costs. To compare the different level of amputation, clinical data shows that the MA of trans-femoral amputees is more serious than that of trans-tibial amputees [19]. That is not only because the missing of knee joint would inevitably reduce the movement forms and ability greatly, but also because the thigh RL is relatively short, thus its low effective leverage would weaken the ability of thigh muscles to control the prosthesis [20] and hinder the rehabilitation exercise of patients. In fact, targeted for MA, there has been many achievements in the biomedical research area, such as the microscopic pathological characteristics analysis about the MA occurrence mechanism [11, 21, 22]; to prevent MA by optimizing the immediate postoperative management [23], prosthetic socket design [14-16] and rehabilitation training methods [24, 25]; to relieve MA by seeking physical or pharmaceutical treatments [26-28] etc.. However, these studies have not solve the fundamental problem yet. Therefore, researches focusing on various diseases and physiological changes of lower RL would still be the main topic in the field of rehabilitation medicine and biomechanics in the future.

To achieve the in-depth systematic investigation on RL MA and other issues, there is an unavoidable crucial factor whether from the perspective of physiology or biomechanics---the blood supply and circulation matters. Blood and its circulation system, which nourishes the entire lower extremity musculoskeletal system, supplies nutrition and oxygen, and discharges metabolic waste, are involved in all the physiological activities of the lower limb. For amputees, the surgery makes the spatial structure of lower limb vascular system has undergone tremendous changes. The cutted vessels not only lose the length, but also get some direction changes, extrusion deformation and even lumen reconstruction due to the muscle re-fixation and postoperative atrophy. Such a major change of vascular spatial configuration would inevitably cause the variation of endovascular blood flow situation. That means the hemodynamic state of RL is highly probably different from that of sound limb (SL). In recent years, as a relatively new research direction, the hemodynamics study of lower limb has attracted more and more attention. Some reports have shown that, the occurrence mechanism of the peripheral vascular diseases leading to amputation is directly related to the distribution of hemodynamic parameters. A consensus conclusion is that the disorder flow field, high blood pressure and low wall shear stress are the predisposing factors of atherosclerosis and thrombosis, and their changes are likely to continuously damage blood vessels after amputation [29]. In addition, some studies have demonstrated that hemodynamic state is related to the occurrence and development of pressure ulcers, deep tissue injury (DTI) and MA [30, 31]. These existing researches considering the impact of blood circulation showed the importance to learn about lower limb hemodynamics, but meanwhile illustrated that most of the studies concerned the stage before amputation, and the investigations on RL blood flow after the surgery are few. For the common clinical symptom MA, the targeting hemodynamic study of RL has not yet been reported.

In summary, the comprehensive study about RL MA, hemodynamic state and their correlation could help to explain the pathological mechanism, and provide a theoretical basis to promote the improvements on surgical technique, postoperative management, rehabilitation treatment, prosthetic socket design etc., with important clinical significance.

1.2 ANATOMICAL STRUCTURE OF THIGH MUSCLES AND ARTERIES

1.2.1 Anatomical structure and physiological function of thigh muscles

According to Gray's Anatomy (Susan Standring, the 39th edition), the main function of lower limb muscles is to maintain upright posture and balance while moving. The thigh muscles are divided into three functional groups: anterior group (extensor), medial group (adductor) and posterior group (flexor). The anterior group includes sartorius (SART) and quadriceps---rectus femoris (RF), vastus intermedius (VI), vastus medialis (VM), vastus lateralis (VL), wherein the SART and RF could act on both hip and knee with a variety of functions, while the other parts of quadriceps form a strong extensor for knee joint. Meanwhile, VL and VM are also involved in the tibial rotation, and their role is to stabilize the knee from the side. The medial group includes adductor magnus (AM), adductor longus (AL), adductor brevis (AB), gracilis (GRAC) and pectineus which connect the fore-pelvis and femur. When the ilium is fixed, they pull the femur for adduction, flexion and external rotation. While when the femur is fixed, they pull the ilium to form medial flexion, forerake and external rotation. Because of its proximal attachment range and dual innervation, AM also participates in the trunk extension. The posterior group includes semitendinosus (SEMI_T), semimembranosus (SEMI_M) and the long head and short head of biceps femoris. The combined term of the long head of biceps femoris (BF), SEMI_T and SEMI_M is hamstrings which across the hip and knee, and their role is to make femur extension, knee flexion and rotation when the ilium is fixed, to make trunk extension when the femur is fixed.

Hip is the proximal joint of lower limb, connecting the femur and pelvis. Many human activities and postures require the larger curvature of hip movement, however this part is often inflexible, and limit the activities of trunk, knee and feet. Knee joint is in the middle of lower limb with strong ability of flexion and extension. It can greatly change the distance between foot and trunk, but the stability of knee bone is relatively weak, and it is mainly strengthened by ligament and muscle system. The function of the hip and knee muscles in motion state is shown in **Table 1.1**.

Table 1.1 The function of the hip and knee muscles in motion state

Joint	Movement	Muscle	Joint	Movement	Muscle
Hip	Flexion	RF	Knee	Flexion	SEMI_M
		AL			SEMI_T
		AB			BF
		GRAC			BF(short head)
		SART			SART
	Extension	AM			GRAC
		BF		Extension	RF
		SEMI_M			VM
		SEMI_T			VL
	Abduction	SART			VI
	Adduction	GRAC		Internal rotation	SART
		AB			SEMI_T
		AL			SEMI_M
		AM			GRAC
		BF		External rotation	BF
	External rotation	AM			BF(short head)
		AL			
		AB			
		BF			

The anatomy of thigh muscles is shown in **Figure 1.1** and **Figure 1.2**.

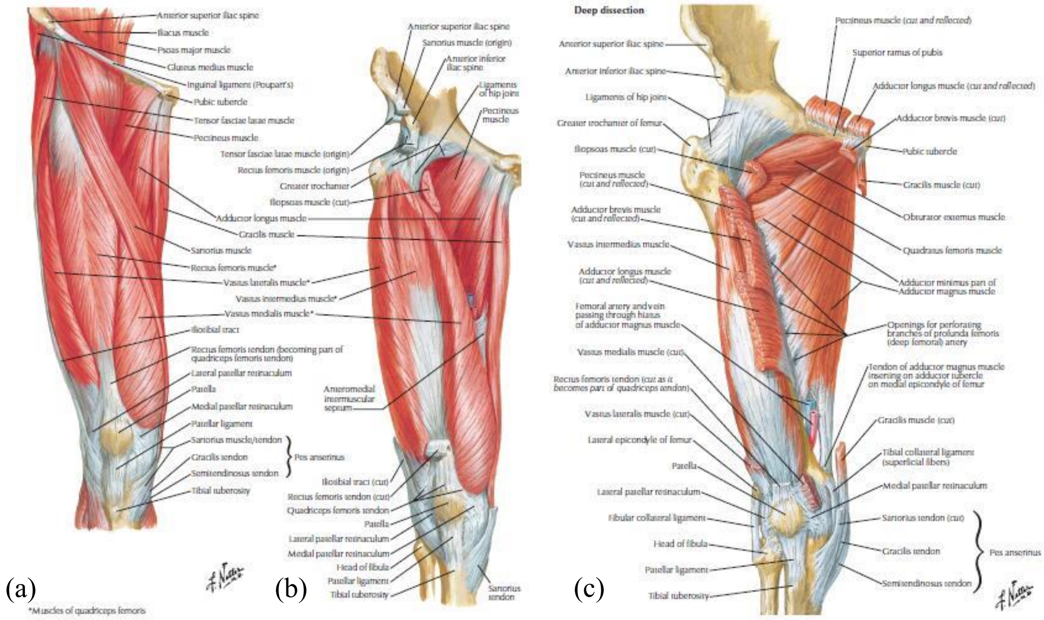

Figure 1.1 The anterior view of thigh muscle anatomy [32]. (a) superficial dissection; (b) middle dissection; (c) deep dissection.

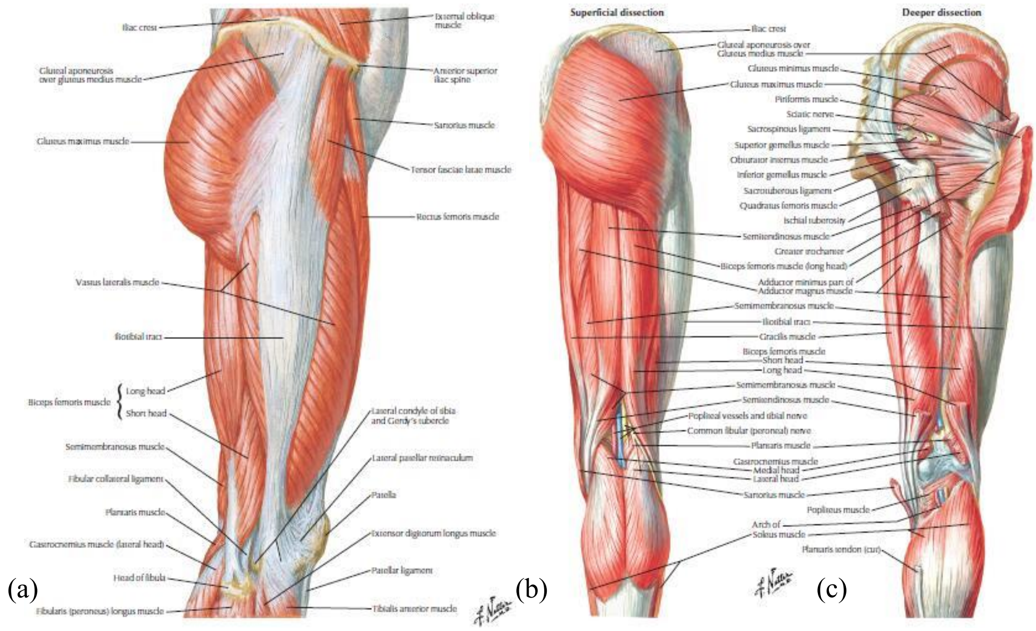

Figure 1.2 Anatomy of hip and thigh muscles [32]. (a) lateral view; (b) posterior view: superficial dissection; (c) posterior view: deep dissection.

1.2.2 Anatomical structure and branches of thigh main vessels

According to Gray's Anatomy (Susan Standring, the 39th edition), the main arteries of thigh are common/superficial femoral artery (CFA/SFA), deep femoral artery (DFA), lateral femoral circumflex artery (LFCM) and medial femoral circumflex artery (MFCA). SFA is a section of femoral artery, which starts from the beginning of DFA to the foramen of AM. The small branches of CFA in the proximal part are superficial epigastric artery, superficial circumflex iliac artery, superficial/deep external pudendal artery, and the muscular branches. DFA, which passes through pubic muscle, AL and AM, is a large branch of femoral artery, and its terminal part is sometimes called the fourth perforating artery. LFCA starts from the root of DFA, going through femoral nerve branches to SART and RF, and divides into ascending, transverse and descending branches. MFCA begins at the posteromedial site of DFA in general, but also often comes from femoral artery. Its medial bent part goes around pubic muscle and psoas muscle, and its end part divides into transverse and ascending branches in quadratus femoris and the upper AM.

The main veins of thigh are femoral vein, deep femoral vein and great saphenous vein. Femoral vein is concomitant with femoral artery, which starts from adductor foramen as a continuation of popliteal vein, and ends at external iliac vein behind inguinal ligament. There are many muscular branches of femoral vein, wherein deep femoral vein enters its posterior part and great saphenous vein enters its anterior part at the distal end of inguinal ligament. Deep femoral vein locates in the foreside of DFA with many branches. The distal part of these branches is connected with popliteal vein and their proximal part connects to superior gluteal veins. Great saphenous vein starts from the inner side of dorsal venous arch and ends at the femoral vein a little bit below the distal inguinal ligament, which is a convergent blood vessel of the inner marginal veins and the longest vein in the body.

The anatomical structures of the main arteries and veins of thigh are shown in **Figure 1.3**.

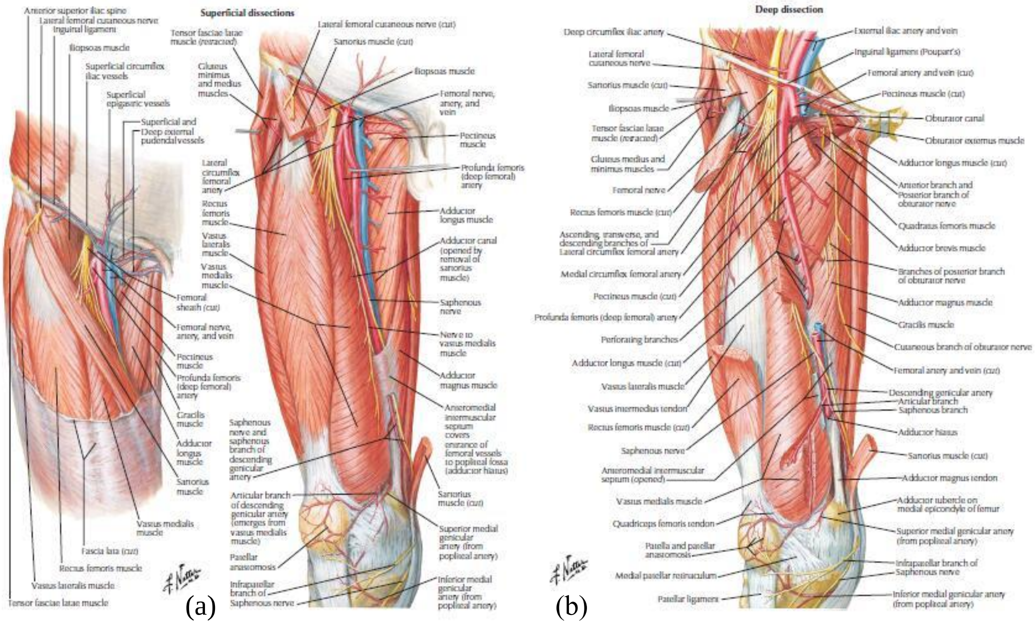

Figure 1.3 The anterior view of thigh arteries and veins anatomy [32]. (a) superficial dissection; (b) deep dissection.

1.2.3 Blood supply of thigh muscles

(1) The main supply of SART comes from the femoral artery system. The upper part gets blood from CFA, the main trunk of DFA, quadriceps artery, SFA, or LFCA; the middle part is fed by SFA; SFA and descending genicular artery provide blood-supply to the distal part. (2) The blood-supply of RF is two main arterial stems, wherein the upper stem which is a large branch originates from quadriceps artery, and sometimes RF also receives the blood supplement from LFCA. (3) VM is nourished by three superficial branches of SFA and some subbranches of DFA and descending genicular artery. (4) VL gets blood mainly from these three arteries: the superior internal artery directly branching from LFCA; the inferior internal artery branching from quadriceps artery; the lateral artery branching from the first perforating branch of DFA. (5) VI receives the blood-supply from the lateral artery branching from quadriceps artery and a distributing branch of DFA. (6) The upper part of GRAC is fed by the adductor arteries branching from DFA; the lower part of GRAC gets blood from a relatively minor branch originating from SFA. (7) The

blood-supply of AL is as follows: mainly comes from the adductor arteries of DFA; in the proximal site there is supplementary blood from MFCA; SFA or descending genicular artery feeds the distal part. (8) The blood-supply of AB is variable. Usually its distal part is directly nourished by DFA, and the proximal part receives blood from adductor arteries and the supplement from MFCA. (9) AM gets its blood from both front and rear, yet the supply in front is relatively more important. The providers are obturator artery, DFA, SFA, wherein the main source is the distal section of DFA. The branches of MFCA feed the rear part. (10) SEMI_T has two main feeding arteries. The upper one comes from MFCA or the first perforating artery; the large branch of the lower one comes from the distal site of the beginning of the first perforating artery. (11) The blood providers of SEMI_M are usually all perforating arteries, but the first or fourth is the most important one. (12) BF (long head) is fed by the first and second perforating arteries, and there are inferior gluteal artery and MFCA as the supplementary at sciatic junction. In general, a large number of muscular branches originate from DFA, so DFA is the main blood-supply vessel of thigh muscles. The cross-sectional anatomy of thigh muscles, arteries and veins is shown in **Figure 1.4**.

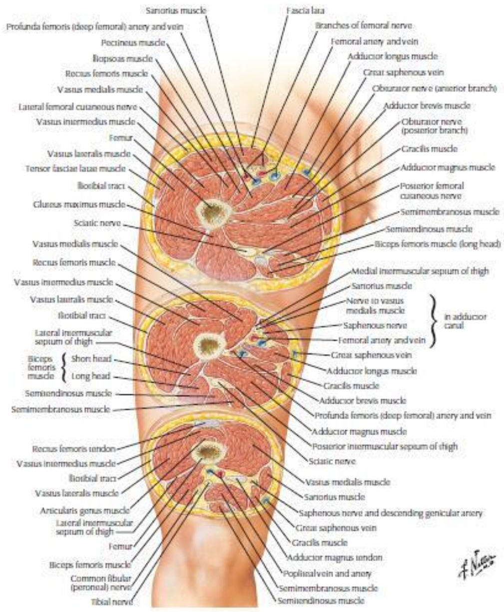

Figure 1.4 The cross-sectional anatomy of thigh muscles, arteries, veins and nerves [32].

1.3 RESEARCH PROGRESS ON LOWER RESIDUAL LIMB MUSCLE ATROPHY

The quick adaptation to external environment changes is a characteristic of skeletal muscles. The corresponding hypertrophy or atrophy would occur when muscles are subjected to mechanical force, disuse, ischemia, hypoxia and other environmental changes of tissue [33]. Muscle atrophy (MA), namely striated muscle nutritional disorder, whose definition is widely known as the loss of muscle mass and reduction of muscle volume due to the narrowed cross-sectional area (CSA) of myofibers [11]. According to the cause of formation, MA can be mainly categorized into neurogenic atrophy, myogenic atrophy and disuse atrophy etc. The first two types belong to primary lesion whose pathogenesis is not yet fully understood, and they are difficult to cure. However, disuse muscle atrophy which mostly occurs in the circumstances of bed rest, limb movement diminution, immobilization, weightlessness and so on [34] could be classified as a secondary disease, and it has the potential to be mitigated or cured. It is generally believed that MA in residual limb (RL) is disuse atrophy. Even after apparent volume changes in the early stage of rehabilitation (defined as 1 to 1.5 years after surgery), many patients with relatively stable RL still undergo MA in different degree in the long-term rehabilitation process [35, 36]. In order to ease the annoyance and suffering from RL MA for amputees, multi-directional studies have gained many valuable achievements in the past few decades.

1.3.1 Clinical symptom of residual limb muscle atrophy

With the progress of detection techniques, the indicators for defining muscle atrophy and determining the degree developed from morphological to histological indices. In recent years, some studies have looked at the microstructure changes in tissue and the variation of biochemical indices. Morphological indices of muscles include the dry weight, wet weight, thickness, CSA, volume etc. [10, 19, 37]. Histological parameters consist of muscle cell structure, the composition and CSA of muscle fibers and so on [38], while biochemical indicators refer to the activity of enzymes and signaling molecules that impact the synthesis and decomposition of muscle protein [39, 40]. In addition, from the perspective of biomechanics, the variation of muscle tone and muscle strength caused by the mechanical environment change of RL also belong to the clinical manifestation of skeletal MA [12, 20].

It has been reported that, the atrophy degree of each muscle group of lower RL is inconsistent, and some muscles even show the phenomenon of growth. Schma-lz, T., et al. [10] performed Ultrasonography on 17 trans-tibial amputees and found that the quadriceps femoris and SART of RL exhibited predominant loss of mass, whereas the reduction of the thickness and CSA of dorsal muscle group including GRAC, SEMI_T and BF was not significant. That was probably due to compensatory hyperfunction, which means the extremely active hamstrings had offset the loss of gastrocnemius function and knee movement, thereby ensuring the normal thickness of thigh knee flexors. Meanwhile, the contralateral thigh also showed a slight muscle atrophy in quadriceps. Through the contrast measurements of trans-femoral and trans-tibial amputees by Sherk, V. D., et al. [19], the conclusion is that MA was prevalent in both thigh and lower-leg muscles regardless of amputation level, but it was more evident in trans-femoral amputees with larger percent of fat in thighs. In addition, large amounts of inter-muscular adipose tissue existed in the end of RL. Fraisse, N., et al. [9] did the comprehensive analysis about the bilateral MA of trans-tibial amputees, and they pointed out that in the process of adapting to the new muscle state after amputation, the change of symmetrical gait and the increase of walking energy expenditure led to the different atrophy degree of muscles. They thought that was essentially because the anatomical structure changes of RL gave rise to the variations in the physiological tension and movement forms of muscle groups. Hamstrings replaced triceps to be the main motion propulsion, as well as the guarantee of the good contact between RL and prosthetic socket. That's why hamstrings hardly showed atrophy but even growth. As for the internal mechanical state of RL, Isakov, E., et al. [20, 41] investigated the bilateral leg muscle strength of trans-tibial amputees with different RL length by electronic dynamometer. The results illustrated that MA in the thigh of trans-tibial amputees was accompanied with a significant reduction in quadriceps and hamstrings strength, especially in patients with a short stump. They thought the inefficient leverage provided by the short RL compromised the ability of the thigh muscles to control the prosthesis. This conclusion was verified by the muscle strength test on traumatic trans-tibial amputees of Tugcu, I., et al. [12].

In summary, RL MA is not the simple disuse atrophy caused by unloading, but a comprehensive result influenced by multifaceted effects like the operation structure reconstruction, the external mechanical environment, etc.

1.3.2 Microscopic pathology of residual limb muscle atrophy

There are three main theories about the mechanism of disuse atrophy: nerve impulse loss hypothesis [42], neurotrophic disturbance hypothesis [43] and oxidative stress hypothesis [44]. In addition, some studies showed that glucocorticoids [45], growth hormone [46], thyroid hormone and androgen [47] also have a certain relationship with disuse atrophy. Integrating these theories it can be found that although the occurrence of disuse atrophy is multi-source and complicated, the essential microscopic pathological features are inseparable from the increased muscle proteolysis, reduced protein synthesis and apoptosis.

In 2005, Glass, D. J. [39] systematically collated and summarized the interactions between the various muscle protein factors and molecular signaling. In terms of anabolism, the protein growth factor insulin-like growth factor 1 (IGF-1) activates the signaling pathway IGF-1/phosphatidylinositol-3 kinase (PI3K)/Akt and the three pathways secondary to Akt including glycogen synthase kinase 3 beta (GSK3-β), tuberous sclerosis complex-1 and -2 proteins (Tsc1/2)/mammalian target of rapamycin (mTOR) and FOXO family to regulate and promote protein synthesis. Furthermore, IGF-1 can also block the transcriptional upregulation of ubiquitinligases MuRF1 and MAFbx which are the key mediators of muscle atrophy. While in terms of catabolism, TNFα is sufficient to induce skeletal muscle atrophy by promoting protein breakdown in two pathways. One is activating NF-κB to mediate the upregulation of muscle ring finger-1 (MuRF1). The other is triggering the expression of muscle atrophy F-box (MAFbx) via p38 pathway. In 2008, Ferreira, R. [40] used the disuse model of hindlimb suspension mice to investigate the occurrence and time-course of apoptosis in soleus within 48 hours after unloading. The results displayed that soleus atrophy presented as a significant decrease in muscle-wet weight and the slight decline in protein concentration/muscle wet-weight ratio. In addition, the time axis of caspases activity and the maximum value of apoptotic index, apoptosis-inducing factor and p53 showed that the mitochondrial apoptosis pathway might contribute to the early phase of soleus atrophy. In numerous studies, there are also some controversial issues. A lot of studies have reported that muscle atrophy is accompanied by apoptotic loss of myonuclei, therefore its supplement from muscle stem cells would be required for muscle recovery. But the study carried out by Bruusgaard, J. C. and Gundersen, K. [42] raised objections to this suggestion. They employed denervation, nerve impulse block or mechanical unloading to induce muscle atrophy in the extensor digitorum longus and slow soleus muscle of mice, and then observed the in vivo loss and replenishment of myonuclei in muscle fibers. Different from their prediction, imaging of single fast- or slow-twitch fibers for up to 28 days exhibited no loss of myonuclei despite a greater than 50% decrease in fiber CSA. Furthermore, although high levels of apoptotic nuclei from the fragmented DNA on histological sections of inactive muscles were observed, there was virtually no myonuclei loss in laminin and dystrophin. That means apoptosis localized in stromal and satellite cells. They proposed that disuse atrophy is not a degenerative process but a balance change of protein metabolism.

Since the microscopic pathological research is highly specialized and complex, and most of the studies were conducted on animal models or experiments instead of for lower limb amputees.

1.3.3 Treatment methods of residual limb muscle atrophy

The conventional methods for preventing, alleviating or even curing disuse atrophy could be broadly sorted into three categories of movement functional training, physical therapy and drug therapy. Besides these rehabilitation means, the surgical processing for muscles, immediate postoperative management and prosthetic socket design could also make a contribution [48].

Early amputation performed muscle annular cutting that led to hypomyotonia because of the loss of muscle attachment points, and thereby resulted in atrophy. Some patients even suffered from the degradation of local circulation and subsequently had a conical residual limb which is very unfavorable for wearing prosthetics. Modern surgical processing for muscles is myodesis [49] or myoplasty [50]. Myodesis is a technique suturing the amputated muscles to the drilled fixing holes on bone with an appropriate tension, whereby muscles could maintain contractile function. In this way the prevention of residual limb atrophy could be achieved [51]. Myoplasty requires to cut off muscles below the level of osteotomy, and then to suture the corresponding extensor and flexor to form a muscle flap for protecting the end of bone. This approach could also keep muscular tension and better blood circulation as far as possible to reduce atrophy.

After amputation, immediate postoperative treatment of the residual limb is identified to be the crucial first step of rehabilitation and its primary tasks are controlling oedema and promoting wound healing [23]. In the early several decades, an immediate postoperative prosthesis which is a multipart weight-bearing device (as shown in **Figure 1.5**) has been used after the application of a standard soft dressing and a compressive residual limb shrinker to achieve the immediate ambulation. In recent years, a removable rigid dressing that is a part of immediate postoperative prosthesis was proved to be conducive to the acceleration of wound healing. The usage of removable rigid dressing could produce supplemental compression for reducing oedema and provide protective environment for avoiding trauma to the wound. Although immediate postoperative prosthesis supports walking, it gives rise to some problems and risks, whereas removable rigid dressing allows partial weight bearing evading these issues. Achieving wound stability and prosthetic adaptation within shorter time through a good immediate postoperative treatment could advance rehabilitation training as early as possible, and thus minimize the disuse atrophy of residual limb.

Figure 1.5 Plastic removable rigid dressing and immediate postoperative prosthesis [23].

When amputees received their definitive socket, the distribution of stump/socket interface pressure is a major factor affecting the application comfort and the compensatory function of prosthesis [17]. With the development of computer technology, digital simulation broke the limitation in local measurement of early experimental method employing pressure sensor, and can provide the overall pressure distribution. Therefore, the theoretical studies on computer-aided design/computer-aided manufacturing (CAD/CAM) of socket begin to take shape in the past decades [14]. For example, Portnoy, S., et al. [52] used a patient-specific 3D finite-element (FE) model to investigate the mechanical conditions in muscle flap of the residual limb, because the increase of muscular internal strains and stresses due to the stump/socket interaction is a potential incentive for many complications. Moo, E. K., et al. [53] and Wolf, S. I., et al. [16] respectively used FE analysis and 3D gait analysis to investigate the stump/socket interface pressure profiles produced by the hydrostatic socket and the Proprio-Foot (Ossur) prosthesis during level, stair and incline walking. The purposes of them are to provide better prosthetic support than the conventional PTB socket and to reduce the possible negative consequences of interface pressure whereby residual limb atrophy could be mitigated. The finite element models of RL and socket are shown in **Figure 1.6**. The stress distribution on the surface of RL and in the truncated bones is shown in **Figure 1.7**.

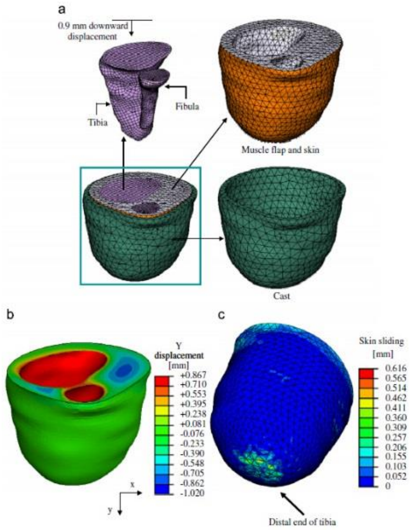

Figure 1.6 Finite element models of truncated tibia and fibula bones [52].

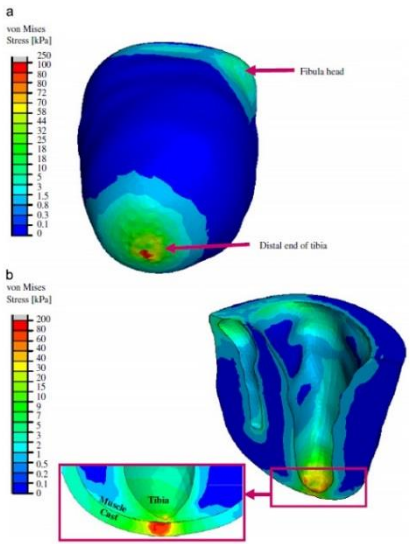

Figure 1.7 The von Mises stress distribution in the residual limb of a trans-tibial amputee [52].

Regularly accepting the scientific and effective rehabilitation exercise training with a prosthesis, would help patients to improve the muscle condition of RL. Darter, B. J., et al. [54] invited 8 unilateral trans-femoral amputees to participate a walking training on home-based treadmill with strict schedule for 8 weeks, and then compared the indicators including energy expenditure and energy cost, optional and maximum walking speed, as well as 2-minute walk test before and after the training. They concluded that the home-based treadmill walking training was an effective way to improve the gait performance and the rehabilitation outcome of trans-femoral amputees with declined energy consumption.

In the field of occupational, physical and drug therapies, there are many studies from multi-angle of view. Kubota, A., et al. [55] performed a control experiment on 15 healthy males whose left ankles were immobilized and walked with crutches for 2 weeks. Those subjects were divided randomly into the restriction of blood flow group, the isometric training group, and the control group. The results showed that the muscle strength of different muscles and the leg girth in the control group and isometric training groups significantly decreased, but these changes were not found in the restriction of blood flow group. So they drew the conclusion: periodic restriction of blood flow to lower limb produced anti-atrophic effect and prevented disuse muscular weakness. Guo, B. S., et al. [26] used the tail suspension model on mice for hindlimb unloading, and implemented electrical stimulation on a hindlimb. The mass, CSA, peak tetanic force and the satellite cell proliferative activity of soleus muscles in the electrical stimulation limbs were found significantly increased compared with the contralateral limbs. Meanwhile, reduction in the apoptotic myonuclei and the apoptotic satellite cells was observed in electrical stimulation limbs. Furthermore, the anti-apoptotic protein was upregulated whereas the apoptosis inducing factor was down-regulated in electrical stimulation limbs. The study suggested that electrical stimulation could effectively relieve disuse MA and inhibit the loss of muscle nucleus and satellite cells. In the animal experiment of Staresinic, M., et al. [56], Pentadecapeptide BPC 157 was intraperitoneally given to rats undergoing right quadriceps transection for a total of 72 days, and the foot print length ratio, extensor postural thrust ratio, girth percentage of quadriceps, and myofibril diameters at different days were measured and recorded. The data demonstrated that consistent improvement showed in the indexes of biomechanics, motor function, walking recovery and immunochemistry of the transection limbs, as well as significant atrophy mitigation. Hence Pentadecapeptide BPC 157 was considered to be effective in facilitating the regeneration of injured muscle, and it played a role in attenuating MA. Dirks, M. L., et al. [27] carried out a control experiment on 24 healthy young males subjected to one knee immobilization for inducing MA, and then applied neuromuscular electrical stimulation to one group. Through the analysis of the CSA of thigh and quadriceps, maximal calf circumference, calf lean mass and maximum strength, as well as the gene expression of myostatin, they proposed that neuromuscular electrical stimulation was an effective intervention to rescue muscle mass from the short-term but substantial disuse atrophy, although it could not prevent the reduction of muscle strength. Brooks, N., et al. [28] pointed out that the combination of resistance training and amino acid supplementation could reduce the loss of thigh muscle mass and strength caused by bed rest. The optimization effect was significantly higher than that of only amino acid supplementation.

In summary, the loss of muscle mass and strength in the lower RL of amputees is a common phenomenon which is difficult to avoid. A lot of researches tried to find the fundamental mechanism of this kind disuse atrophy at the cellular and molecular level in order to curb this issue, and they have gained some achievements. The current therapeutic strategies could still be broadly classified as rehabilitation training, drug treatment and physical therapy. In recent years, the effectiveness of some new attempts and combined methods was verified. Besides, technical changes in surgery, immediate postoperative management and prosthetic design also contributed to the prevention or mitigation of RL MA. However, there is a certain distance away from the solution of this problem.

1.4 HEMODYNAMIC STUDIES FOR LOWER LIMB AMPUTATION AND REHABILITATION

1.4.1 Preoperative diagnosis and assessment

For such a major surgery, the preoperative diagnosis and the amputation level evaluation are essential before lower limb amputation. Especially for patients suffering from peripheral vascular diseases, the choice of limb salvage or amputation will directly affect their therapeutic outcome and life quality. Meanwhile, the length of residual limb is closely related to the muscle strength reduction [20], the stress-strain relationship within organization [8] and the adaptability to prosthesis. Therefore, the earliest hemodynamic application in lower limb amputation is the treatment program selection and the amputation level determination.

Balloon angioplasty, atherectomy, endarterectomy and bypass surgery etc. are common treatment methods for occlusive arterial diseases with limb salvage. In 1997, Bhargava, J.S., et al. [57] put forward that the pulse oximetry and stress testing was a simple and objective method to evaluate the effectiveness of revascularization and the success of limb salvage. Subsequently, Santilli, J. D. and Santilli, S. M. [58] summarized the diagnostic criteria of chronic critical limb ischemia set by hemodynamic parameters. Those threshold values include an ankle-brachial index of less than or equal to 0.4, an ankle systolic pressure of less than or equal to 50 mmHg, and a toe systolic pressure of less than or equal to 30 mmHg. However, diabetes is usually associated with severe peripheral arterial disease, and those distal arterial lesions are less suitable for revascularization. That means the patients suffering from both diabetes and distal arterial lesions have a higher probability to be amputated. In fact, the deterioration process of diabetic foot ulcers and the severity of limb ischemia could be predicted and those predictive parameters could provide reference for the choice of intervention. Based on some previous investigation of concomitant microcirculatory disturbances [59, 60] and numerous studies about hemorheological impairments in ischemic limb [61, 62], Khodabandehlou, T. and Le Devehat, C. [63] designed their experiment and concluded that, the combination of hemorheological and transcutaneous oxygen pressure (TcPO2) measurements might forecast or monitor the disease progression in diabetic patients, so as to make an early diagnosis of amputation. Over the past decade, researchers are constantly trying new therapies or adjuvant medications to avoid amputation, for example, the vascular endothelial growth factor gene-carrying plasmid by intramuscular administration---phVEGF165 [64], the hypertensive extracorporeal limb perfusion [65], and the stent implantation including drug eluting stent [66-69]. Although these methods could more or less improve the hemodynamic state, from a long-term point of view, they are only expediencies for temporary relief but did not significantly reduce the amputation rate.

When a patient has to be amputated because of trauma, malignant tumor, neuropathy etc., or due to all standard treatment options of peripheral vascular disease have been exhausted, the decision of amputation level, namely residual limb length is particularly important. The amputation level evaluation must follow the principles of both etiology and functionality. Etiological criteria are to remove all diseased, abnormal and inactive tissues, and to operate at the most distal site where the soft tissue is in good condition and the skin can achieve satisfactory healing. Functional criteria are to guarantee that the patient can wear prosthesis, can carry on rehabilitation training wearing prosthesis, and can be restored to independent movements and self-care. In recent years, with the application of total surface bearing socket and increasing sophisticated prosthetic fitting technology, amputation level selection has obviously changed. Today, the general principle is to retain RL as long as possible on the premise of that the etiological criteria are achieved in order to make its function be maximized. Amputation level has a direct impact on the installation and compensatory function of prosthesis, the energy expenditure and the ambulation rate while walking with prosthesis, so it requires an extremely prudent choice. Since the 70s of last century, various hemodynamic evaluation techniques have been used as valuable aid to clinical judgment to choose amputation level. As early as in 1979, Lee, B.Y., et al. [70] reported that compared with the indication of vascular status given by blood pressure measurements, a more accurate result could be provided using noninvasive electromagnetic flowmeter to measure the peak pulsatile flow especially for patients with severely calcified non-compressible arteries. Subsequently, by the measurements of local and cutaneous blood flow and pressure, blood volume, and skin temperature, Cheng, E.Y. [71] concluded that the skin capillary blood flow was the most accurate parameter for predicting the wound healing potential. In fact, at the beginning of the past two decades, many test methods had been available to assist in predicting the likelihood of successful healing of residual limb, for instance, the measurements of ankle-brachial index, segmental pressure and pulse volume [72], partial TcPO2, laser Doppler flow indexes, skin perfusion pressure and thermography [73]. However, none of them have been widely recognized and applied. In 1995, Adera, H.M., et al. [74] used their statistic analysis results to produce the evidence that, the painless, quick and simple laser Doppler skin perfusion pressure test is a reliable method for selecting major amputation level. Then, Wutschert, R. [75] and Misuri, A. [76] et al. validated that the accuracy threshold of TcPO2 is 20 mmHg with an accuracy of approximately 80%. By the year 2006, the clinical controlled trial of Figoni, S.F., et al. [77] demonstrated that laser Doppler imaging flux with local heating performed more accurate than TcPO2, and it also provided the capability of detecting a proximal to distal gradient of perfusion which reflected the advantage in amputation level selection. Another clinical controlled trial was carried out in 2010 by Scremin, O.U., et al. [78]. From the outcomes it could be learned that the H215O positron emission tomography (H215O-PET) technique could reliably identify ischemia at the distal limb level, and there was no significant differences between the performances of muscle blood flow, TcPO2 and laser Doppler imaging. It indicated that skeletal muscle blood flow could be used routinely to help determine the optimal site of amputation.

In a brief summary, all amputation sites are selected with the intent of successful primary healing, while the aim and significance of longest possible residual limb are to preserve maximal mobility and function. Many reliable and complementary indicators could be employed to assist in determining the level of amputation, but none of them is absolute or universal. The accuracy of each hemodynamic parameter is different against specific diseases, conditions (major or minor amputation) and tissues (skin or skeletal muscle). Although no indicator can replace good clinical judgment, the integration of these parameters with other clinical criteria may optimize prognosis and reduce re-amputation rate to the utmost.

1.4.2 Improvement of surgical techniques

Surgical principles of amputation involve the comprehensive treatment of bone, muscles, nerves, blood vessels and skin. Briefly speaking, the maturation process and major evolution of the surgical techniques of limb amputation have been made from the 16th to the 18th century [79]. During that period, the artery forceps and vessel ligation were introduced by Pare, and soon afterwards Morell introduced the tourniquet to reduce the bleeding. As of today, lower limb amputation can be called a ripe and meticulous surgery.

For the teaching theoretical handling of blood vessels, except the ischemic limb with vascular disease, the other types of amputation should apply a tourniquet in order to provide a clear non-bleeding surgical field. The large vessels should be freed and double ligated (ligated and sutured) separately before being cut off. For smaller vessels, single ligation could be employed, but even the fine vessels need a complete hemostasis. Prior to closing wound, deflate the tourniquet and clamp all the bleeding points using vessel forceps, followed by ligation or electrocautery hemostasis. Since careful hemostasis is very important for avoiding the formation of hematoma and infection. The use of tourniquet in amputations with different causes is a controversial issue that should not be ignored. The usage history of pneumatic tourniquets is long in orthopedics and trauma. But when the surgery is for patients suffering from severe peripheral vascular diseases, the tourniquet application is a contraindication in current teaching theories, because many references recorded vascular complications that might be caused by a tourniquet. Despite this, there are some clinical studies to challenge this rule and to verify the safety of liberal use of tourniquets. Bruce, A.S., et al. [80] used a tourniquet in 92 total knee arthroplasties, and there was no postoperative wound infection, limb ischemia indication or the complications associated with tourniquet use. Moreover, the median ankle-brachial index increased significantly. These results encouraged Wolthuis, A.M., et al. [81] to conduct a controlled study of trans-tibial amputations. In their study, 42 patients who had end stage peripheral vascular diseases underwent a trans-tibial amputation with a tourniquet. The results showed that employing tourniquets in the surgeries did not lead to deep vein thrombosis, acute postoperative skin flap necrosis and other associated complications. The non-tourniquet group and the tourniquet group had similar postoperative morbidity rates, but the need for transfusion, the residual limb revision rate and the re-amputation rate of the former were all significantly higher. Subsequently, Choksy, S.A., et al. [82] performed a randomised controlled trial on 64 transtibial amputated patients due to peripheral arterial diseases, and similar conclusions were drawn. Although the types of tourniquet used in these two studies were distinct, both of their conclusions were that, the tourniquet application was safe and could significantly reduce intra-operative blood loss and transfusion requirements. In 2006, Welling, D.R., et al. [83] made a detailed and comprehensive summary about the application of tourniquets from the historical, double-sided of pros and cons, military and civil perspectives. They reported that in the modern operating room, tourniquets are used with very few complications or mishaps. However, today even for traumatic surgery or amputation, the tourniquet use is still controversial especially the pre-hospital use [84, 85].

Besides the traditional controversy of tourniquet, the new concept of angiosome, which was given rise by the corresponding anatomical territories of a source artery in the skin and deep tissues, has also been widely discussed in recent years. The perfusion of residual limb often affects the chance of recovery. For most patients suffering from peripheral arterial disease, in addition to major amputation, the optimization of perfusion may require bypass or angioplasty. Taylor, G. I. and Palmer, J. H. [86] presented the concept of angiosome in 1987, and they thought the adequately perfused angiosomes, namely three-dimensional tissue blocks could be used to create a viable RL. Then, Taylor, G. I. and Pan, W. R. [87] specifically defined the angiosomes of lower limb. The findings of these angiosomes combined with the patient's individual vascular anatomy, provide the basis for better planning of incisions and make it possible to reserve the functional length of a residual limb. In recent years, there are many studies focusing on the application of angiosomes in revascularization [88, 89], but works with respect to amputation or residual limb are still few.

Overall, there is no significant technical innovations of vascular management in lower limb amputation over the past two decades, but the concerns about hemodynamic factors has been maintained. Postoperative wound healing, tissue perfusion and the incidence of various complications directly indicate the recovery potential, while these are closely related to the blood flow state of residual limb. A good operation is a critical procedure for reducing the risk of reamputation and promoting the long-term rehabilitation. Therefore, some unsettled or controversial issues deserve more detailed research.

1.4.3 Residual limb problems

For those prevalent RL problems such as pressure ulcers, deep tissue injury (DTI) and MA, some investigators have taken into account the blood flow state and obtained valuable research findings.

Among a considerable number of hypotheses for the occurrence of pressure ulcer, the local ischemia, hypoxia and malnutrition arising from blood flow occlusion may be the earliest one. The consensus of this hypothesis is that pressure ulcers are generally associated with external pressures exceeding internal capillary pressures [90, 91]. Developed from the ischemia and hypoxia theory, the hypothesis of reperfusion injuries concomitant with reactive hyperemia is a study hotspot in the pathogenesis of pressure ulcers in recent years. Sundin, B.M., et al. [92] studied the effects of intermittent pressure and two anti-free radical agents on pressure ulcer prevention in a pig model, and an intermittent pressure of 150 mmHg was used to produce reperfusion injuries resembling the early stages of pressure ulcers. By quantifying the cutaneous blood flow, transcutaneous oxygen tension, skin and muscle damage, and muscle levels of adenosine triphosphate, they found that the damage secondary to ischemia was induced by the repeated pressure application in tissue, and both allopurinol and deferoxamine could increase cutaneous blood flow and tissue oxygenation, whereas only the latter could remarkably prevent cutaneous and skeletal muscle necrosis. Through their animal experiments, Tsuji, S., et al. [93] observed that the repetition of ischemia-reperfusion cycle damaged the microcirculation more heavily than the single lengthy ischemic insult, because the cyclic compression-release procedure more significantly decreased the functional capillary density. For breaking the perfusion measurement limitation in cutaneous microcirculation, Bergstrand, S., et al [94] employed a multiparametric system combining laser Doppler flowmetry and photoplethysmography into a single probe to do the simultaneous measurement of blood flow at different depths in the tissue exposed to external loading. The result analysis showed that the laser Doppler flowmetry combined photoplethysmography could measure a larger area and reflect the difference of blood flow responses in the different depths of tissue. So it was believed that this new system could promote the understanding of pressure ulcer formation. As the above examples, most of the hemodynamic studies about pressure ulcers are for normal lesion-prone areas including lower limb, but not specifically for the residual limb. Although there are some biomechanical researches [17] or treatment optimization studies [95, 96] for residual limb ulcer, few of them considered the blood flow.

Pressure ulcer is often considered as the most easily observed skin problem with the highest incidence. In fact, tissue damage caused by pressure appears from deep to shallow. In the early stages, Daniel, R.K., et al. [97] performed a controlled animal trial to continuously monitor the pressure-duration threshold for the pressure ulcers formation. From their full-thickness damage analysis from bone to skin, the conclusion was that muscle is more sensitive than skin to the effects of pressure, so the initial pathologic changes actually happen in muscles. The works of Salcido, R., et al. [98] and Bouten, C.V., et al. [99] further corroborated that underlying muscle tissue showed lower tolerance to the damage from mechanical loading and hypoxia compared with skin. The former using a rat model demonstrated that the lesion most often associated with pressure was necrosis of the panniculus carnosus muscle accompanied by underlying adipose tissue damage. The latter reported that the influencing factor of capillary closure is not only the interface pressures at skin level, but also the local pressure gradients across the vessel wall. In 1990, Levine, S.P., et al., [100] first proposed that electrical stimulation could effectively help to prevent pressure ulcers by improving the muscle blood flow. Since then, a number of researchers have investigated the effectiveness of electrical stimulation on increasing muscle mass and thickness [101, 102], producing positive short-term changes in local blood flow and pressure distribution [101], increasing tissue oxygen levels [101], and improving muscle blood flow meanwhile reducing regional interface pressures [102]. Based on the widespread recognition of the above benefits of electrical stimulation, Solis, L.R., et al. [103] examined the impact of intermittent electrical stimulation on DTI in 2007. They did a contrast experiment on the quadriceps muscles of rats and a case study on a human volunteer. The findings combined the subsequent research of them in 2011 [104] could interpret the dual mechanism of intermittent electrical stimulation as follows: on the one hand, intermittent electrical stimulation-induced contractions reduced the high stress levels at the muscle-bone interface; on the other hand, each contraction would also contribute to the periodical blood flow restoration and the enhancement of tissue oxygenation, in this way to reduce the damage caused by durative ischemia-reperfusion. Therefore, they suggested that intermittent electrical stimulation may be an effective means for the prevention of DTI.

As for the most common problem MA, a minority of researches related to blood flow discussed the pathological features and occurrence mechanism of it. A control experiment carried out by Tyml, K., et al. [105] suggested that the short-term tetrodotoxin-induced atrophy affected both microvascular structure and resting state blood flow in skeletal muscle, but it maintained the absolute number of capillaries and did not alter the pattern of reactive hyperemia. Brevetti, L.S., et al. [106] ligated the left common iliac, femoral arteries and their branches of rats to set an ischemic environment for peroneal nerve stimulation, and then monitored the blood flow rates of exercise-induced region. According to the data of tibialis anterior and gastrocnemius muscles, they found that although ischemia caused pressure ulcers, MA and weakness, the resting blood flow rates of muscles were not significantly different from those of control rats. However, the hyperemia, namely the blood flow increase of muscles induced by peroneal nerve stimulation was significantly weakened in the ischemic group compared with the control group. This study provided an inspiration that the hyperemia induced by nerve stimulation may assist to evaluate and improve the therapies for ischemic MA. In microscopic research, as mentioned in the previous section, blood flow is usually involved in the studies about muscle protein synthesis and degradation or apoptosis. For example, Wang, Q., et al. [107] evaluated DNA degradation in nuclei of muscle cells during ischemia in a rabbit limb amputation model. A bone marrow cell therapy was performed by Liu, Q., et al. [108] on a model of severe lower limb ischemia, and they proposed that through this therapy, the skeletal muscle formation may produce more benefits than angiogenesis to patients suffering from skeletal MA. Caron, M.A., et al. [109] demonstrated a temporal regulation of protein homeostasis which provided a direct evidence for that hypoxia contributed to MA. Huang, C.C., et al. [110] using an ischemic limb of mouse model verified that the gratifying results of cell transplantation for neovascularization included promoting functional vessels formation, improving regional blood perfusion, and significant weakening bone losses and MA.

From the perioperative stage to lengthy rehabilitation process, lower limb amputees need comprehensive and cautious therapies to help them rebuild their physical and mental confidence. Hemodynamic study consistently runs throughout the entire treatment period and played a significant positive role. Whether from clinical or biomechanical perspective, the investigations of preoperative diagnosis and surgical techniques have been relatively mature and gained some clear outcomes. Whereas in terms of the postoperative problems, there is a lack of vascular or blood flow state studies specifically for lower RL. Therefore, the detailed researches on the relationships between various blood flow parameters and certain common complications are pending to be carried out.

1.5 MULTI-SCALE NUMERICAL MODEL OF BLOOD CIRCULATION SYSTEM

Blood circulation system continuously transports oxygen and nutrients to various target organs, while taking away metabolites, delivering hormones and signal substances, as well as participating in temperature regulation, in order to coordinate the entire body's function. Therefore, to maintain the blood circulation system in a good operating state is the basic premise of human health. Since 1628 Harvey created blood circulation theory, the cardiovascular hemodynamics which sought to explore mysteries of the circulation system has been developing with each passing day. From the Windkessel theory [111], the pulse wave theory [112], the arterial pulsatile flow theory to the fluid transmission line theory [113], it has grown into a relatively systematic new interdisciplinary today. With the rapid development of computer technology, the numerical simulation of circulation system as an important research tool has become the key technology to study the systemic characteristics of blood flow from various aspects.

1.5.1 Classification of circulation system models

Commonly used vascular models include the lumped parameter models, one-dimensional (1D), two-dimensional (2D) and three-dimensional (3D) distributed parameter models (as shown in **Figure 1.8**).

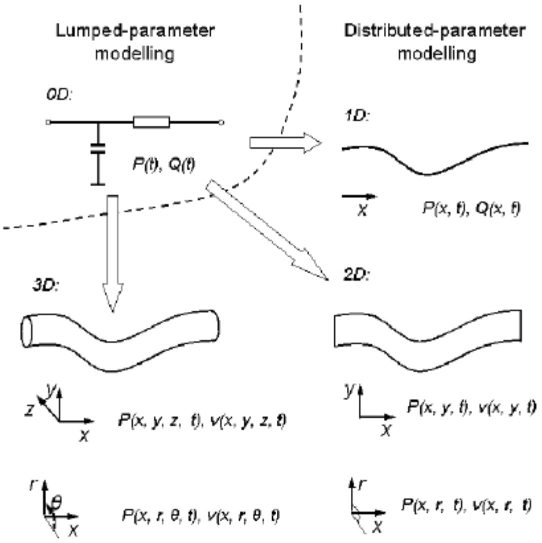

Figure 1.8 Schematic diagram of vascular models with different scales [114].

Lumped parameter model, namely 0 dimension (0D) model, in a nutshell is dividing blood vessels into finite segments, and in each segment (the segment length is *l*), taking into account that the wavelength of pulse wave is much greater than *l*, so it could approximately consider the time derivative of the pressure and flow of this segment would not change along the tube axis. Then the distributed parameter transmission line equation is integrated along the tube axis, and thus the lumped parameter transmission line equation and the corresponding network element model which characterise the flow in this segment can be obtained. This approximate method is based on the principle of "electro-hydraulic analogy", that means the congruent relationship of voltage---blood pressure, electric current---blood flow, capacitance---liquid capacity (compliance), electric resistance---liquid resistance, inductance---fluid inertia. The advantage of lumped parameter model is not only to simplify the processing of equations, but also to effectively describe the variation of concentrated pressure, concentrated flow and concentrated resistance, etc. along the pipeline of entire system. Noordergraaf, A., et al. [115] have created a computer model of arterial system considering all the main branches of aorta, and the system was composed of many lumped parameter units. They discussed the unit length issue and concluded that the appropriate length was 6cm by simple calculation and comparison. Westerhof, N., et al. [116] proposed a more detailed arterial tree model which contained almost all the main artery branches, and by this model they presented a new "π" shape network model that could simply simulate the geometry and the elastic taper of arteries. Subsequently, Westerhof, N. and Noordergraaf A. [117] further introduced the viscoelastic mechanism of vascular wall into this systemic arterial system. Pietrabissa, R., et al. [118] built a lumped parameter model of full circulation system containing coronary artery as shown in **Figure 1.9**.

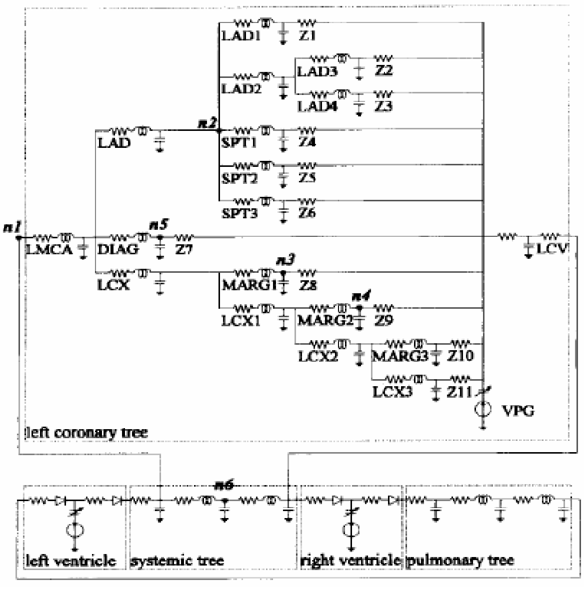

Figure 1.9 The lumped parameter model of full circulation system [118].

Since the building and calculation of lumped parameter model are relatively simple, fast and easy to solve, it is still widely used until today. However, the result of lumped parameter model is obtained by integral along the vascular axis, it cannot specifically describe the flow characteristics of local blood vessels. Meanwhile, some important nonlinear phenomena of arterial system such as nonlinear wall compliance are difficult to be simulated by linear models. Therefore, the detailed hemodynamic study of a certain vessel need more precise distributed parameter model. The 1D, 2D and 3D models all belong to distributed parameter model, and their differences lie in the selections of coordinate axis and direction vector. In this regard, the studies of Taylor, M.G. [119, 120] were groundbreaking. He built the randomly branching elastic tube model of systemic arterial system and suggested several basic ideas for the later complex simulation from his results: (1) the arterial tree branches and its distributed parameter features could greatly reduce the effect of wave reflecting on the input impedance; (2) the viscosity of arterial wall was the main source of attenuation in large vessels; (3) blood viscosity only performed significant impact in small arteries; (4) changes in vessel cross-sectional area had great influence on wave propagation (Fan, Y.B., 1992).

Although quasi-1D model is relatively simplified, but it can be a good solution to the expandable pulsating flow problem of 1D case. Since Schaaf, B.W. and Abbrecht, P.H. [121] constructed the motion equation and the continuity equation of quasi-1D expansion tube pulsating flow, so far, there are still many studies using 1D model to simulate the entire systemic circulation or some local arteries [122, 123]. 2D model is neither as simple as 1D model nor as accurate as 3D model, so the hemodynamic study using 2D distributed parameter model is relatively rare. But there were also researchers employed 2D model to simulate and analyze the fluid-structure interaction or drug delivery issue [124]. Unlike the 1D and 2D models which are constructed through many assumptions and simplifications, the 3D model is a kind of mathematical model directly based on 3D Navier-Stokes equation (N-S equation). So it is the most accurate simulation method to study blood flow. However, its limitations are that 3D modeling is relatively difficult, time consuming, requiring large computation and difficult to obtain convergence results, plus a variety of complex boundary conditions, so there is no complete 3D model of systemic circulation has been reported. At present, it is mainly used in the local vascular segments simulation. In recent years, with the development of computer technology, both modeling accuracy and calculation speed are improved, so the 3D model is more and more employed to simulate the high incidence area of cardiovascular diseases, such as coronary artery [125, 126], carotid artery [127-129], aortic arch [130] and pulmonary artery [131].

1.5.2 Application of multi-scale model

If only the local vessels with high precision demand are established to be 3D model, this region is artificially considered as an isolated system, and thus only the characteristics of the regional blood flow could be gained while ignoring the influence of systemic or full circulation system. In addition, the boundary conditions of the independent 3D model are not easy to obtain in the real physiological condition, which makes the numerical simulation results have certain hypothesis error. In order to get closer to the real physiology, researchers used 0D or 1D model which is relatively simple to simulate the systemic or full circulation, meanwhile applying 3D model on the focused area, and then performed the mathematical coordination of the boundary conditions of two different scale models to couple them. Finally, the simulation result combining physiological status and local accuracy could be achieved, that is the application of multi-scale vascular model. For example, in 1999 Quarteroni, A., et al. [132] created a multi-scale model including the 0D model of full circulation system, 1D model of aorta and 3D model of carotid. The findings indicated that the results of multi-scale model and pure 0D model were basically consistent, but the multi-scale model did better reflect local hemodynamic characteristics. In 2005, Lagana, K., et al. [133] carried out the 3D modeling of systemic and pulmonary arteries for two different shunt modes (central shunt and side shunt) in Norwood surgery coupling the 0D model of full circulation system (as shown in **Figure 1.10**). The effects of different shunt diameters on pulmonary artery and coronary circulation were separately analyzed in the two models, and the conclusions had an important significance for the assessment of coronal arterial circulation and ventricular function. In 2009, Liang, F., et al. [134] used 1D model to describe the main arterial tree of the whole body, and used 0D model to simulate the other parts, thereby coupling the entire cardiovascular system into a computational model (as shown in **Figure 1.11**). This multi-scale model formed a closed loop, which made the arterial wave propagation form a global hemodynamic environment. The model was applied to study the effects of the different locations of aortic vaives and arterial stenosis on the overall blood flow.

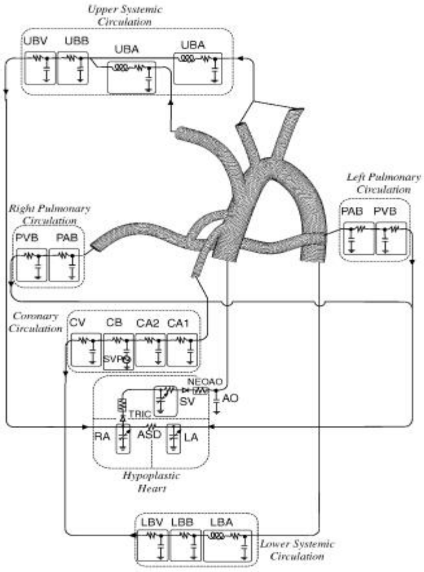

Figure 1.10 The multi-scale model of Norwood central shunt [133].

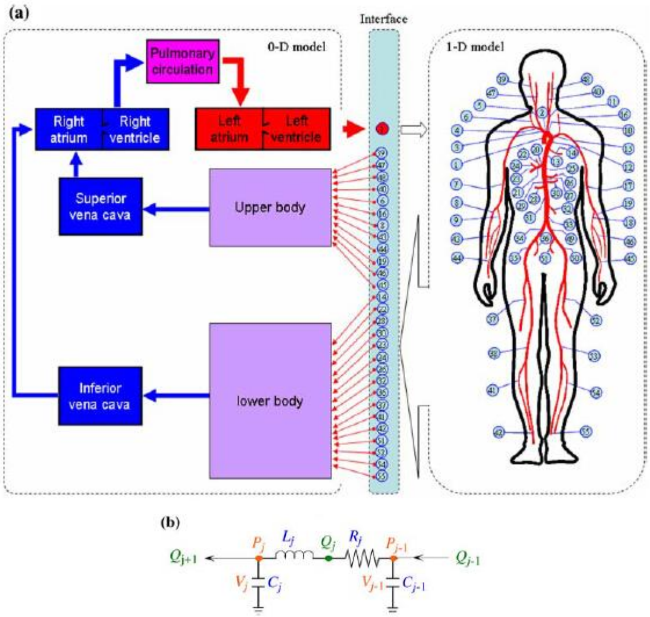

Figure 1.11 A multi-scale model of cardiovascular arterial system [134].

As can be seen from the above review, the complexity of the model construction should depend on the number of variables simulated and the vessels distribution of the target part, etc. instead of one-sided pursuit of complexity or simplicity.

1.5.3 Application of lower limb model

Since relatively simple and easy to detect, a considerable number of vascular simulation theory and solution methods were applied first on limb blood flow (particularly the arteries). In 1974, Raines, J. K., et al. [135] established a leg artery quasi-1D nonlinear simulation model and solved it using the finite difference method. Law, Y. F., et al. [136] used a simple lumped parameter model to characterize the arterial system of lower limb in 1983, and this model could predict success or failure of surgery with the help of a discriminant function. Porenta, G., et al. [137] built the finite element model of human femoral artery with coarctation, stenosis, branches and other phenomena for carrying out the numerical simulation. Willemet, M., et al. [138] implemented and compared different inlet boundary conditions of a 1D blood flow model, and tested their boundary conditions on the patient-specific lower limb model of a femoral bypass.

In summary, the multi-scale numerical model of blood circulation system has achieved rapid development and full utilization in recent decades. Its value and important clinical significance have been authenticated by many hemodynamic or biomedical studies. However, in lower extremities especially the RL after amputation, there is no relevant reports. In order to explore the specific distribution of blood flow within RL, in this study, we choose the multi-scale model which coupling the 3D model of lower limb arterial tree and the lumped parameter model of peripheral resistance to perform the calculation of hemodynamic parameters.

1.6 RESEARCH WORK OF THE THESIS

From the introduction of thigh physiological anatomy, the literature review of lower limb muscle atrophy and hemodynamics, as well as the development history of the multi-scale numerical model of blood circulation system, we can sum up the relatively mature or untapped research directions as follows:

(1) A lot of phenomenon illustrations of the clinical symptoms of RL MA have been done. Various theoretical studies about the pathogenesis of disuse atrophy have contributed many valuable results. However, since the microscopic pathological research is highly specialized and complex, at present the unanimous conclusion has not yet been achieved, and the animal models or experimental methods employed by most studies have not been used for the investigation on lower RL.
(2) The therapeutic strategies of RL MA, including rehabilitation training, drug treatment, physical therapy, as well as the technical changes in surgery, immediate postoperative management and prosthetic design, have been in development and improvement. However, there is still a certain distance away from the solution of this problem.
(3) In the hemodynamic direction, the earliest and most mature application associated with lower limb amputation is the determination of treatment options and amputation level. There is no significant technical innovations of vascular management in the surgical operation over the past two decades, but the concerns about hemodynamic factors has been maintained. Some unsettled or controversial issues deserve more detailed research. As for the solutions of common RL problems, many studies more or less considered the influence of blood factors in non-amputated limb, but there is still a lack of systemic vascular or blood flow state studies specifically for lower RL.
(4) In terms of technical means, the multi-scale numerical model of blood circulation system has achieved rapid development and full utilization in recent decades. Its value and important clinical significance have been authenticated by many studies. However, in lower extremities especially the RL after amputation, there is no relevant reports.

Therefore, this thesis strives to combine the clinical and biomechanical perspectives, and conducts the quantitative analysis and case study of unilateral trans-femoral amputees. Specific work contents are as follows:

(1) Recruited unilateral trans-femoral amputees as the clinical experiment subjects by cases screening, and performed enhanced CT scan, MRI scan and Doppler ultrasonography on the both thighs of each subject.

(2) By measuring the morphological indexes of thigh muscles and arteries using the MRI and CT images, the quantitative comparison and analysis of MA degree and arterial narrowness degree were carried out respectively, and then discussed their correlation and the potential influence factor. Meanwhile, using the concept of Hausdorff distance, investigated the spatial structure deformation degree of bilateral vascular trees of two follow-up cases.

(3) Based on the arterial CT images, established the 3D models with finite element analysis (FEA) and computational fluid dynamics (CFD) format of main arteries. The ultrasonic data was applied to set up the boundary conditions of calculation. After convergence, compared the distribution of steady flow field in each artery of bilateral limbs.

(4) Combining the 3D model of main arteries and the lumped parameter (0D) model of peripheral resistance, and the coupling calculation mothed, the distribution of hemodynamic parameters during a cardiac cycle was obtained. Then did the bilateral contrast analysis.

(5) Compared the steady flow results of 3D model with the unsteady flow results of multi-scale model to discuss the methodology of modeling and numerical simulation.

(6) Compared the numerical calculation results and the morphological measurement results to check the consistency of the quantitative investigation conclusions at different angles. Proposed some suggestions on the use of methodology in different purposes and conditions.

CHAPTER 2: CLINICAL DATA COLLECTION

2.1 INCLUSION CRITERIA AND CASE SCREENING

The subjects of this study are unilateral trans-femoral amputees. The research purpose is to detect and compare the thigh muscles and arteries states of their residual limb (RL) and sound limb (SL). Since this frontier study with a pioneering feature is mainly aimed to explore some unknown phenomena and the conclusion is expected to be applicable to as many patients as possible, the amputation reason is not an inclusion criterion, which means the patients amputated by any cause could be a candidate. Besides the same reason, the detailed case study about the RL state would discuss the influence of movement form, so wearing prosthesis is not an inclusion criterion too. That means whether or not the patient wears a prosthesis, what kind of prosthesis, whether or not participates in rehabilitation training or regular exercise, he/she could be a candidate. As for the time length after surgery, it is concerning the recovery and the atrophy degree of RL, thus the follow-up patients are limited to the initial stage of rehabilitation (the first year after amputation [35]), and the other cases have no time limitation. Compared to these relaxed conditions, the good wound healing and skin condition of RL is necessary in order to minimize the impacts of pressure ulcer, deep tissue injury and other problems on muscles and blood vessels. In addition, patients still with peripheral vascular diseases of lower limb after amputation were excluded for avoiding the interference of various lesions to hemodynamic parameters.

Based on the research objectives and the representativeness of samples, the inclusion criteria of this clinical experiment subjects are as follows:

(1) unilateral trans-femoral amputees;

(2) age between 18 and 60 years old and the gender is not limited;

(3) the amputation level is middle or lower thigh to provide the RL length;

(4) no specific vascular procedure for injured blood vessels during the amputation;

(5) received a current general standard postoperative immediate treatment,

implying the normal postoperative muscle initial state;

(6) no peripheral vascular diseases of lower limb after amputation;

(7) good skin and soft tissue conditions of RL with no obvious injury;

(8) no long term bedridden or sedentary, with the ability of independent movement (no limitation on the use of a prosthesis);

(9) the follow-up patients received three times examinations within the 1st year after surgery, and the single examination subjects have no time limitation.

This project has obtained the approval of the Human Subjects Ethics Sub-committee of The Hong Kong Polytechnic University, and the cooperation unit is West China Hospital of Sichuan University. There is a total of 291 cases of amputees in the Department of Orthopedics of West China Hospital from 2010-2013. 59 unilateral trans-femoral cases with middle/lower amputation level were preliminarily screened out, and then 17 patients who met all the above inclusion criteria were identified. After informing the purpose, examination items, procedures, possible adverse reactions, and privacy protection of this clinical investigation by telephone contact, finally 8 voluntary patients were recruited, including 2 follow-up patients. In these 8 cases, there are 2 females and 6 males, aged between 20 and 48 years old. Their personal details are as follows:

Case-1: female, 20 years old, left thigh middle level amputation caused by bone tumor. Used a total-surface-bearing prosthesis for daily walking since the 6th month after surgery. Received 3 times follow-up examinations within the 1st year after surgery.

Case-2: male, 43 years old, left thigh middle level amputation caused by bone tumor. Used crutches for daily walking during the follow-up period. Received 3 times follow-up examinations within the 1st year after surgery.

Case-3: male, 28 years old, left thigh middle level amputation caused by bone tumor. Used crutches for daily walking instead of a prosthesis. Received the examination at the 10th month after surgery.

Case-4: male, 29 years old, right thigh lower level amputation caused by trauma.

Used a total-surface-bearing prosthesis for daily walking. Received the examination at the 30th month after surgery.

Case-5: male, 28 years old, right thigh middle level amputation caused by trauma. Used crutches for daily walking instead of a prosthesis. Received the examination at the 16th month after surgery.

Case-6: male, 48 years old, right thigh middle level amputation caused by bone tumor. Used a total-surface-bearing prosthesis for daily walking. Received the examination at the 33rd month after surgery.

Case-7: male, 46 years old, left thigh middle level amputation caused by trauma. Used a total-surface-bearing prosthesis for daily walking. Received the examination at the 31st month after surgery.

Case-8: female, 43 years old, left thigh middle level amputation caused by trauma. Used a total-surface-bearing prosthesis for daily walking. Received the examination at the 16th month after surgery.

2.2 EXAMINATION ITEMS AND MEASUREMENT INDICES

Each subject was arranged to receive his/her MRI (magnetic resonance imaging) scan, enhanced CT (computed tomography) scan, and Doppler ultrasonography of both thighs in the departments of Radiology and Ultrasound of West China Hospital, and these three items were conducted on the same day in order to ensure that the results came from the same physiological state as far as possible. We used Siemens MAGNETOM Avanto 1.5T to do MRI scan, and the enhanced CT instrument was Siemens SOMATOM Definition Flash. MRI scan includes coronal plane, sagittal plane and transverse plane. The slice thickness of these 3 planes are respectively 6.5mm, 8.7mm, 20mm, and the image resolution are 512×512, 256×132, 256×320. Enhanced CT images were used for 3D reconstruction, their slice thickness was 0.2mm and the resolution was 512×512. The Doppler ultrasonic diagnostic apparatus is Philips iU22.

The follow-up interval is 4 months, which means that the 2 follow-up subjects were examined 3 times of those 3 items at the 4th, 8th and 12th month after her/his surgery. The enhanced CT images were used to achieve the 3D reconstruction of arterial tree computational model in the general medical image processing software MIMICS, so that the geometric parameters of each main artery and the spatial deformation degree of arterial trees could be output or calculated. The horizontal MRI images were used to carry out the CSA measurement of each thigh muscle at different positions in the open-source image processing software ImageJ, for the atrophy degree datamation. Whereas the ultrasound data of main arteries were subsequently applied to set up the boundary conditions and the coupling coefficients of multi-scale model in the general FEA software ANSYS. With the support of the measured physiological data, the numerical calculation could more accurately simulate the blood flow and show the distribution of hemodynamic parameters. The specific purposes and the measurement indicators of enhanced CT, MRI and ultrasonography are shown in **Table 2.1**.

Table 2.1 The description of three examination items

Examination item	Enhanced CT	MRI	Ultrasonography
Observation objects	Arteries	Muscles	Arteries
Processing software	MIMICS 15.0	ImageJ 1.49j	ANSYS 14.0
Measurement indices	Hydraulic diameter Circumference Cross-sectional area	Cross-sectional area (at different levels)	Diameter Velocity Resistance coefficient Flow

2.3 TARGET MUSCLES AND ARTERIES SELECTION AND THEIR BLOOD-SUPPLY RELATIONSHIP

For the quantification of MA degree, we used the residual/sound limb ratio of the CSA of each muscle to illustrate. First, according to the general definition of RL length---the distance between ischial tuberosity and the end of RL, the MRI horizontal slices at the 30% (±5%), 50% (±5%) and 70% (±5%) levels of it were selected (as shown in **Figure 2.1**). Considering the amputation level of each case is not the same, the muscle anatomical structure in the midpiece of RL (50% level) was taken as the main basis for target muscles selection. Thus, sartorius (SART), rectus femoris (RF), vastus medialis (VM), vastus intermedius (VI), vastus lateralis (VL), gracilis (GRAC), adductor longus (AL), adductor magnus (AM), semitendinosus (SEMI_T), semimembranosus (SEMI_M) and the long head of biceps femoris (BF), a total of 11 muscles in each thigh (as shown in **Figure 2.2**) were manually measured the CSAs and calculated the bilateral ratio. Since in the 8 cases, there are 6 middle slices without adductor brevis, and the short head of biceps femoris are very small or even negligible in all the middle slices, they are not included in the comparative analysis.

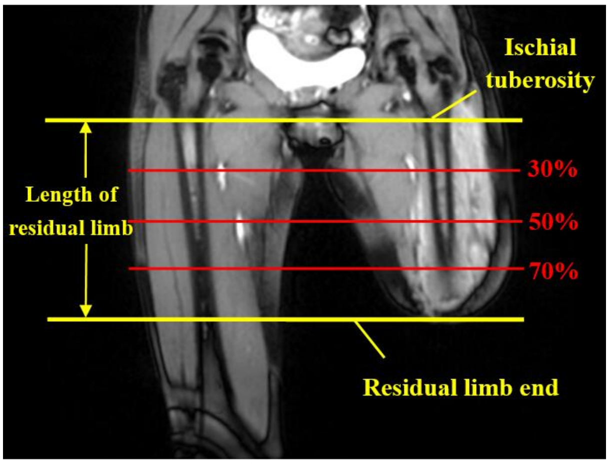

Figure 2.1 The MRI horizontal slices selection: at 30% (±5%), 50% (±5%) and 70% (±5%) levels of residual limb length.

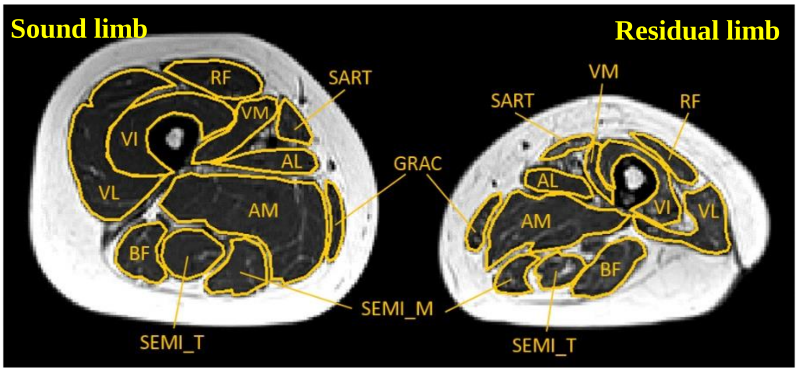

Figure 2.2 The 11 selected target muscles of bilateral thighs (at 50% level).

The structure of thigh arterial tree is complex with numerous branches, therefore based on the anatomy of thigh muscles and arterial system and their corresponding blood-supply relationship introducted in the Chapter 1, common femoral artery (CFA), superfacial femoral artery (SFA), deep femoral artery (DFA), the descending branch of lateral femoral circumflex artery (LFCA) and medial femoral circumflex artery (MFCA) were extracted from the 3D arterial models to compare their hydraulic diameter, circumference, and CSA in RL and SL. The starting points of bilateral CFAs are in the top plane of caput femoris. As for the end position of arteries, in order to correspond to the muscle analysis within the RL length, the vascular model of SL was cut off at the same level with the RL model---in the end plane of residual bone (as shown in **Figure 2.3** and **Figure 2.4**). In this way, the arterial geometrical indices of bilateral limbs in the same section were compared.

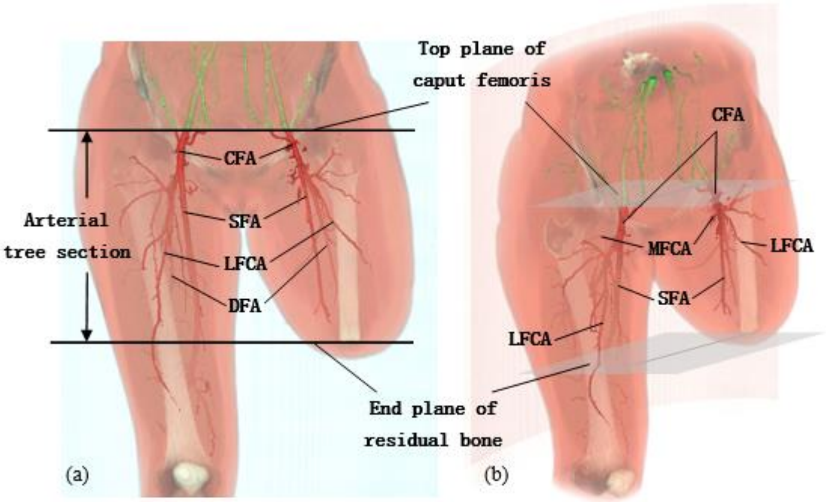

Figure 2.3 The arterial tree section of both thighs and the 5 selected target arteries. (a) the front view; (b) the isometric view.

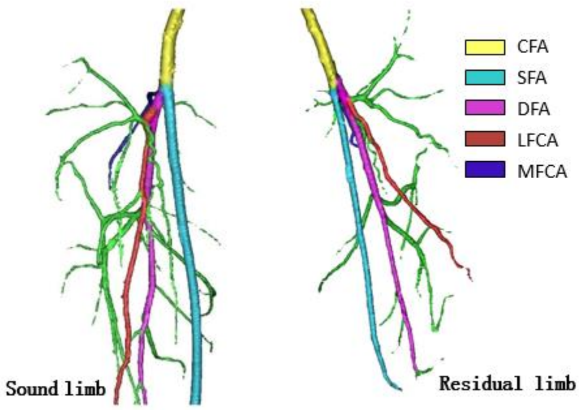

Figure 2.4 The 3D model of bilateral thigh arterial trees.

The corresponding relationship between each muscle and its main nourishing arteries is shown in **Figure 2.5**.

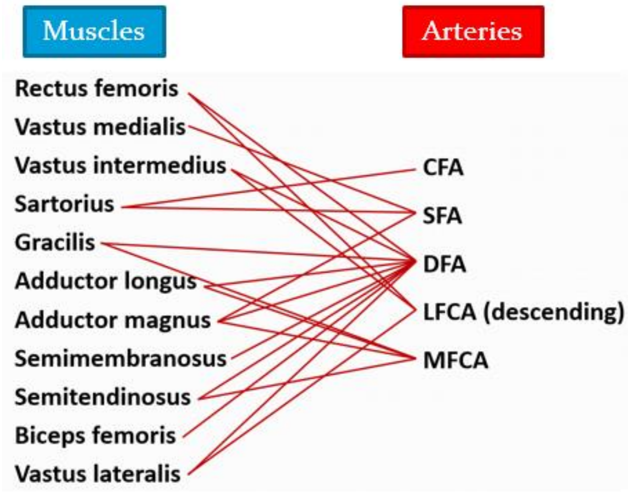

Figure 2.5 Blood-supply relationship between muscles and arteries in thigh.

2.4 MODELING AND DATA MEASUREMENT METHODS

After the clinical examinations, the enhanced CT and MRI images of subjects were respectively imported to the softwares MIMICS 15.0 and ImageJ 1.49j for modeling and morphological measurements.

ImageJ is a public image processing software based on Java developed by National Institutes of Health. It can display, edit, analyze, process, save, and print 8 bit, 16 bit, and 32 bit pictures, supporting TIFF, PNG, GIF, JPEG, BMP, DICOM, FITS and other formats. Image sequence could be imported to ImageJ, so that multiple images could be stacked and parallel processed in one window in the form of multithreading. In addition to the basic operation such as zoom, rotation, distortion and smoothing, it can achieve area and pixel statistics, spacing and angle calculation, the creation of histograms or section plans, and Fourier transform, etc. In this study, we used it to measure the area of a custom polygon in a single image. Importing the selected slices at 3 different levels to ImageJ individually, adjusted the brightness and contrast according to different image quality for the clear and distinguishable boundary of each muscle. Subsequently, manually selected the polygon which fit the target muscle as far as possible and the software would automatically calculate its CSA. Of course, calculating the volume of muscles can best explain the degree of muscle atrophy. But considering the workload and taking reference to previous study, we suggested that the comparison of cross-sectional area could describe residual limb atrophy to a certain extent.

The arterial morphological data were exported from the 3D models reconstructed through the enhanced CT images in MIMICS. The full name of MIMICS is Materialise's interactive medical image control system, which is a highly integrated and easy to use 3D image generation and editing software produced by Materialise company. It could read various scanning data, establish 3D model for editing, and convert the large-scale data by the format output of general CAD (Computer Aided Design), FEA (finite element analysis), and RP (rapid prototyping). The FEA module of MIMICS could export the corresponding format for FEA or CFD. Users could use the scanning data to do 3D modeling, and then perform meshing for FEA analysis. For modeling, we imported the CT images of arterial phase to MIMICS 15.0, and adjusted image threshold to obtain clear arteries, so that femur, skin and soft tissue etc. could be removed to generate the isolated arterial tree 3D model. Besides carrying out CFD calculation on these 3D models for hemodynamic study, in the morphological study part, the MedCAD module of MIMICS could export the geometric series of the target arteries. Through the RL/SL ratio of these indices, the arterial narrowness degree was quantified.

CHAPTER 3: MORPHOLOGICAL STUDY

3.1 CLINICAL MEASUREMENT RESULTS

3.1.1 Results and discussion of muscle morphological indices

This study used the residual/sound limb percentage of the cross-sectional area (CSA) of each muscle to illustrate the muscle atrophy (MA) degree. The 2 follow-up subjects received three times examinations within the first year after her/his surgery and the follow-up interval is 4 months. MRI images carried the unit information millimeter (mm.). After importing them to the processing software ImageJ, the muscle area and the RL length of every subjects were measured and recorded, followed by sorting out and drawing the data into the following charts for the visual display of numerical results.

The follow-up results of Case-1 and Case-2 at 30%, 50%, and 70% levels are shown in **Figure 3.1-3.3** and **Figure 3.4-3.6** respectively. The results at different time after the surgery of Case-3, Case-4, Case-5, Case-6, Case-7 and Case-8 at 30%, 50%, and 70% levels are shown in **Figure 3.7-3.12** respectively.

In the **Figure 3.1-3.6**, the Y axis of (a), (b) shows the name of muscles; the X axis of (a), (b) indicates the CSA (mm2); the Y axis of (c) represents the residual/sound limb ratio of CSA (%); the X axis of (c) indicates the time of follow-up. In the **Figure 3.7-3.12**, the left side of Y axis and histogram represent the CSA of muscles (mm2); the right side of Y axis and line chart show the residual/sound limb ratio of CSA (%); the X axis shows the name of muscles.

Meanwhile, the percentage of total muscle area to total thigh area of bilateral sides at different levels are shown in **Table 3.1** (2 follow-up cases) and **Table 3.2** (Case-3 to Case-8). In the measurement of total muscle area, adductor brevis (AB) and the short head of biceps femoris (BF) were included. The RL length of each subject is shown in **Table 3.3** (2 follow-up cases) and **Table 3.4** (Case-3 to Case-8).

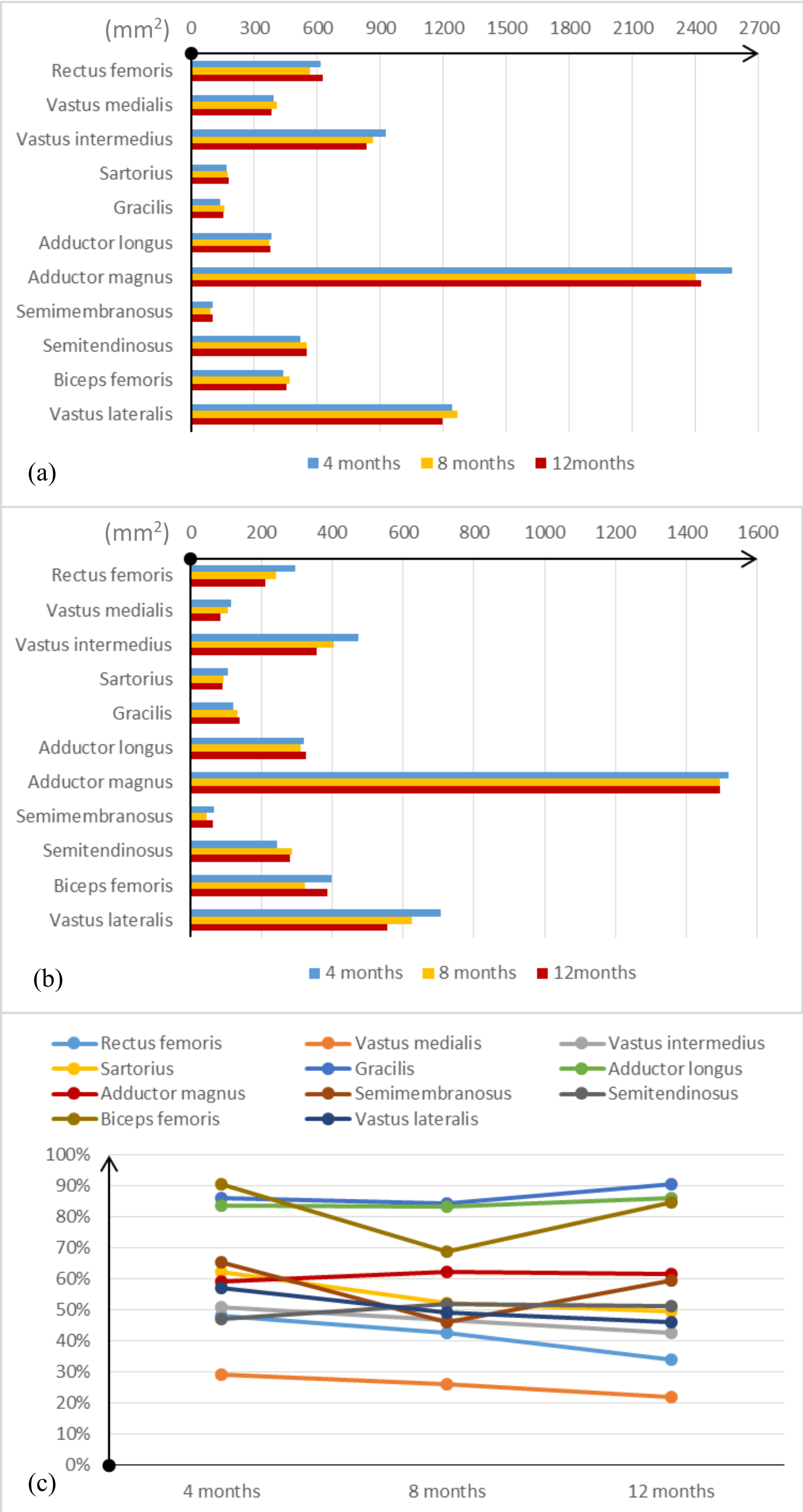

Figure 3.1 The follow-up measurement results of the muscle CSA of Case-1 at the 30% level. (a) sound limb; (b) residual limb; (c) residual/sound limb percentage.

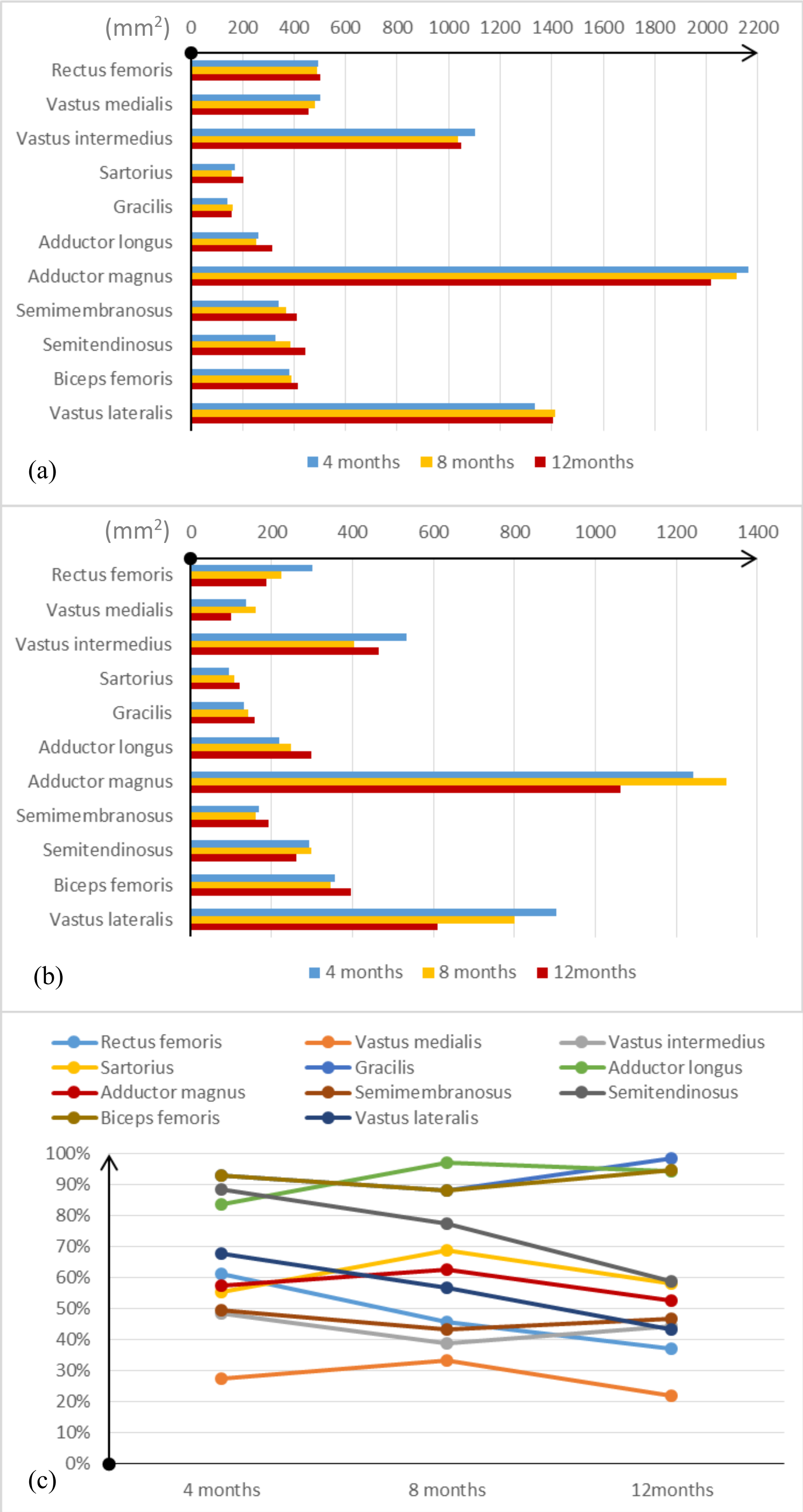

Figure 3.2 The follow-up measurement results of the muscle CSA of Case-1 at the 50% level. (a) sound limb; (b) residual limb; (c) residual/sound limb percentage.

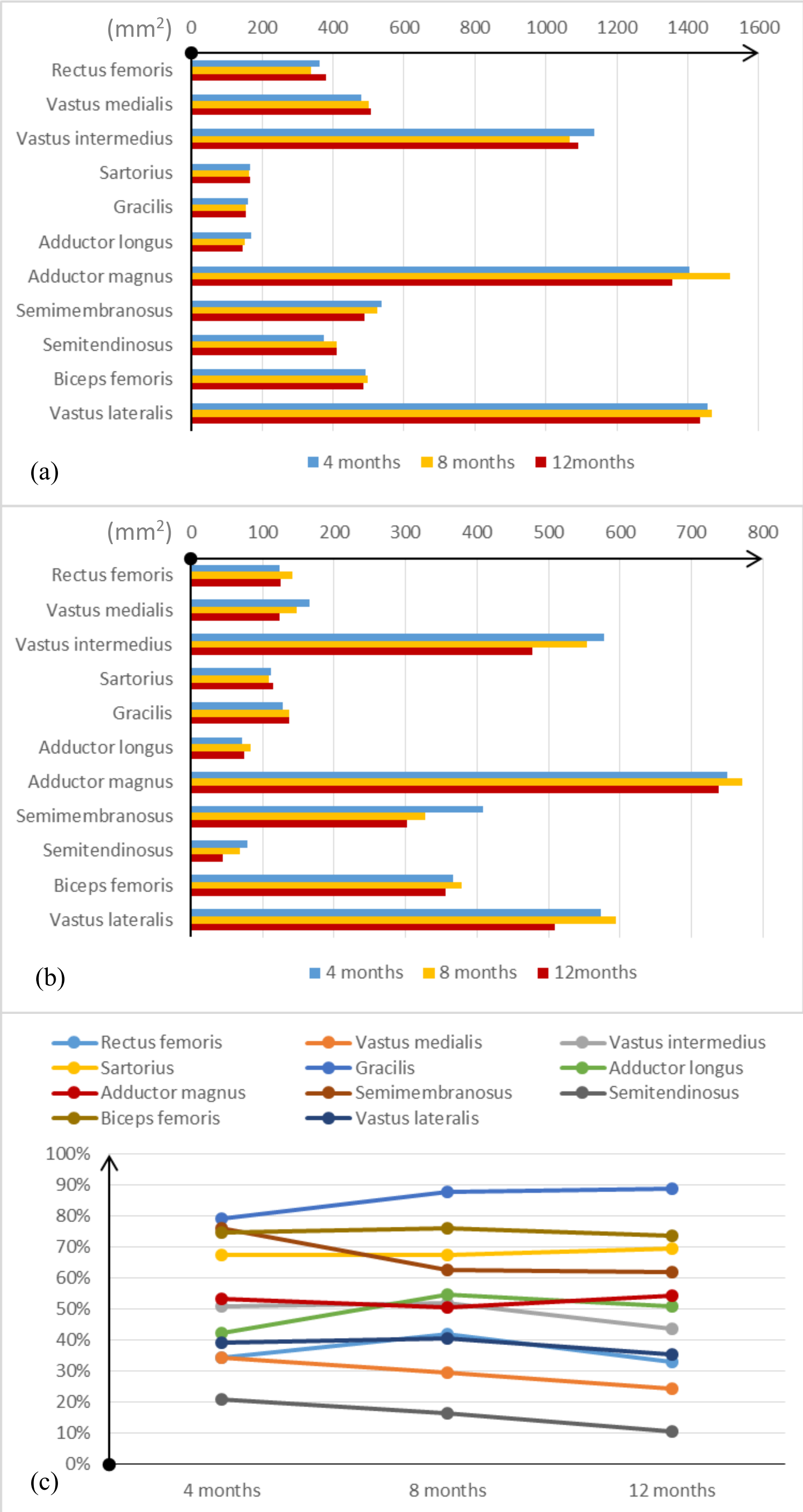

Figure 3.3 The follow-up measurement results of the muscle CSA of Case-1 at the 70% level. (a) sound limb; (b) residual limb; (c) residual/sound limb percentage.

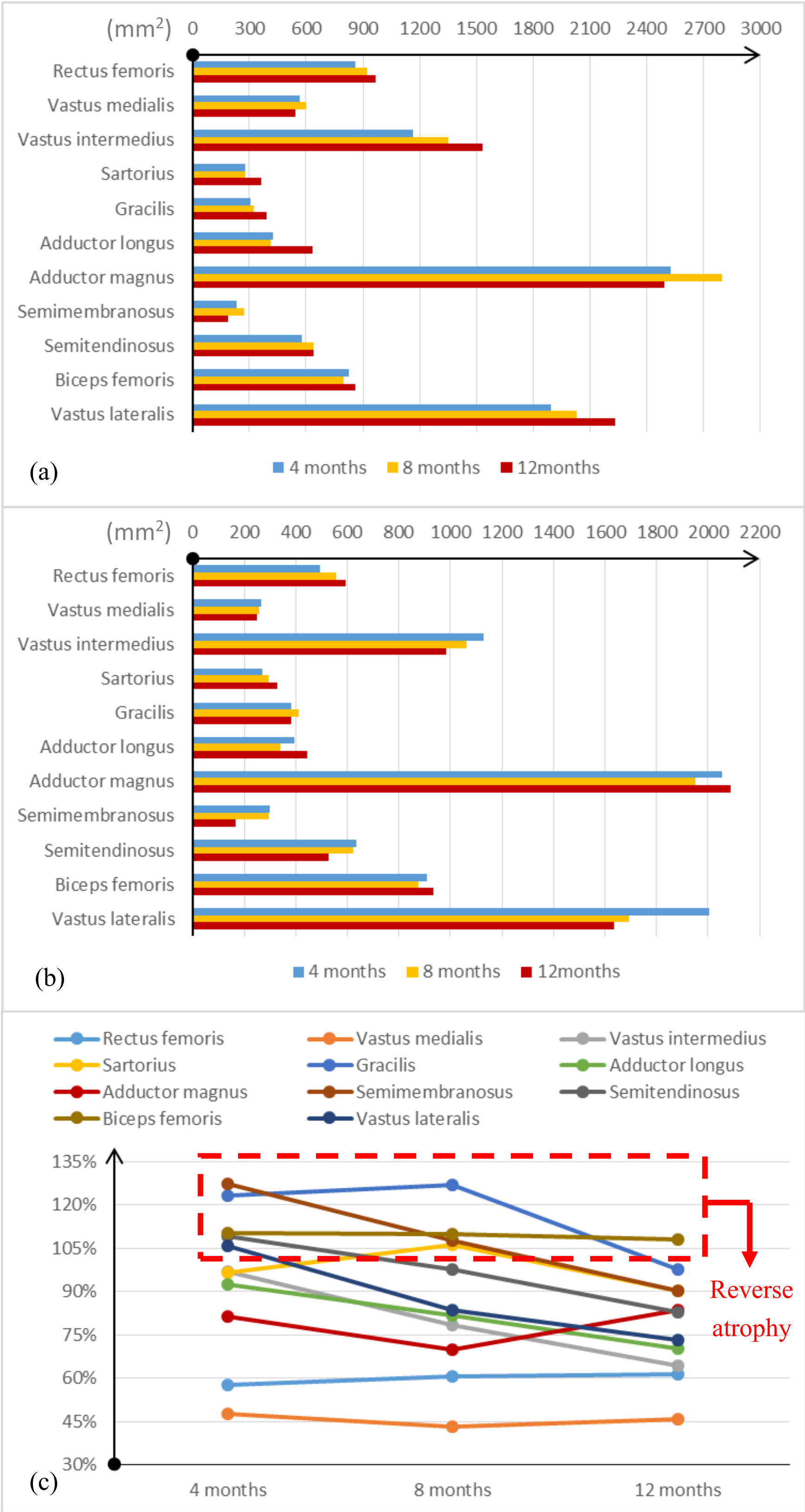

Figure 3.4 The follow-up measurement results of the muscle CSA of Case-2 at the 30% level. (a) sound limb; (b) residual limb; (c) residual/sound limb percentage.

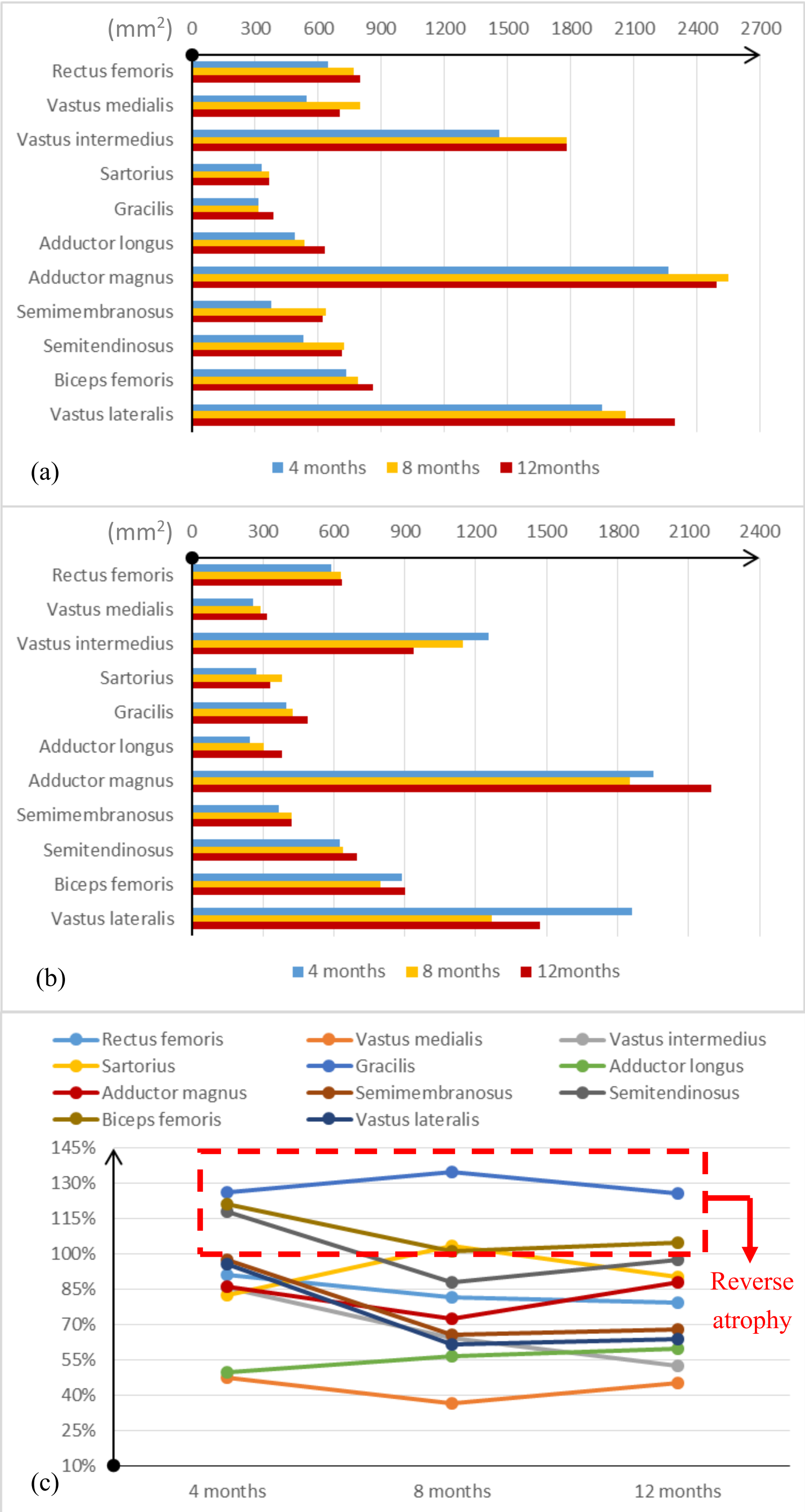

Figure 3.5 The follow-up measurement results of the muscle CSA of Case-2 at the 50% level. (a) sound limb; (b) residual limb; (c) residual/sound limb percentage.

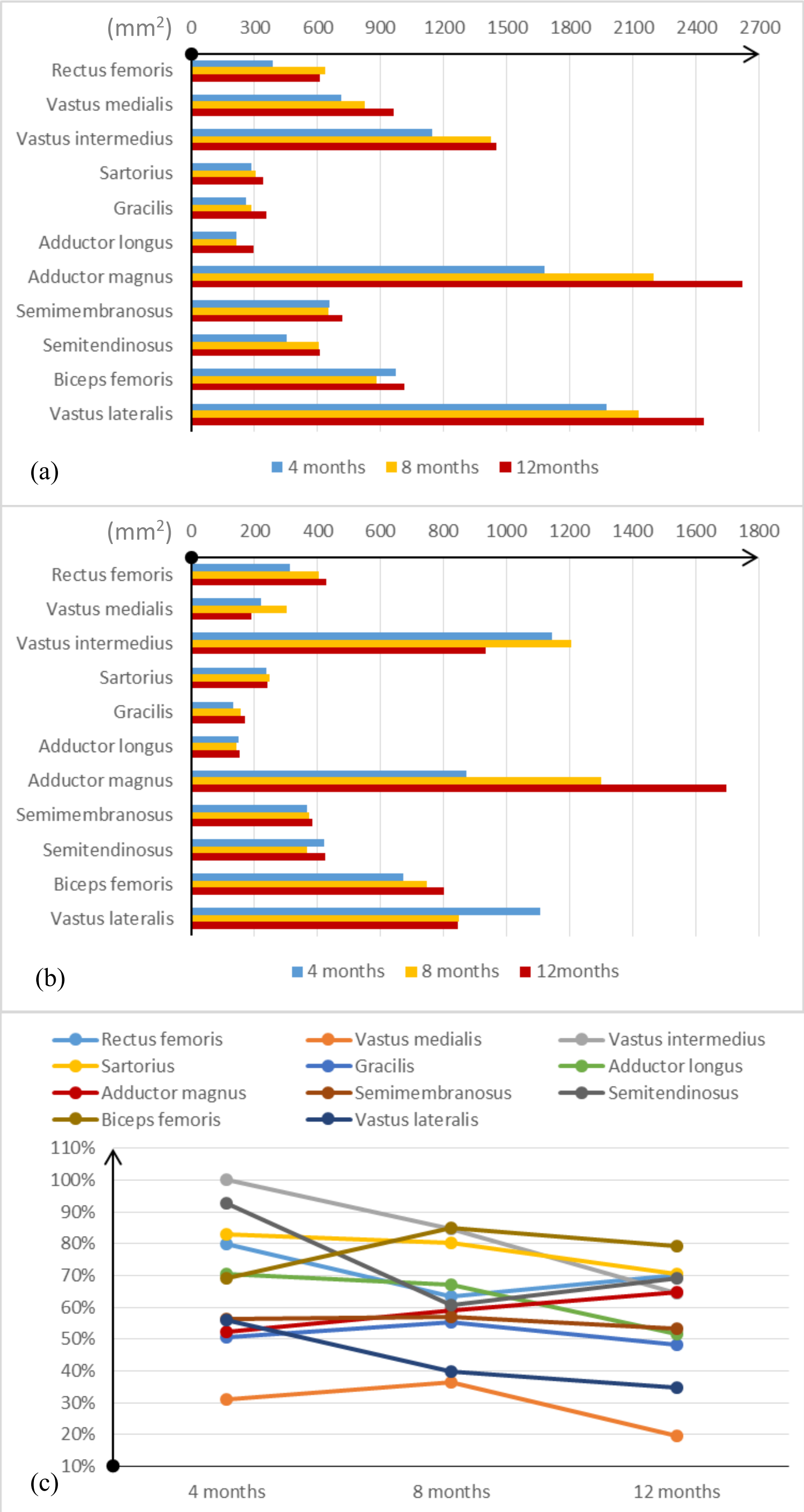

Figure 3.6 The follow-up measurement results of the muscle CSA of Case-2 at the 70% level. (a) sound limb; (b) residual limb; (c) residual/sound limb percentage.

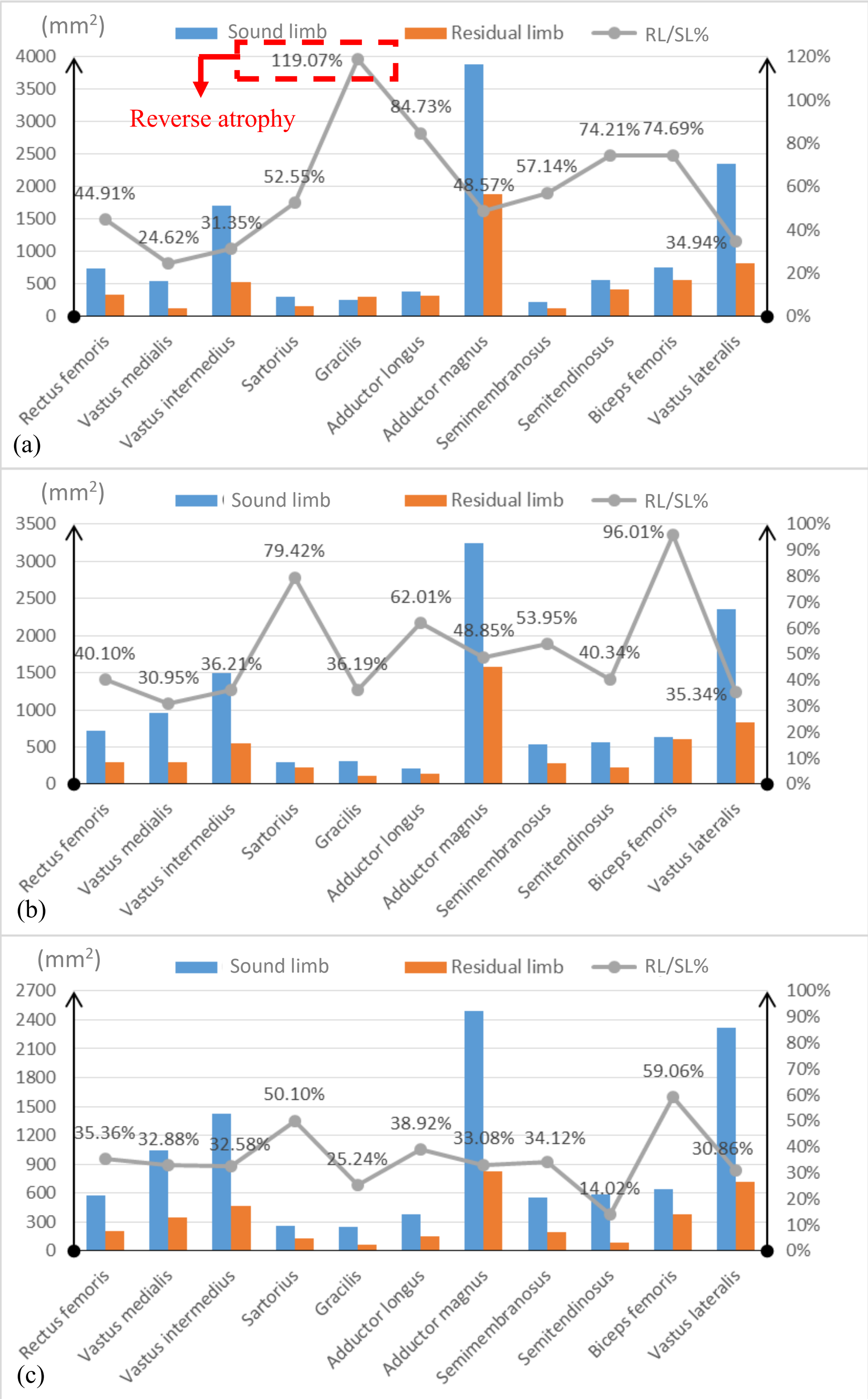

Figure 3.7 The measurement results of the muscle CSA of Case-3. (a) at the 30% level; (b) at the 50% level; (c) at the 70% level.

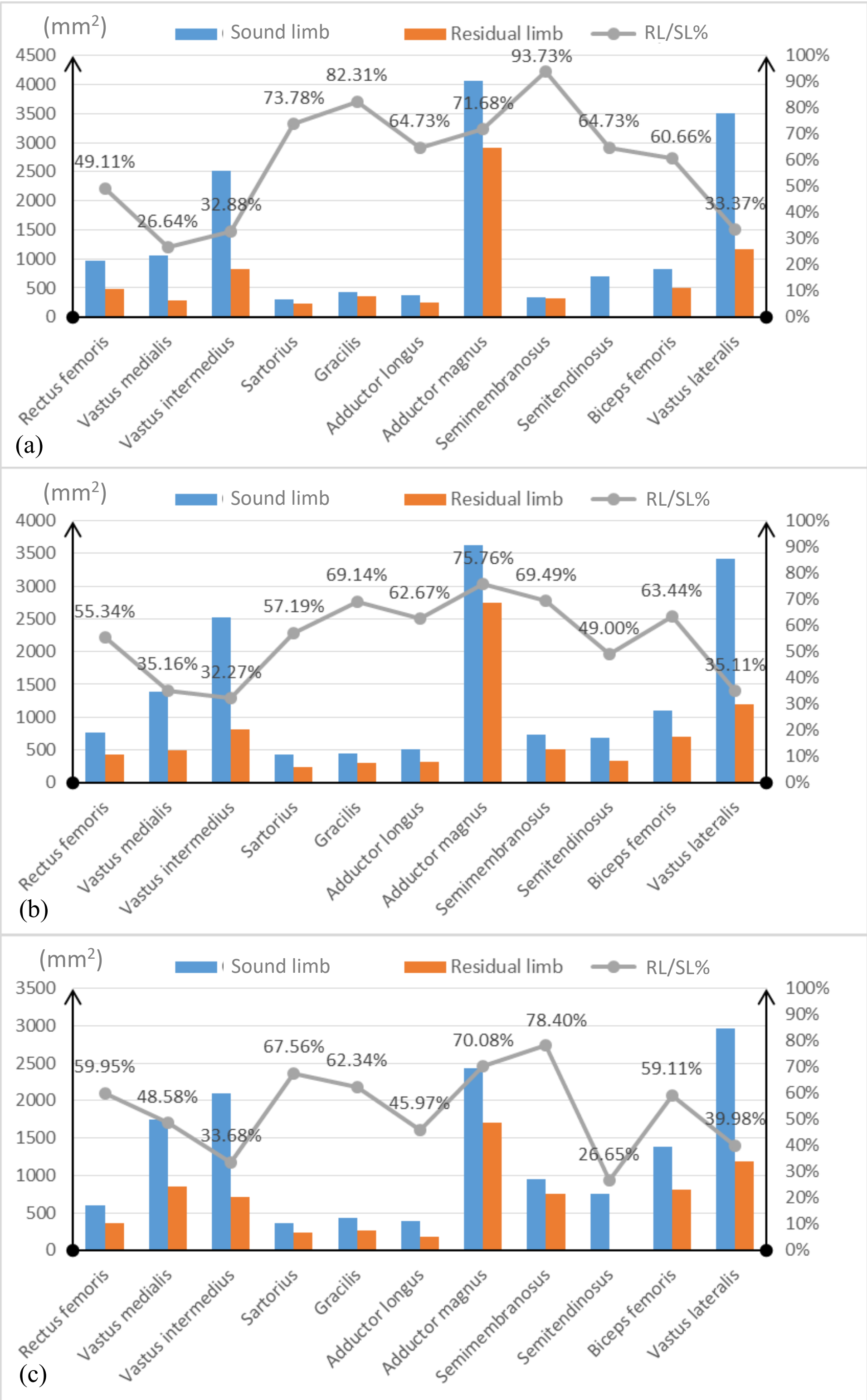

Figure 3.8 The measurement results of the muscle CSA of Case-4. (a) at the 30% level; (b) at the 50% level; (c) at the 70% level.

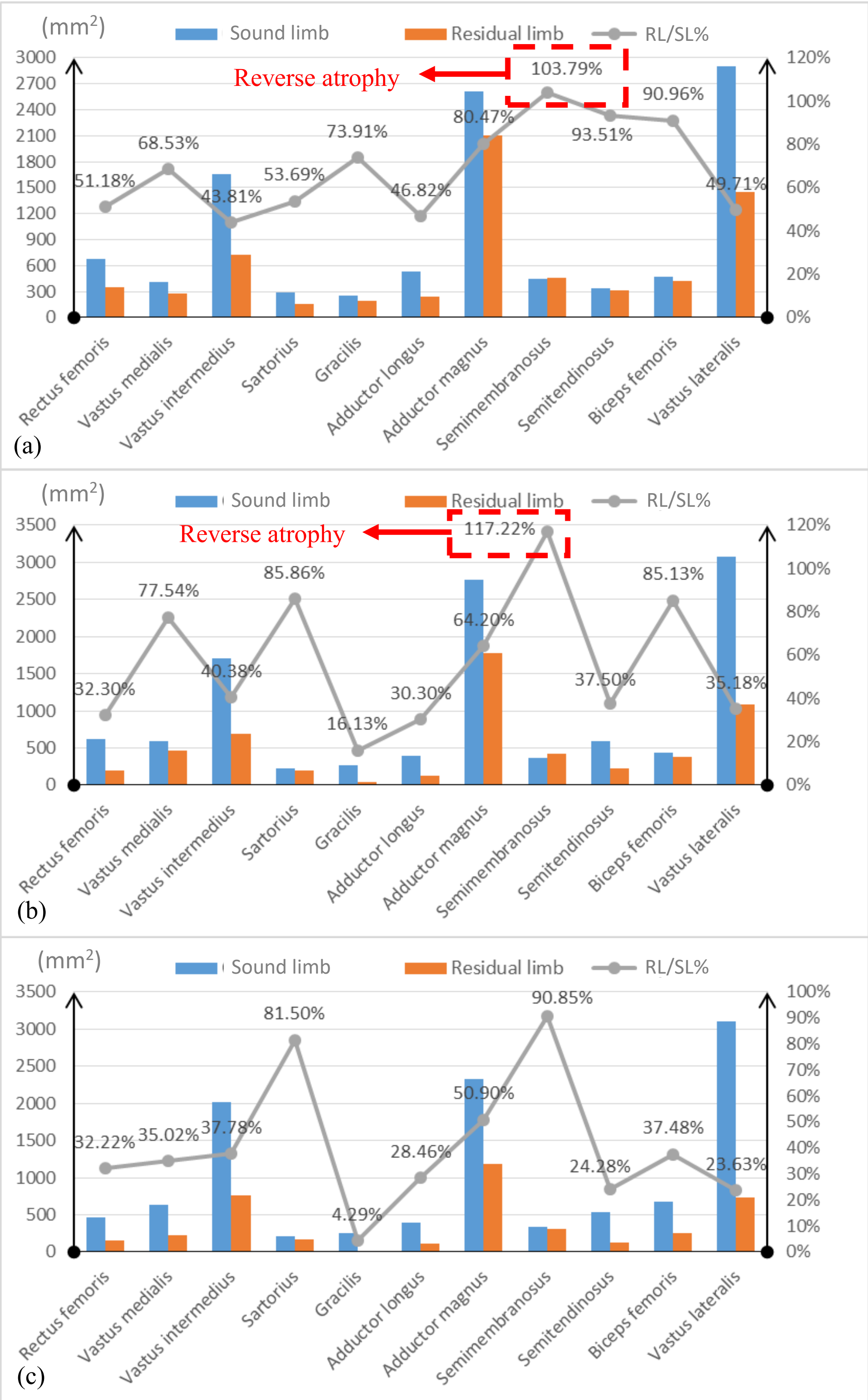

Figure 3.9 The measurement results of the muscle CSA of Case-5. (a) at the 30% level; (b) at the 50% level; (c) at the 70% level.

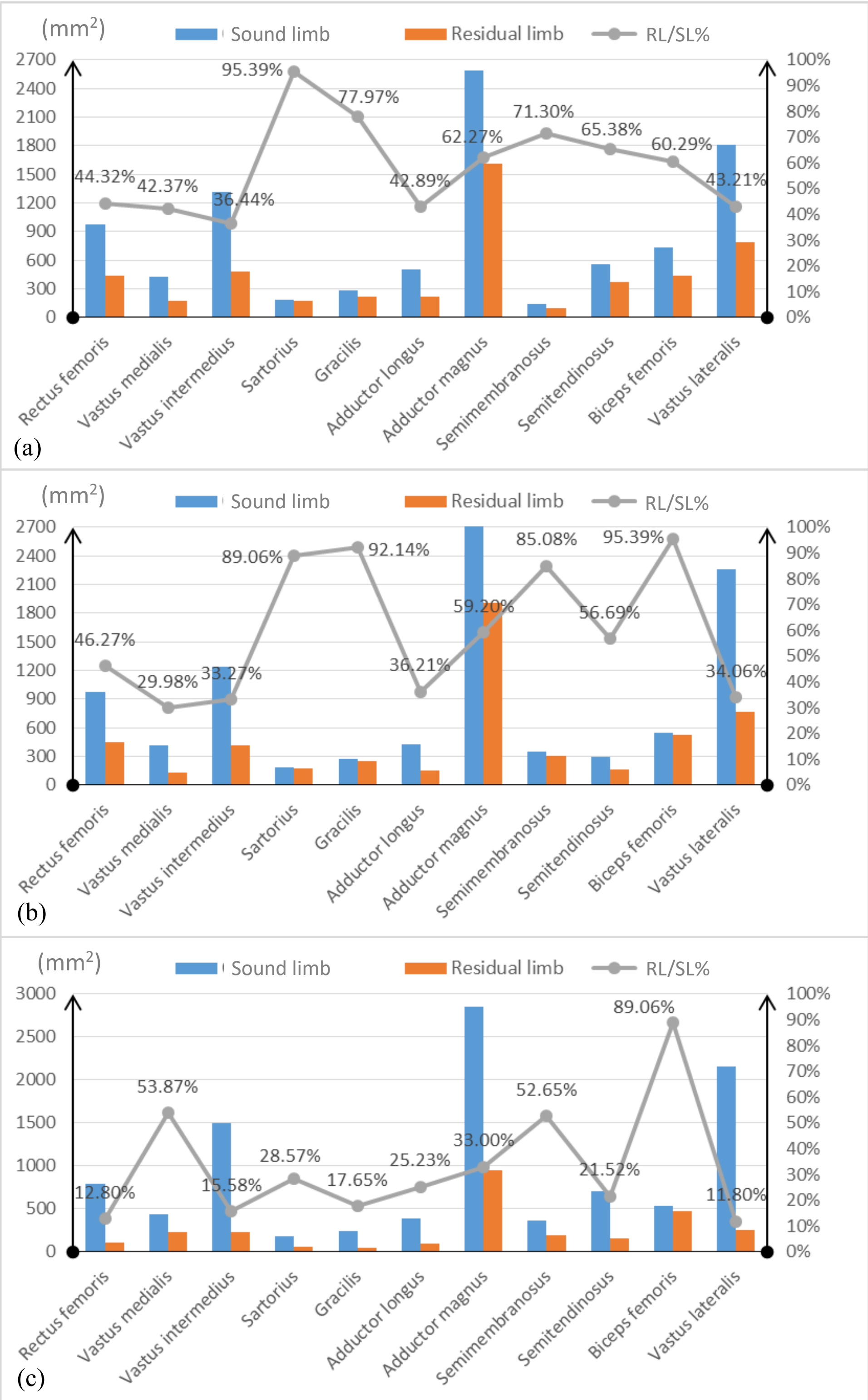

Figure 3.10 The measurement results of the muscle CSA of Case-6. (a) at the 30% level; (b) at the 50% level; (c) at the 70% level.

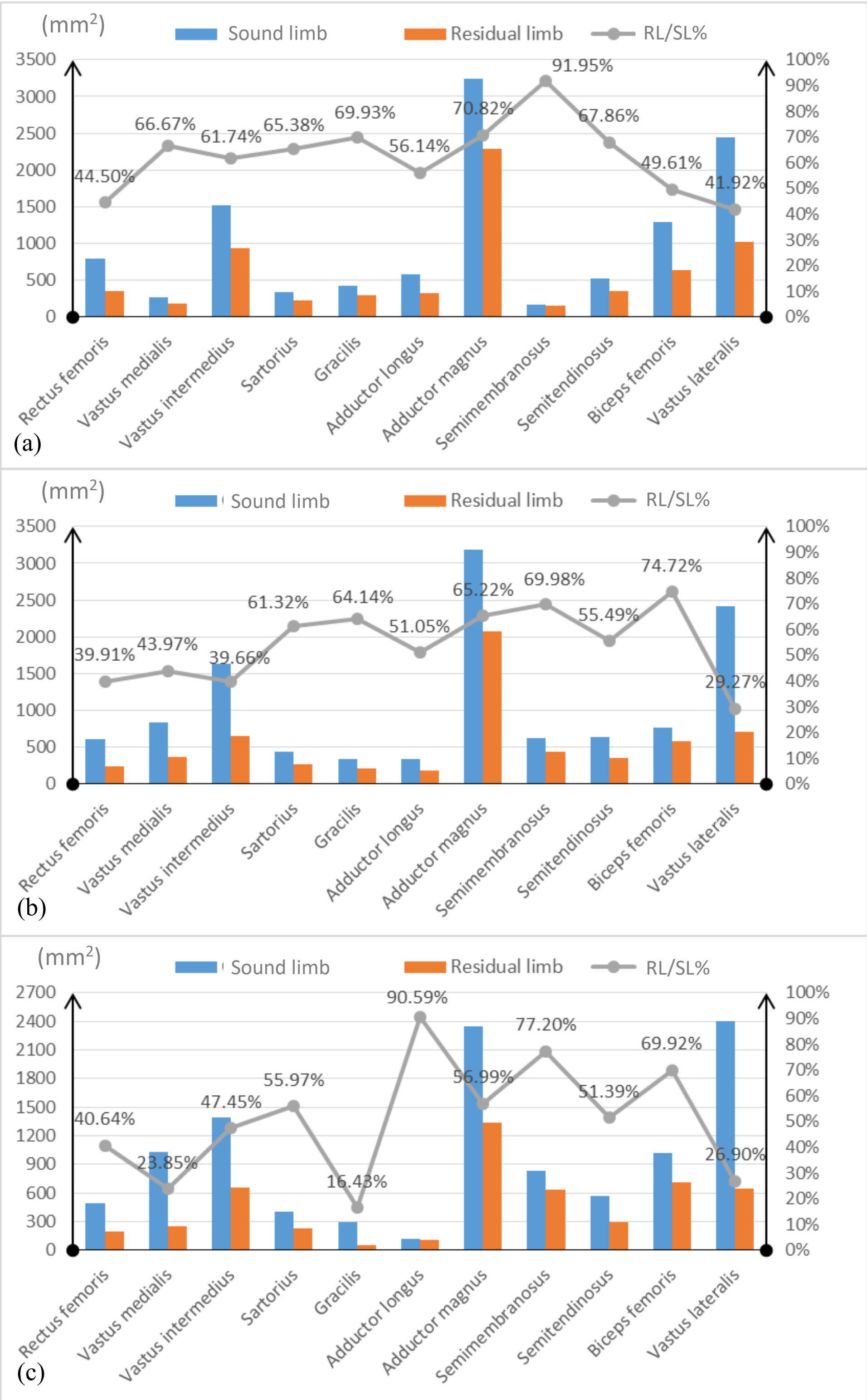

Figure 3.11 The measurement results of the muscle CSA of Case-7. (a) at the 30% level; (b) at the 50% level; (c) at the 70% level.

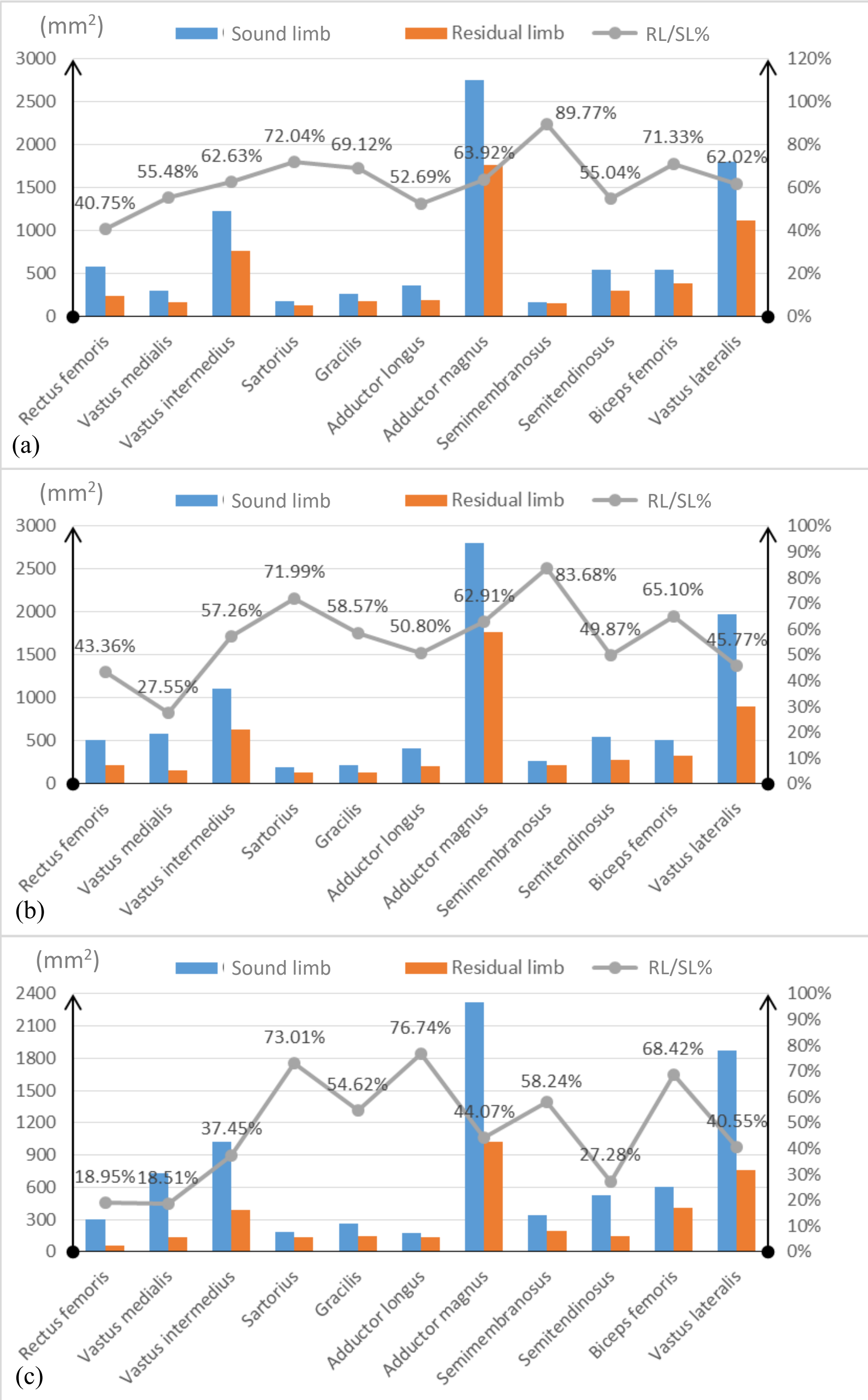

Figure 3.12 The measurement results of the muscle CSA of Case-8. (a) at the 30% level; (b) at the 50% level; (c) at the 70% level.

Table 3.1 The ratio of total muscle area to total thigh area: 2 follow-up cases

Muscle/thigh total area ratio (%)		Case-1			Case-2		
		SL	RL	Bilateral difference	SL	RL	Bilateral difference
4th month	30% level	44.47	31.44	13.03	50.96	46.67	4.29
	50% level	48.27	33.34	14.93	57.49	49.46	8.03
	70% level	48.04	29.94	18.10	58.28	42.38	15.90
8th month	30% level	42.66	30.03	12.63	49.21	44.19	5.02
	50% level	45.71	32.06	13.65	55.17	45.39	9.79
	70% level	46.45	27.88	18.57	56.45	41.95	14.49
12th month	30% level	42.53	31.58	10.95	46.49	40.87	5.62
	50% level	46.26	33.23	12.43	53.12	42.65	10.47
	70% level	45.03	28.35	16.68	56.75	37.52	19.23

Table 3.2 The ratio of total muscle area to total thigh area: Case-3 to Case-8

Muscle/thigh total area ratio (%)		SL	RL	Bilateral difference
Case-3	30% level	75.01	58.64	16.37
	50% level	76.12	58.44	17.68
	70% level	73.02	48.02	25.00
Case-4	30% level	58.74	45.09	13.65
	50% level	61.68	47.41	14.28
	70% level	60.02	43.21	16.81
Case-5	30% level	74.13	65.14	8.99
	50% level	76.93	62.98	13.95
	70% level	78.33	53.42	24.91
Case-6	30% level	66.83	58.61	8.21
	50% level	67.87	58.13	9.74
	70% level	68.98	53.39	15.59
Case-7	30% level	51.33	43.60	7.73
	50% level	57.48	42.90	14.58
	70% level	57.38	41.06	16.33
Case-8	30% level	35.11	28.89	6.21
	50% level	37.20	26.44	10.76
	70% level	37.66	20.34	17.33

Table 3.3 The residual limb length and bilateral ratio: 2 follow-up cases

mm / %		Case-1	Case-2
4th month	Residual limb length	161.44	196.44
	RL/SL length ratio	54.04	56.73
8th month	Residual limb length	161.25	193.91
	RL/SL length ratio	53.98	55.99
12th month	Residual limb length	158.18	190.06
	RL/SL length ratio	52.95	54.88

Table 3.4 The residual limb length and bilateral ratio: Case-3 to Case-8

mm / %	Case-3	Case-4	Case-5	Case-6	Case-7	Case-8
Residual limb length	208.63	256.17	167.64	121.68	221.56	188.43
RL/SL length ratio	58.32	75.71	47.59	39.27	69.36	60.77

From **Figure 3.1-3.12**, it can be seen that the residual/sound limb CSA percentage of each muscle at the three levels was different, that could be attributed to the relative physiological position of each muscle and the different amputation level (RL length) of each case (**Table 3.3, 3.4**). Among the three levels, the muscle tissue of RLs at the 70% level were too deranged with no clear borders to identify since the muscular morphology was damaged by surgical trimming. Thus, the proximal slices (around 60%-65%) were referenced during measurements, and there were relative rough estimates of the muscle boundary. Therefore, the data at the 70% levels are mainly used for the analysis of muscle/thigh total area ratio, and provide clues for muscle changes from proximal to distal (30% to 70%). The following detailed analyses of atrophy amount mainly concern the data at 30% and 50% levels. For the two follow-up cases, the three times examination showed that the bilateral CSA ratio of each muscle varied within the first year after surgery, reflected in Case-1 with smaller amplitude of 21.74% maximum difference (**Figure 3.1-3.2 (c)**), and Case-2 with larger amplitude of 33.96% maximum difference (**Figure 3.4-3.5 (c)**).

Despite of the individual differences of 8 cases, in general, the quadriceps femoris in anterior muscle group of RLs showed greater MA degree, wherein the atrophy of VM (average of 31.75%) and VL (average of 38.75%) was most significant. In contrast, the long head of BF (average of 80.71%), SEMI_M (average of 68.59%) and SEMI_T (average of 49.56%) which are collectively referred to as hamstrings in posterior muscle group, as well as GRAC (average of 68.20%) in medial muscle group showed smaller MA degree in RLs. In Case-2, Case-3 and Case-5, hamstrings and GRAC even showed larger CSAs in RL than those in SL at 30% or 50% level (>100%, marked with reverse atrophy in **Figure 3.4, 3.5, 3.7, 3.9**). These phenomena are consistent with the previous studies of Schmalz [10], Sherk [19], and Fraisse [9], namely that the atrophy degree of each muscle group of RL is different, and even individual muscles appear growing larger than that of SL.

According to the previous researches about lower stump MA (mainly trans-tibial RL), in the process of adapting to new muscle state after amputation, the increase in energy consumption and the change of walking gait symmetry lead to the different degrees of atrophy. The fundamental reason is that the anatomical structure changes of RL caused the variations of the physiological tension and mobility pattern of muscles [9]. From sports anatomy point of view, the structural difference makes the movement forms of hip joint more than those of knee joint, and hip joint is usually involved in pelvis movements. From sports anatomy point of view, the structural difference makes the movement forms of hip joint (**Figure 3.13**) more than those of knee joint (**Figure 3.14**), and hip joint is usually involved in pelvis movements (**Figure 3.15**). However, after trans-femoral amputation, due to the loss of foot, calf and knee joint, the motions of RL only relying on hip are greatly reduced and the range is also clearly limited. Meanwhile, in the collaboration of hip and pelvis, the pressure and motion amplitude of SL would increase to compensate the function loss of RL.

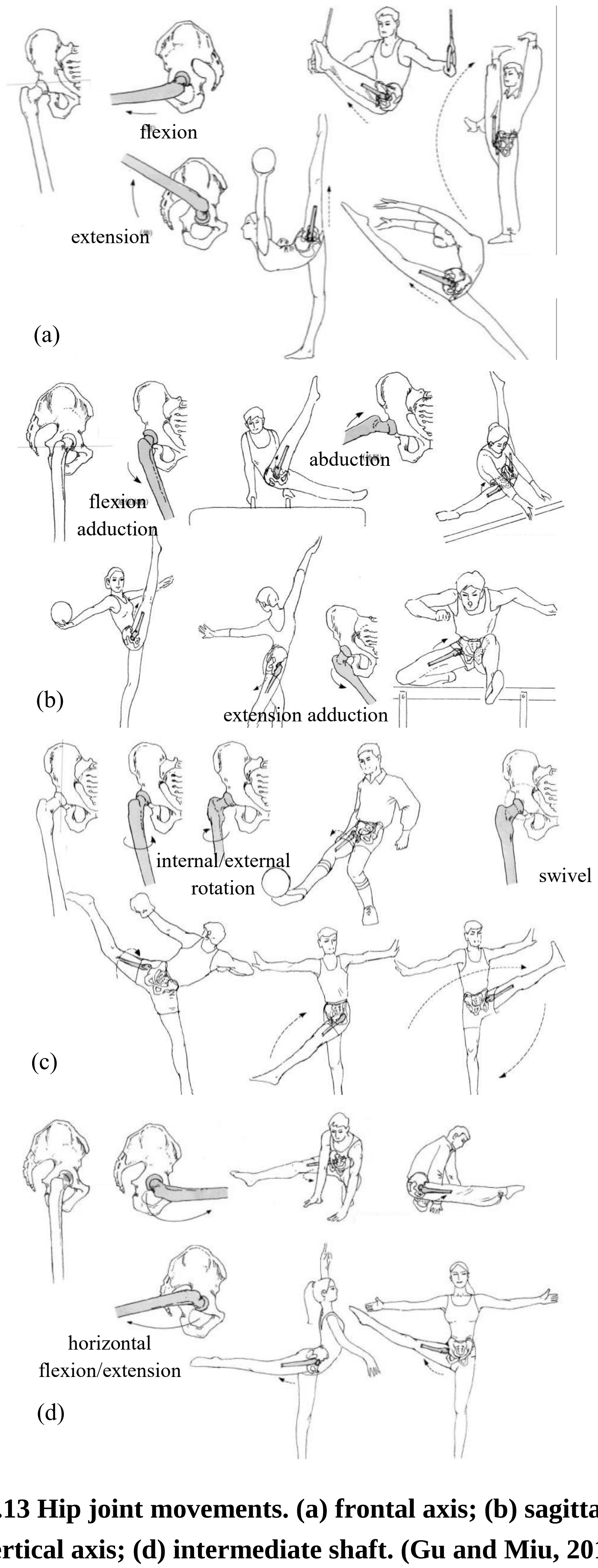

Figure 3.13 Hip joint movements. (a) frontal axis; (b) sagittal axis; (c) vertical axis; (d) intermediate shaft. (Gu and Miu, 2013)

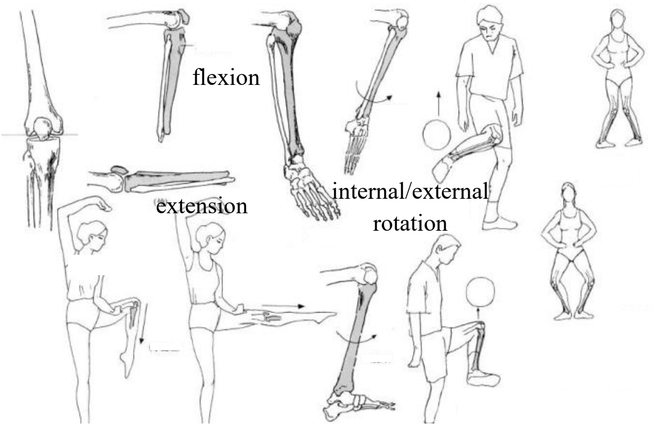

Figure 3.14 Knee joint movements. (Gu and Miu, 2013)

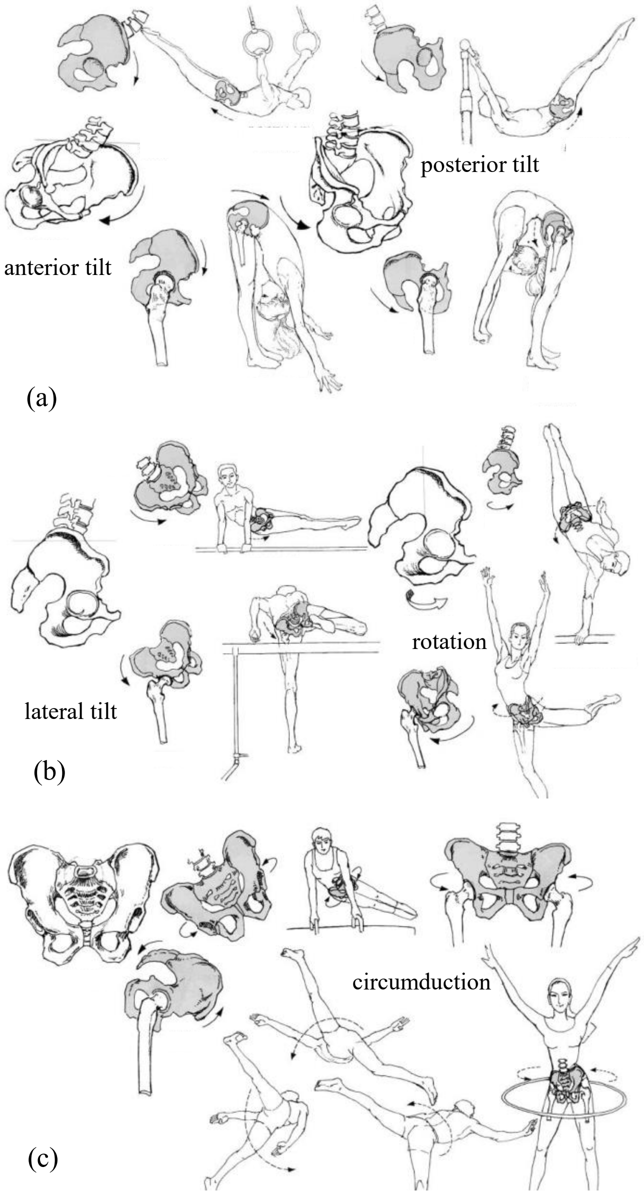

Figure 3.15 Pelvis movements. (a) frontal axis; (b) sagittal and vertical axis; (c) intermediate shaft. (Gu and Miu, 2013)

Table 1.1 showed the attached joints and active functions of thigh muscles. Each muscle is innervated by nervous system to perform the integrative movement of lower limb by synergistic action. After trans-femoral amputation, those knee joint movements in affected side has been unable to achieve. However, assisted by pectineus, iliopsoas and gluteus etc. (**Figure 3.16**), most hip joint movements of RL (as long as not too short) could still be achieved, despite the reduced range of motion. In addition, pelvis movements would still involve the proximal thigh muscles of RL (**Figure 3.17**). Therefore in RL, adductors and hamstrings which participate in hip and pelvis movements retain more functionality than quadriceps.

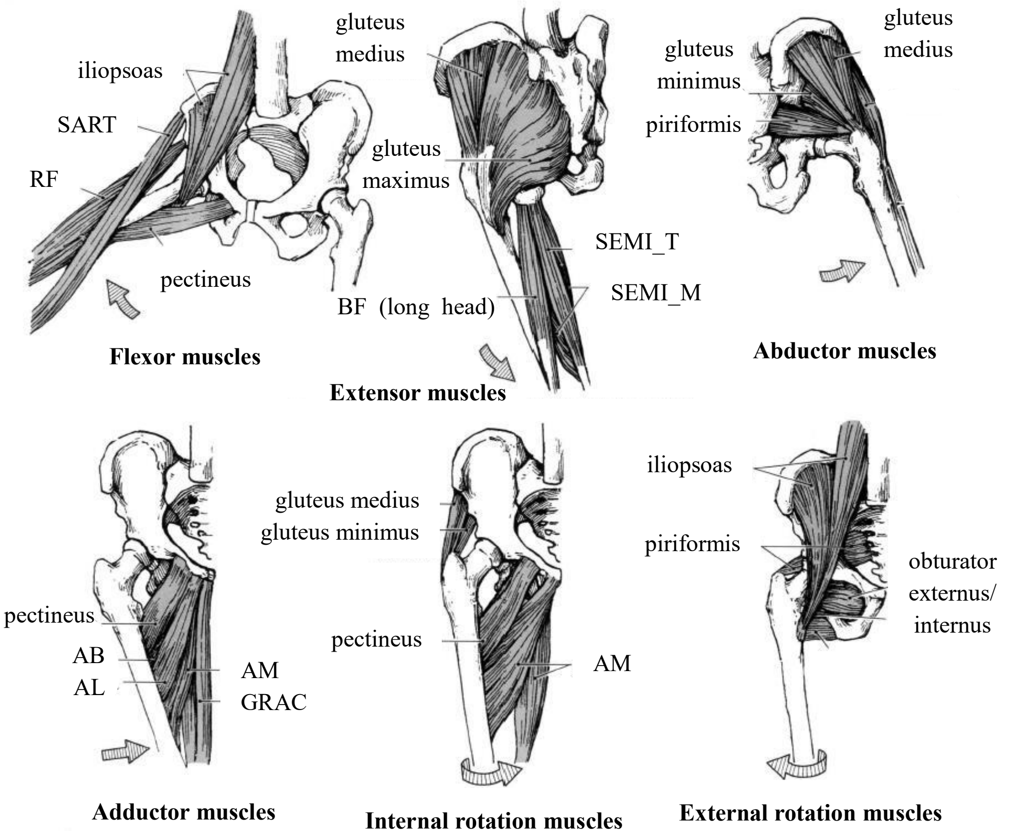

Figure 3.16 Hip joint moving muscles. (Gu and Miu, 2013)

Combining the change of physiological tension, the origin/insertion (**Figure 3.18**) and the specific function of individual muscle, the differences of atrophy degree could be detailed explained. The proximal RF attaches to pelvis, making it a bi-articular muscle. Whereas VM, VI, and VL originate from femoris, and they are uni-articular muscles attached to knee joint, strong extensor with simple function.

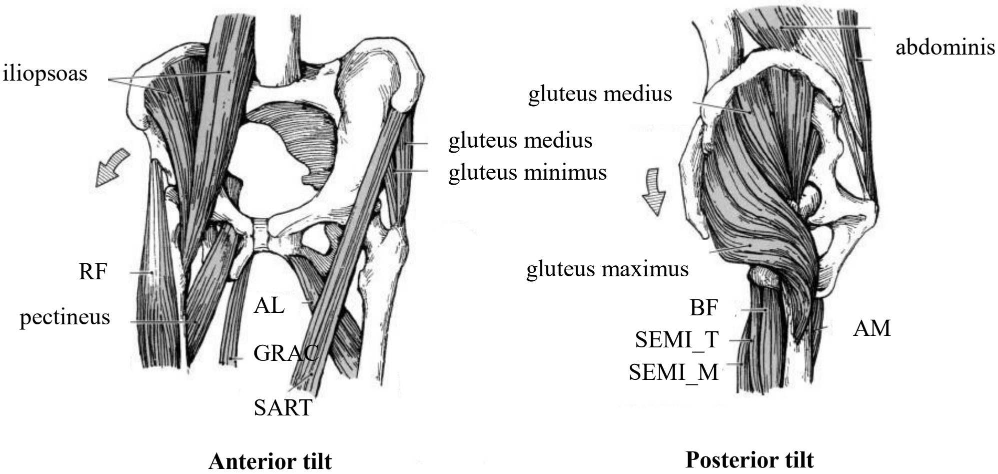

Figure 3.17 Pelvis moving muscles. (Gu and Miu, 2013)

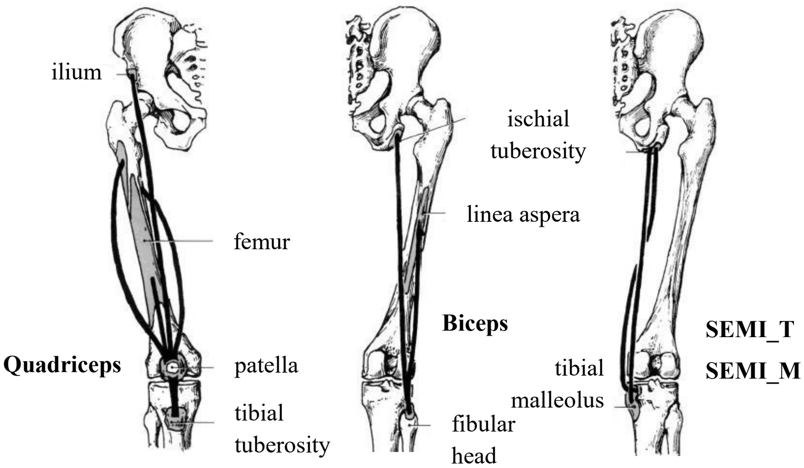

Figure 3.18 The origin and insertion of quadriceps and hamstrings. (Gu and Miu, 2013)

Trans-femoral amputees lost their knee, which means the extension function of quadriceps is greatly reduced, derectly resulting in MA and the loss of muscle strength. The unitary function muscle VM and VL are directly responsible for the extension of knee joint, so their atrophy degrees are the greatest. The researches about trans-tibial amputees of Isakov et al. [20, 41] and Tugcu et al. [12] showed that, the thigh muscle strength of SL was significantly higher than that of RL. The thigh MA in RL accompanied by a marked decrease of quadriceps strength, especially the shorter RL. They explained that the low effective leverage produced by short RL weaken the ability of thigh muscles to controll prosthesis. In general, the prosthesis control by trans-femoral RL is inferior to that by trans-tibial RL due to weaker leverage. Moreover, although a prosthesis could compensate for part of knee joint function, it can not replace the terminal attachment point lost by quadriceps. That is to say, even if wearing prosthesis, the extension of quadriceps could only get a certain degree of recovery, and it depends on the service condition of prosthesis.

In comparison, hamstrings which originate from ischial tuberosity and distal attach on knee (**Figure 3.18**) are bi-articular muscles connected to hip and knee. They are involved in various forms of movement of lower limb, hip and pelvis **(Figure 3.16-3.17**). Thus the loss of knee would not impair their function too much. During comfortable symmetrical standing, based on the activation of quadriceps, adductors and gluteus, hamstrings are inactive. But when any action leading to the deviation from hip axes and centre-of-gravity shifting occurs, hamstrings would immediately intensely contract. After amputation, patients' standing and walking posture are no longer symmetrical, implying that the hip deviation and pelvis tilt (**Figure 3.13, 3.15**) often occur, even wearing prosthesis. Therefore, hamstrings are always in a state of emergency response and often activated. In some researches for trans-tibial amputees, the slight atrophy of hamstrings in RL was discussed. Schmalz et al. [10] proposed that, in the process of looking for balance and adapting to new gait, there might be compensatory hyperfunction of hamstrings, as hyperactive flexion to compensate for part of knee function. So that the normal thickness of thigh flexor was ensured. The analysis of Fraisse et al. [9] from biomechanical point of view pointed out that, after surgery, the great anatomical structure changes of RL caused a comprehensive variation in muscle tone, physiological tension, and mobility patterns. Then hamstrings instead of triceps surae became the main propulsion muscle, and also ensured a good contact between RL and prosthetic socket. These arguments are still applicable to trans-femoral amputees, and even produce greater effects in order to compensate for the loss of knee and the impaired function of quadriceps.

In summary, the different atrophy degrees of quadriceps and hamstrings in above-knee RL could be briefly generalized as the use and disuse theory. This study infers that whether use a prosthesis and the therefrom form and amount differences of daily exercise are key factors affecting the muscle state in RL.

It can be seen from **Table 3.1**, **3.2**, from the 30% level to 70% level, the bilateral difference of muscle/thigh total area ratio increased gradually, especially Case-3 and Case-5 with bilateral percentage difference up to 25.00% and 24.91% at the 70% level, who were not use prostheses. This could be explained by the better preservation of the muscle attachments, strength, and hip motor function at upper and middle levels. In addition, Sherk et al. [19] refered that thigh has larger relative amounts of fat, and there are a lot of intermuscular fatty tissues at the end of RL, making wrapping muscles relatively few. Therefore, the lower level is easier to arise the loss of attachment points, decreased muscle tone, and muscle sliding or retraction at the end of residual bone because of the surgical treatment of muscles. Table 3.1, 3.3 showed the muscle/thigh total area ratio and the residual/sound limb length ratio of two follow-up cases. Comparing the results of the first and third examination, both cases' bilateral muscle areas and RL length decreased, yet the decrements of Case-1 who used a prosthesis (muscle ratio of RL -0.11%, muscle ratio of SL -2.01%, RL length ratio -1.09%) were less than those of Case-2 without using prosthesis (muscle ratio of RL -6.81%, muscle ratio of SL -4.37%, RL length ratio -1.85%). Meanwhile, the bilateral difference of the muscle ratio of Case-1 was gradually narrowing from 14.93% to 12.43%, whereas this difference of Case-2 was gradually increased from 8.03% to 10.47%. It also illustrated that using prosthesis to save the muscle motor function in RL and to increase patient's activity could relieve bilateral atrophy. As for the relationship between the atrophy degree and RL length and postoperative time, the 8 cases of this study did not show a consistent trend. This may be due to the individual differences caused by various factors like the service condition of prosthesis, daily activity patterns and amounts, etc.

3.1.2 Results and discussion of artery morphological indices

This study measured the hydraulic diameter (Dh), circumference (Scf) and cross sectional area (Area) of the five main arteries of both thighs in the arterial tree section (equivalent to residual limb length as shown in **Figure 2.3**), followed by their average value calculation, and then used the residual/sound limb percentage of these indices to quantify the arterial narrowness degree. After the 3D reconstruction of vessels by enhanced CT images with unit information (mm) in medical image processing software MIMICS, the control points and center lines of the vascular tree can be automatically generated by the MedCAD module (resolution and control point spacing of 1.0mm, 2 iterations). Output the control point parameters series of five main arteries, including 3D coordinates, Dh, Scf and Area, and then calculated and recorded the arithmetic means and the residual/sound limb ratios of these indices of each subject. Whereafter, sorted out and drew the data into the following charts for the visual display of numerical results.

The follow-up results of Case-1 and Case-2 are shown in **Figure 3.19-3.20** and **Figure 3.21-3.22** respectively. The results at different time after the surgery of Case-3, Case-4, Case-5, Case-6, Case-7 and Case-8 are shown in **Figure 3.23-3.28** respectively.

In the **Figure 3.19, 3.21, 3.23-3.28**, the left side of Y axis and the histogram simultaneously indicate arterial Dh (mm), Scf (mm) and Area (mm^2), wherein the grey parts represent the excess value of SL than RL; the right side of Y axis and the line charts simultaneously show the residual/sound limb ratios of those three indices (Dh%, Scf%, Area%); the X axis shows the name of arteries. In the **Figure 3.20, 3.22**, the Y axis represents the residual/sound limb ratio of CSA (Area%); the X axis indicates the time of follow-up.

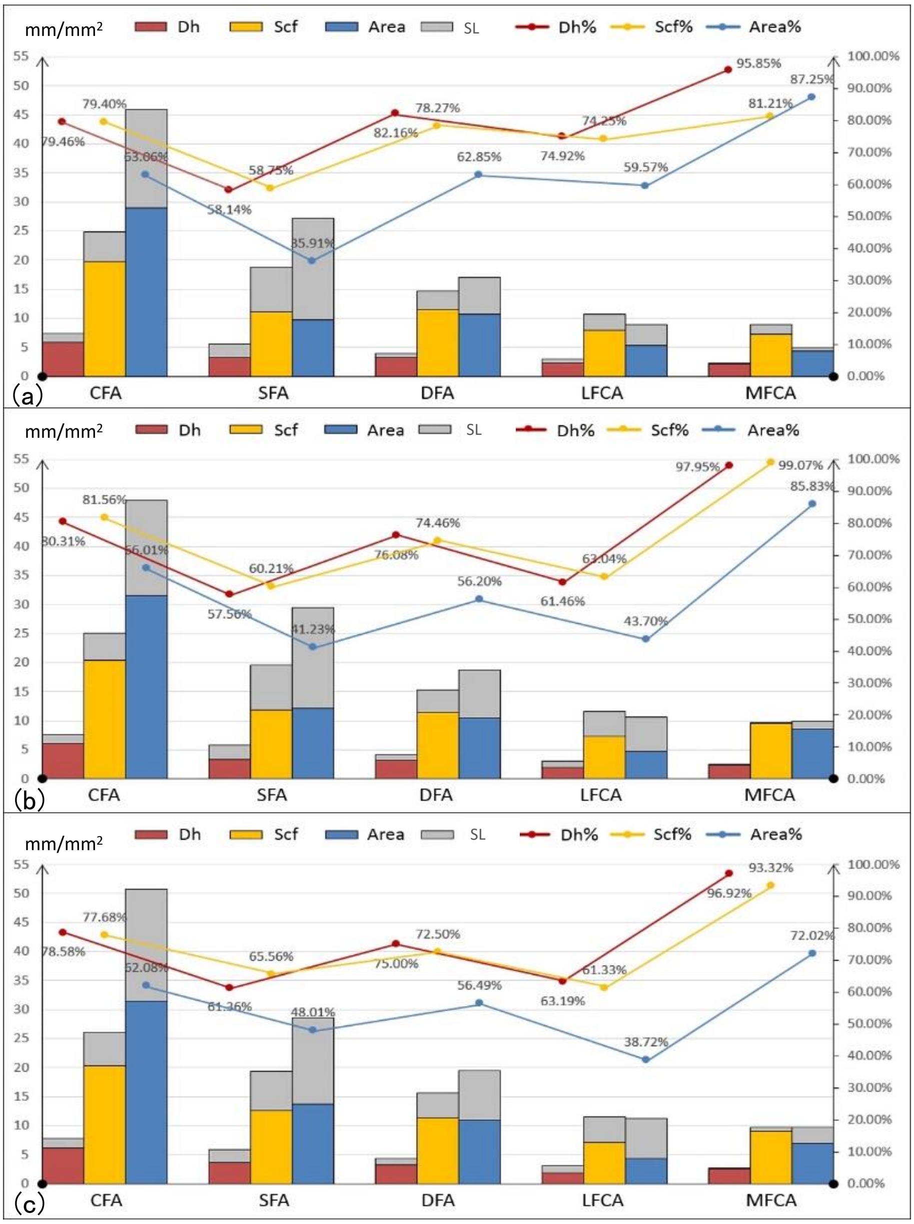

Figure 3.19 The measurement results of the arterial indices of Case-1. (a) 4th month; (b) 8th month; (c) 12th month after amputation.

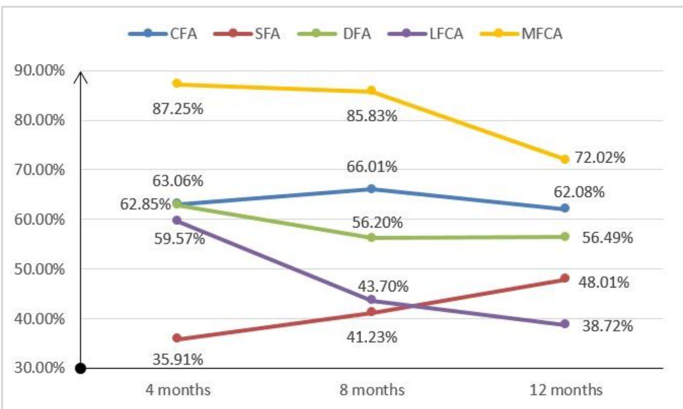

Figure 3.20 The follow-up arterial bilateral Area ratios of Case-1.

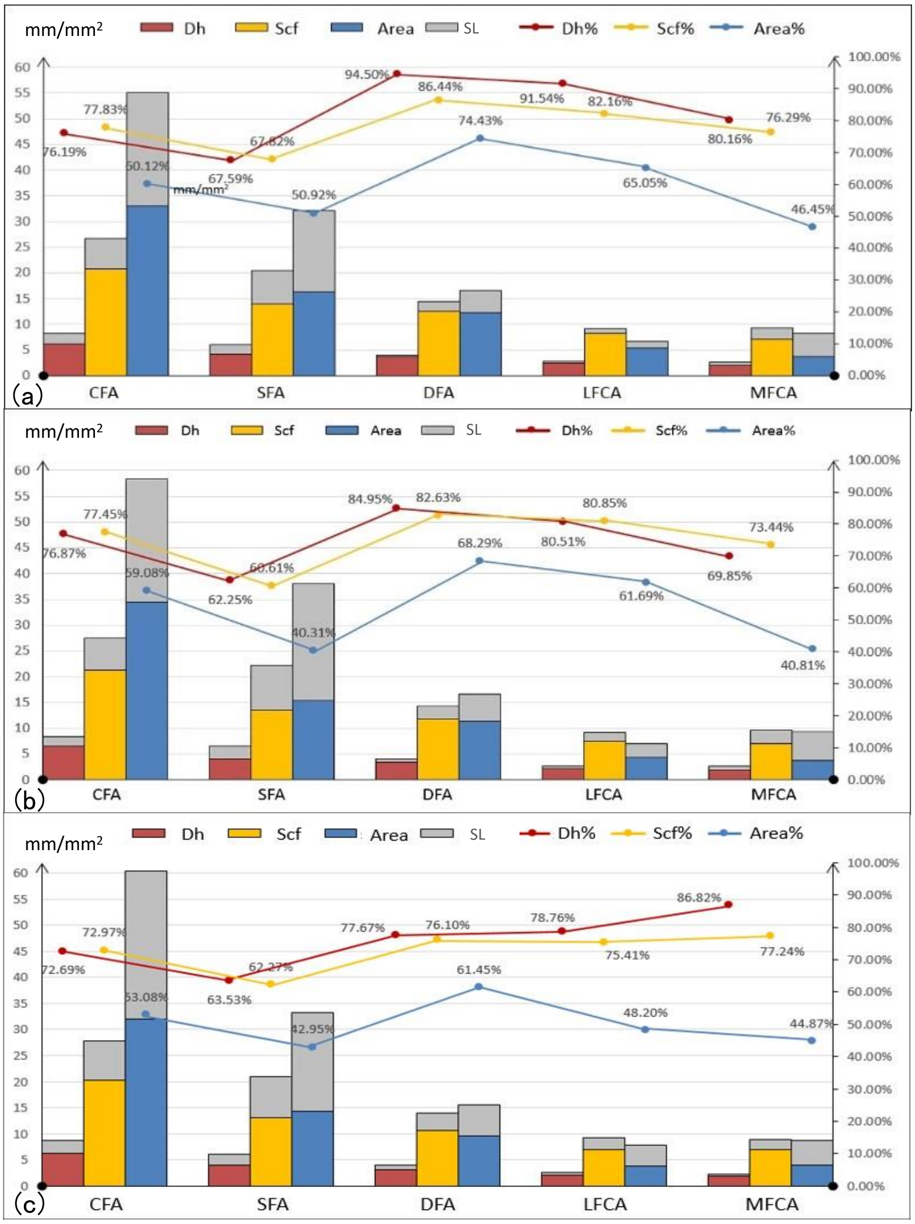

Figure 3.21 The measurement results of the arterial indices of Case-2. (a) 4th month; (b) 8th month; (c) 12th month after amputation.

Figure 3.22 The follow-up arterial bilateral Area ratios of Case-2.

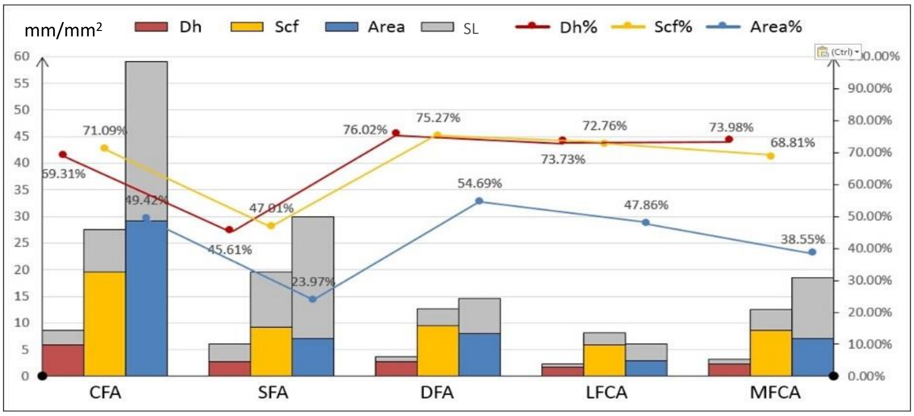

Figure 3.23 The measurement results of the arterial indices of Case-3.

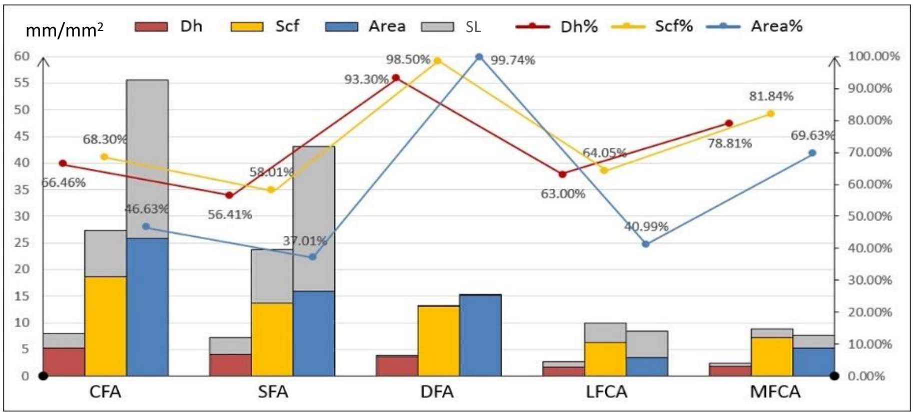

Figure 3.24 The measurement results of the arterial indices of Case-4.

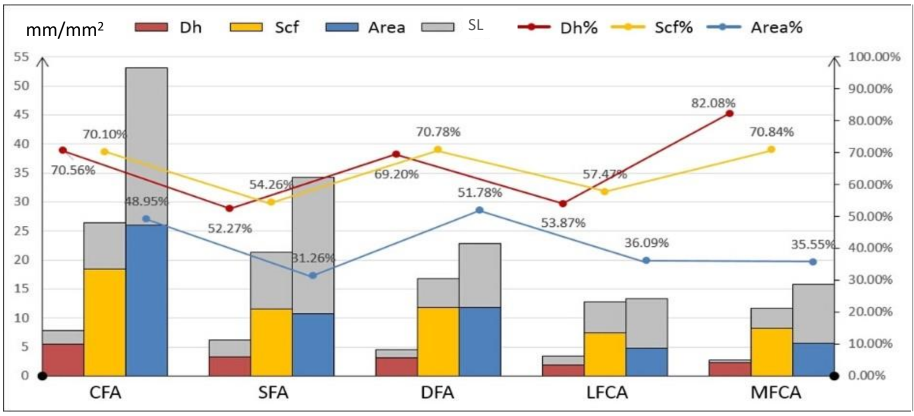

Figure 3.25 The measurement results of the arterial indices of Case-5.

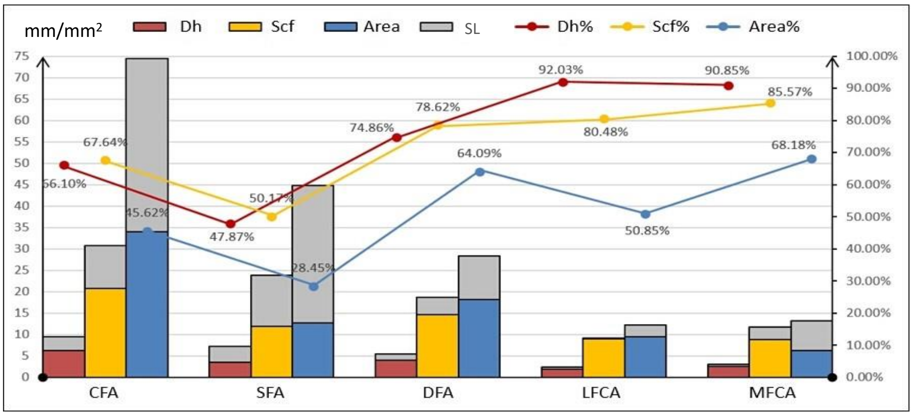

Figure 3.26 The measurement results of the arterial indices of Case-6.

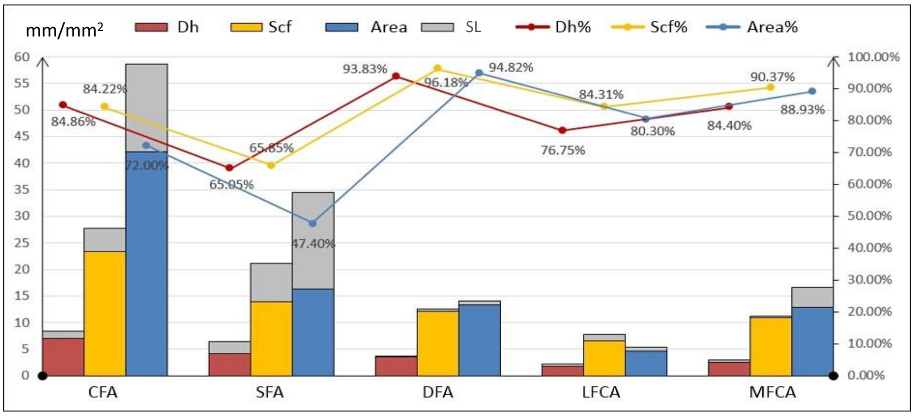

Figure 3.27 The measurement results of the arterial indices of Case-7.

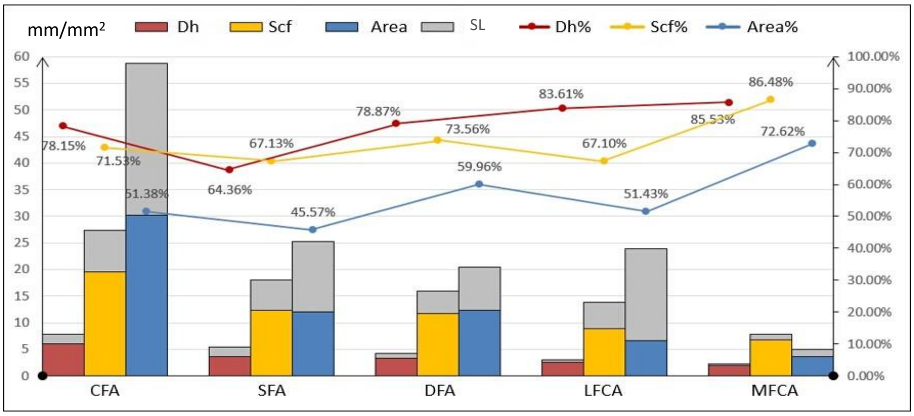

Figure 3.28 The measurement results of the arterial indices of Case-8.

As shown in **Figure 3.19-3.22**, the average Dh (red), Scf (yellow) and Area (blue) values of the bilateral main arteries of two follow-up cases showed numerical changes and residual/sound limb ratio fluctuations in different examining time. It indicated that in the first year after amputation, not only the muscle state has not yet been fully mature, but also the arterial blood flow is not completely stable. **Figure 3.20** and **Figure 3.22** illustrated the Area ratios which could directly reflect blood flow magnitude, and the Area percentage fluctuations of Case-1's arteries are less than those of Case-2 during the follow-up period. This corresponds to the follow-up fluctuations of the muscle CSA ratios of these two cases. From **Figure 3.19-3.28**, it can be seen that although there were individual differences of 8 cases, in general, the superficial femoral artery (SFA) of RLs showed the most obvious narrowness (average Area% of 39.41%), followed by the lateral femoral circumflex artery (LFCA, average Area% of 52.03%) and medial femoral circumflex artery (MFCA, average Area% of 62.56%), whereas the deep femoral artery (DFA) displayed the smallest narrowness degree (average Area% of 67.07%).

These different narrowed trends could be explained by the blood supply relationship of lower extremity. Trans-femoral amputees lost a big part of the affected side limb, which means the total blood supply required by RL is far less than SL, making the blood flow and the lumen CSA of common femoral artery (CFA) in RL accordingly substantially reduced. Yet the branches of CFA include superficial epigastric artery, deep/superficial circumflex iliac artery, and deep/superficial external pudendal artery etc., its narrowness degree was not too great (average Area% of 53.12%). As the two main branches of CFA, SFA and DFA presented opposite narrowing situation. The three perforating arteries and numerous muscular branches originate from DFA, so that DFA is the most important blood supply vessel for thigh muscles. Meanwhile, the nutrient arteries of femur usually originate from the perforating branches of DFA. Therefore, the decrease of the blood flow and lumen CSA of DFA in RL was relatively small. While SFA starting from femoral triangle goes down through adductor canal and adductor hiatus to popliteal fossa, renamed popliteal artery. Its distal branches include descending genicular artery, saphenous artery and some joint muscular branches which mainly supply blood to VM, AM, as well as knee joint, and the proximal muscular branches mainly nourish SART, VL, and adductors. In RL, the blood flow of SFA greatly reduced due to the loss of popliteal artery and the main branches concentrated in the femoral lower segment near knee joint, so the corresponding narrowness degree of SFA was the highest. In the normal anatomic structure, the lumen diameter and CSA of SFA were significantly greater than those of DFA. After trans-femoral amputation, five out of the eight cases showed the lumen Area of DFA exceeded that of SFA in the RLs, and the remaining three cases presented very close values of these two Areas. As for the narrowness degrees of the descending branch of LFCA and MFCA, there were considerable case differences, and the specific analysis is in the section 3.2 of this chapter.

Although the detailed study for RL vessels and hemodynamics has not been reported, in the research field of rehabilitation, the effect of blood flow on various stump problems has been confirmed. For example, among the many hypotheses of the formation cause of pressure ulcer, the local ischemia, hypoxia and malnutrition as a result of blood blocking are the consensus and foundation of various theories [90-94]; studies on the ischemical reperfusion injury induced by pressure showed that, the tolerance of muscle tissue to external loading and hypoxia injury is lower than that of skin [97-99]; a few investigations considering blood flow factors in muscle atrophy also provided valuable conclusions: muscle atrophy affected microvascular structure and the resting blood flow of skeletal muscles [105], ischemia caused bedsore, muscle atrophy and weakness, and significantly reduced exercise hyperemia [106], ischemia, hypoxia and local blood perfusion could affect muscle protein metabolism and apoptosis [107-110], etc. Although the above studies are not for RL, these clinical symptom and pathological investigations on the one hand showed the importance to take into account blood supply in various topics, on the other hand demonstrated that there are correlations between external stress, tissue pressure gradient, blood flow and perfusion, and a variety of common skin and muscle problems. According to the clues and ideas provided by these researches, this study compared the atrophy degree of muscles and the narrowness degree of their main feeding arteries, and then analyzed the correlation based on the biggest reason of the differences of external stress source and distribution---prosthesis usage.

According to the blood supply relationship of thigh muscles, three perforating branches of DFA mainly feed adductor and posterior muscle groups. Compared to anterior muscle group, these two groups showed relatively smaller atrophy degrees in RL, especially the hamstrings in posterior group. DFA just presented a correspondingly lowest narrowness degree, and its Area was close to or even beyond that of SFA. In thigh, SFA mainly supplies blood to VM, AM and SART which showed higher atrophy degrees, superadding less feeding objects than DFA, thus SFA presented the largest narrowness degree associated with this. Comparing Case-2 (**Figure 3.21, 3.22**), Case-3 (**Figure 3.23**) and Case-5 (**Figure 3.25**) who were not using prostheses and the other five cases (**Figure 3.19, 3.20, 3.24** and **Figure 3.26-3.28**) wearing prosthesis, the residual/sound limb percentages of each arterial index of the prosthesis users were overall higher than those of the three cases without using prostheses, which implied that prosthesis users' total blood flow of RL was greater. This phenomenon corresponded to the difference in muscular atrophy. As for the relationship between the narrowness degree and RL length and postoperative time, the 8 cases of this study did not show a consistent trend. This could also be attributed to individual differences in small sample sizes.

3.2 COMPARATIVE ANALYSIS OF MORPHOLOGICAL CHANGES BETWEEN MUSCLE AND ARTERY

As discussed in the previous sections, the muscle and vascular morphological changes in RL were affected by many factors. When only focus on muscle or arterial changes, some consistent trends could be found through the comparison between cases. But the individual difference under multi-factor conditions usually make these results too general and not enough to dig deeper. Therefore, the intra-case analysis could explain more concretely whether there is an exact relationship between the morphological changes of muscles and arteries, as well as the existing conditions, specific performance, and future enlightenment of this relationship.

3.2.1 Index comparison between muscle atrophy and arterial narrowness of each case

On the basis of the blood-supply relationship between muscles and arteries in thigh as shown in **Figure 2.5**, the muscle CSA ratios with top three lightest or heaviest atrophy degree and the bilateral Area ratios of their feeding arteries were individually correspondingly analyzed. In the following charts, the index of muscle atrophy (MA) degree is residual/sound limb muscular CSA percentage by using the measured data at 50% level; the index of artery narrowness degree is residual/sound limb vascular Area percentage. BF represents the long head of biceps femoris, and LFCA represents the descending branch of lateral femoral circumflex artery. The red and blue fonts respectively indicate the largest and the smallest atrophy/narrowness.

1. Case-1: female with left thigh middle level amputation, follow-up case, residual/sound limb length ratio of 54.04% at 4th month after surgery:

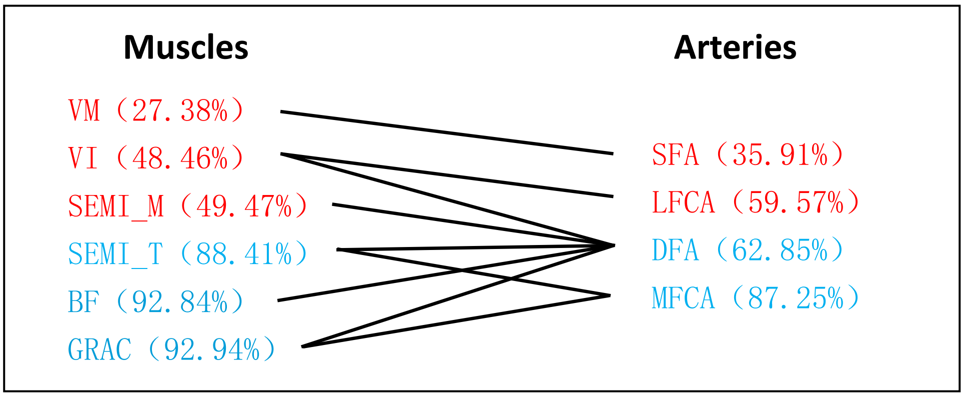

Residual/sound limb length ratio of 53.98% at 8th month after surgery:

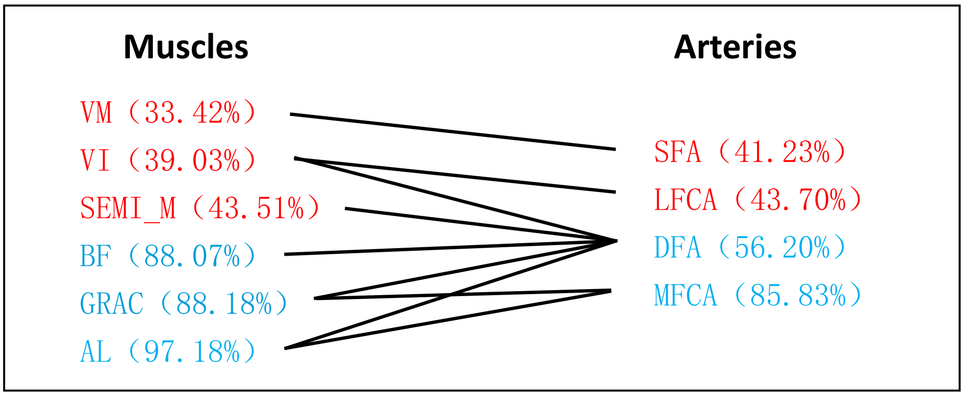

Residual/sound limb length ratio of 52.95% at 12th month after surgery:

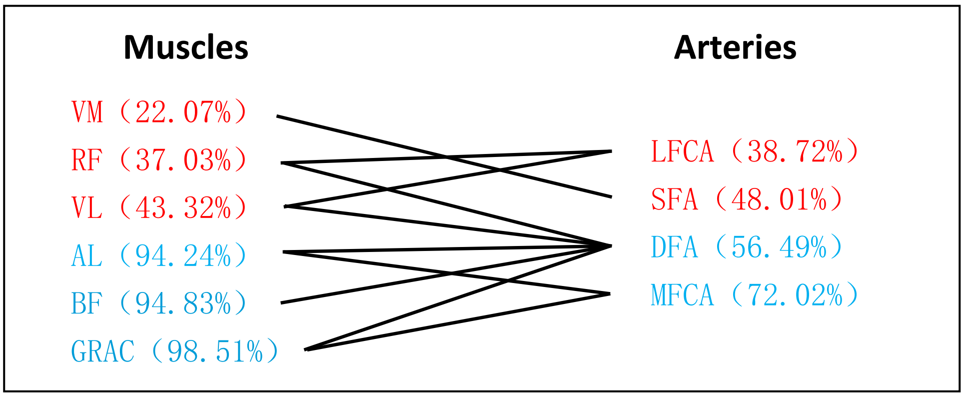

Case-1 used a total-surface-bearing prosthesis for daily walking since the 6th month after surgery. Her RL length was shortened by 1.09% throughout the follow-up period. The Area index of CFA and DFA decreased slightly from 63.06% and 62.85% to 62.08% and 56.49%, whereas the index of MFCA and LFCA sharply dropped from 87.25% and 59.57% to 72.02% and 38.72%, respectively. The difference was that the rapid decrease of MFCA occurred in the later phase (8th to 12th month), yet that of LFCA occurred in the earlier phase (4th to 8th month). SFA showed the only growing trend from 35.91% to 48.01% during follow-up, however, it was still the largest narrowing artery in RL.

Corresponding to the blood-supply relationship, the largest atrophy degree showed in VM that was mainly nourished by SFA, while SEMI_T, GRAC and AL which were mainly fed by MFCA with the least narrowness presented the lightest atrophy degree. Although the Area index of SFA had picked up at the 12th month, the muscles supplied by it were not only VM, but also SART with a slight CSA increase and AM with stable CSA ratios. During the follow-up period, corresponding to the significant reduction of the Area index of LFCA, the most atrophied muscle changed from VI and SEMI_M to RF and VL which got blood-supply from LFCA, and meanwhile the CSA index of VI was still lower. As for DFA which has many branches, the muscles fed by it and its perforating arteries have a wide coverage. That could explain the relative stability of the Area index of DFA. Taken altogether, the muscular atrophy degree and the arterial narrowness degree of Case-1 both deepened with the increase of postoperative time, and they showed positive correlations at all stages.

2. Case-2: male with left thigh middle level amputation, follow-up case, residual/sound limb length ratio of 56.73% at 4th month after surgery:

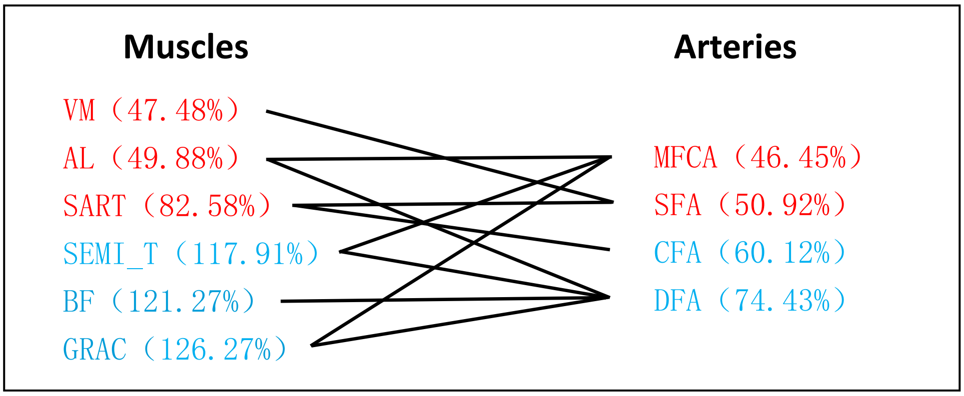

Residual/sound limb length ratio of 55.99% at 8th month after surgery:

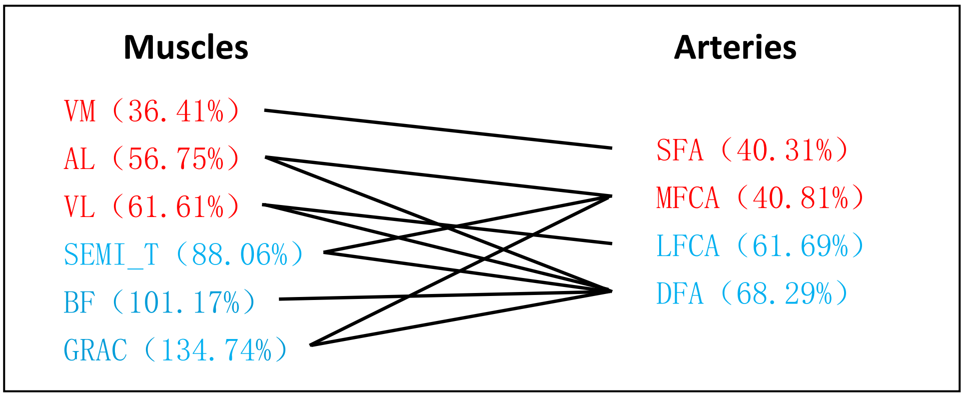

Residual/sound limb length ratio of 54.88% at 12th month after surgery:

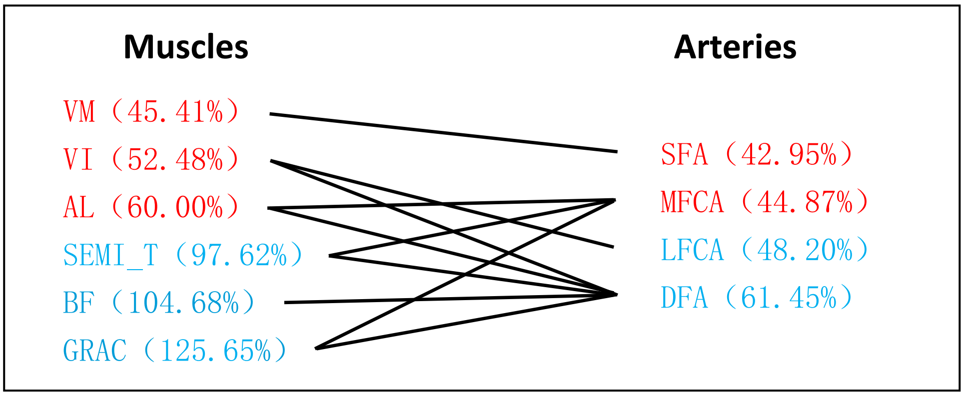

Case-2 used crutches for daily walking during the follow-up period. His RL length was shortened by 1.84% which was larger than that of Case-1. The Area index of CFA showed a slight decline from 60.12% to 53.08%, which was a consistent trend with Case-1. Whereas the index of DFA sharply dropped from 74.43% to 61.45%. MFCA and LFCA displayed different trends of changes. The Area index of the former dropped from 46.45% and then rose to 44.87%, while the latter continued to decline from 65.05% to 48.20%. SFA decreased from 50.92% to 42.95% with the major change occurred in the earlier phase (4th to 8th month). The difference between Case-1 and Case-2 was mainly reflected in the opposite narrowness degree of MFCA and LFCA.

Similar to Case-1, the largest atrophy degree of Case-2 also showed in VM which was mainly fed by SFA. From the 4th month to the 12th month, the atrophy amounts of VI and VL increased markedly with the great decrease of the Area index of LFCA. As for MFCA, one of its feeding objects AL showed obvious atrophy, whereas the others GRAC, AM and SEMI_T presented little atrophy but even bigger CSA than SL (>100%). These three muscles also received the blood supply from DFA whose Area index was stable and higher, and that might be a part of the support for this reverse atrophy. Taken altogether, the muscular atrophy degree and the arterial narrowness degree of Case-2 fluctuated during the follow-up period, and the positive correlation between them found in Case-1 was indeterminate in Case-2.

3. Case-3: male with left thigh middle level amputation, received the examination at the 10th month after surgery. Residual/sound limb length ratio was 58.32%:

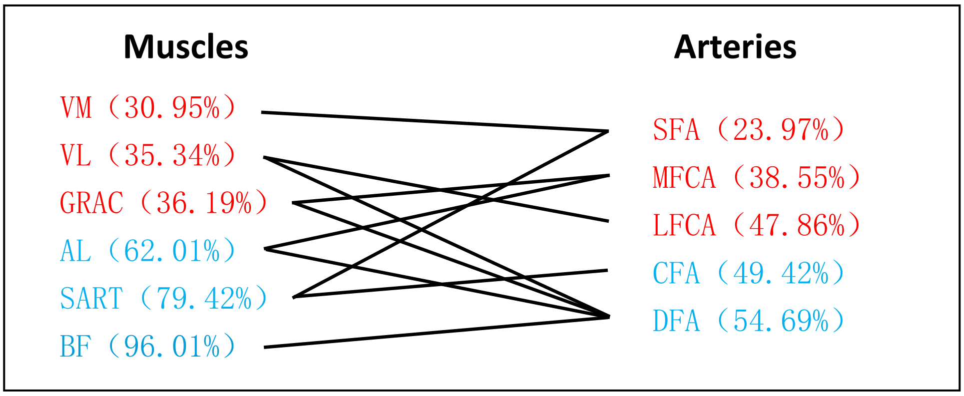

Case-3 used crutches for daily walking after the surgery and his daily activities were few. At the 10th month, the bilateral differences of muscle/thigh total area ratio were as high as 16.37% (30% level), 17.68% (50% level) and 25% (70% level), which means the total atrophy in RL was significant. The Area index of the five main arteries in RL showed a corresponding marked narrowness. SFA was still the most narrowed vessel with the Area index of 23.97%, and its feeding object VM showed the largest atrophy degree. MFCA narrowed to 38.55%, and GRAC, SEMI_T and AM receiving its blood supply presented relatively lower CSA ratios, espacially GRAC of 36.19%. The narrowness of LFCA was smaller than that of MFCA, however this case still showed a great atrophy of quadriceps nourished by LFCA. The minimal narrowness occured in DFA, yet its Area index was only 54.69%. Corresponding to this, only BF in the posterior muscle group showed slight atrophy, whereas the CSA index of SEMI_M was greater than that of SEMI_T which also received the supply from MFCA. Although there were some differences in atrophy situation, the arterial narrowness and the muscle-artery correlation of Case-3 were similar to the results of Case-2 at the 8th month, namely that the positive correlation between atrophy and narrowness was not as clear as shown in Case-1.

4. Case-4: male with right thigh lower level amputation, received the examination at the 30th month after surgery. Residual/sound limb length ratio was 75.71%:

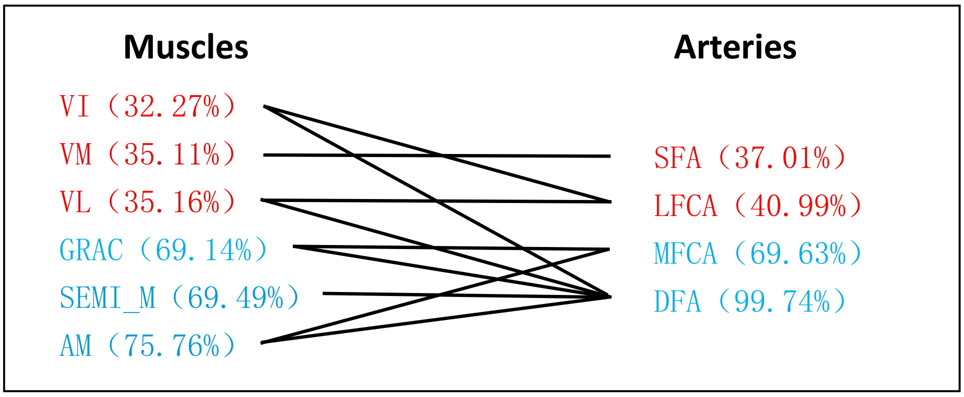

Case-4 used a total-surface-bearing prosthesis for daily walking after the surgery. At the 30th month, the bilateral difference of muscle/thigh total area ratio was 14.28% at the 50% level, implying that the total atrophy amount in RL was not low. In this case, SFA was still the most narrowed vessel with the Area index of 37.01%, and followed by LFCA narrowed to 40.99%. The most severe muscle atrophy occured in quadriceps which was mainly fed by these two arteries. MFCA showed a relatively greater Area index, while DFA was hardly narrowing. Their nourishing objects GRAC, SEMI_M and adductors, as well as BF, displayed corresponding smaller atrophy degrees. In addition, the posterior and medial muscle groups of this case always showed less atrophy than the anterior muscle group at the three levels. This corresponded to the narrowness degrees of DFA, MFCA and LFCA. Taken altogether, the positive correlation between muscular atrophy and arterial narrowness was basically explicit in Case-4.

5. Case-5: male with right middle level amputation, received the examination at the 16th month after surgery. Residual/sound limb length ratio was 47.59%:

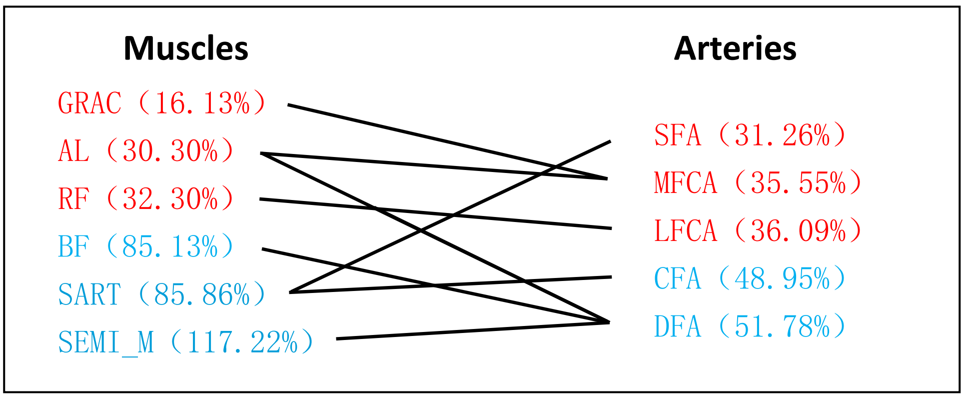

Case-5 used crutches for daily walking after the surgery, and sometimes he hopped for close range activities. At the 16th month, the bilateral differences of muscle/thigh total area ratio were 8.99% (30% level), 13.95% (50% level) and 24.91% (70% level), which means the total atrophy in RL was significant. Similar to Case-3, there were many intermuscular adipose tissues in the end portion of RL leading to less muscle percentage. All the five main arteries in RL showed a marked narrowness. The Area indices of SFA, MFCA and LFCA were 31.26%, 35.55% and 36.09% respectively, not much difference. Their feeding objects RF, VI, VL, and medial muscle group showed corresponding greater atrophy. The minimal narrowness occured in DFA. BF reseiving blood-supply from DFA was lightly atrophic, and SEMI_M presented reverse atrophy which means its CSA was greater in RL than in SL (>100%). By inter-case analysis, it could be found that Case-2, Case-3 and this case who were not using prosthesis similarly showed the reverse atrophy in hamstrings or GRAC, and the vascular narrowness degrees of these three cases were relatively greater. Overall, the atrophy degrees of the anterior and posterior muscle groups in this case were consistent with other cases. The difference was that there was a substantial decrease in the CSA index of the medial muscle group in this case, which was corresponded to the large narrowness of MFCA. Therefore, the positive correlation between atrophy and narrowness in Case-5 was indeterminate but more clear than in Case-2 and Case-3.

6. Case-6: male with right middle level amputation, received the examination at the 33rd month after surgery. Residual/sound limb length ratio was 39.27%:

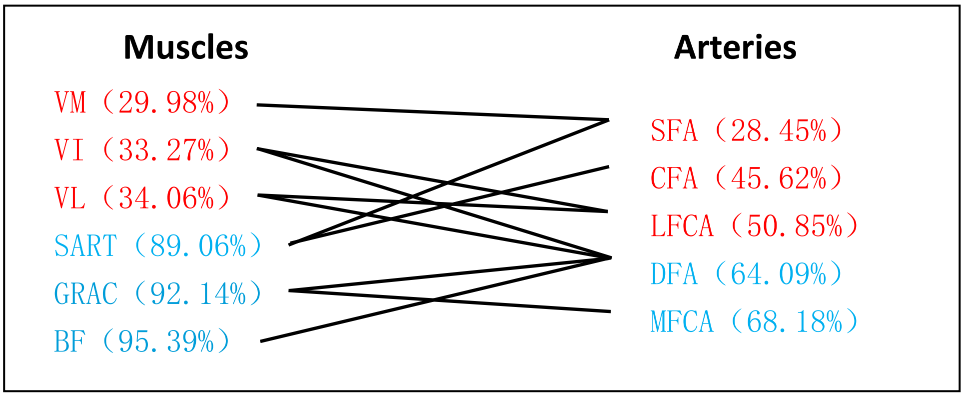

Case-6 used a total-surface-bearing prosthesis for daily walking after the surgery. At the 33rd month, the bilateral difference of muscle/thigh total area ratio was 9.74% at the 50% level, implying that the total atrophy amount in RL was relatively small. This may be because the RL length of this case was short and the 50% level was closer to hip joint. In this case, SFA was still the most narrowed vessel with the Area index of 28.45%. The most severe muscle atrophy occured in VM which was mainly fed by SFA. CFA narrowed to 45.62%, yet SART nourished by it and SFA showed only a slight degree of atrophy. Quadriceps in the anterior muscle group getting blood-supply from LFCA displayed significant atrophy. DFA and MFCA narrowed to a lesser degree, and their feeding objects GRAC, AM and hamstrings showed corresponding smaller atrophy degrees, whereas the CSA index of AL decreased significantly. Taken altogether, although the atrophy degrees of SART and AL were opposite to the narrowness degrees of their main blood-supply arteries, the positive correlation between muscular atrophy and arterial narrowness was basically explicit in Case-6.

7. Case-7: male with left thigh middle level amputation, received the examination at the 31st month after surgery. Residual/sound limb length ratio was 69.36%:

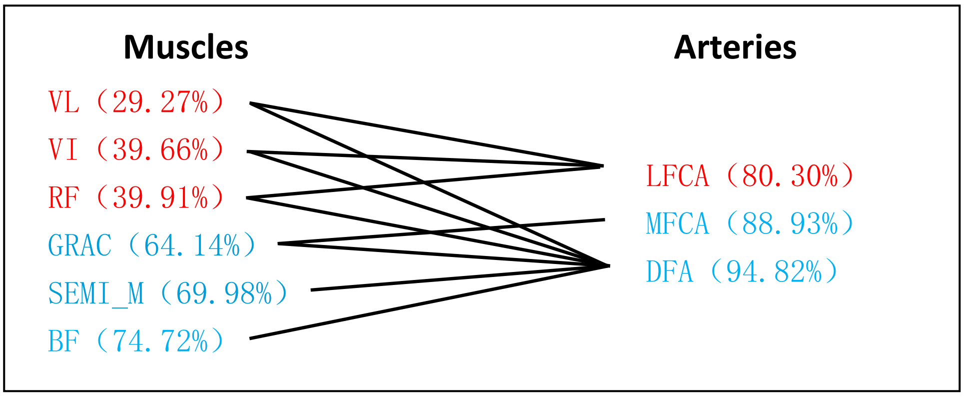

Case-7 used a total-surface-bearing prosthesis for daily walking after the surgery. At the 31st month, the bilateral difference of muscle/thigh total area ratio was 14.58% at the 50% level, very close to Case-4. In this case, DFA was rarely narrowing with the Area index of 94.82%, which was also similar to Case-4. The narrowed amount of the other four arteries were relatively smaller too, wherein the Area indices of

LFCA and MFCA were respectively as high as 80.30% and 88.93%, far greater than those of the other seven cases. Although muscles in RL did not show corresponding slight atrophy, the positive correlation based on the blood supply relationship still existed in this case. Quadriceps mainly fed by LFCA were more severe atrophic than hamstrings and GRAC receiving blood supply from MFCA and DFA. There were many common points in Case-7 and Case-4. Both of them used a prosthesis; their amputation levels and the examination time were close; the total atrophy degrees in RL have not much difference; DFAs showed only a very slight narrowness. In addition, in these two cases, the atrophic difference between the anterior and posterior muscle groups was not large, which means the CSA index of each muscle was closer. Taking the reverse into consideration, Case-5 and Case-6 showed bigger muscle atrophy gaps, and they were the two cases with shortest RL length. Thus this study infers that the imbalance of muscle atrophy degree may be related to the length of RL.

8. Case-8: female with left middle level amputation, received the examination at the 16th month after surgery. Residual/sound limb length ratio was 60.77%:

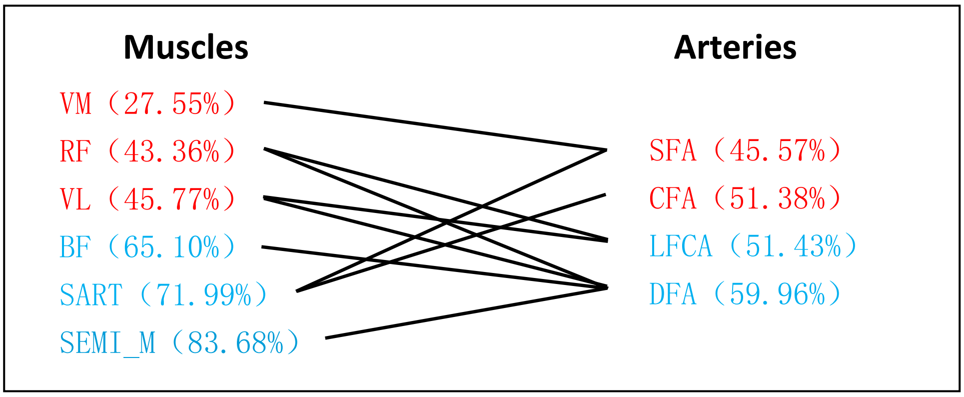

Case-8 used a total-surface-bearing prosthesis for daily walking after the surgery. At the 16th month, the bilateral difference of muscle/thigh total area ratio was 10.76% at the 50% level, implying that the total atrophy amount in RL was relatively small. Similar to the above seven cases, in this case SFA was still the most narrowed vessel with the Area index of 45.57%. The most severe muscle atrophy also occured in VM which was mainly fed by SFA. The narrowness degrees of CFA and LFCA were very close. Quadriceps in the anterior muscle group getting blood-supply from LFCA displayed greater atrophy, whereas SART nourished by CFA and SFA was relatively light atrophic. DFA and MFCA narrowed to a lesser degree. Among their feeding objects, althrough the CSA indices of SEMI_T and AL were lower, SEMI_M, BF, GRAC, and AM showed corresponding smaller atrophy degrees, which was similar to the situation of Case-6. In addition, like Case-4 and Case-7 who also had longer RLs, the atrophic difference between the anterior and posterior muscle groups was not as large as the others. Taken altogether, the positive correlation between muscular atrophy and arterial narrowness was basically explicit in Case-8.

3.2.2 Inter-case discussion on the correlation between muscular atrophy and arterial narrowness

In the previous section it has been concluded that, in the 8 cases, neither muscle atrophy degree nor arterial narrowness degree reflected a clear relationship with RL length or postoperative time. Through the above individual analysis, it can be found that there was indeed no absolute correlation between them. Yet the most influential factor on those correlations was whether the patient used a prosthesis, implying the magnitude and distribution of external stress, the specific circumstances of movement form, gait coordination, exercise amount and other relevant issues.

Comparing the prosthesis users (Case-1, Case-4, Case-6, Case-7, Case-8) with the crutches users (Case-2, Case-3, Case-5), the three patients without using prosthesis showed more severe muscle atrophy and arterial narrowness, with greater atrophy degree gaps and smaller narrowness degree gaps. On the contrary, the atrophy and narrowness of the five prosthesis users were relatively mild, whereas the narrowness degree gaps were larger, and the atrophy degrees were more average. Based on the blood-supply relationship, in the five prosthesis users, DFA, MFCA, and their feeding muscles, the medial group (adductors and GRAC) and hamstrings presented corresponding lesser narrowing/atrophic degrees; SFA, LFCA and their feeding muscles quadriceps presented corresponding greater narrowing/atrophic degrees. That is to say, a kind of positive correlation between muscular atrophy and arterial narrowness was basically clear in these five cases. However, this positive correlation was indeterminate in the other three cases. The concrete reflection was that MFCA narrowed to a marked extent, but GRAC or hamstrings nourished by it showed only a little or even reverse atrophy. During the follow-up period, Case-1 who wore a prosthesis showed smaller fluctuations in muscular CSA percentages, and gradually reducing bilateral differences of muscle/thigh total area ratio, as well as lesser RL length shortening speed. As for the arterial changes, Case-2 without using prosthesis showed smaller fluctuations in arterial Area percentages.

To explain this positive correlation, this paper argues that in the process of wearing prosthesis, various physiological conditions within RL including muscle tension and blood supply were able to maintain the original work pattern and relationships (nourishing, synergy, etc.) due to the movement function being played as much as possible. In other words, good blood supply provides support for the recovery of motor function, while active muscle fibers promote the blood demand to ensure vascular diameter and volume. The reverse atrophy phenomenon is more complicated. On the one hand, without the prosthetic assistance, the function loss of quadriceps may cause hamstrings show stronger compensatory hyperfunction in femur activities and play more synergistic role in hip. On the other hand, there is a considerable heterogeneity among different tissues and muscle components inside RL, which is represented by muscle fibres degenerating, connective tissue increasing and fat imbibition. In earlier studies, Hedberg et al. [37] ascribed the loss of many individual muscle fibres and the abundant connective tissue components to relative inactivity and long-standing arterial insufficiency among trans-femoral amputees. Lilja et al. [37] proposed a severe amount of fat imbibition within muscle could be a result of inactivity in combination with ischaemia among trans-tibial amputees. Therefore, the thickness retention or even growth of hamstrings and GRAC could be related to both hyperfunction and ischemic component changes (increased connective tissue and adipose tissue). That means in the cases who did not use a prosthesis and had relatively small amount of activity, the larger narrowness degree of MFCA may be responsible for the fatty hypertrophy of its feeding muscles---GRAC and hamstrings.

From the first chapter review it can be learned that, whether the hypoxic-ischemic injury investigation from the macroscopic point of view, or the pathological study of muscular atrophy from the micro perspective, they all took into account the combined effects of the internal and external mechanical states and the biochemical environment determined by blood flow. After amputation, the biggest difference of the movement form and the external stress of RL comes from prosthesis usage, and the duration and frequency of rehabilitation training or routine walking using the prosthesis. The location, area, time length differences of the RL/external force contact could result in the variation of muscle and tissue stress and strain [52], thus changing the internal mechanical environment of RL. On the one hand, it would affect the synthesis and apoptosis of muscle cells, on the other hand, it would affect the microvascular structure and the local pressure gradient across vascular wall, etc. The consequent interaction and adjustment of the entire internal physiological state are induced. In a few words, muscle atrophy degree and blood flow state are closely related, and whether or not use a prosthesis could exert influences on both muscles and arteries by changing the internal and external stress and strain of RL.

Based on the conclusions of previous studies combining with our experimental data and comparative analysis, this study drew the following corollaries for trans-femoral amputees: using prosthesis not only could make each muscle of RL adjust to new movement form and save physiological tension, by maintaining original body balance and gait, and increasing activity amount as much as possible, but also could contribute to the retention of blood flow and arterial lumen volume within RL , so that to ensure the supply of oxygen and nutrients. In those five prosthesis users, the variations of vessel size and blood flow of each main artery might just cooperate with the adjustments of muscle strength and function, which means muscles and blood-supply formed a benign interaction to jointly promote the rehabilitation of RL. On the contrary, patients without using prosthesis are prone to sedentary (including the use of wheelchair) or bedridden, single foot standing or hopping, thus their walking amount often significantly reduce and the gait energy consumption mainly concentrates on SL (including the use of crutches). The three cases in this study showed the overall narrowness of the main arterial system and the dramatic atrophy of individual muscles in RL. These phenomena not only may cause the function deterioration and blood-supply disorder which would form a vicious circle with muscle atrophy or other skin and soft tissue problems, but even also affect the changes of blood flow field and hemodynamic parameters, followed by inducing various arterial lesions. In addition, the hypofunction of RL would aggravate the burden of SL, and simultaneously implicate SL in disuse atrophy and the loss of muscle strength.

3.3 SUMMARY

This chapter through a case study of 8 subjects with unilateral trans-femoral amputation, completed the morphological index analysis of bilateral muscle atrophy, arterial narrowness, as well as their relationship. According to the measurement results and muscular blood-supply sources, this paper proposed that for the first time, the prosthesis user cases presented a positive correlation between muscular atrophy and arterial narrowness in residual limb, however, this kind of positive correlation was indeterminate in the cases without using prosthesis.

The explanation for this difference is from multi-aspect. For prosthesis users, the external pressure stimulation from socket and the induced changes of internal tissue stress, combining with a relatively qualified walking amount, could make each muscle of residual limb adjust its functional status and save physiological tension as far as possible. While the arterial blood flow and lumen volume would show corresponding changes to ensure the supply of oxygen and nutrients for muscles.

So that there is a benign interaction in residual limb. Meanwhile, the cooperate of both limbs would reduce residual limb disuse and sound limb overwork. On the contrary, without the prosthetic assistance, there are usually sedentary, bedridden, and the concentration of gait energy consumption on sound limb, etc.. Patients' inactivity is prone to result in the dramatic atrophy of individual muscles and overall narrowness of main arteries, which may lead to function deterioration and blood-supply disorder in residual limb, and even may pose a high risk of arterial lesions by influencing blood flow field and the distribution of hemodynamic parameters. Thus, the uncertain correlation could be the result of a non-benign collaboration of various physiological factors. In addition, inactivity coupled with insufficient blood supply may cause heterogeneity among muscle components. It could be characterized by connective tissue increase and a kind of hypertrophy arising from fat imbibition.

Therefore, the conclusion is the use of prostheses not only can achieve the functional compensation of residual limb effectively, but also can promote the joint adjustment of bilateral limbs on the entire physiological state including muscles and arteries, forming a benign collaborative environment. At the same time we suggested that, the prosthetic design in the future should consider the extrusion and influence from the stress and strain changes of interior tissue caused by external pressure on capillary network or even large supply arteries. Combined with electrical stimulation, drug therapy and exercise training, prostheses could help to increase muscular blood flow while reduce regional interface pressure, in order to promote the comprehensive rehabilitation of residual limb.

CHAPTER 4: SPATIAL STRUCTURE CHANGES OF ARTERIAL TREE

As can be seen from the previous chapter, muscle/thigh total area ratio is an overall atrophy index, while the CSA bilateral percentage of each muscle indicates the individual atrophic degree. Like that, in addition to the individual evaluating, arterial system also requires an index to characterize the changes of whole structure which is a complete vascular tree containing all branch vessels with effective image development.

Studies have shown that, the changes of many diseases and physiological processes are related to the variation of vascular tree structure (Wellnhofer E, et al., 2002). At present, the researches of vascular tree were mainly around pulmonary vessels (Tong Jia, et al., 2010), retinal vessels [139], coronary arteries (Fotiadis D.I., et al., 2005), hepatic vessels [140] and cerebral vessels [141]. Those work mostly focused on the extraction and modeling methods, vascular distribution characteristics, or mechanical analysis of vessels, and they illustrated that the morphological information of vascular tree has important and multifaceted clinical implications. For the relatively larger vascular tree within thigh, especially within the residual limb (RL) after amputation, its spatial structure variation has not been reported yet. To this end, this chapter innovatively employed a topological concept *Hausdorff* distance to quantify the overall spatial deformation of unilateral thigh artery tree. Because human body is not absolutely bilateral symmetrical, and the vascular structure in RL has changed greatly due to the surgery, to compare the vessel structure difference between the RL and the sound limb (SL) has no actual meaning. Therefore, the spatial deformation analysis is only applicable to two follow-up subjects, namely Case-1 and Case-2. Hausdorff distance values were used to illustrate the deformation degrees of ipsilateral arterial system between different stages during the follow-up period. And then the change trends of RL and SL were compared.

4.1 ARTERIAL TREE MODELING AND COORDINATE MATRIX EXPORT

As described in the previous section 2.1.3 and 2.1.4, the CT images were imported into software MIMICS v10.0 to perform the 3D reconstruction of the arterial tree of RL and SL separately, removing some small branches with poor imaging quality in order to ensure the accuracy and reliability of the models. Different from the above morphological study, in this chapter, the vascular tree of SL did not need to be cut at the same level of residual bone end, since it was no longer a bilateral comparison but the follow-up contrast in the same side. Therefore, the arterial tree zone of SL was from ischial tuberosity to the bottom of femur medial condyle (**Figure 4.1** and **Figure 4.2**).

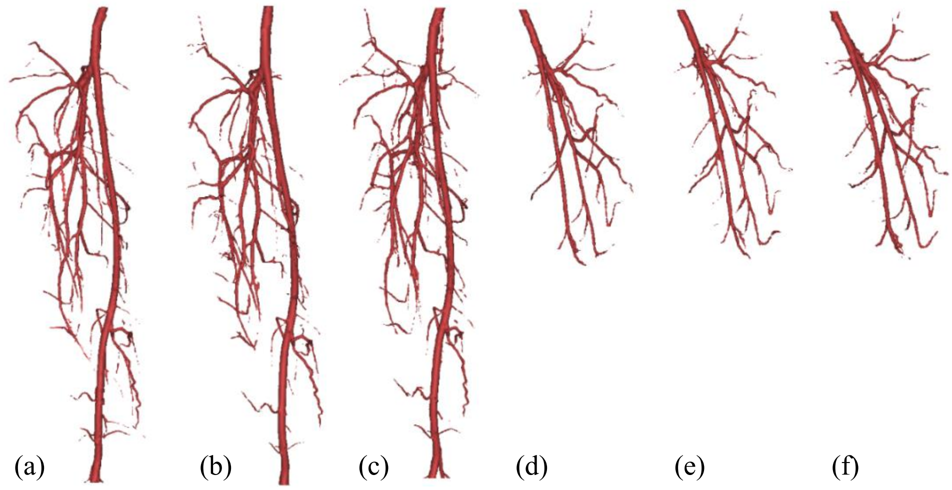

Figure 4.1 The 3D model front view of Case-1's bilateral arterial trees. (a), (b), (c) are the SL models at the 4th, 8th,12th month after surgery; (d), (e), (f) are the RL models at the 4th, 8th,12th month after surgery.

After modeling, as described in section 2.1.4, the MedCAD module was used to achieve the format conversion from scanned data to CAD data. Through automatic fitting and drawing the control points and centerlines of the entire model (**Figure 4.3**), the 3D coordinate series of each artery, namely the coordinate matrix of the arterial tree could be obtained for describing its spatial structure. The fitting parameters were set as resolving resolution of 1.0mm, iterations of 2, and the distance between control points of 1.0mm. The matrix data of each arterial tree was exported as a text file for further calculating and comparing the amount of deformation between them during the follow-up period.

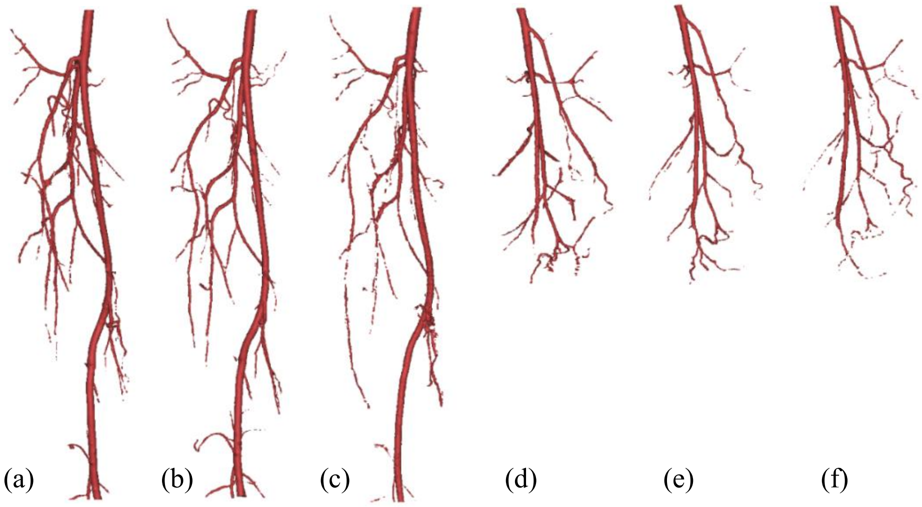

Figure 4.2 The 3D model front view of Case-2's bilateral arterial trees. (a), (b), (c) are the SL models at the 4th, 8th,12th month after surgery; (d), (e), (f) are the RL models at the 4th, 8th,12th month after surgery.

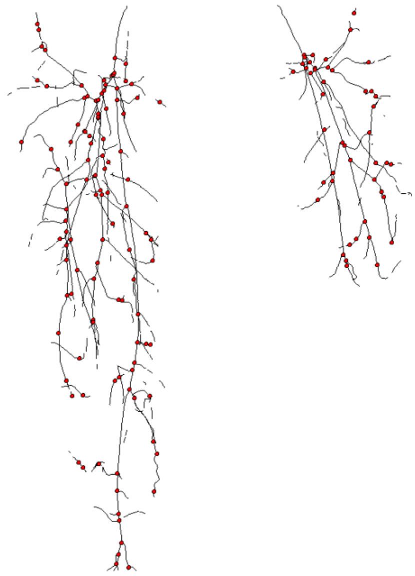

Figure 4.3 The fitting control points and centerlines of bilateral arterial trees.

4.2 THEORY AND CALCULATION OF HAUSDORFF DISTANCE

Hausdorff distance was proven to be an effective tool to illustrate the resemblance between two geometric entities or real space algebraic curves through computing the maximum distance between two proper subsets. This concept was first proposed by the German mathematician Felix Hausdorff, and it has been developed to several variants to adapt its wide range of applications in computer aided design, such as image registration and shape matching (Hu S. and Wallner J., 2005), pattern recognition (Bai, Y. B., et al., 2011), collision detection and geometric approximation (Varadhan G. and Manocha D., 2006), as well as the haptic simulation (Kim K. J., 2003). The magnitude of *Hausdorff* distance value is proportional to the difference in spatial structure.

Given two finite point sets $A = \{a1, a2, a3, ..., an\}$, $B = \{b1, b2, b3, ..., bm\}$, then the *Hausdorff* distance of these two sets is defined as (Rucklidge W. J., 1997):

$$H(A,B) = \max(h(A,B), h(B,A)) \tag{4.1}$$

wherein

$$h(A,B) = \max_{a_i \in A} \min_{b_j \in B} \left\| a_i - b_j \right\| \tag{4.2}$$

$$h(B,A) = \max_{b_j \in B} \min_{a_i \in A} \left\| b_j - a_i \right\| \tag{4.3}$$

Equation (4.1)-(4.3) are the basic form of *Hausdorff* distance formula. ||.|| is the distance norm between the point sets A and B. The result of Equation (4.1) is susceptible to feature points, therefore some improved algorithms have been proposed to avoid this sensitivity. In the present study, a kind of modified *Hausdorff* distance formula was employed (Sim D. G., 1999):

$$MH(A,B) = \max(Mh(A,B), Mh(B,A)) \tag{4.4}$$

wherein

$$Mh(A,B) = \frac{1}{N_A} \sum_{a_i \in A} \min_{b_j \in B} \left\| a_i - b_j \right\| \tag{4.5}$$

$$Mh(B,A) = \frac{1}{N_B} \sum_{b_j \in B} \min_{a_i \in A} \left\| b_j - a_i \right\| \tag{4.6}$$

N_A and N_B in Equation (4.5) and (4.6) are the point number of set A and set B. This version reduces the interference of outliers, thereby making the result more accurate.

A program was written according to the above modified formula. Meanwhile, to avoid the errors caused by the different supine postures and different original axes during each test, the branch point of deep femoral artery and superficial femoral artery was selected as the reference point for coordinate registration. And another program was written for this purpose. Thereafter, these two programs were applied in the mathematical software MATLAB 7.11 to calculate the *Hausdorff* distance value between two imported arterial tree matrices.

4.3 RESULTS AND DISCUSSION

The pairwise *Hausdorff* distance calculations were carried out among the three CT angiography of the SL arterial tree (HD_{S1-2}, HD_{S2-3}, HD_{S1-3}) and the RL arterial tree (HD_{R1-2}, HD_{R2-3}, HD_{R1-3}) for both subjects. **Table 4.1** showed the numerical results of Case-1 and Case-2, and **Table 4.2** showed the normalized figures relative to the HD_{S1-2} of Case-1.

Table 4.1 Hausdorff distance values during the follow-up period

Subjects	Hausdorff distance (mm)					
	HD_{S1-2}	HD_{S2-3}	HD_{S1-3}	HD_{R1-2}	HD_{R2-3}	HD_{R1-3}
Case-1	4.51	6.11	4.26	7.52	8.77	6.01
Case-2	9.25	8.37	9.12	6.35	5.19	6.23

Table 4.2 Normalized Hausdorff distance relative to the HD_{S1-2} of Case-1

Subjects	Hausdorff distance (mm)					
	HD_{S1-2}	HD_{S2-3}	HD_{S1-3}	HD_{R1-2}	HD_{R2-3}	HD_{R1-3}
Case-1	1	1.35	0.94	1.67	1.94	1.33
Case-2	2.05	1.86	2.02	1.41	1.15	1.38

Comparing these results it could be known that the arterial deformation in lower limbs of Case-1 and Case-2 were different. Case-1 who wore a prosthesis presented larger changes in her RL than in the SL, and the greatest difference of both sides occurred in the second phase, namely between the 8th and 12th month after surgery. In contrast, Case-2 who walked with crutches instead of using prosthesis exhibited larger changes in his SL than in the RL, and the greatest difference of both sides occurred in the first phase, namely between the 4th and 8th month after surgery. By inter-case comparison, the arterial deformation gaps between bilateral limbs of Case-2 were slightly larger than those of Case-1. Meanwhile, the deformation degree gap between SL and RL of Case-1 was gradually reduced over time, while there was little change in the gap of Case-2.

Case-1 and Case-2 were amputated for the same reason (bone tumor), with the same surgical procedure (operator was the same orthopedist), postoperative treatment and follow-up interval, as well as the similar RL length (bilateral thigh length ratios were 54% and 57%), but the different mobility patterns in their rehabilitation process. It implies that during the follow-up period, the differences between Case-1 and Case-2 including body balance, gait adjustment, energy consumption, daily activity forms and exercise amount etc. were mainly due to whether prosthesis usage. Human beings are bipeds and the only vertebrates have arches of foot [142]. This bipedal biomechanics and functional anatomy of the human body structure determines that lower limbs not only play a major role in standing, walking, jumping and other locomotion, but also maintain the upright posture and body balance all the time. The synergy of both legs and the cooperation of hip, knee and ankle joints have significant impact on symmetric gait and systemic motor coordination. In fact, the six major determinants of gait are pelvic rotation, pelvic tilt, lateral pelvic displacement, hip and knee flexion, knee and ankle interaction (Saunders, J. B., 1953). Any irregularity in these determinants could lead to the pathological gait. Apparently, trans-femoral amputation results in severe irregularities as the loss of knee and ankle function of RL. This kind of pathological gait would not only cost several fold inevitable energy consumption, but also increase the burden of SL during standing and walking. Besides, during sitting or lying, the absence of most part of distal limb on one side would cause the contralateral limb to undertake the primary activity tasks, like the translation of the center of gravity, balance control, postures switch and various hip or trunk movements. Such a disabled gait makes spontaneous effective compensation impossible, so patients need assistive devices for walking to avoid the disuse muscle atrophy, cardiopulmonary function degradation or other problems produced by sedentariness or prolonged bed rest. Prostheses could effectively provide this kind of functional compensation for residual limb and maximize the recovery of normal walking. This also means that the load of SL could be reduced and the symmetric physiological state of bilateral lower limbs would be remained as much as possible.

Case-1 started to wear a prosthesis with a comprehensive contact socket from the 5th month after amputation, implying that during the whole follow-up period she experienced the process from adaptation to be an active prosthesis user. This process obliged both RL and SL to adjust their entire physiological states to accommodate the new gait and balance. In addition to the major changes of internal tissue stress, RL also withstood the external pressure from the socket. Bouten, et al. [99] pointed out that pressure on skin surface and its causing local pressure gradient across vascular wall could give rise to capillary collapse, which might result in the deformation of local small vessels and large vessels ending. Daniel, et al. [97] and Salcido, et al. [98] proposed that, muscle was more sensitive than skin to the effects of pressure, thus the extrusion or displacement of muscle and soft tissue might cause the variation of the spatial direction and shape of muscular arteries. Through their experiment, Tyml et al. [105] demonstrated that the short-term tetrodotoxin-induced atrophy would affect microvascular structure. These combined effects of internal and external force could explain why the shape and spatial deformation of the arterial tree in Case-1's RL was greater than that in her SL. And it could also be a reason for that the deformation degree of Case-1's RL was more significant than that of Case-2 who did not carry any load-bearing produced by using prosthesis. At the same time, according to the description and analysis about lower limb movement anatomy in Chapter 3, the cooperation of the bilateral lower limbs of Case-1 diminished the RL disuse and the SL overwork. This progressively normalized and coordinated walking pattern could also facilitate her increasing the amount and frequency of daily exercise, making more adaptively physiological deformation. These synthetical factors involving locomotion pattern and biomechanical environment could explain the greater deformation in the late stage and the decreased bilateral deformation degree gap of Case-1. Based on the same principles but reverse situation, the opposite results of Case-2 could be understood. He was dependent on crutches to stand or to hop by the SL rather than walking, which led to heavy energy consumption and the sharp reduction of exercise. SL had to take responsibility for all the jobs originally accomplished by two legs, such as supporting upright, stabilizing body balance and switching various postures, whereas RL was basically in the state of disuse. However, the potential positive changes of internal biomechanical condition could not be stimulated without the major function restore or external pressure. Therefore, Case-2 showed greater arterial tree deformation in his SL and the bilateral deformation gap got bigger over time.

4.4 SUMMARY

This chapter illustrated that the bilateral thigh artery system of unilateral trans-femoral amputees would undergo spatial structure changes within one year after surgery. The key impact factor on bilateral arterial tree deformation was the locomotion pattern during rehabilitation---prosthesis usage. The subject wearing prosthesis showed greater arterial tree deformation in the RL than in the SL, and the difference of bilateral deformation degree decreased over time. The subject without using prosthesis presented the opposite results. Consistent with the conclusion of the last chapter, these results once again suggested that, using prosthesis not only can achieve the functional compensation for residual limb, but also could promote the joint physiological state adjustment of both lower limbs to accommodate a new bipedal gait pattern. It is further explained that the stump/socket interface pressure would affect not only the state of muscles and soft tissue, but also the overall structure of arterial system. In the future study of prosthetic design, the specific effects produced by internal and external pressure on arterial tree deserve thorough investigation to minimize the negative influence and bilateral difference.

CHAPTER 5: ESTABLISHMENT OF ARTERIAL CALCULATION MODEL

From perioperative period to lengthy rehabilitation, trans-femoral amputees need comprehensive and cautious treatment to help them rebuild their physical and psychological confidence. Hemodynamic study consistently runs throughout the entire process and played a significant positive role. Whether from clinical or biomechanical perspective, the investigations of preoperative diagnosis and surgical techniques have been relatively mature and gained some clear outcomes. Whereas in terms of the postoperative problems, there is a lack of vascular or blood flow state studies specifically for lower residual limb (RL). Therefore, the detailed researches on the relationships between various blood flow parameters and certain common complications are pending to be carried out. In this chapter, computer simulation of fluid dynamics was used to investigate the hemodynamic state in main arteries of thigh.

5.1 ESTABLISHMENT OF THIGH ARTERIAL 3D MODEL

5.1.1 Overview of finite element analysis

Finite Element is a concept proposed by Turner et al. in 1956. In simple terms, it refers to that, a structure can theoretically be decomposed into finite small discrete subregions, and these subregions are called finite elements. In fact, the concept of finite element has been developed and applied several centuries ago, for example, by approximating a circle with a polygon (a finite number of linear units) to obtain the circumference. But developing it into a mature method was owe to the rapid development of computer technology in the latter half of the last century, which made finite element grow based on variational principle. Finite Element Method, first applied to the structural strength calculation of aircraft, rapidly expanded into a practical and efficient modern numerical analysis method which could be employed in any physical fields described by differential equations (continuum, heat conduction, electromagnetic field, hydrodynamics, etc.).

The principle of finite element method is to discretize a continuous solution domain into a combination of units, and use the assumed approximate function within each unit to regionally represent unknown field functions on the solution domain. That approximate function is usually expressed by unknown field functions and the numerical interpolation functions of their derivatives at each node of the unit. Thus, a issue with continuous infinite degrees of freedom becomes a issue with discrete finite degrees of freedom. Similarly, Finite Element Analysis (FEA) is a method of using mathematical approximation. It simulates real physical systems (geometry and loading) applying simple and interactional units---finite elements, to achieve the approximation of an infinite unknown quantity through a finite number of unknowns. Most of practical problems are difficult to obtain the precise solution, whereas finite element method not only is high precision, but also can adapt to a variety of complex shapes, and thus becomes a widely used effective analysis mean in engineering design and scientific research fields.

The basic steps of FEA are usually as follow: (1) to determine the physical properties and geometric region of solution domain according to the actual issue; (2) the discretization of solution domain, namely to divide the solution domain into finite element meshes with different size and shape, and connecting to each other; (3) using a differential equation set containing the boundary condition of state variable to describe the specific physical problems to be solved; (4) to construct a suitable approximate solution for the element, which means the derivation of finite element formulation, including the selection of reasonable unit coordinates, establishing unit shape function, giving the discrete relation of each state variable of a unit, so as to form a unit matrix; (5) in adjacent cellnodes, to assemble elements to form the general matrix equation of discrete domain (joint equation set), and the unit function continuity needs to meet certain continuous conditions; (6) the simultaneous equations system is solved by direct method, iterative method, or stochastic method, and the result is the approximate value of the state variable at unit nodes. In short, finite element method is a process containing the establishment of finite element model, unit mesh generation (discretization), calculation and result analysis, wherein the discretization of solution domain is one of the core technology. The smaller units (the finer mesh) make better approximation of discrete domain and more accurate results, but also increasing calculation amount and error. To sum up, mesh quality directly affects the solution time and the accuracy of results.

Developed to today, Finite Element Method has been used in almost all scientific research and engineering technology fields, such as hydraulic engineering, civil engineering, bridges, machinery, electric motor, metallurgy, shipbuilding, aerospace, aircraft, missiles, nuclear energy, earthquake, geophysical exploration, meteorology, seepage, acoustics, mechanics, etc. FEA software, according to its applicable range, can be divided into professional software and large-scale general-purpose software. After several decades of improvement, various FEA softwares have transformed Finite Element Method to social productivity. Common general FEA softwares are Ansys, Abaqus, LMS-Samtech, Algor and so on. In Computational Fluid Dynamics (CFD) field, FLUENT is the most commonly used commercial CFD software package in the world. Its first feature is employing the Finite Volume Method based on fully unstructured mesh.

The basic idea of Finite Volume Method is to divide computational domain into a series of irrepetitive control volumes surrounding each mesh point. A set of discrete equations are obtained by integrating the differential equation to be solved on each control volume. Wherein the unknown is the value of the dependent variable on mesh points. In order to get the integral of control volumes, it is necessary to assume the change law of the values between mesh points, which means the distribution profile of value segmentations. For a long time, among the discrete methods of the numerical solution of differential equations, Finite Difference Method and Finite Element Method are the most commonly used ones. Finite Volume Method is similar to both of them and even better by absorbing their advantages while overcoming the shortcomings. The discrete equations of Finite Volume Method requires that any set of control volumes satisfy the integral conservation of dependent variables, so the whole computational domain is also satisfied. However, in Finite Difference Method, only when the mesh is extremely fine, discrete equations satisfy the integral conservation. Finite Element Method uses subdivision units which could adapt to complex geometry with the interpolation approximation of shape function to overcome the weakness of difference method. But sometimes it needs to solve large linear equations, neither convenient nor flexible, as well as large deformation discontinuity problem. Therefore, through the integral form of control volumes, Finite Volume Method could adapt to complex solution domain as Finite Element Method, and its discrete method has both the flexibility of difference method and the adaptability of discontinuous solution.

5.1.2 Clinical examination and model extraction

The clinical data acquisition of this study has been detailed described in Section 2.1, including the subject inclusion criteria, examination items and measurement indices, target muscle and artery selection, measurement methods and modeling software. The enhanced CT scan is for achieving the 3D reconstruction of arterial images in software MIMICS 15.0, in order to get the patient-specific computer models for the calculation and analysis of hemodynamic states. Enhanced CT scan, namely the 3D digital substraction angiography, is one kind of medical imaging diagnosis technology. Its characteristic is to measure the attenuation value of X rays passing through human body. The technical term for X-ray attenuation value is density. CT diagnostics uses the "CT value" to describe the difference in density, and the same tissue structure should be of the same density. Angiography is an auxiliary interventional technique in which developer agent is injected into blood vessel. Because X-ray can not penetrate the developer, angiography can accurately reflect the location and extent of vascular lesions. Enhanced CT scan is injecting contrast agents from a vein into blood vessels and meanwhile performs CT scan. The contrast agents, which are the Iodine containing organic compounds of 60%

diatrizoate, are rapid intravenous injected of 1.5~2.0ml/kg to make the blood iodine maintain a certain level. So that the vascular contrast and development quality could be improved in order to reveal the lesions not detected by normal scan. In this chapter, Case-1 who had the best CT imaging quality was used to be the example. For the numerical study of hemodynamics, we used the scanning images at the 12th month after surgery to extract the 3D model of bilateral thigh arterial trees as shown in **Figure 5.1**.

Figure 5.1 Case-1's 3D model of bilateral thigh arterial trees.

5.1.3 Software introduction

In the process of arterial tree 3D modeling, three kinds of software MIMICS 15.0, Gambit 2.4.6, and ANSYS 14.0 (Mesh function and FLUENT module) were applied.

- **MIMICS 15.0**

MIMICS, namely Materialise's interactive medical image control system, it is an interactive medical image control system produced by Materialise company. As a highly integrated and easy to use 3D image generation and editing software, it can be imported various scanning data for building and editing 3D models, and then output the general CAD (Computer Aided Design), FEA (Finite Element Analysis), or RP (Rapid Prototyping) format. This process is the large-scale data conversion processing on the PC machine.

In the present study, MIMISC helped us to implement the transformation from clinical data to simulation models. After getting the enhanced CT image set, imported them into MIMICS 15.0, and then used the Segmentation module to strip blood vessels from muscles, bones, and other soft tissues. This process included the application of Thresholding function to adjust the threshold for image segmentation in order to get a clear image of arteries; carefully erasing femur, skin and muscles in the 3D Objects operation frame with the establishment of 3D models by Calculate 3D from mask function; using Smoothing function to smooth the initial model and manually removing the small or terminal vessels of poor quality. After those three steps, the final 3D model of arterial tree was built. In the numerical study of hemodynamics, we further separated the five main arteries that were concerned with (as shown in **Figure 2.4**).

In addition, the FEA module of MIMICS can rapidly process the scanning imported data and output the corresponding file format for subsequent FEA and computational fluid dynamics research. After building 3D model with scanning data, users can directly mesh in MIMICS through the FEA module which could furthest optimize the input data and carry out the material allocation of volume meshes based on Heinz unit. However, in this study, the pre-processing modeling software Gambit 2.4.6 and the Mesh function in Component of ANSYS 14.0 were used to perform the more rational free volumetric meshing for models. Thus, 3D models were exported in IGES format from MIMICS to complete the subsequent processing.

- **Gambit 2.4.6**

Gambit is a high quality pre-processor oriented to CFD analysis. This software package is designed to help analysts and designers to build and mesh computational fluid/solid dynamics models and other scientific applications. Its main functions include geometric modeling, meshing, setting regional properties and sizes of model, etc. Gambit has the following features: a comprehensive 3D geometric modeling ability on the basis of ACIS kernel; through a variety of ways to directly establish points, lines, faces, and bodies, with strong ability of Boolean operations; most geometries and meshes created by CAD/CAE software could be imported to it, including PRO/E, UG, CATIA, SOLIDWORKS, ANSYS, PATRAN, etc., and there is an automatic tolerance geometry patching function in the import process to ensure the stability and fidelity of Gambit and CAD software interface; geometric checking function will automatically merge the coincidence of points, lines and faces, making high quality geometry and reduced workload; a new geometric correction toolbar improves the short edge elimination, gap suture, sharp corner and chamfer repair, as well as auxiliary line removal more rapid, automatic, flexible, and accurate; powerful meshing capability can meet special requirements for high quality fine meshes such as on the boundary layers; highly intelligent selection of mesh generation method allows fully unstructured mixed meshes making some extremely complex geometric areas contiguous with adjacent regions; the generation and export of needed meshes and format for solvers such as FLUENT, POLYFLOW, FIDAP, ANSYS, etc.

In this study, Gambit was mainly used in the geometric modeling and format conversion, namely its automatic tolerance geometric mending function, in order to guarantee the stability of the interface with CAD software and the high quality and fidelity of geometric model. The specific operation was imported the IGES file output from MIMICS into Gambit, and then used the Geometry/Volume under the Operation tool box to skin the model, which means got points and lines form faces, faces form a body, with gap suture, corner and chamfer repair especially for the interfaces.

- **ANSYS 14.0 (FLUENT)**

ANSYS is a large-scale general FEA software developed by American ANSYS Corporation. It combines the analysis of structure, fluid, electric field, magnetic field, and acoustic field in one, and is the fastest growing Computer Aided Engineering (CAE) software in the world. ANSYS can interface with most CAD softwares in order to share and exchange data. It has three main parts: pre-processing module, analysis and calculation module, and post-processing module. The pre-processing module provides powerful modeling and meshing tools for easily constructing a finite element model; the analysis and calculation module includes structure analysis (linear / nonlinear / highly nonlinear analysis), fluid dynamics analysis, electromagnetic field analysis, sound field analysis, piezoelectric analysis and the coupled analysis of multiple physical fields, which can simulate the interaction of various physical media, with the abilities of sensitivity and optimization analysis; the post-processing module is responsible for displaying or outputting the calculation results in graph, chart, or curve form, such as color contour, gradient, arrow vector, particle flow trace, stereo slice, transparent and translucent display. Meanwhile, ANSYS provides more than 100 types of units to simulate various structures and materials in engineering.

In this study, Mesh function in the Component systems and the FLUENT module of ANSYS 14.0 were applied to mesh the 3D models and to carry out the calculation and analysis of hemodynamics. The four high quality and easy to use meshing methods for CAD models provided by ANSYS are extension, mapped, free, and self-adaption. The mesh generation ways of the former two methods are just as their name implying. Powerful free meshing could directly divide complex models to avoid the mesh mismatch problem during assembling various parts. Adaptive meshing is the automatical generation of finite element mesh for entity models with boundary conditions, and then the program analyze and estimate the mesh discrete error to redefine mesh size, followed by repeated meshing and redefining, until the discrete error is less than the user set value or reach the user defined solution numbers. In our numerical study, the STEP file exported from Gambit was read into ANSYS. The Mesh toolbox was used to set up the boundary layers, to perform free meshing and local mesh refinement, and to set the inlet / outlet / wall areas for the calculation models.

In 2006, ANSYS Company acquired American Fluent Company which was in a leading position in the field of fluid simulation. Therefore, ANSYS software package includes ANSYS CFD (FLUENT/CFX) for the simulation of the complex flows from incompressible to highly compressible. Because of multiple solving methods and the multigrid accelerated convergence technique, FLUENT can achieve the best convergence speed and solution accuracy. Flexible unstructured mesh, adaptive meshing technology based on solution, and mature physical models make FLUENT widely used in the fields of transformation and turbulence, heat transfer and phase change, multiphase flow, moving/deformed mesh, etc. FLUENT employs Finite Volume Method and the gradient algorithm based on mesh node and unit; has strong compatibility to support the discontinuous interface mesh, mixed mesh, moving/deforming mesh, and sliding mesh etc.; contains three algorithms: uncoupled implicit algorithm, coupled explicit algorithm, and coupled implicit algorithm; contains rich and advanced physical models which can accurately simulate the inviscid flow, laminar flow, turbulent flow etc.; has efficient parallel computing function and provides a variety of automatic/manual partitioning algorithm; the built-in MPI parallel mechanism and the unique dynamic load balancing function ensure the global efficient parallel computing. In addition, FLUENT provides a friendly user interface and the secondary development interface (UDF) for users. This study used the FLUENT module for subsequent blood flow calculations (the computational process in FLUENT, ANSYS 14.0 is shown in **Figure 5.2**).

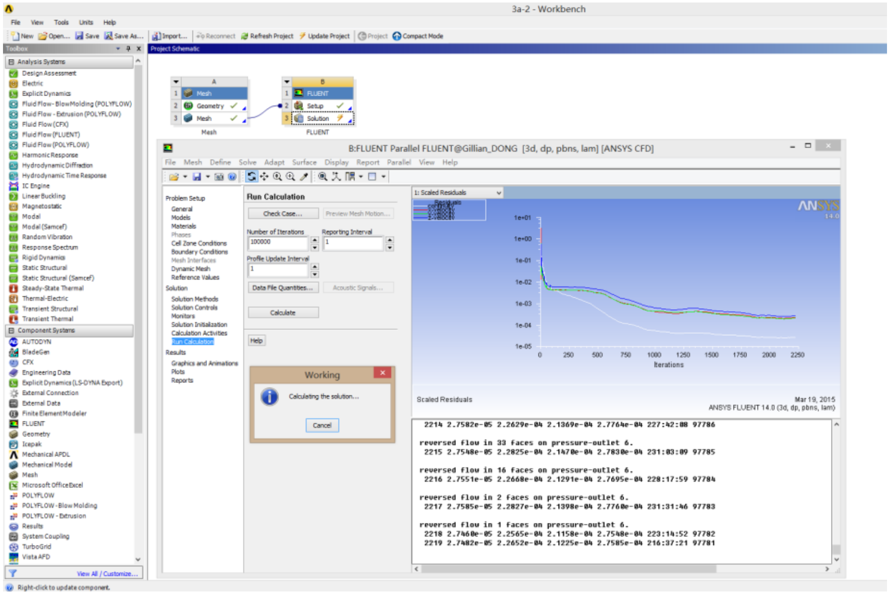

Figure 5.2 Finite element computational process in FLUENT, ANSYS 14.0.

5.1.4 3D finite element modeling procedure

Enhanced CT scan to obtain clinical images

⇩

Arterial 3D model reconstruction by MIMICS

⇩

3D model processing and format conversion by Gambit

⇩

Model meshing and region setting by Mesh in ANSYS

⇩

Blood properties definition and boundary conditions setting by FLUENT in ANSYS

Figure 5.3 3D finite element modeling flow chart.

5.2 ESTABLISHMENT OF LUMPED PARAMETER MODEL OF SYSTEMIC CIRCULATION

5.2.1 Overview of lumped parameter model

Section 1.5 has briefly introduced the model classification of human blood circulation system, as well as the application of multi-scale model and lower limb model. Among the commonly used vascular models in numerical simulation, although lumped parameter (0D) model is the simplest, it not only mathematically simplifies equation processing by transforming partial differential equations into ordinary differential equations, but also physically simplifies the fluid network model with complex distribution characteristics into finite lumped parameter units. That is to say, lumped parameter model can effectively describe the variation of concentrated pressure, flow and resistance along the whole vessel segment, so it is still extensively applied in today's various studies.

The basic theory of lumped parameter model can be traced back to the most early blood circulation system simulation. In 1899, German physiologist Otto Frank established the first quantitative description model of arterial system, the famous Windkessel model, and thus created the Windkessel theory (Yubo. Fan, 1992). The basic equations of the original Windkessel theory are:

$$C\frac{dP}{dt}+\frac{P-P_V}{R}=Q_{in} \tag{5.1}$$

$$C\frac{dP}{dt}+\frac{P-P_V}{R}=0 \tag{5.2}$$

$$C=\frac{V}{P} \tag{5.3}$$

Wherein *P* is the arterial intravascular pressure, *Qin* is the volume flow rate getting into Windkessel, *Pv* is the venous pressure, *R* is the peripheral vascular resistance, *C* is a pressure-volume relationship constant showing the arterial compliance, *V* is the Windkessel volume. When it is assumed that the venous pressure is negligible, Equation (5.1) and (5.2) are exactly the same in form with the state equations of a circuit. That is to say, there is the following electro-hydraulic analogy: blood pressure P corresponds to voltage, volume flow rate Q corresponds to current, liquid compliance C corresponds to capacitance, blood flow resistance R corresponds to electric resistance. This analogy constitutes the single lumped parameter model of arterial system. In simple terms, using more mature circuit analysis theory and its icon and symbol system achieved more convenient establishment and analysis of arterial system Windkessel model. Since then, based on this Windkessel theory, scholars continuously improved and developed various kinds of the lumped parameter model of circulatory system. For example, added the liquid inductance L which represents the inertia of fluid, to form the improved Windkessel theory and fluid transmission line theory widely used later. The governing equations of both are:

$$P_{i-1} - P_i = RQ_{i-1} + L\frac{dQ_{i-1}}{dt} \tag{5.4}$$

$$Q_{i-1} - Q_i = C\frac{dP_i}{dt} \tag{5.5}$$

In Equation (5.4) and (5.5), $R=R'l$, $L=L'l$ and $C=c'l$ are respectively the concentrated liquid resistance, concentrated liquid inductance and concentrated liquid capacitance. The fluid transmission line equations could be obtained from different considerations and through different simplifications and mathematical processing. In addition, R', L', c' could be set according to the specific physiological, anatomical or physical parameters, so its range of application is very wide. The fluid transmission line equation is divided into uniform and nonuniform, linear and nonlinear. Since the existence of geometrical and physical heterogeneity in real vessels, using the nonuniform transmission line equation to describe arterial system could theoretically get more realistic results. But generally, there is no analytic but numerical solution for it, so the nonuniform transmission line equation is seldom used. The essence of nonlinear transmission line equation is the same as that of nonlinear quasi 1D pulsating flow equation and nonlinear Windkessel equation, either in terms of distributed parameter or lumped parameter. Because of the complexity of mathematical processing and solving, and the uncertain relationship between system parameters and pressure and flow, the application of nonlinear transmission line equation is also rare. In fact, although there is a lot of nonlinear in the real blood flow system, it has been proved by theoretical analysis and experimental research that the nonlinear effect is very small. The subsequent studies have shown that linear transmission line equation could describe arterial circulation sufficiently accurately on the system magnitude. If the parameters such as compliance and viscous resistance are properly given, the results of linear transmission line equation are in good agreement with the experimental results, and even better than those of nonlinear equation whose parameters are not well chosen. Moreover, the combination of linear transmission line equation and harmonic analysis method can conveniently derive the basic quantities such as input impedance and wave propagation constant, so that the analytic solving speed could be greatly accelerated. For the above reasons, most of the studies have used uniform and linear transmission line equations to construct lumped parameter models.

Blood vessels were regarded as no-slip, no-leakage rigid walls in this study. The uniform and linear lumped parameter model was employed. The relationship between *R*, *L*, *C* in the transmission line equations and the length *l*, radius R_0, wall thickness *h*, Young modulus *E*, Poisson's ratio σ, blood density ρ and blood viscosity μ of the described vascular segment are as follows (Junkai. Chen, 1990):

$$R = \frac{8\mu l}{\pi R_0^4} \tag{5.6}$$

$$L = \frac{\rho l}{\pi R_0^2} \tag{5.7}$$

$$C = \frac{3\pi R_0^3 (1-\sigma^2) l}{2Eh} \tag{5.8}$$

The *R*, *C* and *L* of each blood vessel segment could be calculated by Equation (5.6)-(5.8) to build a lumped parameter model network.

In the development of lumped parameter model, the most concerned issue is its description of pulse wave propagation characteristics [118]. In the part of theory, from the initial Windkessel theory, to pulse wave propagation theory and arterial pulsatile flow theory, to various fluid transmission line theory; in the part of construction method, from linear lumped parameter model to hybrid parameter model; in the part of simulated content, from the full circulation electric network model, to systemic circulation improved Windkessel model and pulmonary circulation theoretical model, all of these are for the purpose of seeking more accurate and closer to the actual physiological condition descriptions of cardiovascular circulation system. Corresponding to the experimental device structure of most in vitro circulation system, many lumped parameter simulation studies built the equivalent single segments --- N units with lumped three parameters (*R*, *L*, *C*) model (Yubo. Fan, 1992). Its determination of the basic parameters of each unit depends on the division of system units, and the geometric and physical parameters of unit segment and blood. While the unit division needs to refer to the anatomy, physiology and rheology of the cardiovascular system. Althrough a lot of research has been carried out for the selection of segment length, network unit mode, physiological and the corresponding physical parameters in order to approximate the pulse curve, the model establishment still needs to weigh simulation accuracy and purpose, computation speed and rounding error, numerical method type and its function. That is to say, in the process of approximation, lumped parameter model always can not replace the real pulse waveform.

According to the research purpose and focus, this study used the Doppler ultrasound measured velocity waveform as the inlet boundary condition of 3D models; simulated the removed small vascular branches and capillaries into lumped parameter units, which means the outlet boundary conditions were set to terminal impedance by electronic units.

5.2.2 Numerical calculation of ordinary differential equation

The lumped parameter model produces a system of ordinary differential equations.

These equations for characterizing the pressure-flow function relationship are so numerous that it is very difficult to solve them analytically by using mathematical methods. Therefore, it is necessary to use computer and numerical methods to obtain the numerical solution. On the other hand, the solutions of lumped parameter fluid transmission line equations are frequency domain solving and time domain analysis. Although the mathematical processing of frequency domain solving is simple, it is only suitable for the single inlet / single outlet linear time invariant system. This limitation makes it often be replaced by time domain analysis which could reflect the multi inlets, multi outlets, nonlinear or time-varying characteristics. Solving with time domain analysis, the state equations of lumped parameter model are:

$$\frac{dY}{dt} = f(Y, t, u) \tag{5.9}$$

$$Y(t_0) = Y_0 \tag{5.10}$$

Wherein $Y=[y_1,y_2,...,y_n]^T$ is the state vector, $U=[u_1,u_2,...,u_m]^T$ is the input vector of the system. Numerical integration was used to solve Equation (5.9).

The common numerical methods to solve the ordinary differential equations of lumped parameter model are Euler method, Runge-Kutta method, Treanor method and Gear method. The basic idea of Euler is iteration that is characterized by single step, explicit, first derivative accuracy, and two order truncation error. Euler simply takes the end of tangent as the starting point of the next step to calculate. When the number of steps increases, the error will become larger and larger because of accumulation, so Euler scheme is not generally used for practical calculation. Runge-Kutta is a high precision single step algorithm widely used in engineering. This algorithm has high accuracy, convergence and stability (under certain conditions), alterable step size during the calculation process, and no need calculating higher order derivatives etc. advantages. Runge-Kutta method of four order is the most common and classical numerical method. The ordinary differential equations got from fluid grid control system are often stiff, or when the unit number of lumped parameter model is larger or having branches, the equations may also become stiff. Then Treanor method and Gear method are needed to solve these stiff equations. When the lumped parameter model has fewer units and equations, Runge-Kutta method can satisfy the accuracy and convergence of the solution.

This study used the classical Runge-Kutta method of four order. That is the implicit method for updating tangent matrix at each time step (implemented by the user-defined program in FLUENT), and its expressions are:

$$
i=1,2,...,n; \quad m=0,1,2,... \quad
\begin{cases}
y_{im+1}=y_{im}+\dfrac{h}{6}(K_{i1}+2K_{i2}+2K_{i3}+K_{i4}) & (5.11)\\
K_{i1}=f_i(t_m,y_{1m},...,y_{nm}) & (5.12)\\
K_{i2}=f_i(t_m+\dfrac{h}{2},y_{1m}+\dfrac{h}{2}K_{11},...,y_{nm}+\dfrac{h}{2}K_{n1}) & (5.13)\\
K_{i3}=f_i(t_m+\dfrac{h}{2},y_{1m}+\dfrac{h}{2}K_{12},...,y_{nm}+\dfrac{h}{2}K_{n2}) & (5.14)\\
K_{i4}=f_i(t_m+h,y_{1m}+hK_{13},...,y_{nm}+hK_{n3}) & (5.15)
\end{cases}
$$

Wherein *yim* is the approximate value at the *yi* node of the first *i* state variable, and *h* is the integral step size.

5.2.3 Establishment of afterload lumped parameter model

According to the research purpose and focus, and the clinical measured data, the velocity waveform obtained by Doppler ultrasound as mentioned in Chapter 2 was applied as the inlet boundary condition of 3D model at the common femoral artery (CFA) instead of the simulation of lumped parameter model, thus to avoid the limitation of segment centralization and the error caused by system parameters selection. At the four outlets of 3D model, the afterload part representing numerous vascular branches and the microcirculatory system was modeled as electronic units. That means lumped parameter model was used to describe the terminal impedance at the outlet boundary.

The entire arterial tree contains a large number of small branches. In order to reduce the complexity of blood flow simulation and strengthen the investigation of the target arteries, it often needs to truncate long arteries and to remove the small vessels below medium size. For large arteries, to describe the reflection effect of pulse wave with proper boundary condition at the truncation or at the end outlet is very necessary. Some studies pointed out that, outlet boundary condition can greatly influence the pulse waveform of the upper arteries [143]. Therefore, various types of outlet boundary condition have been used in numerical simulation research, including constant resistance (CR) model (Stettler J, et al, 1981), tapering-vessel model (Mynard J, et al, 2008), Windkessel (WK) model (Stergiopulos N, et al, 1999), and structured tree model (Cousins W, et al, 2014). Among them, CR model and WK model are the most common two. CR model is constructed by a resistor in which blood pressure is assumed to be proportional to blood flow. This boundary condition often leads to a large non-physical reflection of pulse wave, because it can not reflect the compliance of the lower arterial wall. The three elements WK model contains three physical parameters, namely peripheral resistance, characteristic resistance, and capacitance (Olufsen, M. S., et al, 2002), wherein capacitance is introduced to characterize the compliance of lower arterial wall [112]. If the parameters of WK model could combine to their impedance and compliance, the 1D model of arterial blood flow can capture the pulse wave.

In this study, the arterial 3D models of bilateral thigh just selected five main arteries: common femoral artery (CFA), superficial femoral artery (SFA), deep femoral artery (DFA), lateral femoral circumflex artery (LFCA), and medial femoral circumflex artery (MFCA). At the four outlets of SFA, DFA, LFCA and MFCA, CR model (**Figure 5.4**) and WK model (**Figure 5.5**) were respectively employed to achieve lumped parameter simulation. The parameter values of these two kinds of model were derived from a series of theoretical formula and empirical data (details in Chapter 7). A user defined function was written in FLUENT to solve those lumped parameter models, so that a fully coupled solution was gained at each time step.

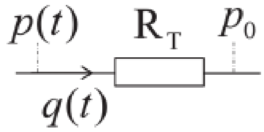

Figure 5.4 Sketch map of constant resistance lumped parameter model.

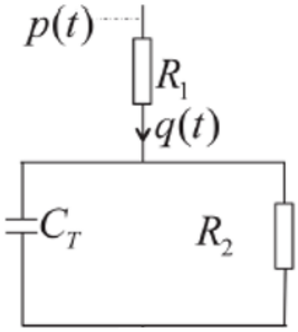

Figure 5.5 Sketch map of Windkessel lumped parameter model.

5.3 ESTABLISHMENT OF MULTI-SCALE COUPLING MODEL

5.3.1 Overview of multi-scale coupling theory

Section 1.5 has made a brief introduction to the application of the multi-scale model of human blood circulation system. In the numerical study of hemodynamics, if only establish a 3D model for local vessels with high precision demand, it artificially makes this region as an isolated system, and could only get the characteristic result of regional blood flow while ignoring the influences of systemic circulation even full circulation system. In addition, the real physiological boundary conditions of independent 3D model are difficult to obtain, so that the numerical simulation results would have some hypothetical errors. In order to solve this problem, lumped parameter or 1D these two kinds of relatively simple model is used to simulate the circulation system, while the focused region is simulated by 3D model, and then the two models of different scale are coupled together by mathematical coordination of boundary conditions to finally achieve the simulation results which are close to the physiological state and take into account the local accuracy. This is the construction principle of multi-scale coupling model. In the past multi-scale model calculation, iterative ideas were usually used to deal with the coupling between 3D model and 1D or lumped parameter (0D) model. As illustrated in **Figure 5.6**, a representative and mature coupling process is widely used [133].

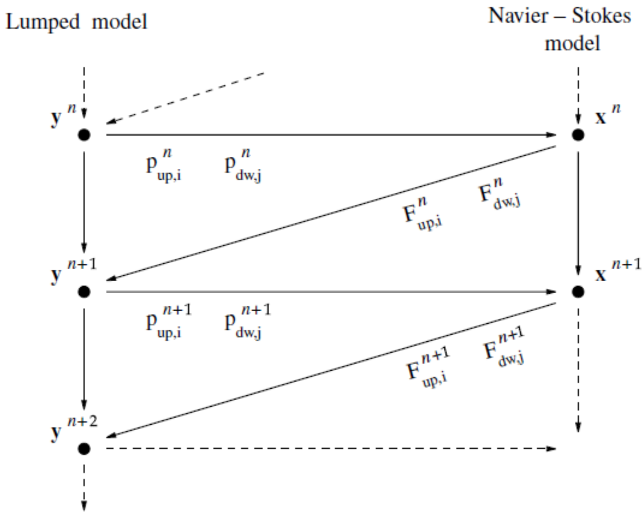

Figure 5.6 The multi-scale coupling principle based on forward Euler method (Alfio Quarteroni, et al., 2001).

5.3.2 Multi-scale coupling model calculation procedure

Figure 5.7 showed the flow velocity waveform of common femoral artery measured by Doppler ultrasound. A cardiac cycle waveform was selected to simulate the velocity curve by spline interpolation method, as the inlet boundary condition of each 3D model. The outlet boundary condition, namely lumped parameter model, was implemented by the CR model and the WK model described in section 5.2.3. The outlet flow rate calculated by 3D model was used as the input condition of lumped parameter (0D) model, and the pressure value solved by 0D model was fed back to be the outlet boundary condition of the 3D model. The entire coupling calculation process was shown in **Figure 5.8** (residual limb of Case-1 as an example).

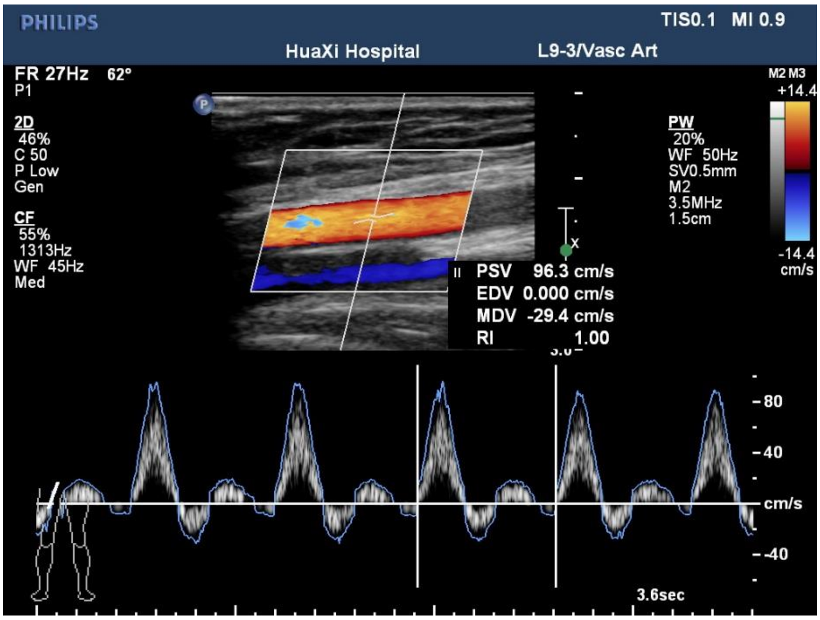

Figure 5.7 Arterial flow velocity waveform measured by Doppler ultrasound.

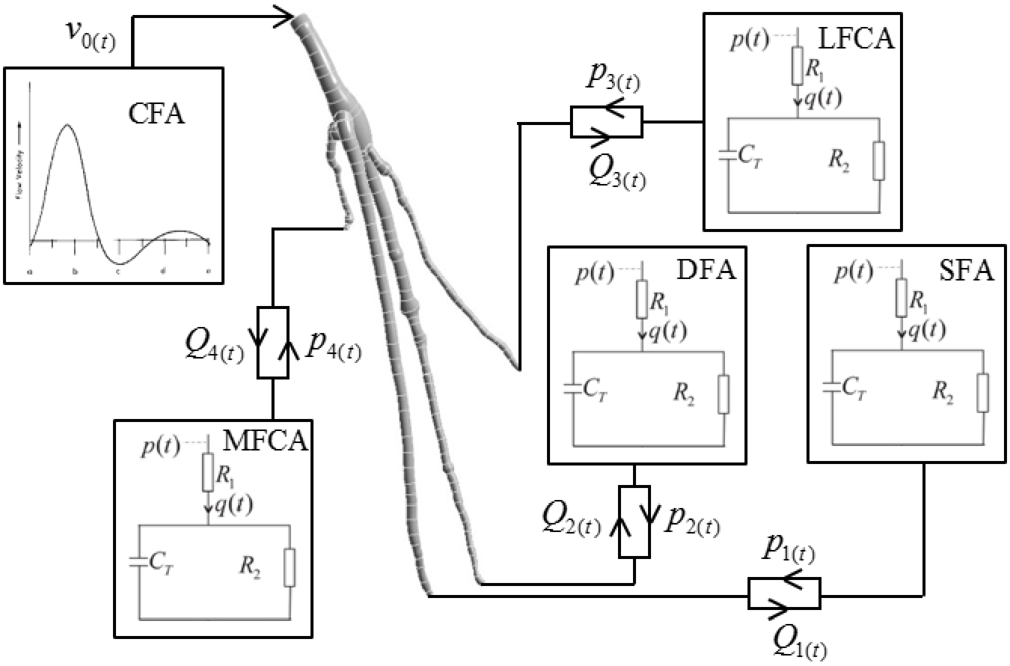

Figure 5.8 Sketch map of the 3D-0D (Windkessel) coupling model.

CHAPTER 6: NUMERICAL STUDY OF 3D MODEL

6.1 MODEL AND FUNDAMENTAL EQUATION

6.1.1 Model and parameter setting

In this chapter, the arterial 3D models of bilateral thigh were derived from the enhanced CT scans of Case-1 and Case-2 at the 12th month after surgery. As described in Section 5.1, the original CT image set was imported into MIMICS 15.0, and then picked out the five main arteries, common femoral artery (CFA), superficial femoral artery (SFA), deep femoral artery (DFA), lateral femoral circumflex artery (LFCA), and medial femoral circumflex artery (MFCA), from muscles, bones, and other soft tissues, to form the initial arterial 3D model (the starting points of bilateral CFAs were the top of caput femoris, while the end positions of bilateral arteries were the end of residual bone). The IGES file output from MIMICS was imported into Gambit for the 3D model machining including geometric patching, wall smoothing and the CFD format conversion under a certain precision. After reading the STEP file exported from Gambit into ANSYS, boundary layers setting, mesh generation, inlet/outlet/wall area setting were implemented in turn. Taking Case-1 as an example, **Figure 6.1** and **Figure 6.2** respectively showed the 3D finite element models of main arteries in residual limb (RL) and sound limb (SL).

Bilateral models both employed tetrahedral meshing with the minimum size of 0.2mm, the maximum size of 2.0mm, and the number of wall boundary layer was 5. For Case-1, the node and mesh number of RL model were respectively 672398 and 2631171, and those of SL model were respectively 1037542 and 4308871. For Case-2, the node and mesh number of RL model were respectively 715526 and 2549023, and those of SL model were respectively 958130 and 3582362.

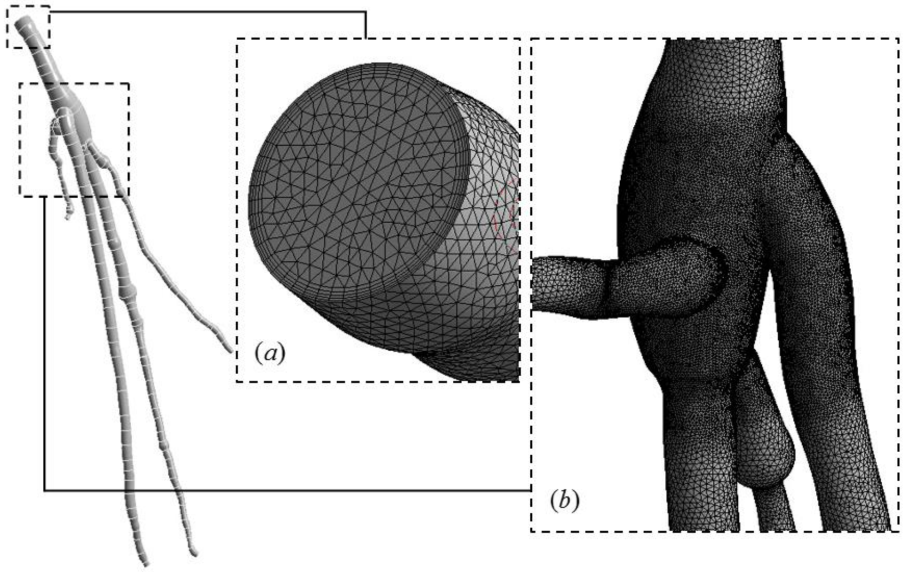

Figure 6.1 The 3D finite element model of main arteries in residual limb. (a) wall boundary layers; (b) local mesh refinement.

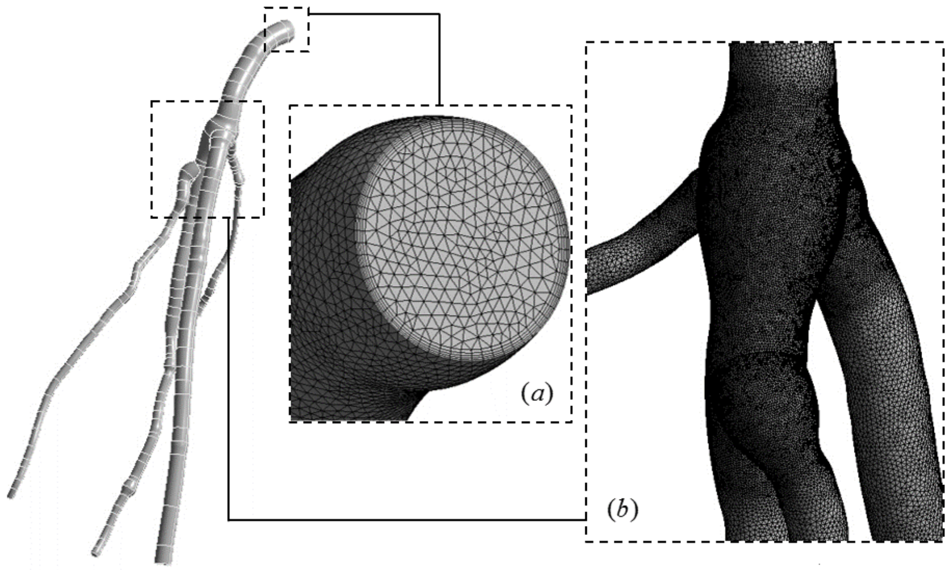

Figure 6.2 The 3D finite element model of main arteries in sound limb. (a) wall boundary layers; (b) local mesh refinement.

6.1.2 Basic assumptions and governing equations

On the basis of the continuity equation $\frac{\partial u}{\partial x}=0$ and Navier-Stokes (N-S) equation $p\frac{dv}{dt}=-\nabla p+pF+\mu\Delta v$, this study assumed that vessels were non-slip stiff walls, and considered blood as non-Newtonian fluid. Casson equation which could better characterize the shear stress-shear rate relationship was adopted as the constitutive equation of blood. In this study blood was assumed as single phase flow, and in the case of plane hypothesis, the non-yielding zone, where the shear stress was less than the Casson yield stress k_0^2, was very small, so the entire flow field was considered in the yield state (Jiang WT, et al., 1998). The Casson expression was as follow:

$$\sqrt{\tau} = k_0 + k_1\sqrt{\bar{\gamma}} \tag{6.1}$$

Here the constant $k_0=0.2(dyn/cm^2)^{1/2}$, $k_1=0.18(dyn \cdot s/cm^2)^{1/2}$, and Equation (6.1) is the form of 1D flow [144]. For 2D and 3D flow, the second invariant D_c of strain rate tensor was introduced and in the 3D case D_c is:

$$D_c = \frac{1}{2}\sum_{i=1}^{3}\sum_{j=1}^{3} d_{ij}d_{ij} \quad \text{(i,j=1,2,3)} \tag{6.2}$$

$$d_{ij} = \frac{1}{2}\left(\frac{\partial u_i}{\partial x_j} + \frac{\partial u_j}{\partial x_i}\right) \quad \text{(i,j=1,2,3)} \tag{6.3}$$

Wherein u_i and u_j are the blood velocity vectors, and the subscripts 1, 2 and 3 respectively denote the direction of x, y, and z. In the 1D case $2\sqrt{D_{\mathrm{II}}} = \bar{\gamma}$, therefore $2\sqrt{D_{\mathrm{II}}}$ was substituted into the Equation (6.1) to obtain the modified Casson equation satisfying 3D flow:

$$\sqrt{\tau} = k_0 + k_1\sqrt{2\sqrt{D_c}} \tag{6.4}$$

The above equation was written as the form of Newtonian fluid:

$$\tau = \frac{1}{2\sqrt{D_c}}(k_0 + k_1\sqrt{2\sqrt{D_c}})^2\bar{\gamma} \tag{6.5}$$

Wherein the expression of apparent viscosity μ was:

$$\mu = \frac{1}{2\sqrt{D_c}}(k_0 + k_1\sqrt{2\sqrt{D_c}})^2 \tag{6.6}$$

Equation (6.6) was directly substituted in the Navier-Stokes equation, and then the flow characteristics of blood represented by Casson equation could be calculated:

$$\rho_f \frac{\partial u_i u_j}{\partial x_j} = -\frac{\partial P}{\partial x_i} + \mu\frac{\partial}{\partial x_j}\left(\frac{\partial u_i}{\partial x_j} + \frac{\partial u_j}{\partial x_i}\right) \tag{6.7}$$

In Equation (6.7), P is pressure and the blood density $\rho f=1055\ kg/m^3$. In this chapter, blood flow was assumed to be steady flow, and the aim was to verify the quality of the 3D models and to preliminarily compare the hemodynamic states of RL with those of SL. The velocity inlet boundary condition took the average value of the flow velocity in a cardiac cycle measured by ultrasonic examination. So after some simple calculations, it was set as follow: RL of Case-1 $u_{1R}\big|_{inlet}=0.23m/s$, SL of Case-1 $u_{1S}\big|_{inlet}=0.38m/s$, RL of Case-2 $u_{2R}\big|_{inlet}=0.27m/s$, SL of Case-2 $u_{2S}\big|_{inlet}=0.43m/s$. The outlet boundary condition of both RL and SL of the two cases was zero pressure $P_{1,2}\big|_{outlet}=0$.

In FLUENT, we used 3D double precision format; pressure velocity correction employed SIMPLEC algorithm; the gradient of spatial discretization used least square method; momentum was calculated by two order upwind scheme; the choices of under relaxation factors were pressure of 0.3, density of 1, volume force of 1, momentum of 0.7, and the residual convergence threshold was set to 0.0001.

6.2 RESULTS AND DISCUSSION

6.2.1 Result analysis of Case-1

The vessel wall pressure (WP), wall shear stress (WSS) and inner flow velocity (FV) of the bilateral arterial 3D models of Case-1 were shown in **Figure 6.3**, **Figure 6.4**, and **Figure 6.5**.

The value range of WP in SL was from 8318.40pa to 8777.33pa, while in RL was from -156.03pa to 1173.05pa. As shown in **Figure 6.3**, the WP of SL was remarkable greater than that of RL but with uniform distribution. From the inlet to four outlets, the WP change gradient along the pipeline of each artery in SL was similar, whereas the upper half of DFA in RL was all in the relatively high pressure zone. WSS state as shown in **Figure 6.4**, the value range in SL was from 0.0062pa to 25.2888pa, and that in RL was from 0.0073pa to 48.3099pa. The WSS differences at different positions in RL was greater than in SL, namely more uneven distribution in RL. On the whole, the LFCA of RL and the SFA of SL presented larger WSS.

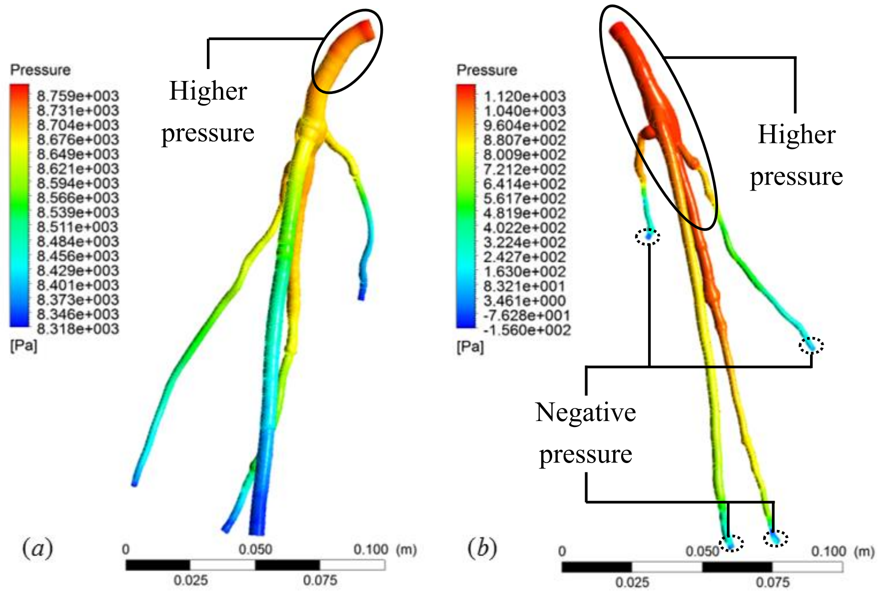

Figure 6.3 The wall pressure distribution contour of bilateral arterial 3D models of Case-1. (a) the sound limb; (b) the residual limb.

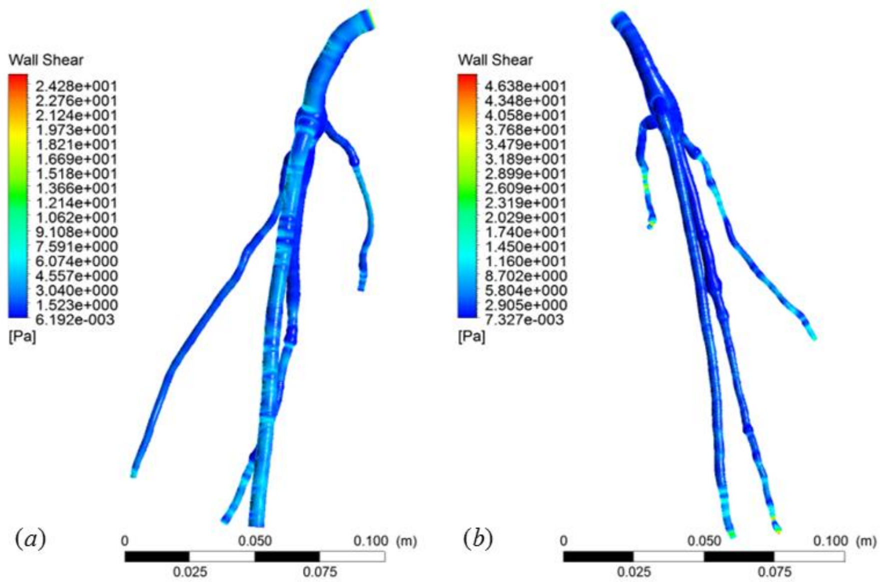

Figure 6.4 The wall shear stress distribution contour of bilateral arterial 3D models of Case-1. (a) the sound limb; (b) the residual limb.

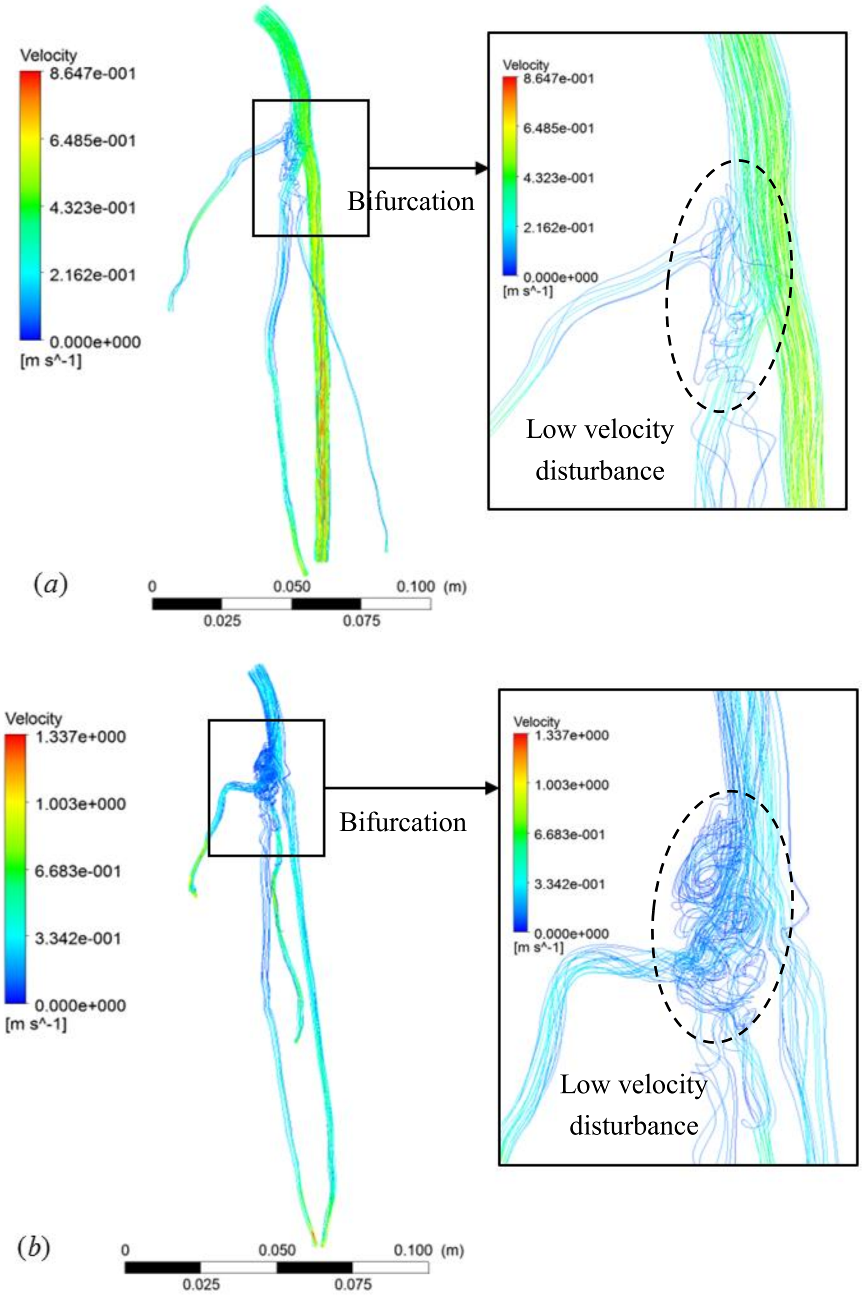

Figure 6.5 The flow velocity distribution streamline of bilateral arterial 3D models of Case-1. (a) the sound limb; (b) the residual limb.

FV within the lumen was shown in **Figure 6.5**. Although the value range of RL (from 0 to 1.34m/s) was larger than that of SL (from 0 to 0.86m/s), in fact the high FV areas in RL were very small and just in the outlets end. The average velocity of RL was slightly less than that of SL, whereas the gradient from the inlet to four outlets of both were not much different. At bifurcation sites, there was obvious difference in the distribution of constant velocity streamlines. In the SL (**Figure 6.5 (a)**), bifurcations between CFA and MFCA, and between DFA and LFCA showed low velocity disturbance. While in the RL (**Figure 6.5 (b)**), at the bifurcation between CFA, DFA and MFCA, there was a wide range of low velocity disturbance, implying that the FV distribution and the flow field of RL might be more complex than those of SL.

As mentioned in the first chapter, in developed countries, lower limb amputation is mainly due to diabetes and its complications, arteriosclerosis obliterans, thromboangiitis obliterans and other peripheral vascular occlusive diseases. Some of these diseases or lesions would result in secondary or even multiple surgeries, or produce a high incidence of complications (34.4%) and a 7.0% 30-day mortality rate. The past a few studies on lower limb hemodynamics have reported that, the disorder flow field, high blood pressure and low wall shear stress are the predisposing factors of atherosclerosis and thrombosis, and their changes are likely to continuously damage blood vessels after amputation. In addition, some studies have demonstrated that hemodynamic state is related to the occurrence and development of pressure ulcers, deep tissue injury and muscle atrophy. However, after amputation, the distribution of these parameters in RL, the differences with SL, the interaction between hemodynamics and various artery lesions and common RL problems, have not been reported, and they are worthy of detailed investigation in order to promote comprehensive rehabilitation.

A large number of cardiovascular hemodynamic studies have made a recognized conclusion, and that is among many parameters, WSS has the clearest and closest relationship with atherosclerosis and other vascular lesions. The principle is the perception of WSS by endothelial cells. As well known, vascular endothelial dysfunction often occurs in the position with low or interruption blood flow, as well as the disordered low shear stress area (LSSA) which may change cell behaviors (turbulent zone). Thus, vascular lesions are particularly easy to be observed in curved segments, branch points, or bifurcation sites [145]. Vascular endothelial cells are the main sensor of WSS, and part of stress can be transmitted to vascular smooth muscle cells through the transmural transmission of extracellular matrix. The vicious circle principle between the biomechanics of blood flow regime near vessel wall and the development of atherosclerosis could be simply expressed as follow (**Figure 6.6**): in the branch points and curved sections of vessels, the abrupt change of WSS would alter gene expression and cell behavior, becoming the initiation factor of atherosclerosis; the resulting plaques could in turn promote lipid, cells and extracellular matrix to grow and to accumulate within arterial wall, making the wall thicker, harder, and decreased compliance; changes in wall stiffness would alter blood flow and local hemodynamics including WSS, whereby the mechanical stimulation further leads to gene expression changes, promoting the development of plaques. In addition, the cyclic strain in low shear stress zone would be significantly affected by the direction and magnitude of tensile action, while cyclic strain is an important determinant of vascular wall cell physiology.

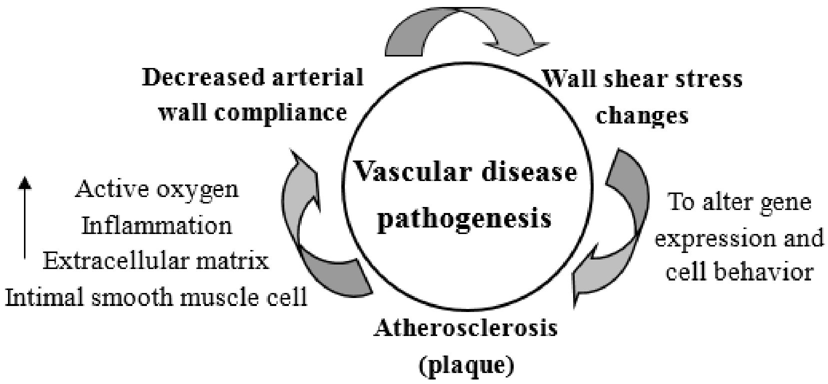

Figure 6.6 The vicious circle between biomechanics and atherosclerosis.

With the growth of plaque, internal necrosis and calcification will further reduce vascular compliance. Meanwhile, unstable plaques are prone to rupture and cause thrombosis under continuous shear and cyclic stress. The decreased compliance of diseased arteries leads to disordered vessel wall motion and shear stress patterns, as well as increases in turbulence, which promote plaque development again. Studies have shown that when the WSS is lower than 0.4pa [146], it is easy to form atherosclerotic plaques. While the plaque growth process tells that turbulence and uneven WP also contribute to vascular diseases. The above conclusions drawn from cardiovascular hemodynamic studies are mainly aimed at large and medium-sized muscle elastic arteries, such as aorta, coronary artery and cerebral artery. The main thigh arteries are classified to medium-sized ones by diameter, and the wall structure differences between various arterial types are shown in **Figure 6.7**.

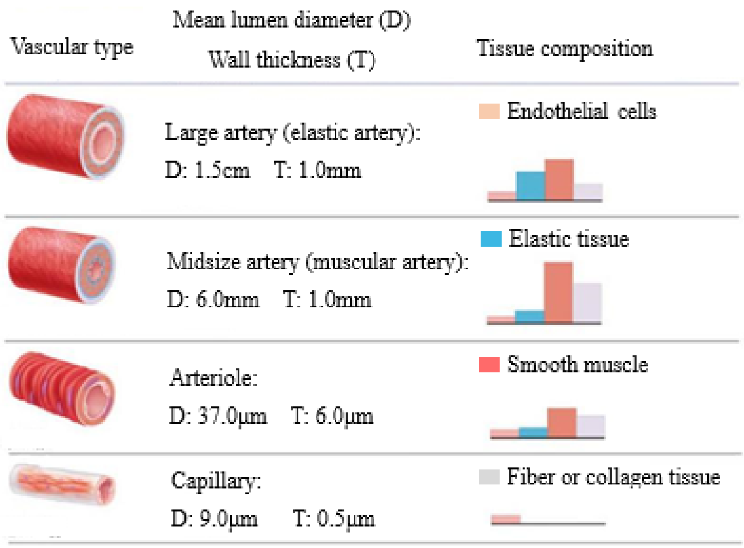

Figure 6.7 Wall tissue composition of various arterial types.

As can be seen from the figure above, the main difference of wall tissue composition between large artery and midsize artery is the proportion of elastic tissue and smooth muscle, namely the tunicae media and adventitia. In the intima contacting with blood, except the difference of subendothelial layer thickness, the amount of endothelial cells which are mainly responsible for the induction and transmission of shear stress is almost the same. Therefore, it can be inferred that, those conclusions about the effects of WSS and flow field on the occurrence and development of atherosclerotic lesions in large artery are still applicable to the midsize arteries of lower limb. That is to say in main thigh arteries, low WSS and disordered flow field are also likely to induce atherosclerosis, thrombosis, and other arterial lesions, and to affect blood flow and the nourishment for musculoskeletal system. According to that, the LSSAs (**Figure 6.8**, **Figure 6.9**) and the velocity distribution and vector at the cross section of each artery about 2mm away from bifurcation (**Figure 6.10**, **Figure 6.11**) were emphatically observed.

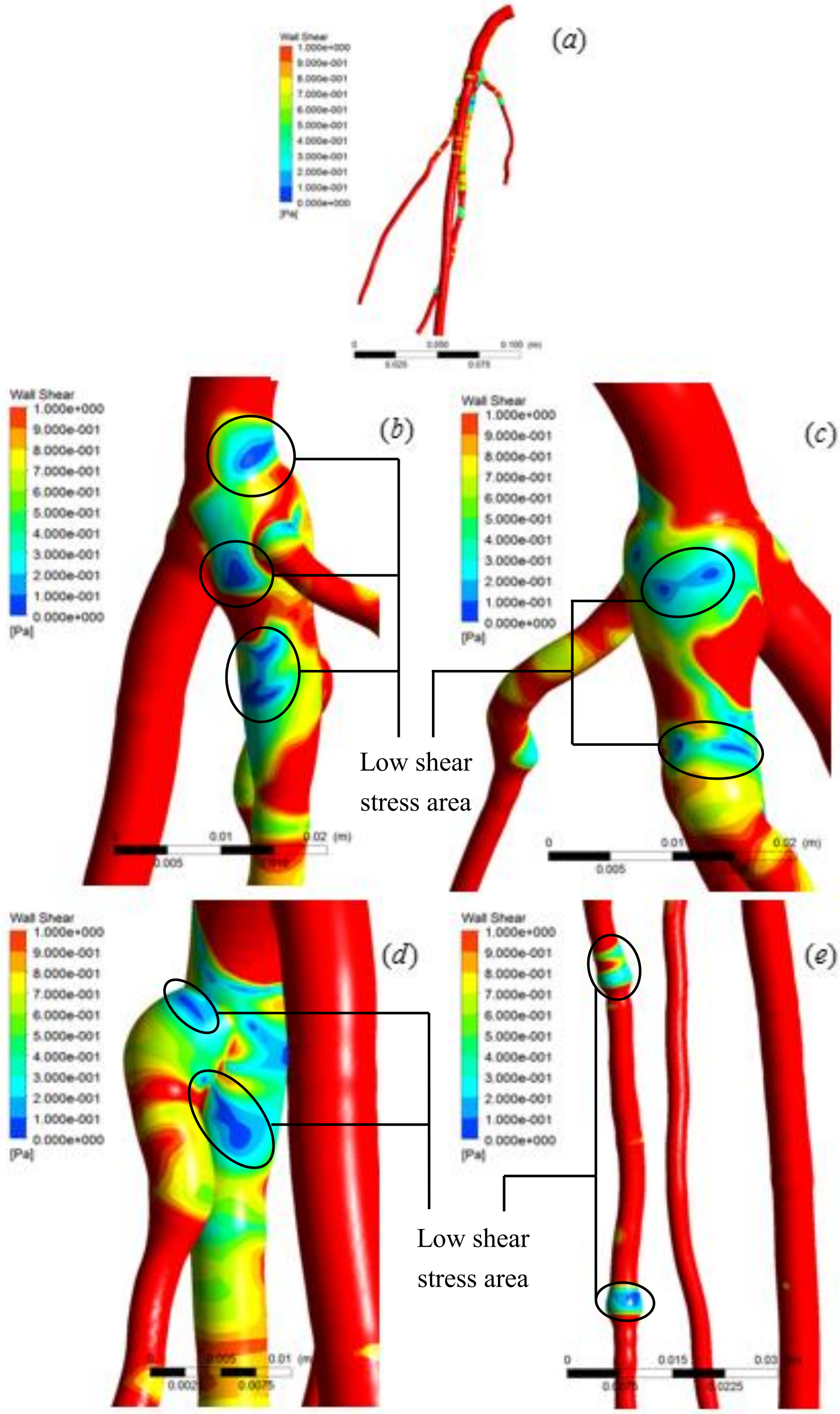

Figure 6.8 The low shear stress areas in the sound limb of Case-1. (a) overall contour; (b) (c) (d) (e) are the local contours.

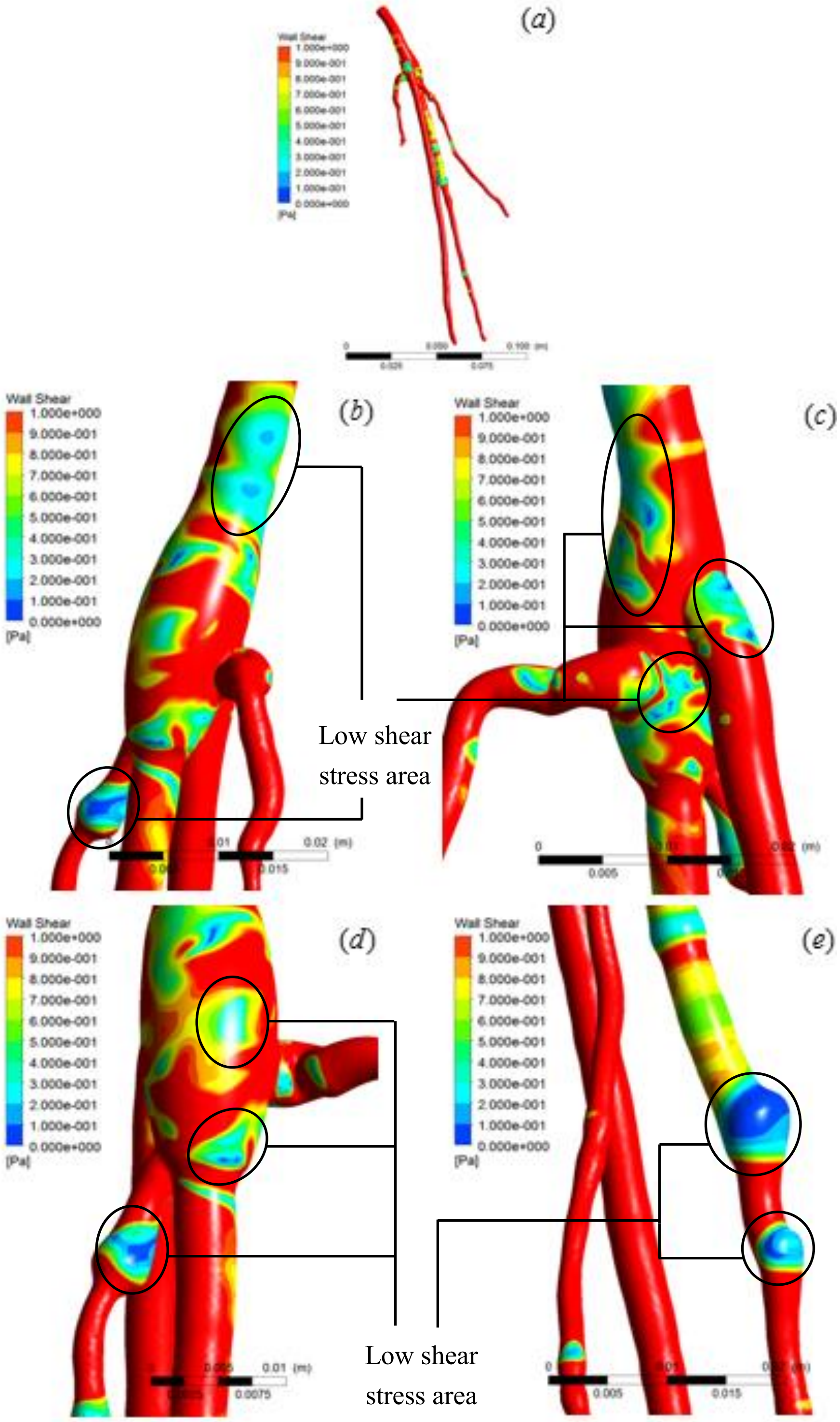

Figure 6.9 The low shear stress areas in the residual limb of Case-1. (a) overall contour; (b) (c) (d) (e) are the local contours.

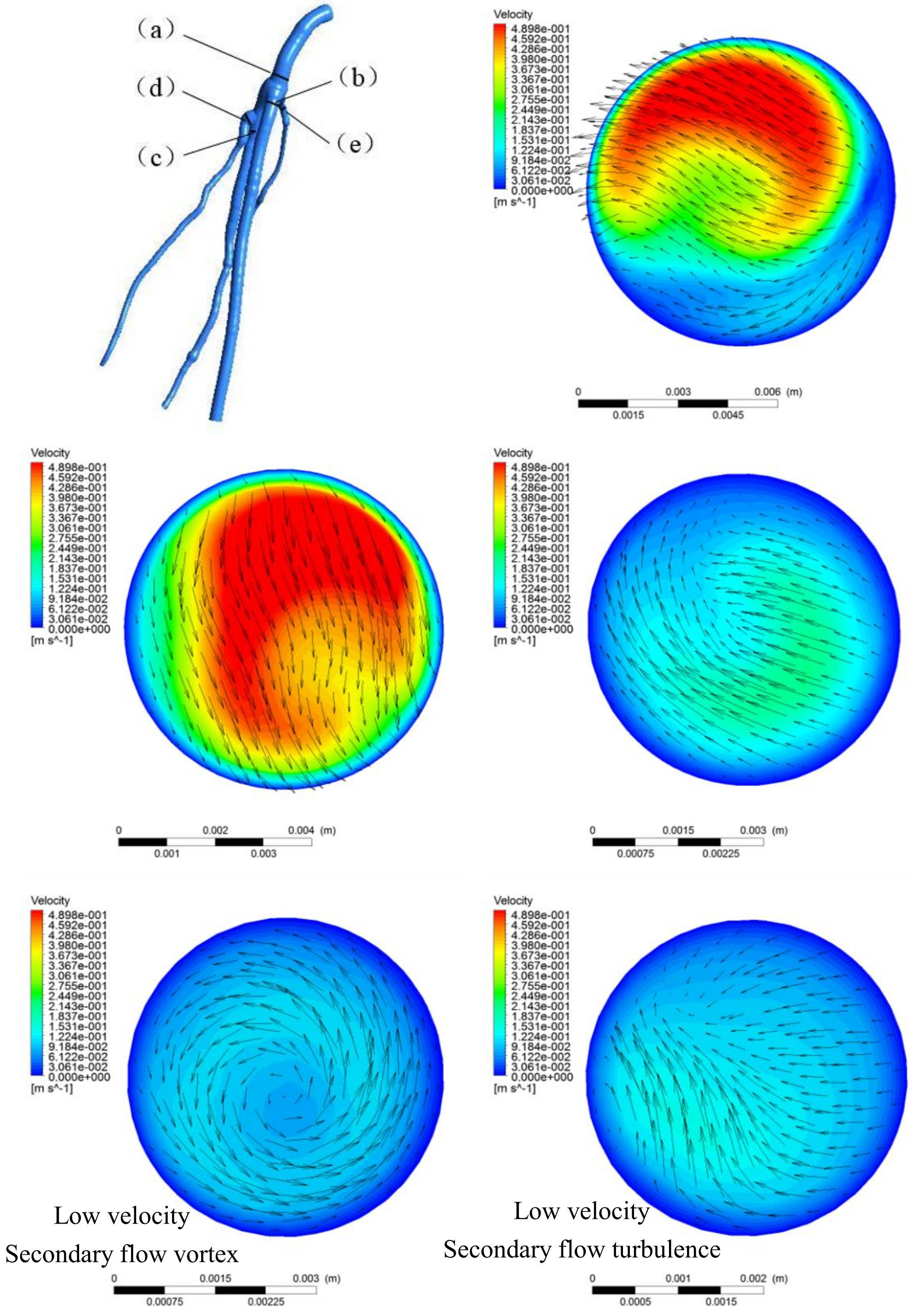

Figure 6.10 The velocity vector on each arterial cross section in the sound limb of Case-1. (a) CFA; (b) SFA; (c) DFA; (d) LFCA; (e) MFCA.

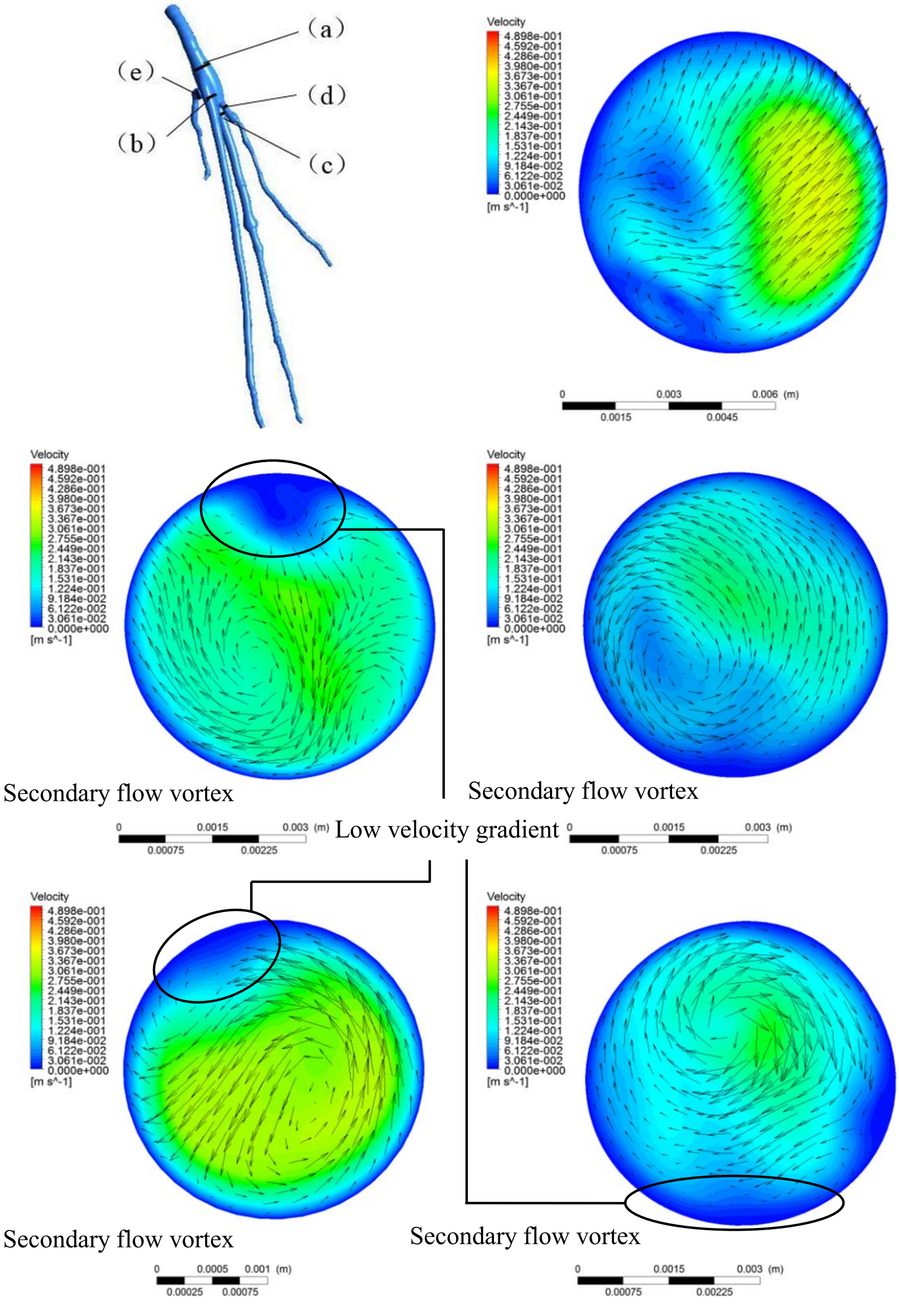

Figure 6.11 The velocity vector on each arterial cross section in the residual limb of Case-1. (a) CFA; (b) SFA; (c) DFA; (d) LFCA; (e) MFCA.

Comparing **Figure 6.8** and **Figure 6.9**, it could be found that the LSSAs of RL were scattered but had smaller range than those of SL. The LSSAs (<0.4Pa) of SL mainly located at the bifurcations between DFA and LFCA, and between CFA and MFCA, as well as the upper half of DFA. While the LSSAs of RL also mainly concentrated around the bifurcations, and the sudden change position of the diameter of DFA. In combination with **Figure 6.3**, the WP of these sites was relatively high, so the possibility of the occurrence of atherosclerotic plaques and other vascular lesions was noteworthy.

In **Figure 6.10** and **Figure 6.11**, in order to directly contrast velocity size, the legends of all five cross sections were set to 0-0.5m/s. The contours showed that around bifurcation, FVs in the CFA and SFA of RL (**Figure 6.11 (a)**, **(b)**) were smaller than those of SL (**Figure 6.10 (a)**, **(b)**); there was little bilateral difference in DFA (**Figure 6.10-6.11 (c)**); whereas FVs in the LFCA and MFCA of RL (**Figure 6.11 (d)**, **(e)**) were slightly greater than those of SL (**Figure 6.10 (d)**, **(e)**). The velocity vector (arrow lines) illustrated remarkable bilateral differences. In the SL, the secondary flow direction at the cross section of CFA, SFA and DFA was basically consistent; at the cross sections of LFCA and MFCA, a wide range of vortex and distinct disturbance could be respectively observed. In the RL, secondary flow directions were more complex with uneven distribution of high and low speed, and different velocity gradient. In the peripheral low velocity region near the wall, velocity gradient decreased. Four cross sections in RL exhibited a wide range of vortex. To sum up, the FV in bifurcation segment of RL was slightly less than that of SL, yet the flow field in RL was more complex and disordered than in SL, implying that the chance of vascular lesions in RL was greater.

6.2.2 Result analysis of Case-2

The vessel wall pressure (WP), wall shear stress (WSS) and inner flow velocity (FV) of the bilateral arterial 3D models of Case-2 were shown in **Figure 6.12**, **Figure 6.13**, and **Figure 6.14**.

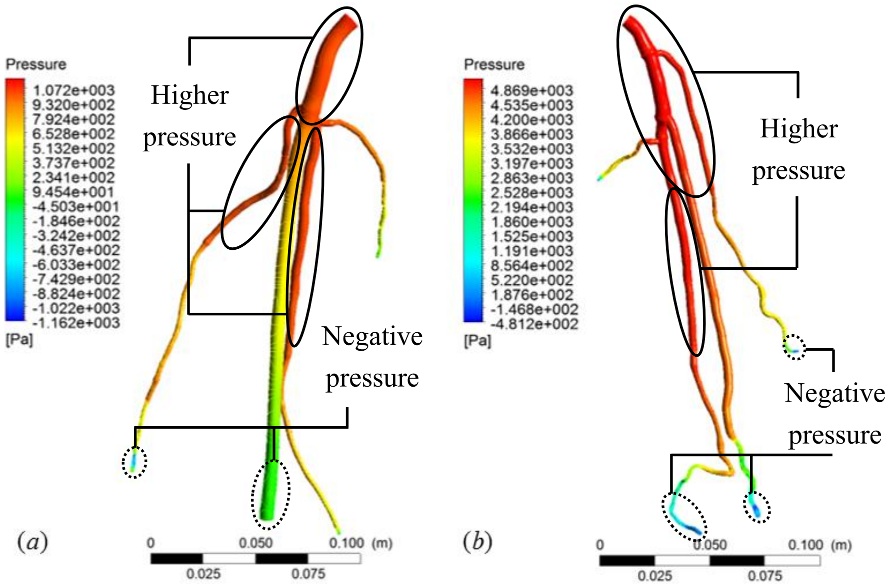

Figure 6.12 The wall pressure distribution contour of bilateral arterial 3D models of Case-2. (a) the sound limb; (b) the residual limb.

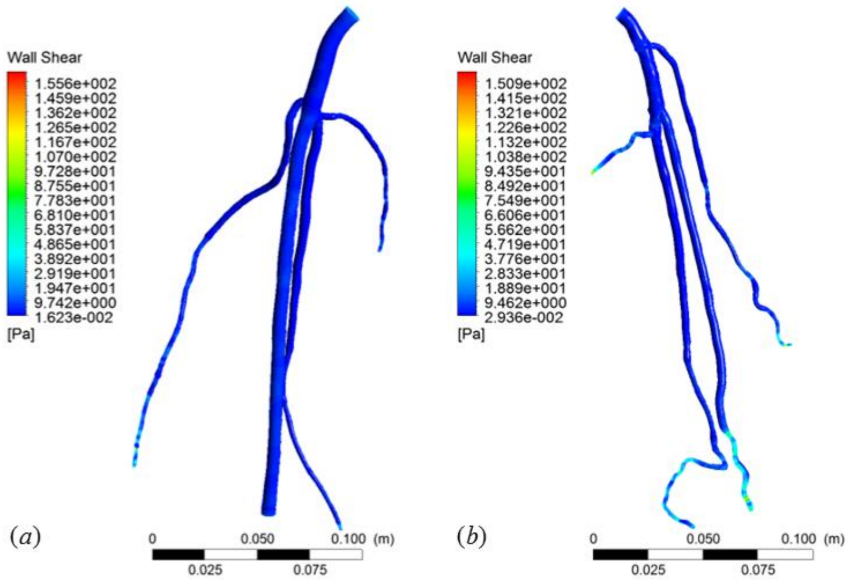

Figure 6.13 The wall shear stress distribution contour of bilateral arterial 3D models of Case-2. (a) the sound limb; (b) the residual limb.

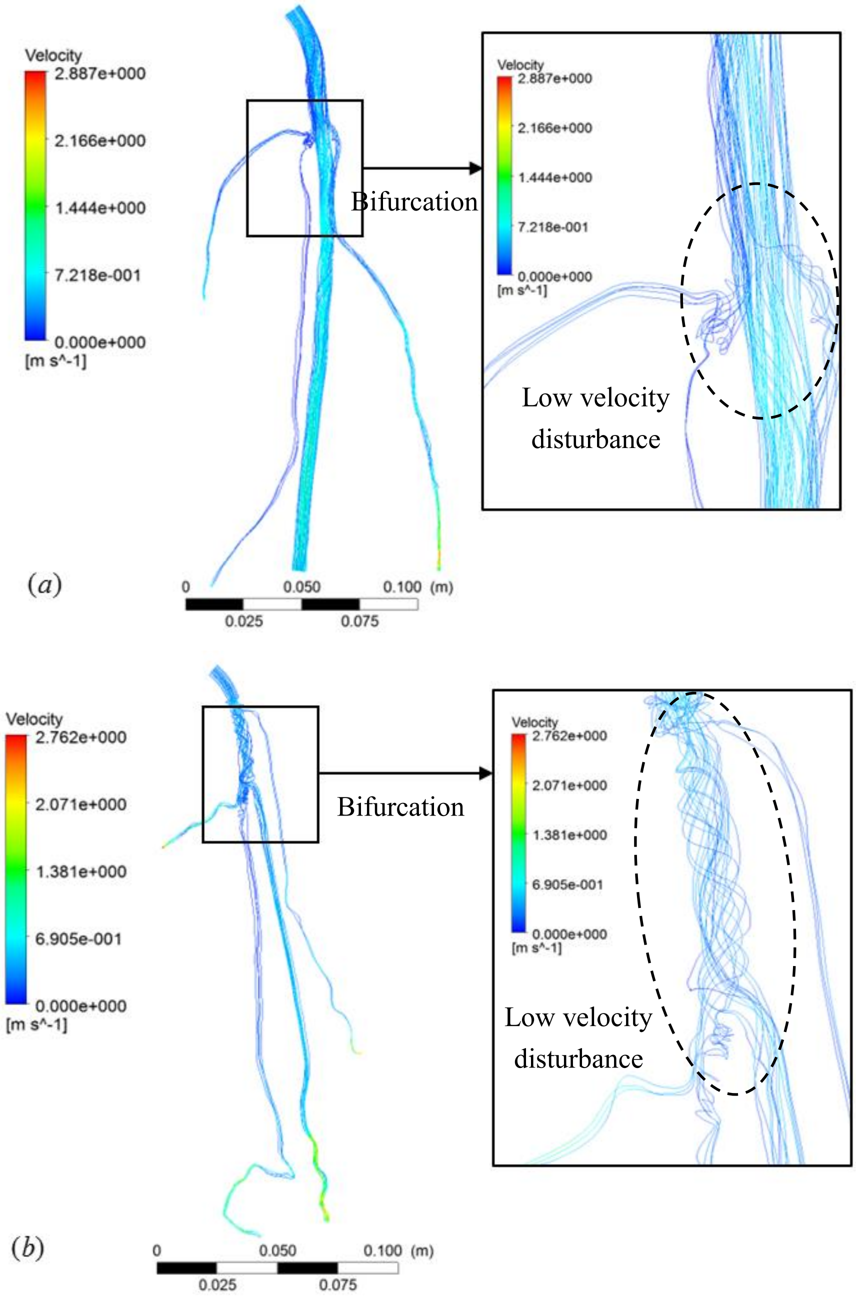

Figure 6.14 The flow velocity distribution streamline of bilateral arterial 3D models of Case-2. (a) the sound limb; (b) the residual limb.

The value range of WP in SL was from -1161.58pa to 1164.57pa, while in RL was from -481.21pa to 5092.10pa. As shown in **Figure 6.12**, the WP of RL was remarkable greater than that of SL and with uneven distribution. From the inlet to four outlets, the WP of each artery in SL became uniformly smaller along the pipeline; the upper half of DFA in RL was all in the relatively high pressure zone, and at the end of each artery, there were obvious low or negative pressure zones. **Figure 6.13** showed the WSS state. The value range in SL was from 0.0162pa to 162.12pa, and that in RL was from 0.0294pa to 157.233pa. The WSS differences at different positions in RL was greater than in SL, evidenced by the increased WSS at the bottom of RL. FV within the lumen was shown in **Figure 6.14**. The value range of RL was from 0 to 2.76m/s, while that of SL was from 0 to 2.89m/s, but the high FV areas in both limbs were very small and only at the outlets end. On the whole, the velocity magnitude and the changes along the pipeline of bilateral limbs had little difference, and both sides showed higher FV in SFA. However, at bifurcation segments, the distribution of constant velocity streamlines in bilateral limbs was obvious different. In the SL (**Figure 6.14 (a)**), bifurcations between DFA and MFCA, and between CFA and LFCA showed a very small range of low velocity disturbance. While in the RL (**Figure 6.14 (b)**), there was a wide range of medium/low velocity disturbance in the lower half of CFA and the bifurcation site, implying that the FV distribution and the flow field of RL might be more complex than those of SL.

Similar to the result analysis of Case-1, the LSSAs of Case-2 (**Figure 6.15**, **Figure 6.16**) and the velocity vector and distribution on each arterial cross section of him (**Figure 6.17**, **Figure 6.18**) were emphatically observed. Comparing **Figure 6.15** and **Figure 6.16**, it could be found that the LSSAs (<0.4Pa) of SL mainly located at the bifurcation between DFA and MFCA, the end of CFA, as well as the upper half of DFA. While the LSSAs of RL were scattered and smaller. They mainly concentrated in the upper half of DFA, local small range near the bifurcation, and the sudden change position of the diameter of LFCA. In combination with **Figure 6.12**, the WP of the upper half of DFA in both limbs were relatively high, so the possibility of the occurrence of vascular lesions in there was greater than in other arteries.

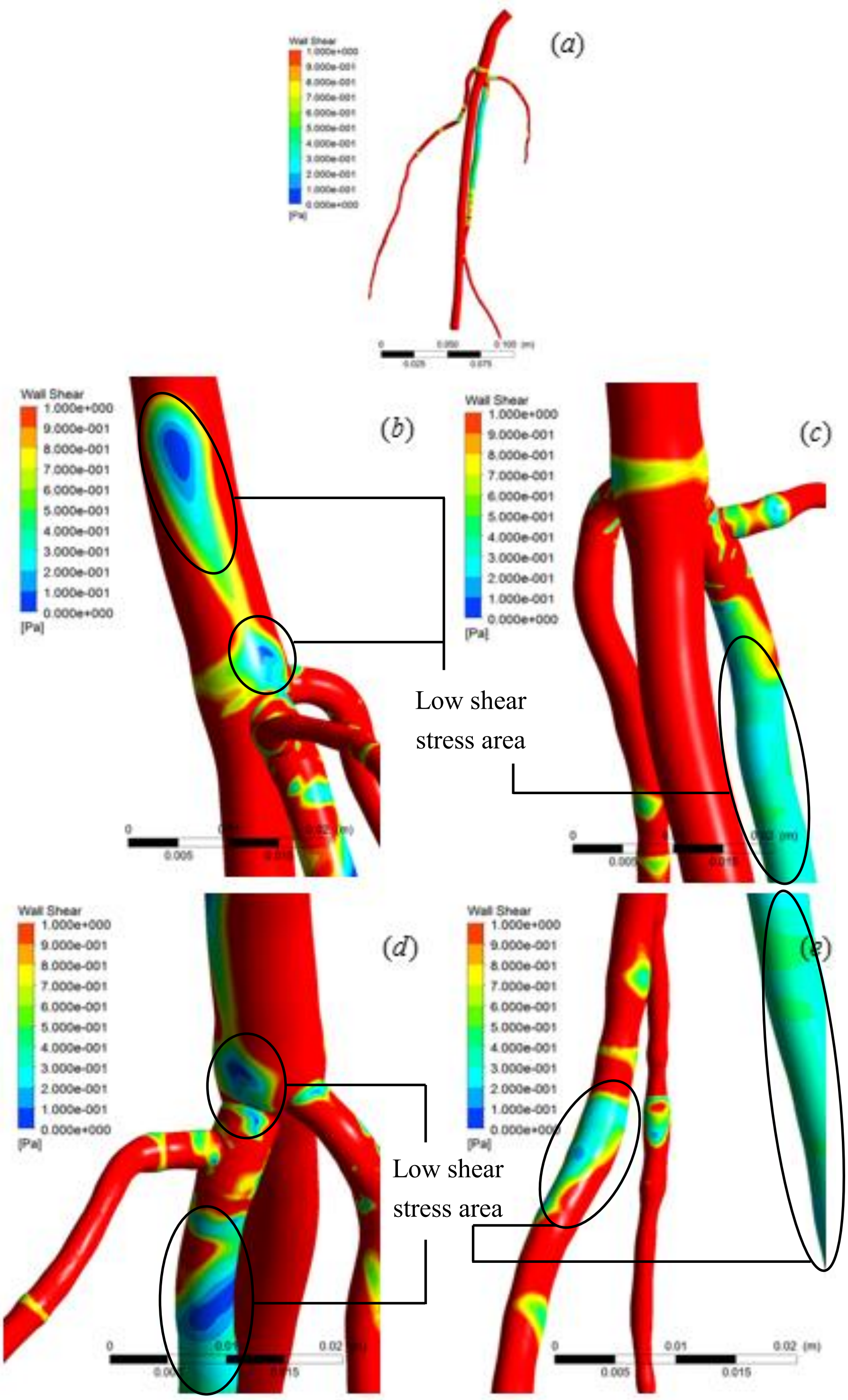

Figure 6.15 The low shear stress areas in the sound limb of Case-2. (a) overall contour; (b) (c) (d) (e) are the local contours.

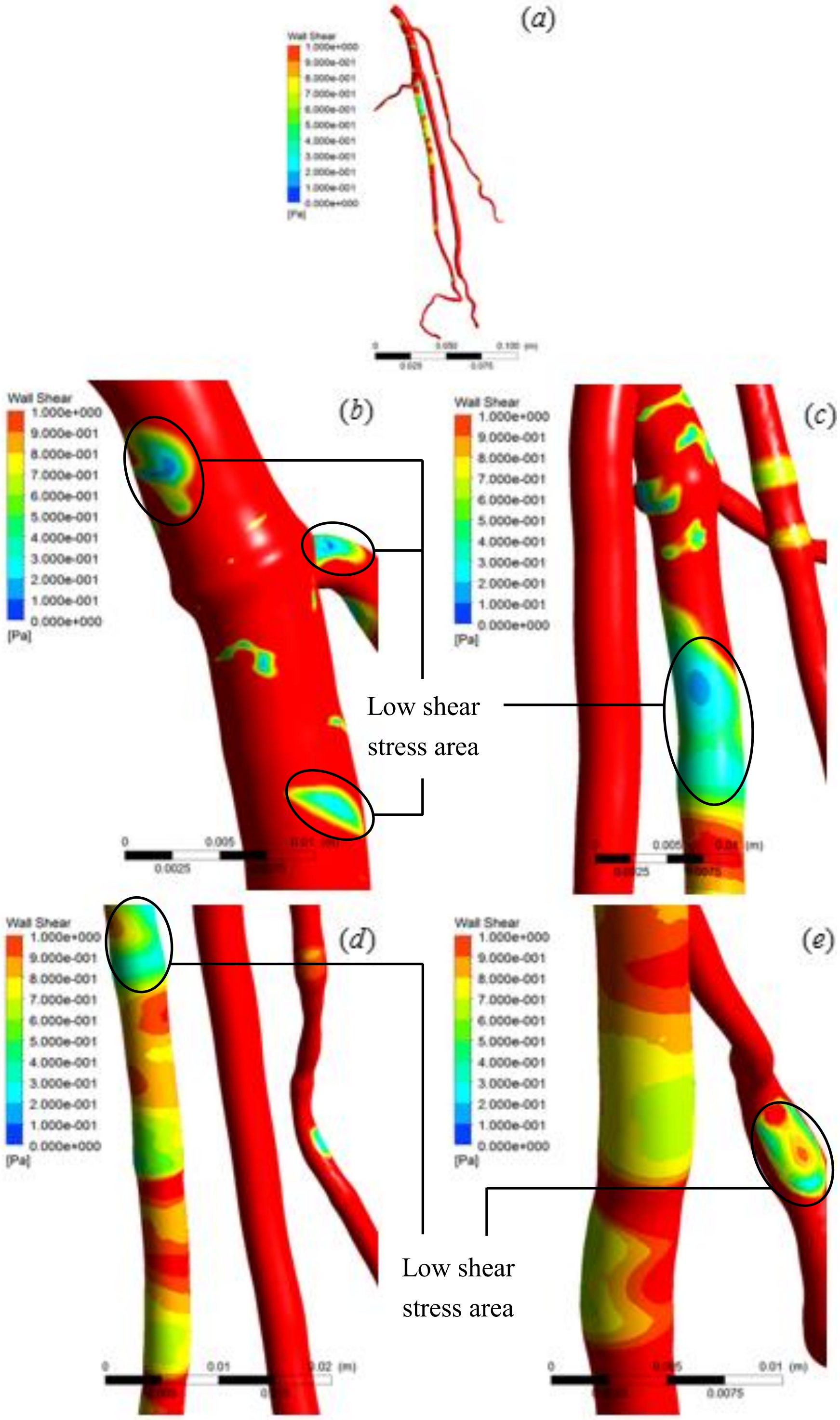

Figure 6.16 The low shear stress areas in the residual limb of Case-2. (a) overall contour; (b) (c) (d) (e) are the local contours.

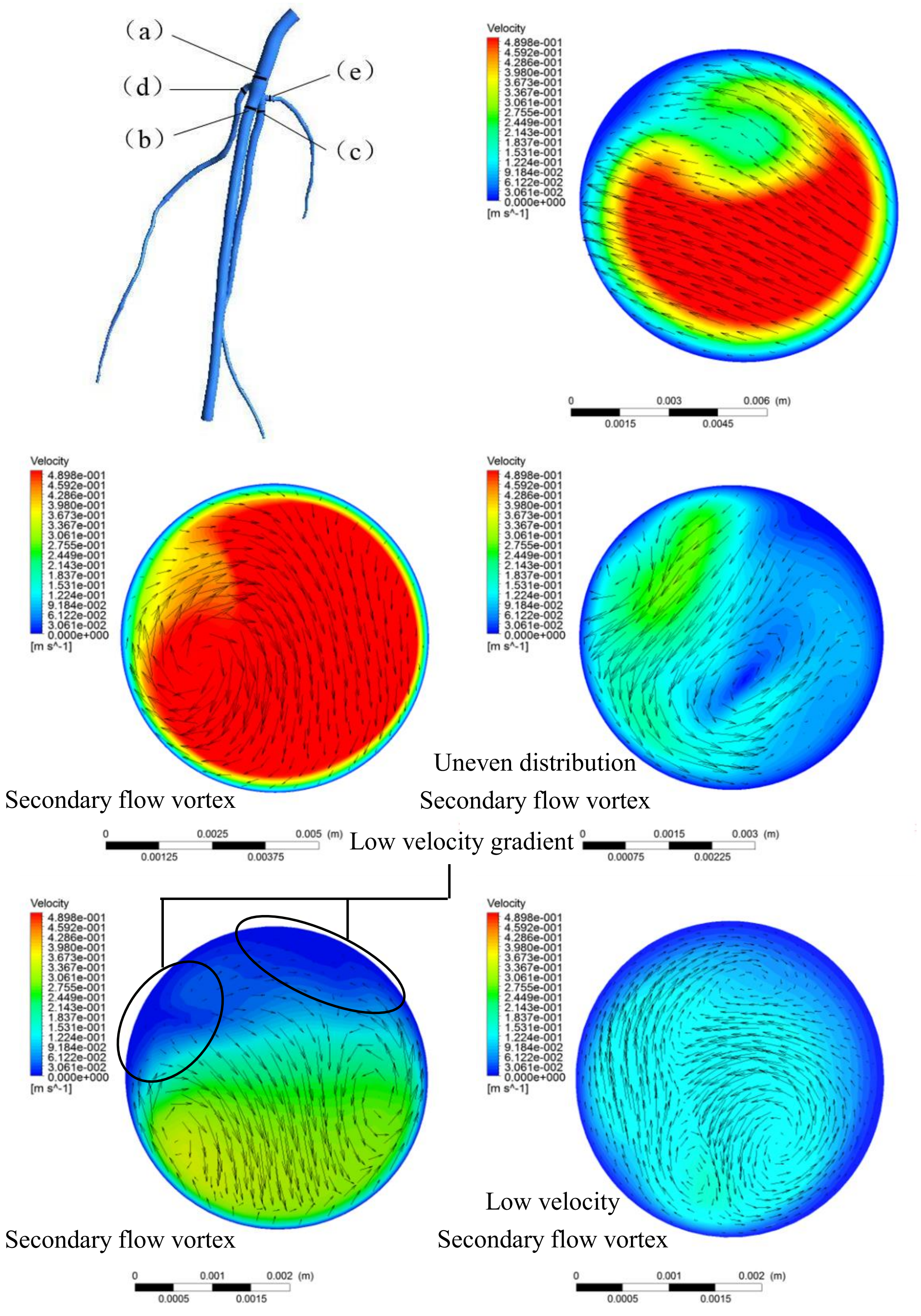

Figure 6.17 The velocity vector on each arterial cross section in the sound limb of Case-2. (a) CFA; (b) SFA; (c) DFA; (d) LFCA; (e) MFCA.

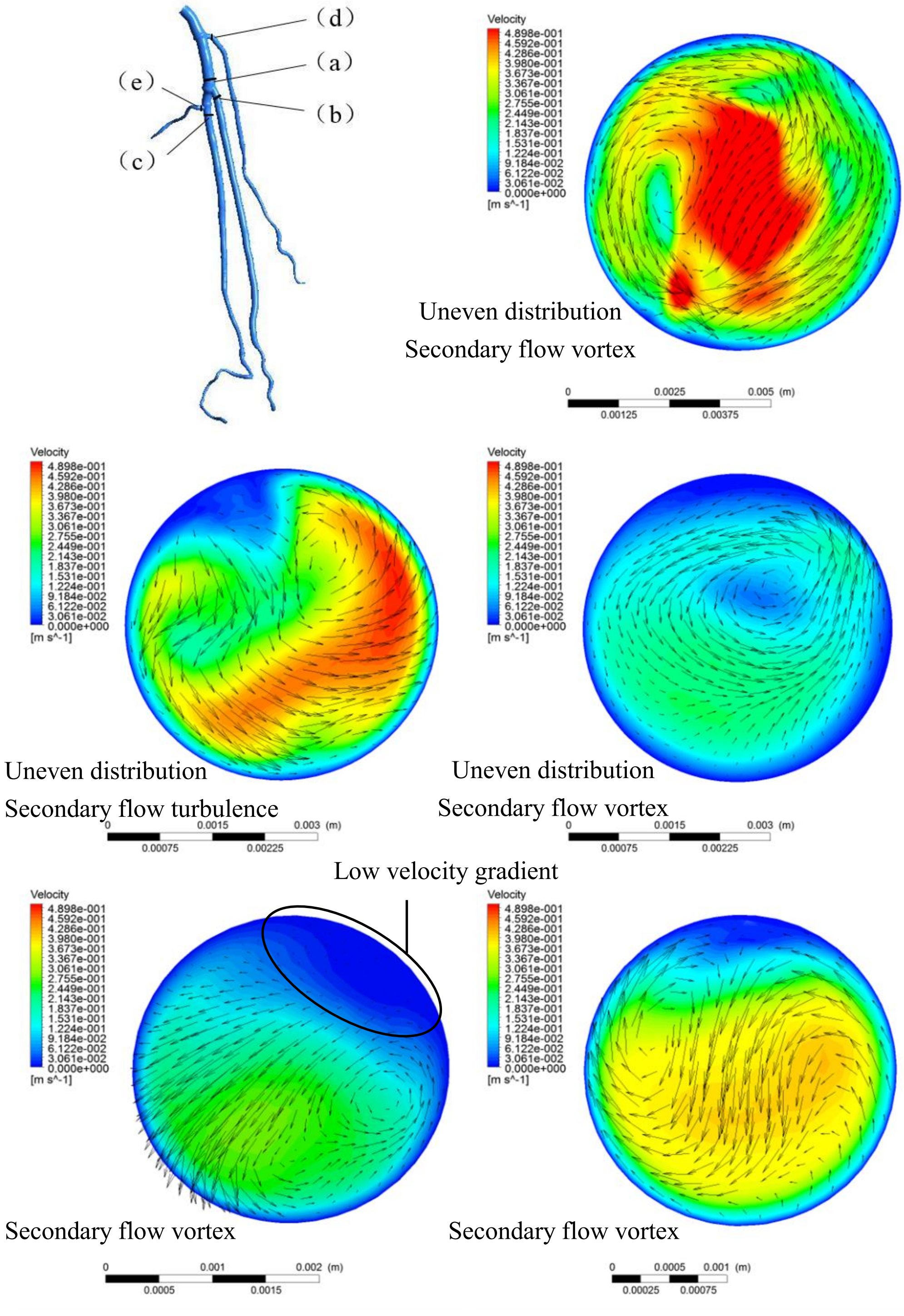

Figure 6.18 The velocity vector on each arterial cross section in the residual limb of Case-2. (a) CFA; (b) SFA; (c) DFA; (d) LFCA; (e) MFCA.

The contours in **Figure 6.17** and **Figure 6.18** showed that (the legends of all cross sections were set to 0-0.5m/s), in the bifurcation segments, FVs in the CFA and SFA of RL (**Figure 6.18 (a)**, **(b)**) were smaller than those of SL (**Figure 6.17 (a)**, **(b)**); there was little bilateral difference in DFA and in LFCA (**Figure 6.17-6.18 (c)**, **(d)**); whereas FV in the MFCA of RL (**Figure 6.18 (e)**) was obviously greater than that of SL (**Figure 6.17 (e)**). In the peripheral region near the wall, the ranges of low velocity and low gradient of bilateral limbs were similar. The velocity vector (arrow lines) illustrated some common features in velocity gradient and secondary flow direction in both sides. In the SL, a wide range of vortex could be observed in SFA, DFA, LFCA and MFCA. In the RL, all the five cross sections exhibited a wide range of vortex or turbulence. Both sides showed more complex flow fields than Case-1. To sum up, the FV in bifurcation site of RL was lower than that of SL except in the MFCA, while the complex and disordered degrees of bilateral flow fields were similar. The high risk areas for vascular lesions of Case-2 were bilateral DFAs.

6.3 SUMMARY

This chapter assumed blood as a kind of non-Newtonian fluid characterized by Casson equation, and performed steady flow calculation on the arterial 3D models of bilateral thighs with given velocity inlet and zero pressure outlet boundary conditions, in order to preliminarily understand and compare the hemodynamic states of RL and SL. Through the result analysis of Case-1 and Case-2, conclusions could be drawn as follow: under the steady flow calculation condition, the results of Case-1 and Case-2 exhibited notable differences, especially in the value ranges of WP and WSS. However, there were also some similarities: the upper half of DFA in RL was in a state of relative high WP; the LSSAs of both limbs mainly located at the bifurcation site and the upper half of DFA, and the LSSAs of SL was slightly bigger; the average blood FV of RL was lower than that of SL; there was a wide range of medium/low velocity disturbance in the bifurcation site of RL; the cross sections of RL showed more complex secondary flow direction and more disordered flow field.

Since WSS has the clearest and closest relationship with peripheral vascular diseases, in addition, the disordered flow field (turbulence or vortex), high blood pressure and low wall shear stress (<0.4pa) are also the predisposing factors of arterial lesions, the originating segment of DFA in RL is the high-risk area of the occurrence of peripheral vascular diseases. Pay attention to this section in the rehabilitation process after amputation not only could avoid severe lumen stenosis and flow reduction, but also could impede the emergence or development of plaque as early as possible. Thus, the occurring or worsening chance of arterial lesions could be minimized, while the stump problems as mentioned in Chapter 3 could be prevented or alleviated.

CHAPTER 7: NUMERICAL STUDY OF MULTI-SCALE COUPLING MODEL

7.1 MODEL AND FUNDAMENTAL EQUATION

In this chapter, the 3D models of Case-1 and Case-2 still employed the same structure, mesh, and computational method with the previous chapter. Constant resistance (CR) model and Windkessel (WK) model were applied as two kinds of lumped parameter (0D) model. The boundary condition setting and 3D-0D coupling method were detailed described in Chapter 5. The constitutive relation of blood was still characterized by Casson equation (section 6.1). Blood flow was considered as unsteady flow, and the numerical calculation in a complete cardiac cycle was carried out based on the ultrasonic measured data.

7.1.1 Inlet boundary condition

In the calculation of multi-scale coupling model, blood flow was regarded as unsteady flow. According to the length of a cardiac cycle of the two cases, the calculation step size of Case-1 was set as 0.01s, and that of Case-2 was set as 0.0124s. The inlet boundary conditions of four 3D models (both limbs of the two cases) were fitting curves obtained by using spline interpolation on the ultrasonic measured velocity waveforms of CFAs (**Figure 7.1** and **Figure 7.2**), as shown in **Figure 7.3** and **Figure 7.4**.

In these inlet velocity waveforms (a cardiac cycle), four feature moments were selected for result analysis: the maximum velocity time in rapid ejection period (t1), the middle velocity time in slow ejection period (t2), the maximum velocity time in isovolumic relaxation period (t3), and the maximum velocity time in slow filling period (t4).

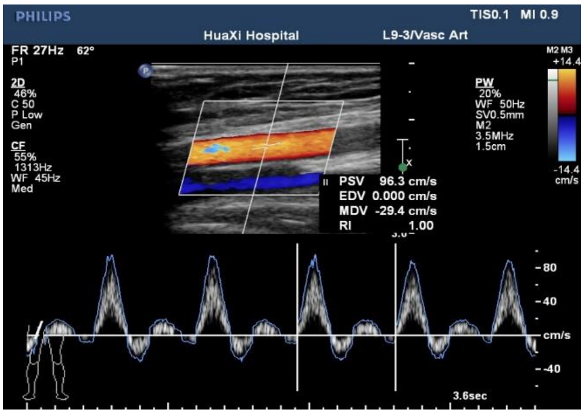

Figure 7.1 The ultrasonic measured velocity waveform of CFA in Case-1's residual limb.

Figure 7.2 The ultrasonic measured velocity waveform of CFA in Case-2's sound limb.

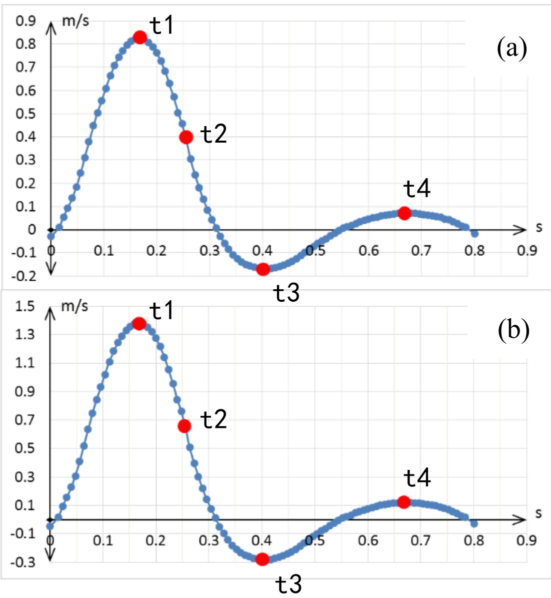

Figure 7.3 The inlet boundary conditions of Case-1's 3D models. (a) velocity waveform of residual limb CFA; (b) velocity waveform of sound limb CFA.

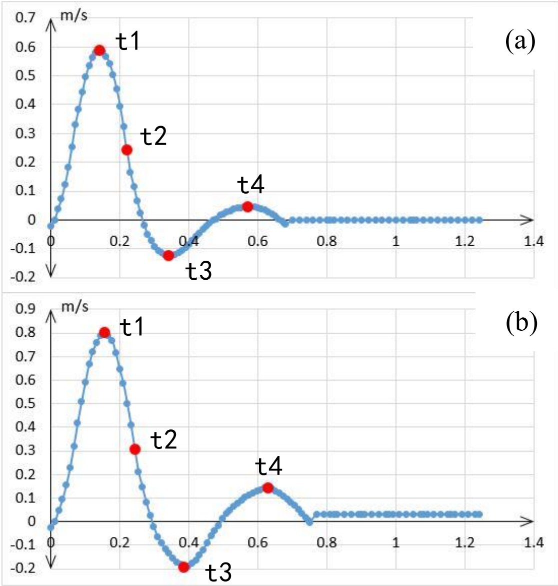

Figure 7.4 The inlet boundary conditions of Case-2's 3D models. (a) velocity waveform of residual limb CFA; (b) velocity waveform of sound limb CFA.

7.1.2 Constant resistance (CR) model

In Fourier space, outlet boundary condition satisfies the equation:

$$\hat{P}(\omega) = \hat{Q}(\omega)Z(\omega) \tag{7.1}$$

Wherein $\hat{P}(\omega)$ is the Fourier form of blood pressure $p(t)$, $Z(\omega)$ is arterial terminal impedance. In the time domain, Equation (7.1) is equivalent to:

$$p(t) = \frac{1}{T}\int_{t-T}^{t} z(t-\tau)q(\tau)d\tau \tag{7.2}$$

Wherein kernel function $z(t)$ is the inverse Fourier transform of $Z(\omega)$.

Constant resistance (CR) model (shown in **Figure 5.4**) is constructed from a resistor, which assumes that the impedance is constant at all wave frequencies [147]:

$$Z_{CR}(\omega) \equiv R_T \tag{7.3}$$

In the equation, R_T is total resistance, ω is wave frequency, the corresponding kernel function is $z_{CR}(t) = R_T T\delta(t)$, thus in time domain, $p(t) = R_T q(t)$. Under this kind of boundary condition, any outlet of arterial tree has no time lag between blood pressure and flow rate, which is not consistent with the experimental observations, but could roughly describe the terminal impedance at vessel ends.

Because the physiological data of each artery outlet pressure is difficult to measure, the total resistance R_T at each outlet was calculated by the following empirical data: mean arterial pressure is 62.5mmHg (Benetos A., et al., 1993), mean venous pressure is 10mmHg (Rod Seeley, et al., 1991), so the pressure difference at each outlet is 52.5mmHg; the flow rate at each outlet used the mean value of ultrasonic measured data in a cardiac cycle. The calculated R_T values of Case-1 and Case-2 were shown in **Table 7.1** and **Table 7.2**.

Table 7.1 The total resistance R_T of Case-1's CR models

Case-1		R_T(Pa*s/m^3)
RL	SFA	1.5670E+11
	DFA	4.8216E+09
	LFCA	2.0894E+10
	MFCA	6.2681E+09

Case-1		R_T(Pa*s/m^3)
SL	SFA	5.0720E+09
	DFA	4.7347E+09
	LFCA	2.3862E+10
	MFCA	5.9067E+09

Table 7.2 The total resistance R_T of Case-2's CR models

Case-2		R_T(Pa*s/m^3)
RL	SFA	2.5700E+11
	DFA	3.1941E+10
	LFCA	8.6541E+10
	MFCA	1.6277E+11

Case-2		R_T(Pa*s/m^3)
SL	SFA	1.1881E+10
	DFA	2.9234E+10
	LFCA	9.1776E+10
	MFCA	2.6753E+10

7.1.3 Three-element Windkessel (WK) model

Three-element Windkessel (WK) model (shown in **Figure 5.5**) is a relatively mature model for describing the relationship between blood flow rate and pressure at arterial outlet [148]. In this electro-hydraulic analogy, blood pressure P corresponds to voltage, volume flow rate Q corresponds to current, and capacitance describes the compliance of downstream vessels. According to Kirchhoff law, the blood pressure and flow rate of three-element WK model satisfy the following relation [147]:

$$\frac{dp(t)}{dt}+\frac{p}{R_2C_T}=R_1\frac{dq(t)}{dt}+\frac{q(R_1+R_2)}{R_2C_T} \tag{7.4}$$

Wherein R_1 is the characteristic resistance, R_1+R_2 is the total resistance. Thus at frequency ω, the impedance is:

$$Z_{WK}(\omega)=R_1+\frac{R_2}{1+i\omega R_2C_T} \tag{7.5}$$

And its corresponding kernel function is:

$$z_{WK}(t)=R_1T\delta(t)+\frac{T}{C_T[1-\exp(-\frac{T}{R_2C_T})]}\exp(-\frac{t}{R_2C_T}) \tag{7.6}$$

The total resistance value of three-element WK model R_1+R_2 is consistent with that of CR model R_T. The characteristic resistance R_1 is calculated as follows:

$$R_1=\sqrt{\frac{\rho}{A_{0r}C_r}}=\frac{\rho c_r}{A_{0r}} \tag{7.7}$$

The A_{0r}, c_r and C_r are respectively vascular unstressed sectional area, pulse wave velocity, and root vessel regional compliance. The value of pulse wave velocity c_r is calculated by empirical inverse curve of output and the best fitting coefficient [122]:

$$c_r=\frac{a}{\bar{d}^b} \tag{7.8}$$

Wherein $a=13.3$, $b=0.3$, $\bar{d}$ is the mean value of vascular diameter. The calculation of capacitance C_T is based on empirical formula and time constant $\tau=1.79\text{s}$ [149]:

$$C_T=\frac{\tau}{R_T} \tag{7.9}$$

The calculated values of these parameters of Case-1 and Case-2 were shown in **Table 7.3** and **Table 7.4**.

Table 7.3 The parameters of Case-1's three-element WK models

Case-1		R_1(Pa*s/m^3)	R_2(Pa*s/m^3)	C_T(m^3/Pa)
RL	SFA	7.6308E+08	1.5594E+11	1.1423E-11
	DFA	9.7176E+08	3.8498E+09	3.7125E-10
	LFCA	2.7496E+09	1.8144E+10	8.5671E-11
	MFCA	2.0458E+09	4.2223E+09	2.8557E-10
SL	SFA	2.2286E+08	4.8491E+09	3.5292E-10
	DFA	4.8815E+08	4.2466E+09	3.7806E-10
	LFCA	1.1333E+09	2.2728E+10	7.5016E-11
	MFCA	1.2103E+09	4.6964E+09	3.0305E-10

Table 7.4 The parameters of Case-2's three-element WK models

Case-2		R_1(Pa*s/m^3)	R_2(Pa*s/m^3)	C_T(m^3/Pa)
RL	SFA	7.6308E+08	1.5594E+11	1.1423E-11
	DFA	9.7176E+08	3.8498E+09	3.7125E-10
	LFCA	2.7496E+09	1.8144E+10	8.5671E-11
	MFCA	2.0458E+09	4.2223E+09	2.8557E-10
SL	SFA	2.2286E+08	4.8491E+09	3.5292E-10
	DFA	4.8815E+08	4.2466E+09	3.7806E-10
	LFCA	1.1333E+09	2.2728E+10	7.5016E-11
	MFCA	1.2103E+09	4.6964E+09	3.0305E-10

7.2 RESULT ANALYSIS AND DISCUSSION OF CASE-1

7.2.1 3D-CR coupling model

- ***Residual limb***

The wall pressure (WP), wall shear stress (WSS), low shear stress area (LSSA) and the flow velocity (FV) in bifurcation segment of the 3D-CR coupling model in Case-1's RL at the four moments t1, t2, t3, and t4 were successively shown in **Figure 7.5**, **Figure 7.6**, **Figure 7.7** and **Figure 7.8**.

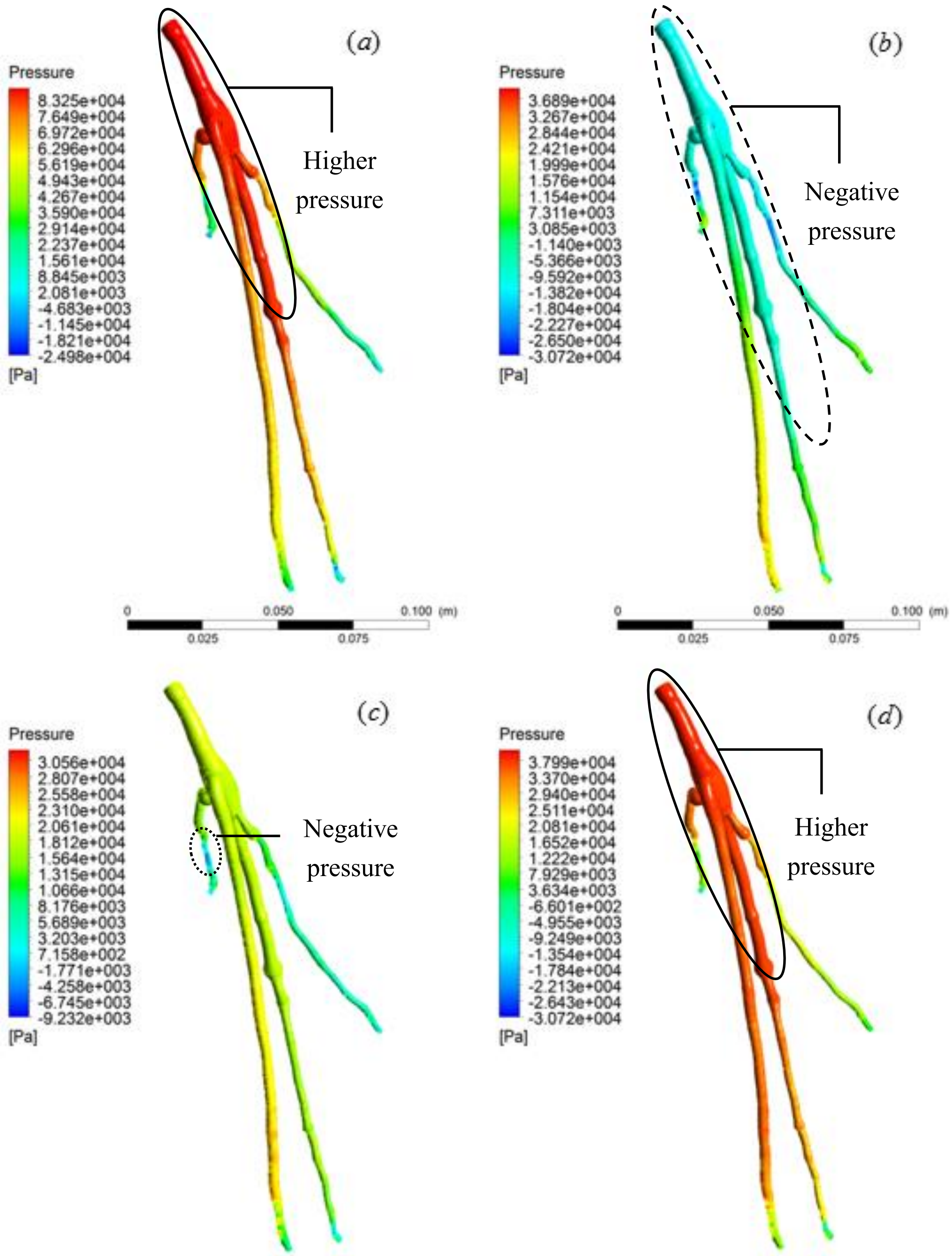

Figure 7.5 The wall pressure distribution contour of the 3D-CR coupling model in Case-1's RL. (a) t1; (b) t2; (c) t3; (d) t4.

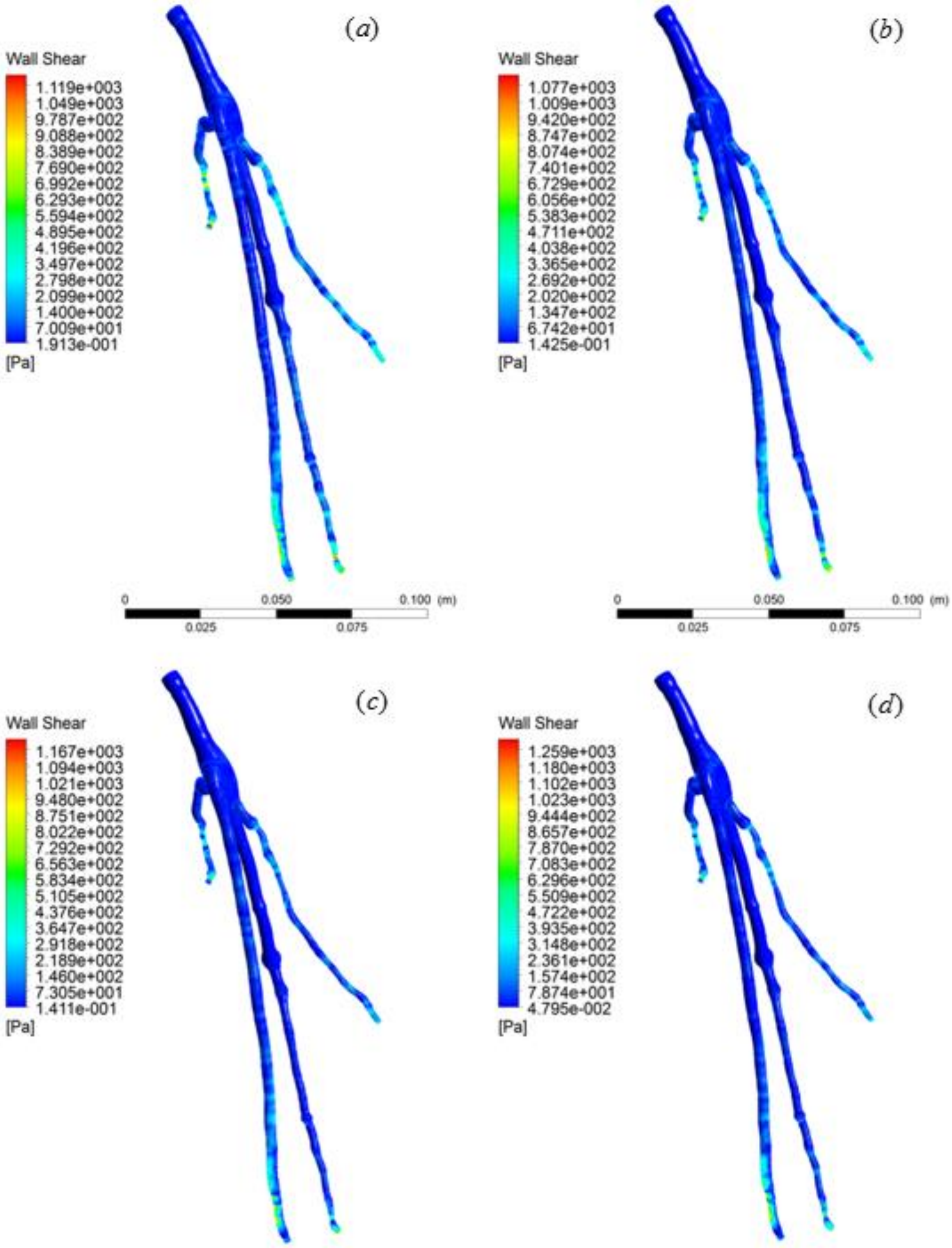

Figure 7.6 The wall shear stress distribution contour of the 3D-CR coupling model in Case-1's RL. (a) t1; (b) t2; (c) t3; (d) t4.

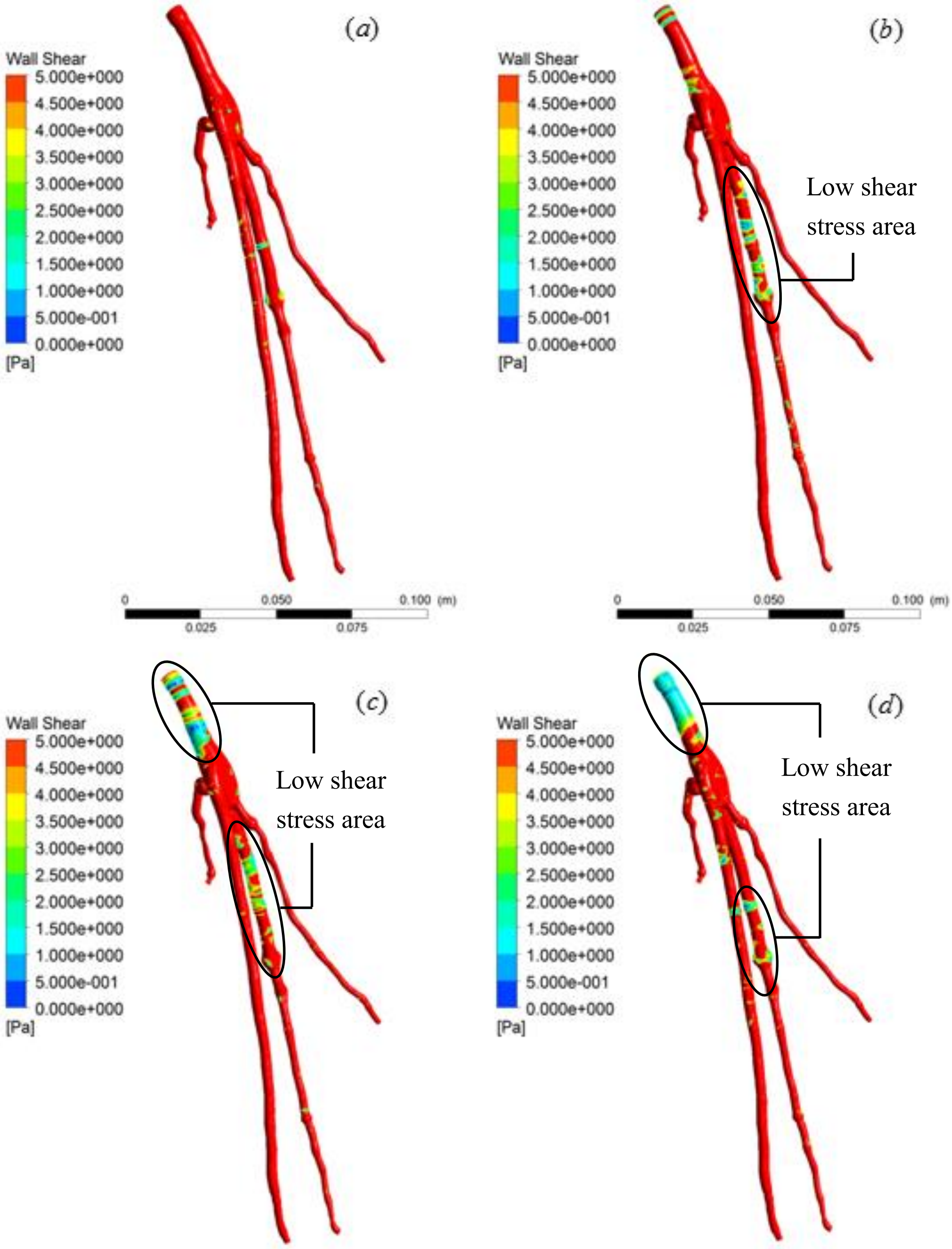

Figure 7.7 The low shear stress areas of the 3D-CR coupling model in Case-1's RL. (a) t1; (b) t2; (c) t3; (d) t4.

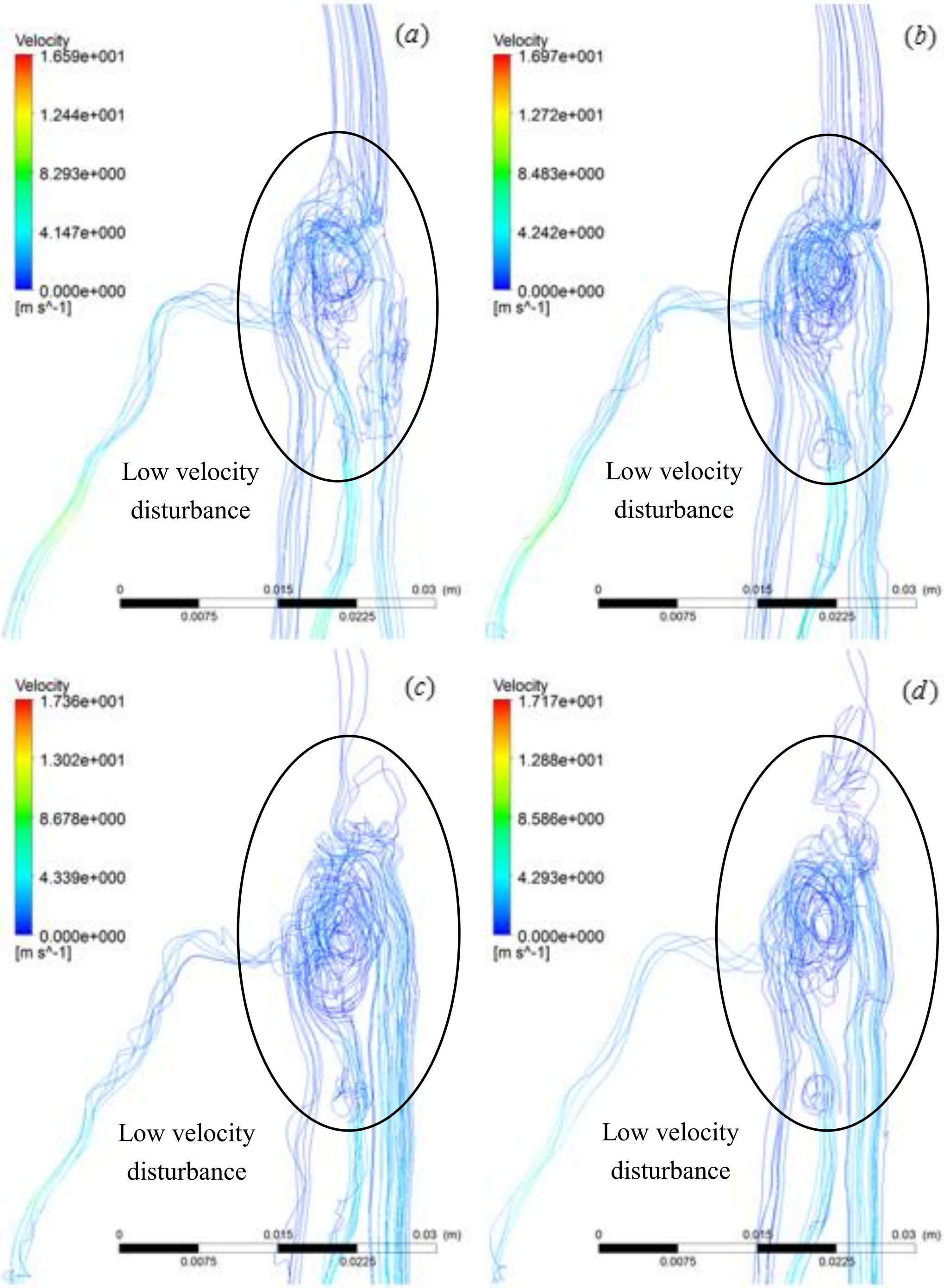

Figure 7.8 The flow velocity distribution streamline of the 3D-CR coupling model in Case-1's RL. (a) t1; (b) t2; (c) t3; (d) t4.

As can be seen in **Figure 7.5**, the WP ranges of the arterial tree in RL at four different moments were respectively -20664.4Pa--87737.1Pa at t1, -30720.9Pa--39709.0Pa at t2, -4557.8Pa--32215.8Pa at t3, -5384.6Pa--40852.4Pa at t4, and the WP distributions were uneven at all moments. At t1, vessel walls bore the largest blood pressure; at t2, the upper half of whole arterial tree was in a negative pressure state and the lower half gradually changed to positive pressure; at t3, the WP was the minimum; at t4, the WP value had picked up and the relative high pressure zone was similar with the situation at t1. Except t2, at the other three moments WP decreased along the direction of blood flow. Comparatively speaking, the WP values of LFCA and MFCA were smaller, whereas that of DFA was larger, and the change along flow direction in SFA was relatively even.

WSS distributions were shown in **Figure 7.6**, and there was little difference between the four moments. The value ranges were respectively 0.1913Pa--1165.12Pa at t1, 0.1425Pa--1121.35Pa at t2, 0.1411Pa--1215.32Pa at t3, 0.0480Pa --1311.63Pa at t4, however, the high shear stress areas were very small and the entire arterial tree was basically blue. Near the outlets, WSS increased with the decrease of lumen diameters. Specific observation on the WSS value of 0-5Pa was shown in **Figure 7.7** to identify the dangerous LSSAs whose value lower than 0.4Pa. Except t1, the other three moments showed notable LSSAs. Especially at t3 and t4, there were larger areas of low shear stress in CFA above the bifurcation. While the upper half of DFA also displayed some scattered LSSAs at t2 and t3.

Figure 7.8 illustrated the velocity streamlines in the bifurcation segment. The velocity ranges of entire arterial tree were respectively 0--16.59m/s at t1, 0--16.97m/s at t2, 0--17.36m/s at t3, 0--17.17m/s at t4. Similar to WSS, the high FV areas were very small and only in the four outlets. At all moments, there were wide scopes of low velocity disturbance in bifurcation site, indicating the more complex flow field. The velocity vector on each arterial cross section 2mm away from the bifurcation site was shown in **Figure 7.9** to **Figure 7.13**.

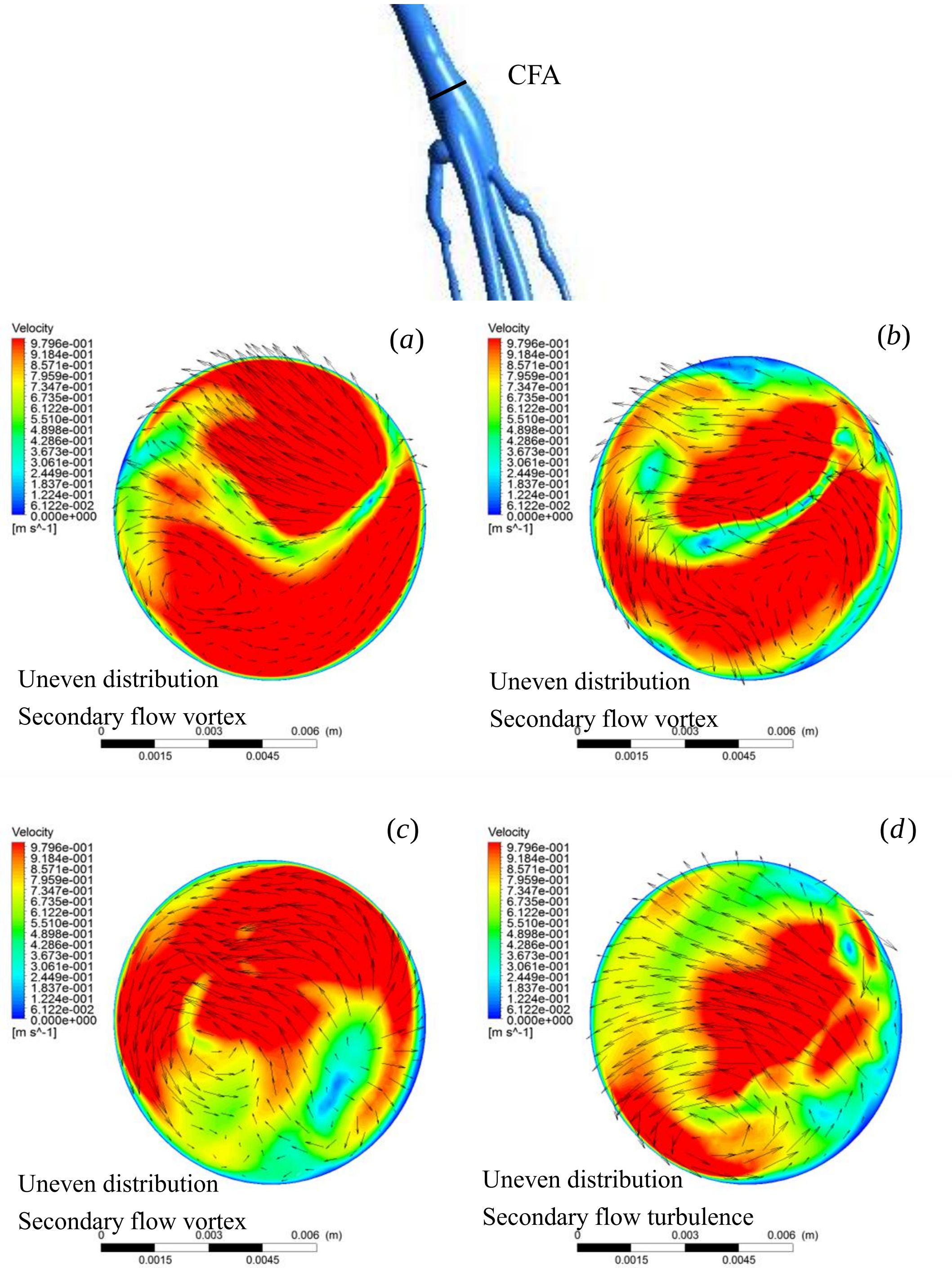

Figure 7.9 The velocity vector on CFA cross section of the 3D-CR coupling model in Case-1's RL. (a) t1; (b) t2; (c) t3; (d) t4.

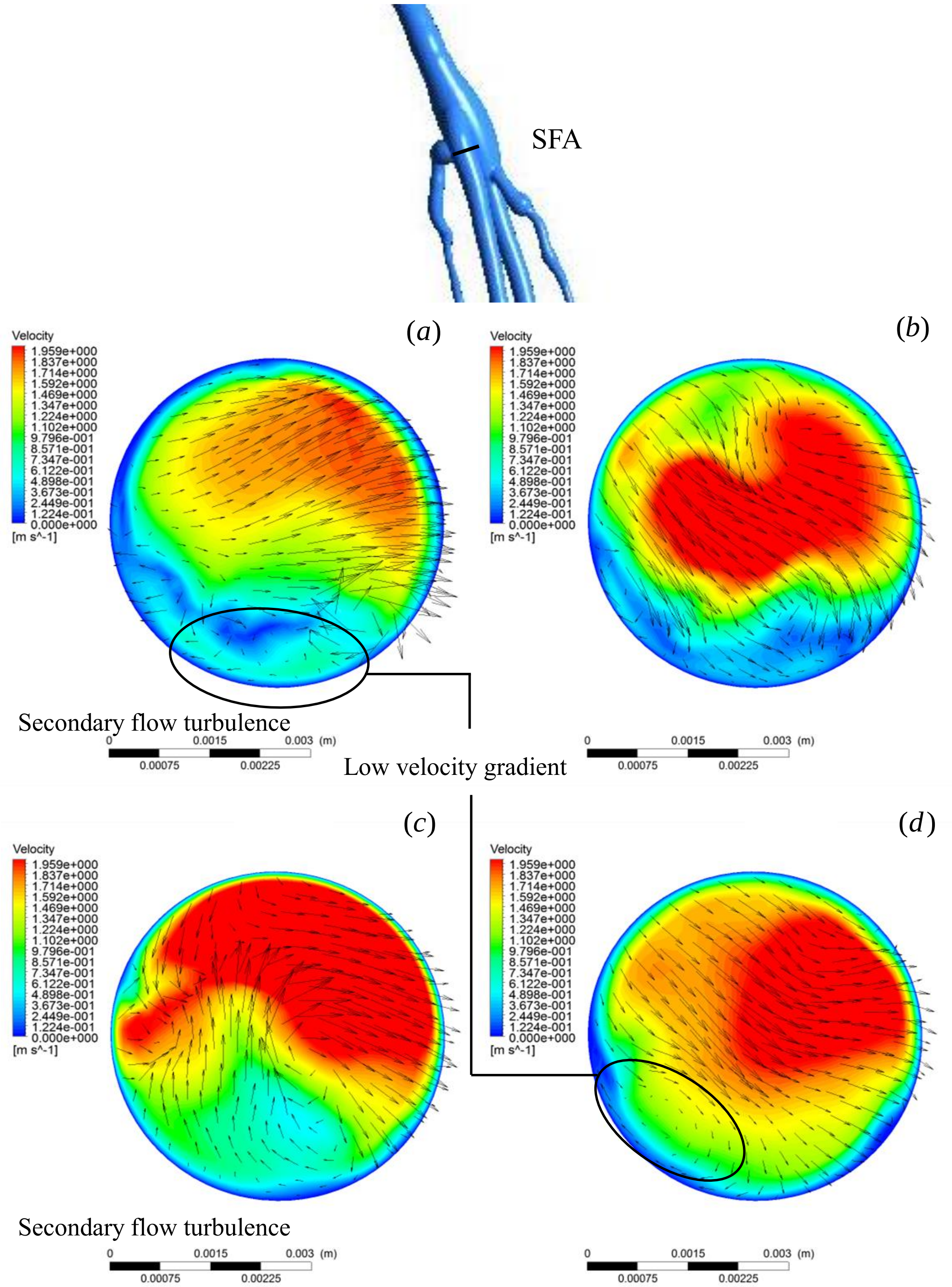

Figure 7.10 The velocity vector on SFA cross section of the 3D-CR coupling model in Case-1's RL. (a) t1; (b) t2; (c) t3; (d) t4.

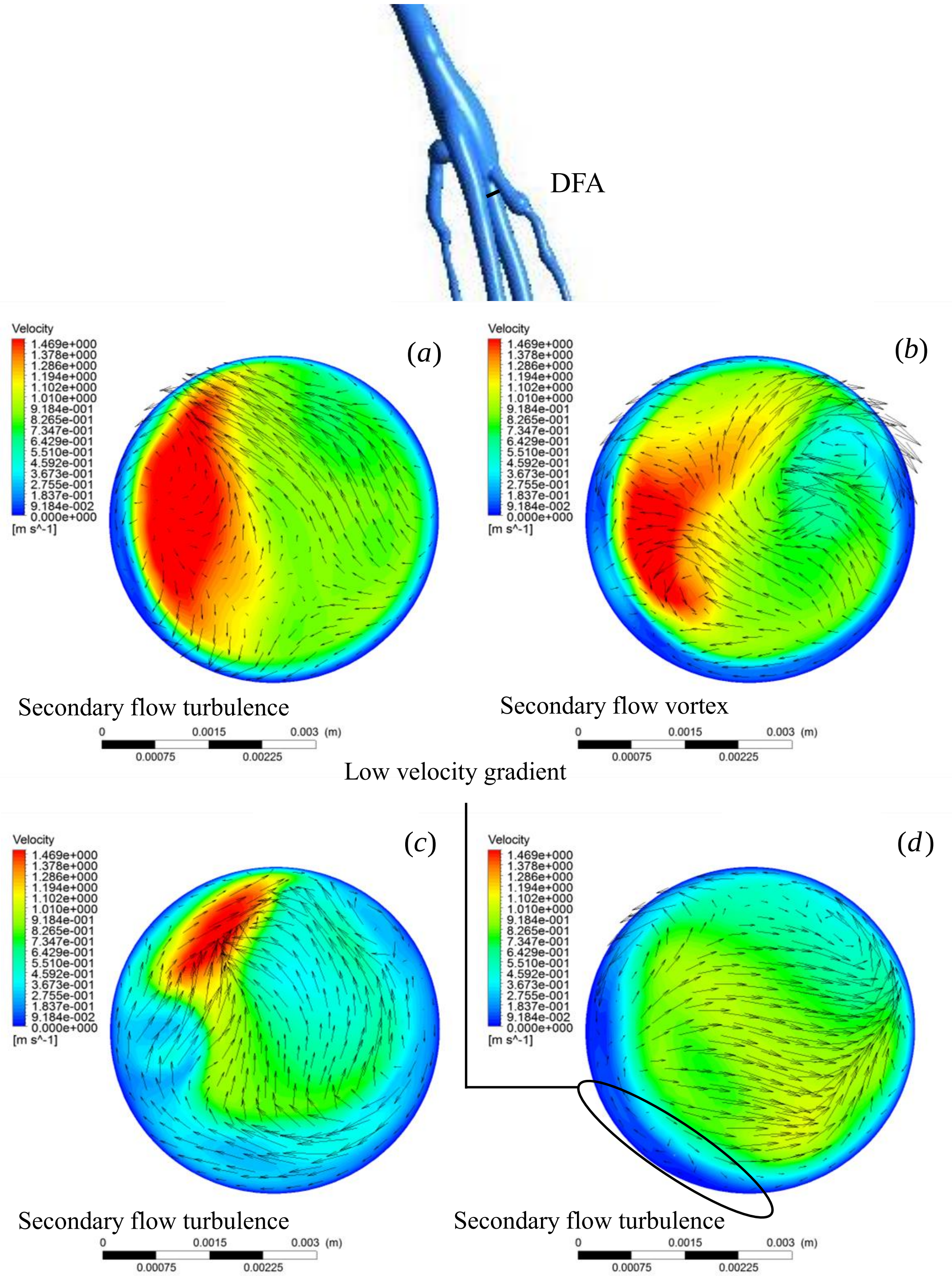

Figure 7.11 The velocity vector on DFA cross section of the 3D-CR coupling model in Case-1's RL. (a) t1; (b) t2; (c) t3; (d) t4.

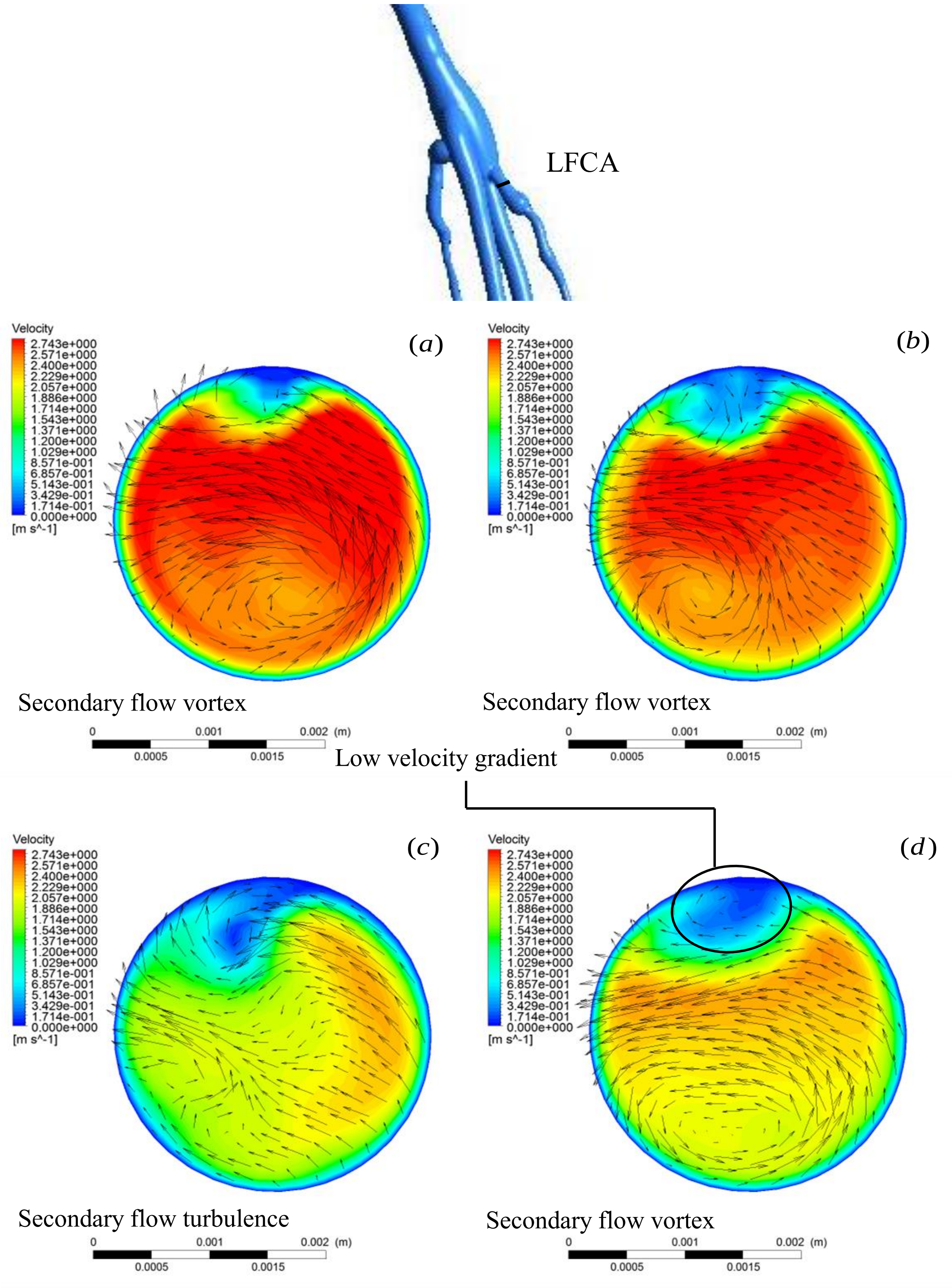

Figure 7.12 The velocity vector on LFCA cross section of the 3D-CR coupling model in Case-1's RL. (a) t1; (b) t2; (c) t3; (d) t4.

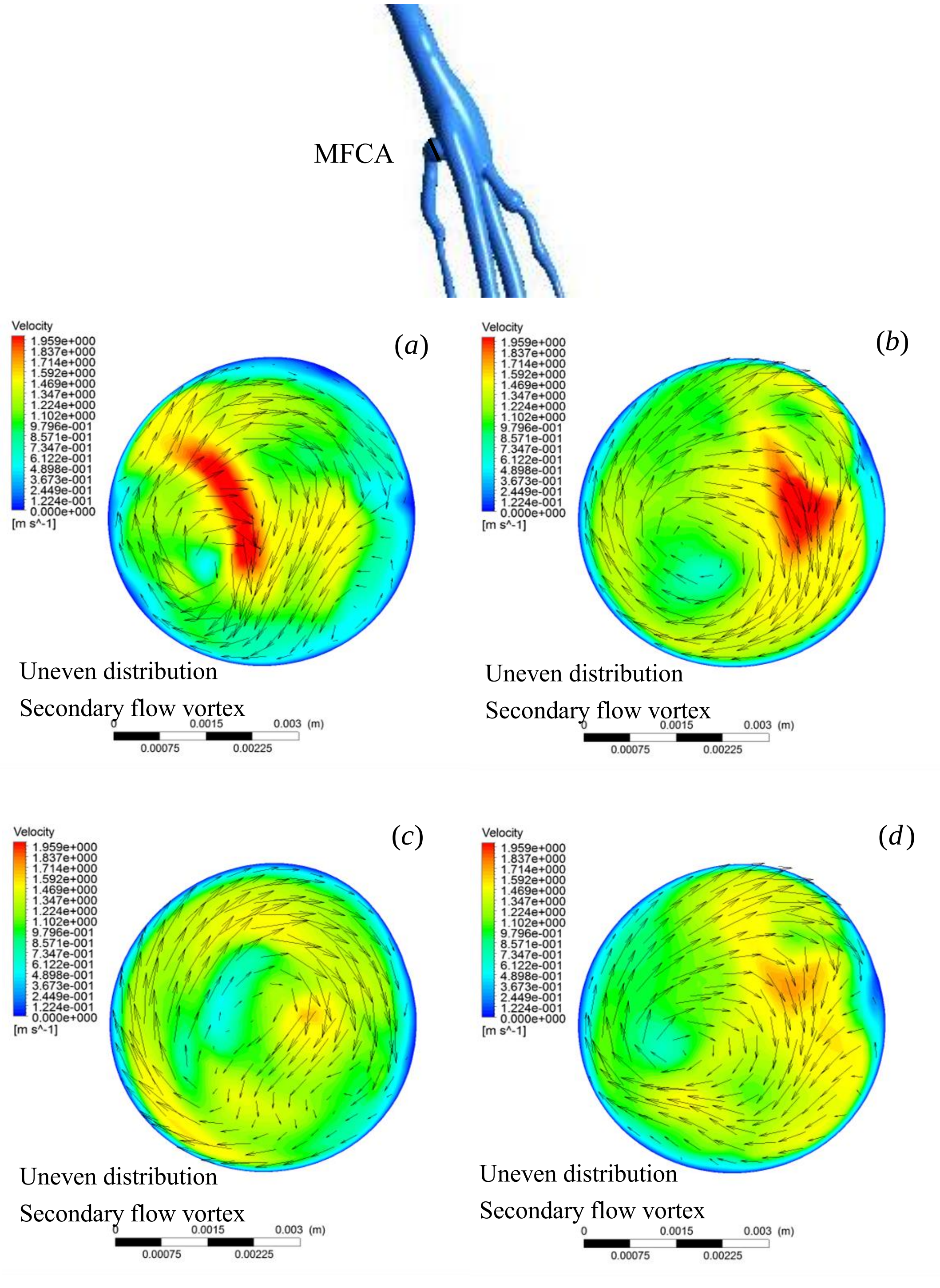

Figure 7.13 The velocity vector on MFCA cross section of the 3D-CR coupling model in Case-1's RL. (a) t1; (b) t2; (c) t3; (d) t4.

Figure 7.9 showed the velocity vector on CFA cross section. It could be seen that the FV distribution of the entrance segment was very nonuniform. At t1 and t2, high velocity zone (the red part) was larger, and the velocity gradient was basically consistent on whole cross section. While at t3 and t4, FV value reduced with becoming uneven velocity gradient. There were messy secondary flow phenomena at all four moments, especially at t2 and t4 as exhibiting disordered multi-direction and larger scope of vortex. As shown in **Figure 7.10**, the average FV value in SFA was higher, and the high velocity zone (the red part) was concentrated. The peripheral velocity (the blue part) near vessel wall was obviously smaller than luminal center velocity, yet the transition between high and low velocity was moderate. All four moments exhibited relatively uniform velocity gradient. Except at t3 there was a turbulence, blood flow directions were generally consistent at the other three moments. The FV distribution on DFA cross section as shown in **Figure 7.11** was similar to that on SFA. Concentrated high velocity zone had smaller area and value than in SFA. The medium velocity zone (the green part) had a larger range, which meant the high/low velocity transition from lumen center to periphery was gentle, but the thickness of the low velocity zone near wall increased. All four moments showed basically even velocity gradient but locally complex secondary flow direction, as a certain range of vortex at t2 and turbulance at t3, t4. The results of LFCA and MFCA were shown in **Figure 7.12** and **Figure 7.13**. Both of them displayed clear high velocity zone at t1 and t2, and the values were greater than those of DFA and SFA. The high velocity area of LFCA was larger than that of MFCA. On LFCA cross section, the velocity gradient in peripheral low velocity region (the dark blue part) decreased. The secondary flow directions were similar between four moments, and local vortex and turbulence could be observed. On MFCA cross section, velocity distribution was uneven reflected in center low velocity area (the light blue part) and mixed medium velocity zone (the yellow/green part), but its velocity gradient was uniform. A wide extent of vortex could be observed in lumen center at all four moments.

- ***Sound limb***

The wall pressure (WP), wall shear stress (WSS), low shear stress area (LSSA) and the flow velocity (FV) in bifurcation segment of the 3D-CR coupling model in Case-1's SL at the four moments t1, t2, t3, and t4 were successively shown in **Figure 7.14**, **Figure 7.15**, **Figure 7.16** and **Figure 7.17**.

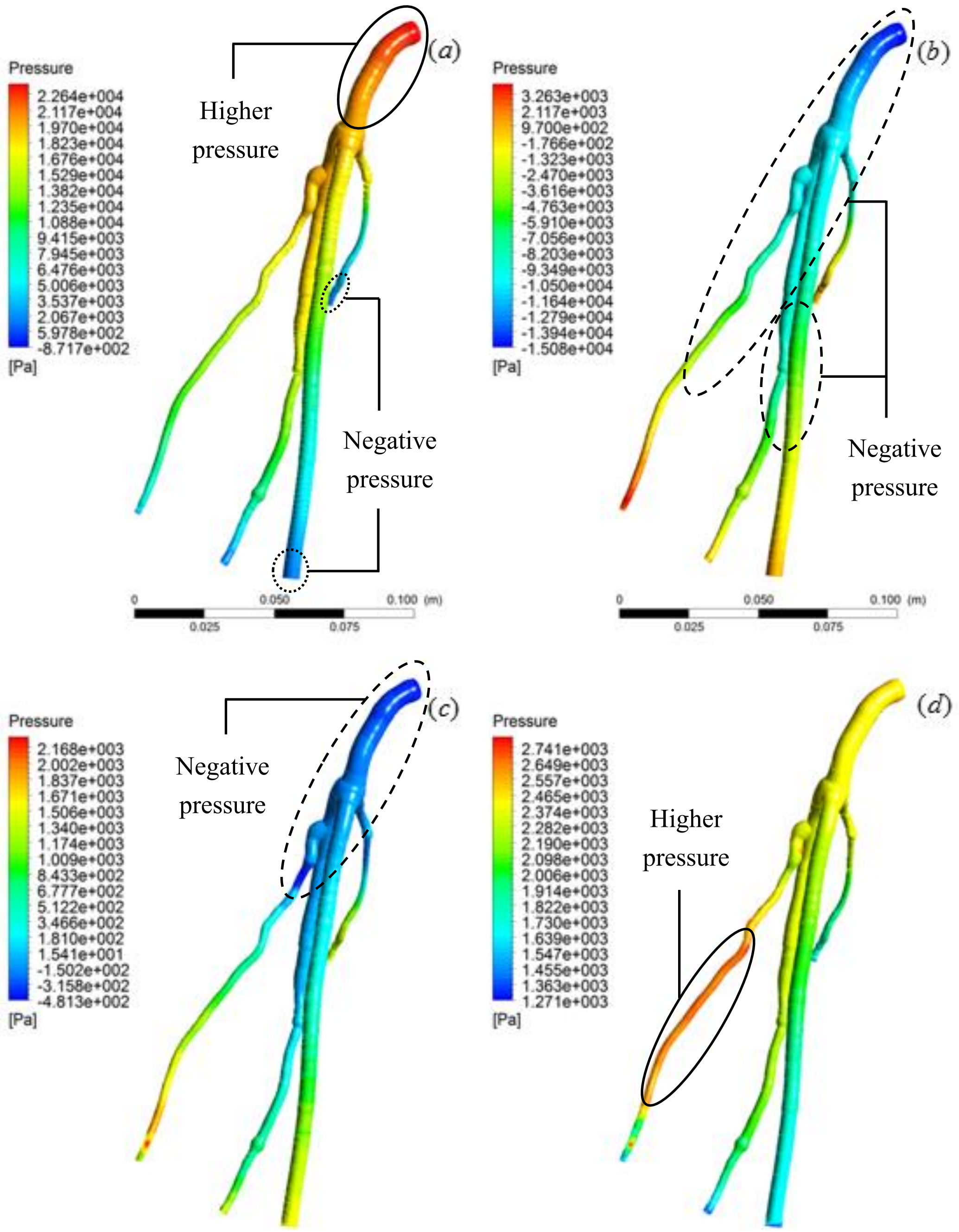

Figure 7.14 The wall pressure distribution contour of the 3D-CR coupling model in Case-1's SL. (a) t1; (b) t2; (c) t3; (d) t4.

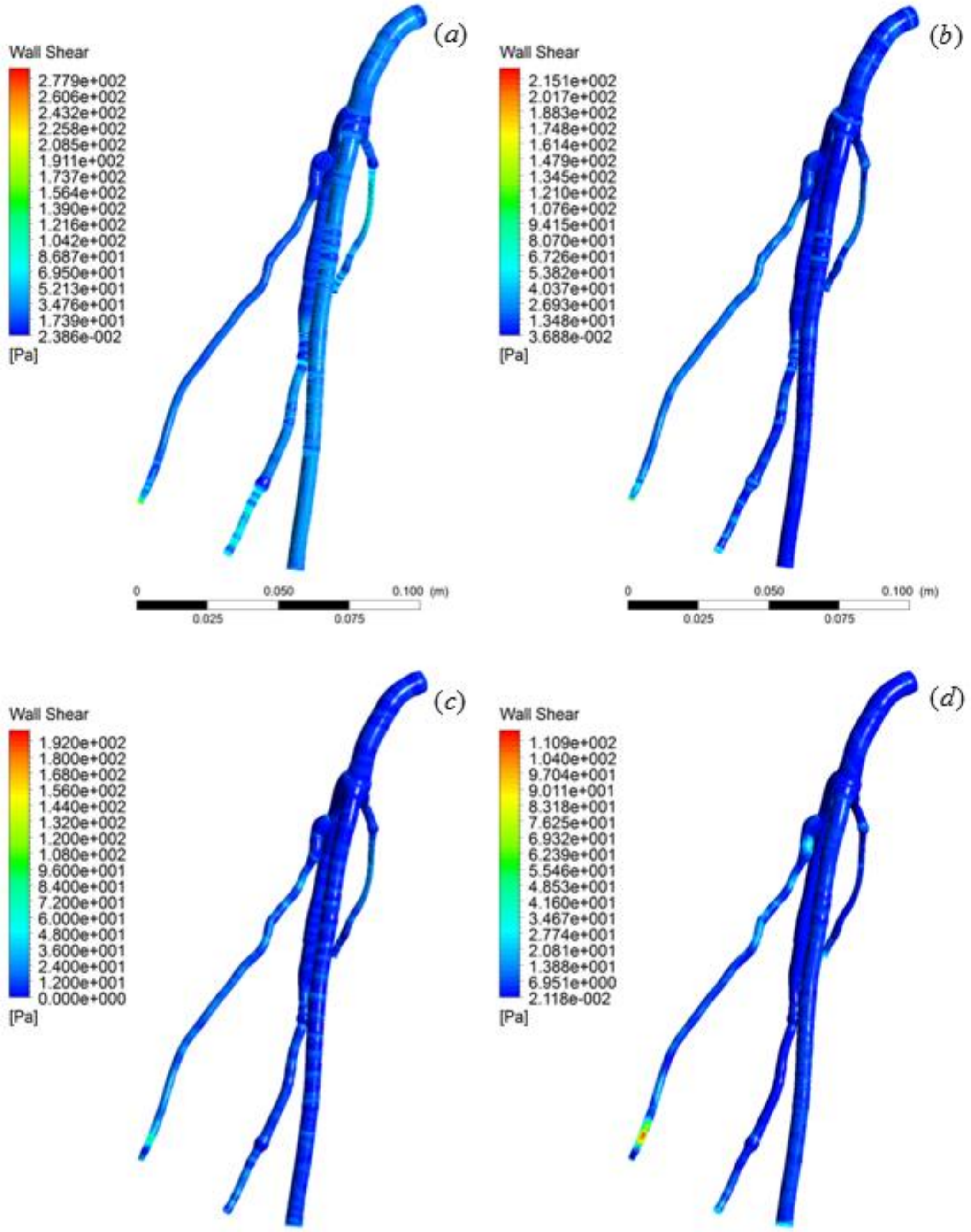

Figure 7.15 The wall shear stress distribution contour of the 3D-CR coupling model in Case-1's SL. (a) t1; (b) t2; (c) t3; (d) t4.

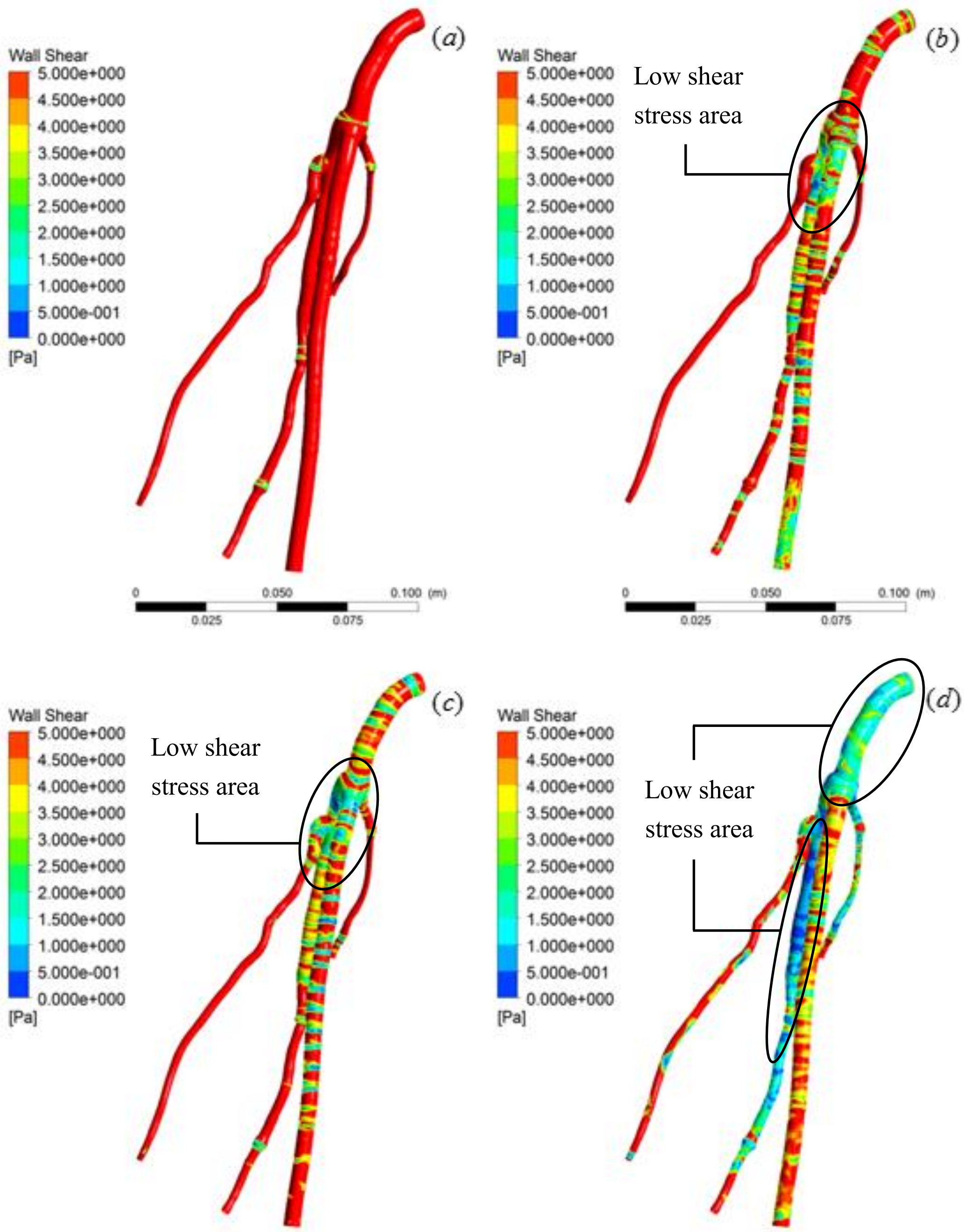

Figure 7.16 The low shear stress areas of the 3D-CR coupling model in Case-1's SL. (a) t1; (b) t2; (c) t3; (d) t4.

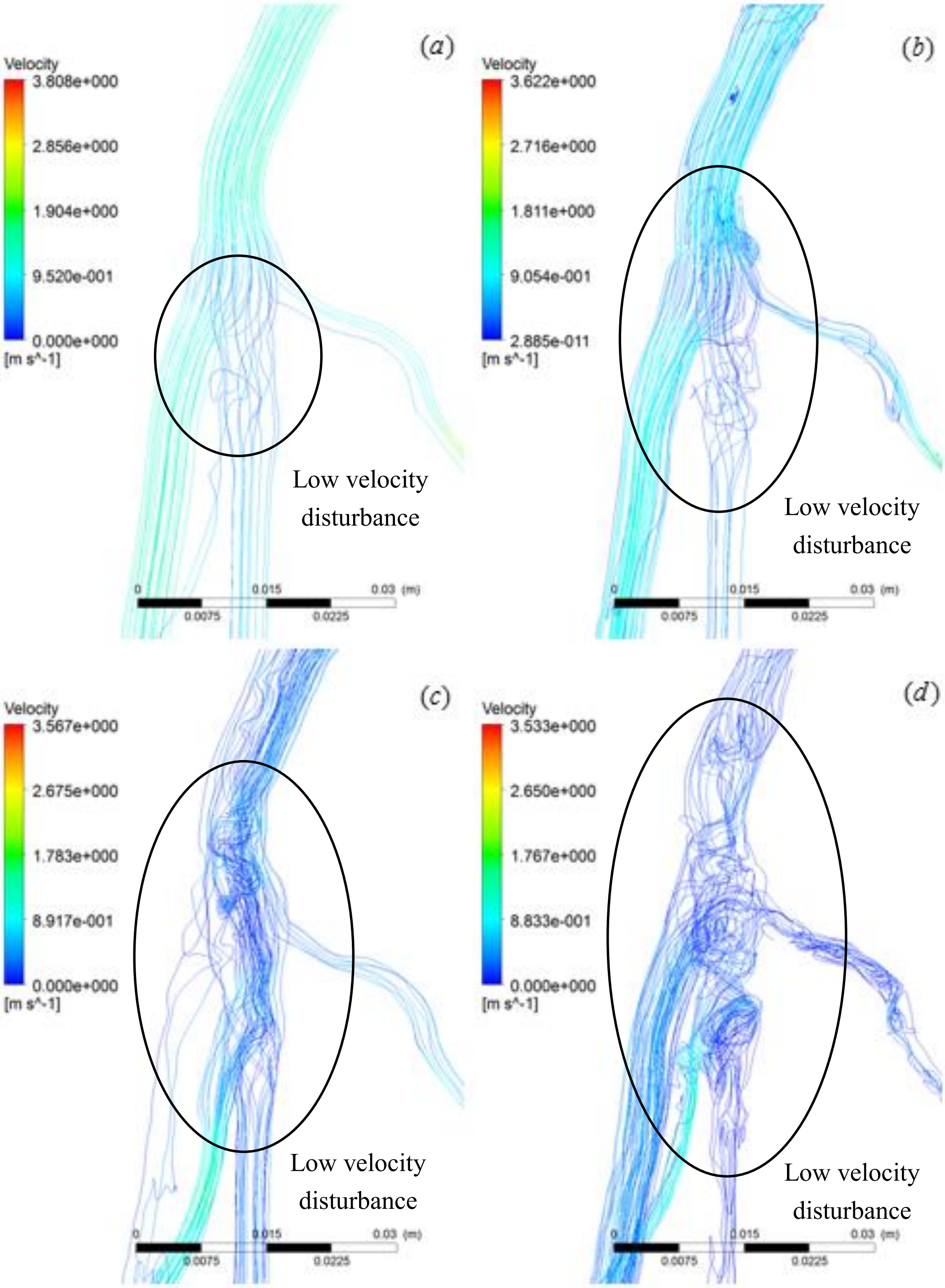

Figure 7.17 The flow velocity distribution streamline of the 3D-CR coupling model in Case-1's SL. (a) t1; (b) t2; (c) t3; (d) t4.

As can be seen in **Figure 7.14**, the WP ranges of the arterial tree in SL at four different moments were respectively -872.8Pa--23620.2Pa at t1, -15082.2Pa--4027.5Pa at t2, -481.3Pa--2278.4Pa at t3, 1271.1Pa--2802.3Pa at t4. The WP distributions were generally even at all moments with a gentle gradient along the flow direction. At t1, vessel walls bore the largest blood pressure; at t2, almost the entire arterial tree was in a negative pressure state; at t3, the WP was the minimum; at t4, the WP value returned to overall positive state. At t1 and t4, WP decreased along the direction of blood flow, whereas at t2 and t3, it increased from negative to positive value. Comparatively speaking, WP value in CFA (the inlet segment) was greater.

WSS distributions were shown in **Figure 7.15**, and there was little difference between the four moments. The value ranges were respectively 0.0239Pa--289.52Pa at t1, 0.0369Pa--224.11Pa at t2, 0.0734Pa--98.01Pa at t3, 0.0212Pa--115.52Pa at t4, however, the high shear stress areas were only in the outlets especially in LFCA. The average value of WSS at t1 was the largest, and all moments showed uniform distribution in each artery. Specific observation on the WSS value of 0-5Pa was shown in **Figure 7.16**. Except t1, the other three moments showed notable LSSAs much more than those in RL, especially in DFA at t4. These LSSAs randomly scattered in CFA, SFA, and DFA. At t4, the dangerous areas whose WSS lower than 0.4Pa (the dark blue part) appeared in the upper half of DFA.

Figure 7.17 illustrated the velocity streamlines in the bifurcation segment. The velocity ranges of entire arterial tree were respectively 0--3.62m/s at t1, 0--1.99 m/s at t2, 0--3.72 m/s at t3, 0--3.53 m/s at t4, which were more reasonable than those of RL. Similar to WSS, the high FV areas were very small and only in the four outlets. At t1, the isovelocity streamlines in bifurcation site were smooth-going and generally uniform. At t2, a small scope of low velocity disturbance appeared in DFA. At t3 and t4, streamlines exhibited local concentration, and a wide range of low velocity disturbance could be observed in CFA and DFA. The velocity vector on each arterial cross section was shown in **Figure 7.18** to **Figure 7.22**.

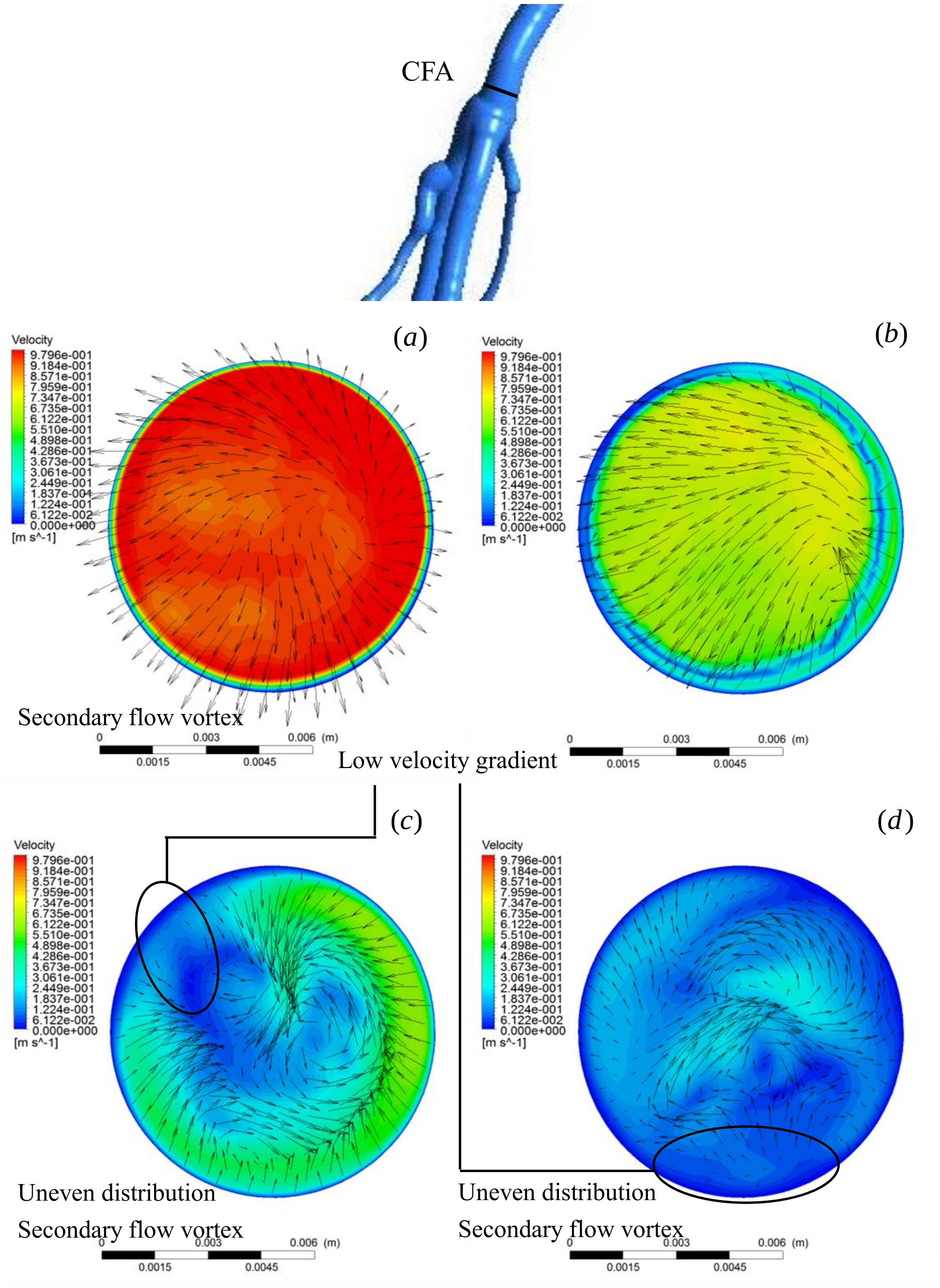

Figure 7.18 The velocity vector on CFA cross section of the 3D-CR coupling model in Case-1's SL. (a) t1; (b) t2; (c) t3; (d) t4.

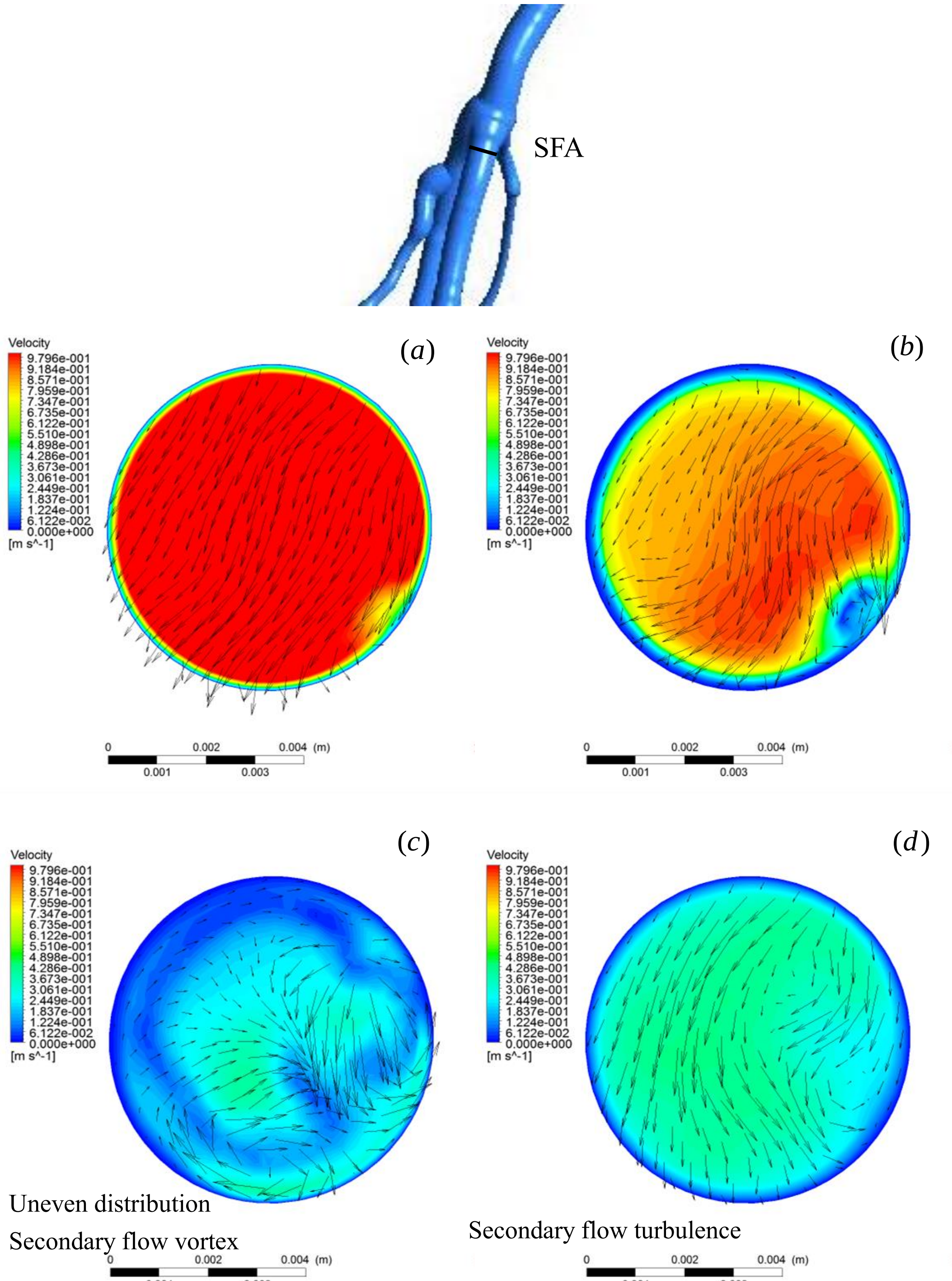

Figure 7.19 The velocity vector on SFA cross section of the 3D-CR coupling model in Case-1's SL. (a) t1; (b) t2; (c) t3; (d) t4.

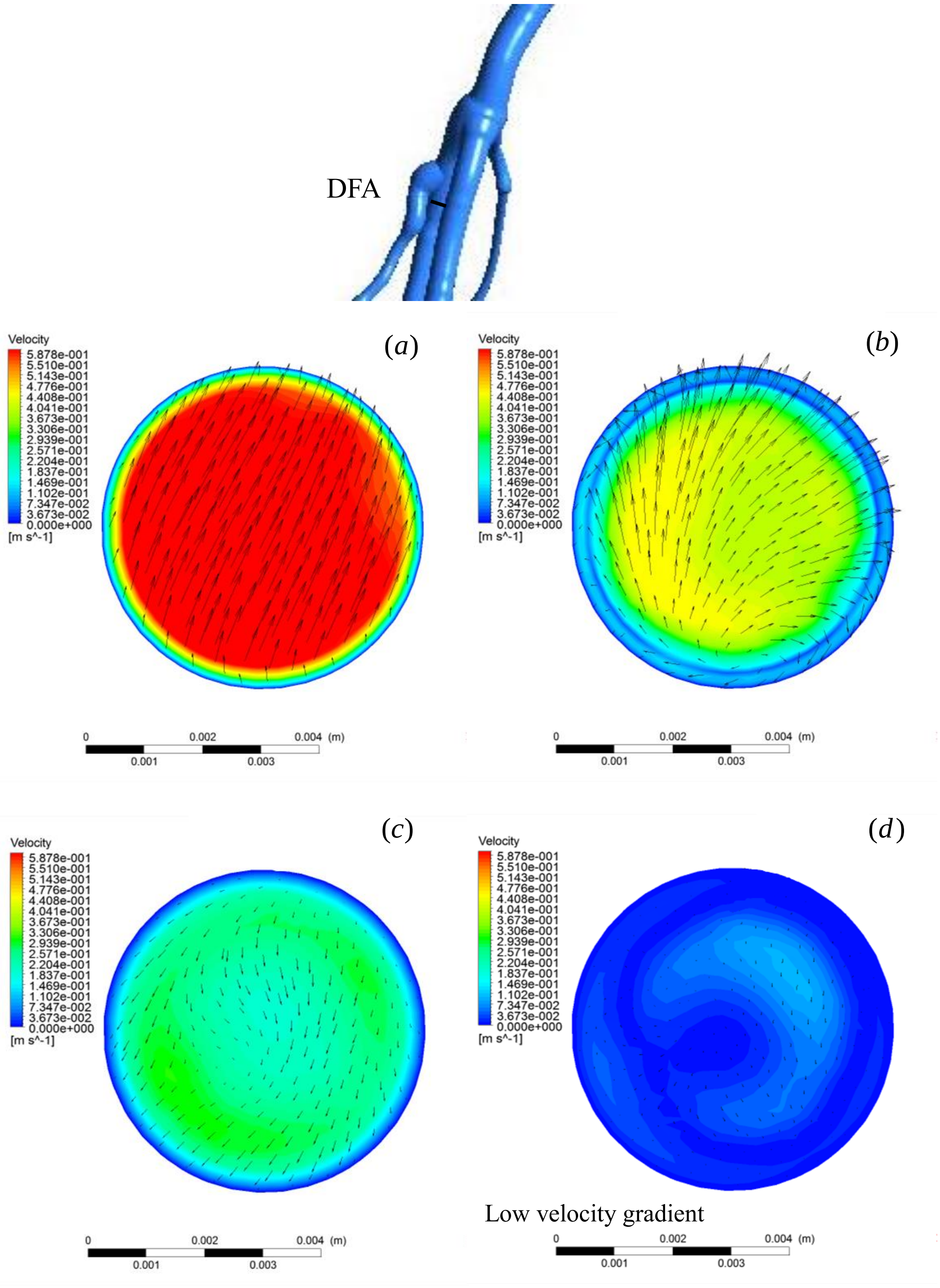

Figure 7.20 The velocity vector on DFA cross section of the 3D-CR coupling model in Case-1's SL. (a) t1; (b) t2; (c) t3; (d) t4.

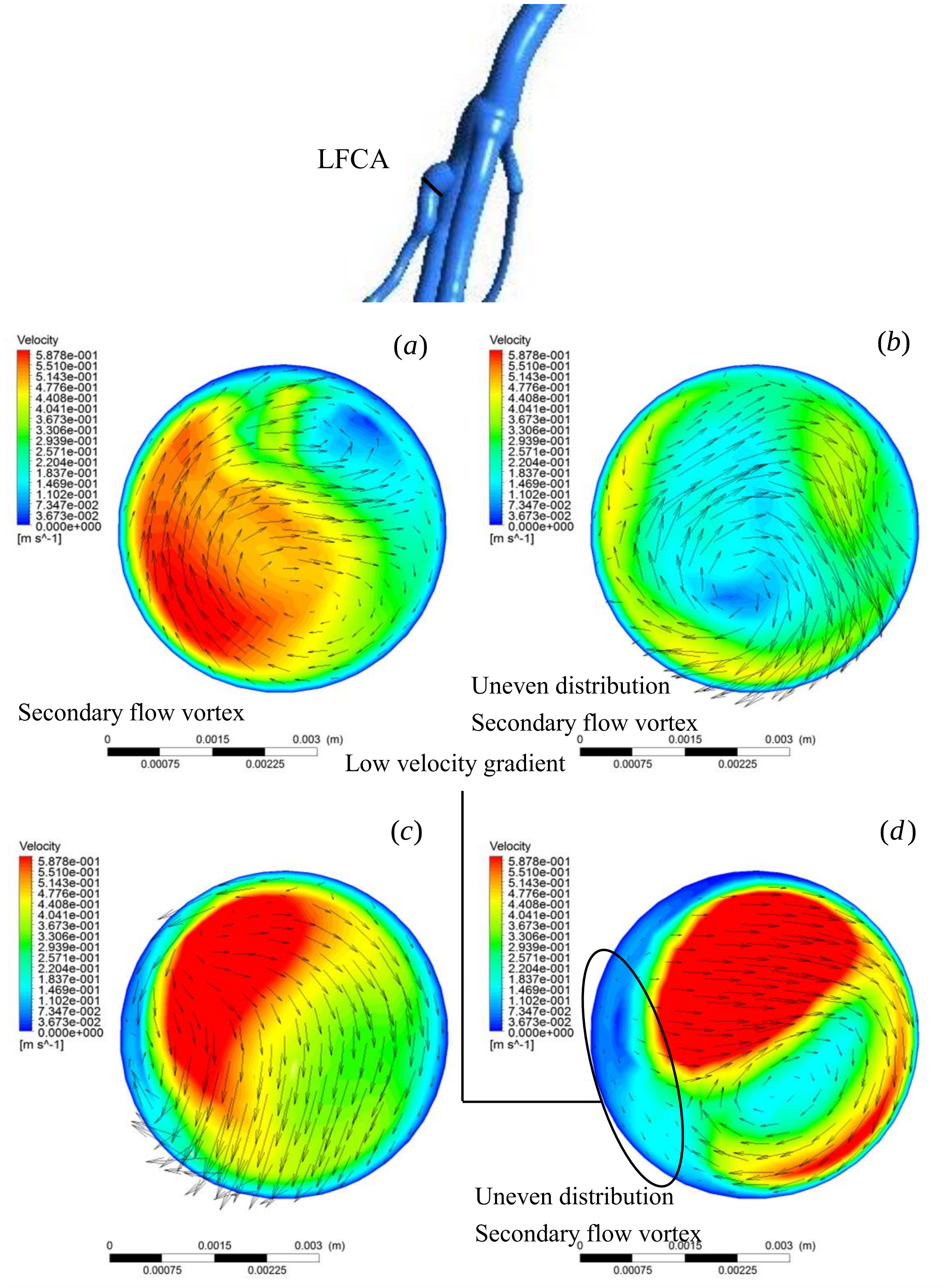

Figure 7.21 The velocity vector on LFCA cross section of the 3D-CR coupling model in Case-1's SL. (a) t1; (b) t2; (c) t3; (d) t4.

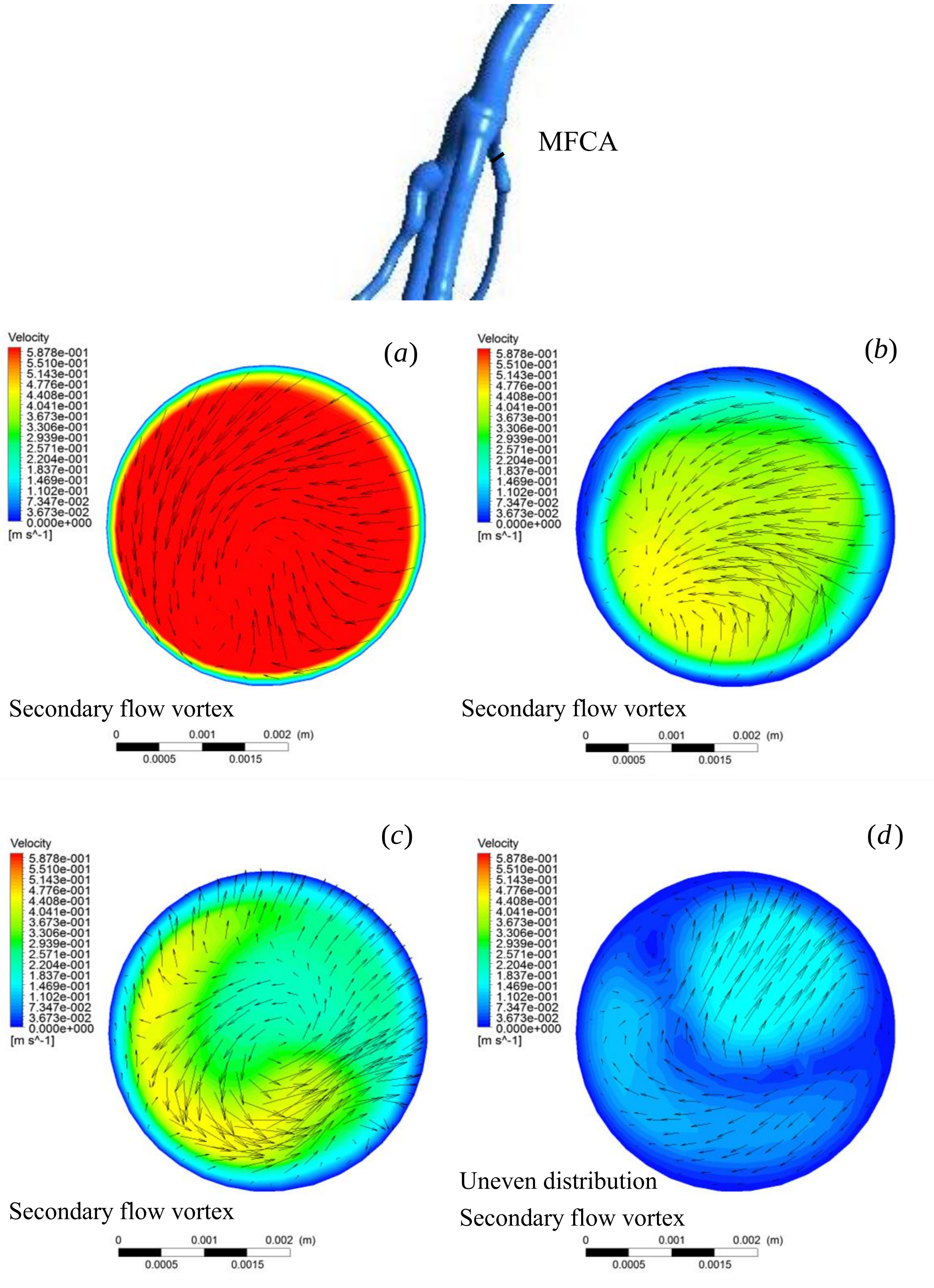

Figure 7.22 The velocity vector on MFCA cross section of the 3D-CR coupling model in Case-1's SL. (a) t1; (b) t2; (c) t3; (d) t4.

Figure 7.18 showed the velocity vector on CFA cross section. It could be seen that the FV distribution of the entrance segment was more uniform than that in RL. At t1 and t2, except the peripheral low velocity zone (the dark blue part near wall), the lumen had similar and larger FV values (the red or yellow part), and the velocity gradient was roughly the same on whole cross section. While at t3 and t4, FV value reduced with becoming uneven velocity distribution and gradient. There were secondary flow vortices at t1, t3 and t4, and the latter two showed more complex directions. As shown in **Figure 7.19**, the FV distribution in SFA was almost the same with that in CFA, but had more uniform velocity gradient and more consistent secondary flow direction. There were two small vortices at t3, and a slight turbulence at t2 and t4. The FV distribution on DFA cross section was shown in **Figure 7.20**. At each moment, the lumen velocity had little value difference with uniform distribution, and quickly transited to low velocity zone in periphery near wall. FV value at t4 was significantly smaller than that of the other three moments. All four moments displayed basically even velocity gradient and consistent secondary flow direction. At t3 and t4, there were even almost no secondary flow phenomenon. The results of LFCA and MFCA were shown in **Figure 7.21** and **Figure 7.22**. LFCA displayed clear but uneven distribution of high velocity zone (the red part) at four moments, and the average values at t3 and t4 were greater than those at t1 and t2. The high/low FV transitions from center to periphery were gently at t1, t2, and t3. At t4, the peripheral velocity gradient decreased. There were wide range of secondary flow vortices at t1 and t2. The FV distribution on MFCA cross section was almost the same with that on DFA. But MFCA showed more disordered secondary flow directions. A wide range of vortex could be observed at all four moments.

7.2.2 3D-WK coupling model

- ***Residual limb***

The wall pressure (WP), wall shear stress (WSS), low shear stress area (LSSA) and the flow velocity (FV) in bifurcation segment of the 3D-WK coupling model in Case-1's RL at the four moments t1, t2, t3, and t4 were successively shown in **Figure 7.23**, **Figure 7.24**, **Figure 7.25** and **Figure 7.26**.

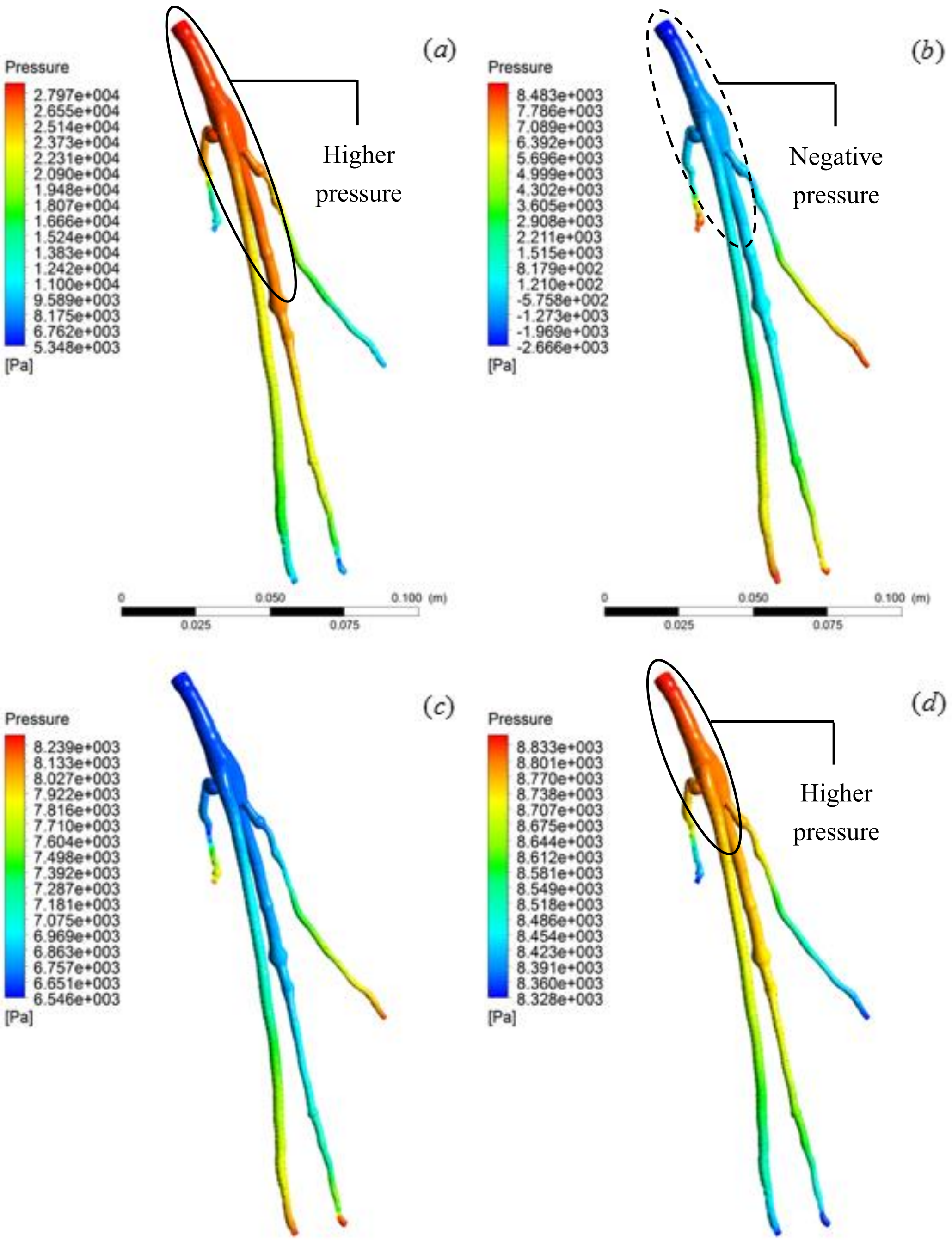

Figure 7.23 The wall pressure distribution contour of the 3D-WK coupling model in Case-1's RL. (a) t1; (b) t2; (c) t3; (d) t4.

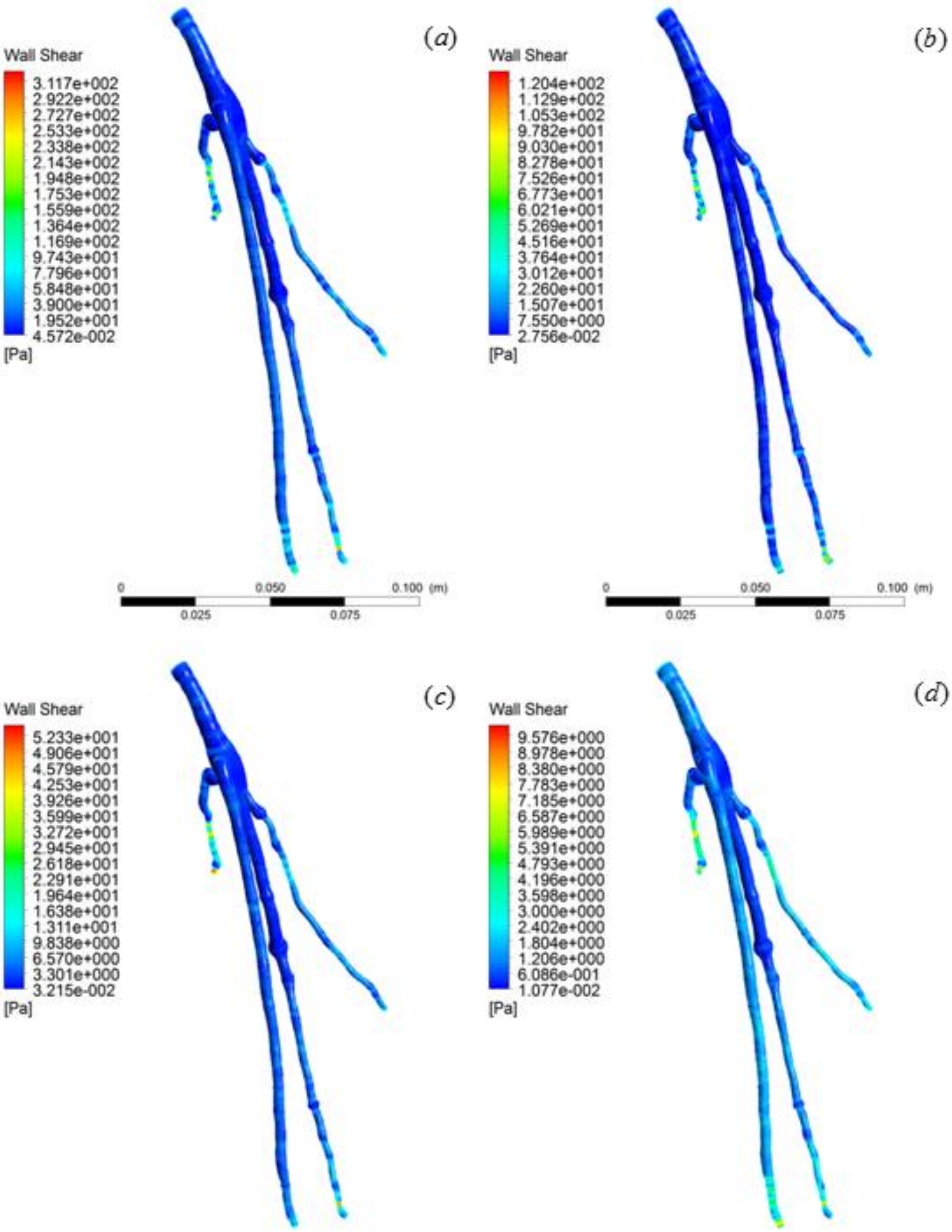

Figure 7.24 The wall shear stress distribution contour of the 3D-WK coupling model in Case-1's RL. (a) t1; (b) t2; (c) t3; (d) t4.

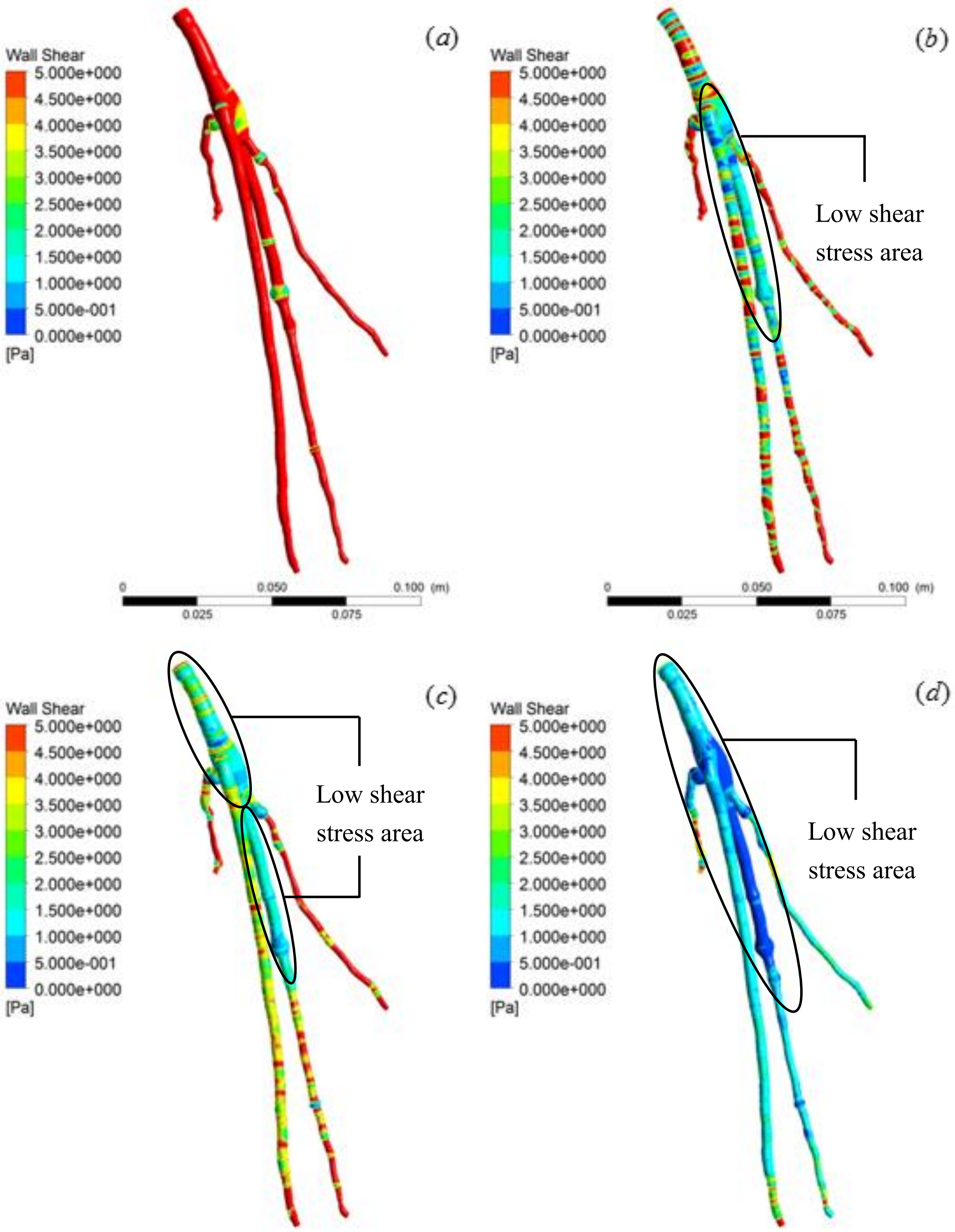

Figure 7.25 The low shear stress areas of the 3D-WK coupling model in Case-1's RL. (a) t1; (b) t2; (c) t3; (d) t4.

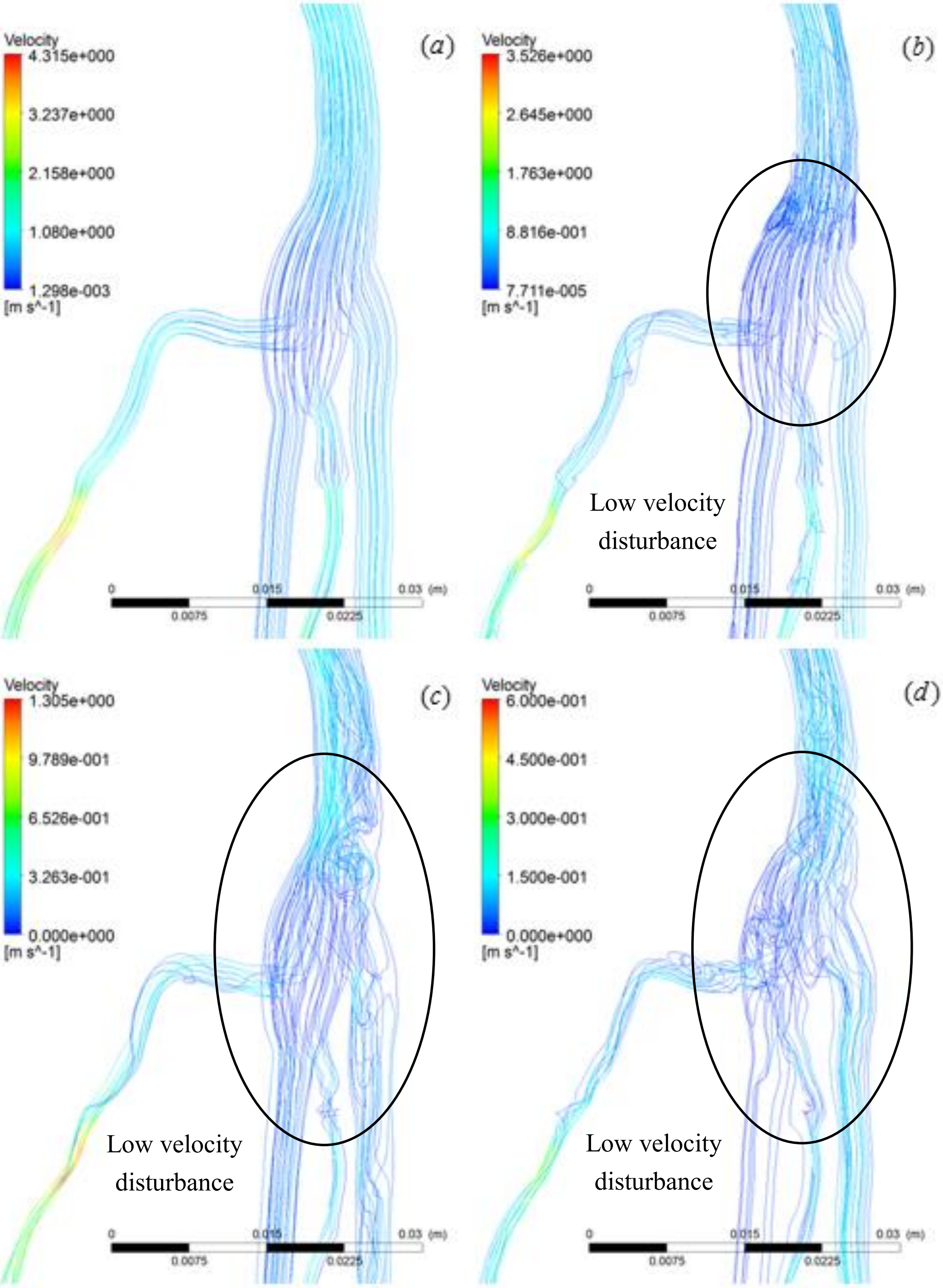

Figure 7.26 The flow velocity distribution streamline of the 3D-WK coupling model in Case-1's RL. (a) t1; (b) t2; (c) t3; (d) t4.

As can be seen in **Figure 7.23**, the WP ranges in RL calculated by the 3D-WK coupling model at the four moments were respectively 5347.9Pa--28908.7Pa at t1, -2666.3Pa--8947.5Pa at t2, 6545.6Pa--8309.7Pa at t3, 8328.3Pa--8853.9Pa at t4. According to clinical experience and data,these values were much more reasonable than the results of the 3D-CR model, and the WP distribution and gradient of each artery along the pipeline were approximately uniform at all moments. At t1, vessel walls bore the largest blood pressure; at t2, the upper half of whole arterial tree was in a negative pressure state and the lower half gradually changed to positive pressure; at t3, the WP was the minimum; at t4, the WP value had a small rebound. At t1 and t4, WP decreased along the direction of blood flow, whereas at t2 and t3, it increased from negative to positive value. Comparatively speaking, unlike the 3D-CR model, the 3D-WK model exhibited a WP result with relatively even distribution and smooth gradient, and having no obvious difference between each artery.

The results of WSS were shown in **Figure 7.24**. At different moments, there were notable differences of values and distributions. The value ranges were respectively 0.0457Pa--324.68Pa at t1, 0.0276Pa--125.41Pa at t2, 0.0321Pa--54.51Pa at t3, 0.0108Pa--9.97Pa at t4, and they were quite different from those produced by the 3D-CR model. The high shear stress areas were still very small, and near the four outlets WSS increased with the reduction of lumen diameter. Similar to the 3D-CR model, the value in LFCA was larger than that in other arteries. Specific observation on the WSS value of 0-5Pa was shown in **Figure 7.25**. At t1, it already showed some small ranges of lower than 2Pa. While the other three moments displayed remarkable wide ranges of LSSAs mainly in CFA, the bifurcation site, and the upper half of DFA. At t4, the high-risk areas whose WSS value lower than 0.4Pa (the dark blue part) appeared in the latter two sections. In contrast, the WSS values of LFCA and MFCA were greater all the time, which was similar to the results of the 3D-CR model.

Figure 7.26 illustrated the velocity streamlines in the bifurcation segment. The velocity ranges of entire arterial tree were respectively 0--4.36m/s at t1, 0--3.43 m/s at t2, 0--1.34 m/s at t3, 0--0.39 m/s at t4. Similar to WSS, the high FV areas were negligible in the four outlets. But in some segments with small diameter, the higher speed could be observed, indicating that the variation of FV distribution with vessel diameter made it uneven. Different from the 3D-CR model, at t1, the isovelocity streamlines in bifurcation site were smooth-going and generally uniform. At t3 and t4, a small extent of low velocity disturbance could be observed. The velocity vector on each arterial cross section was shown in **Figure 7.27** to **Figure 7.31**.

Figure 7.27 showed the velocity vector on CFA cross section. It could be seen that the FV distribution of the entrance segment was much more uniform than that of the 3D-CR model. At t1 and t2, high velocity zone (the red or yellow part) was larger and concentrated, and both velocity gradient and secondary flow direction were basically consistent on whole cross section. While at t3 and t4, FV value reduced with becoming uneven distribution and velocity gradient. Meanwhile, there were disordered multi-direction vortices. As shown in **Figure 7.28**, the average FV value in SFA was higher. At t1 and t2, the distributions were similar to those in CFA, yet the peripheral low velocity areas (the dark blue part) near wall enlarged. At t3 and t4, nonuniform low velocity distribution and the low gradient in periphery appeared. And there was respectively a turbulence and a vortex could be observed at t3 and t4. The FV distribution on DFA cross section was shown in **Figure 7.29**. Except the entire velocity lower than that of SFA, the rest situations were almost the same with those in SFA at four moments. At t3 and t4, secondary flow directions exhibited relatively slight disorder. The cross section contours of SFA and DFA illustrated the apparent difference of calculation results between the 3D-CR model and the 3D-WK model. The results of LFCA and MFCA were shown in **Figure 7.30** and **Figure 7.31**. Both of them had similar FV distribution and the change process from t1 to t4 with the other arteries. MFCA displayed more disordered secondary flow directions, as well as vortices and turbulences at all four moments.

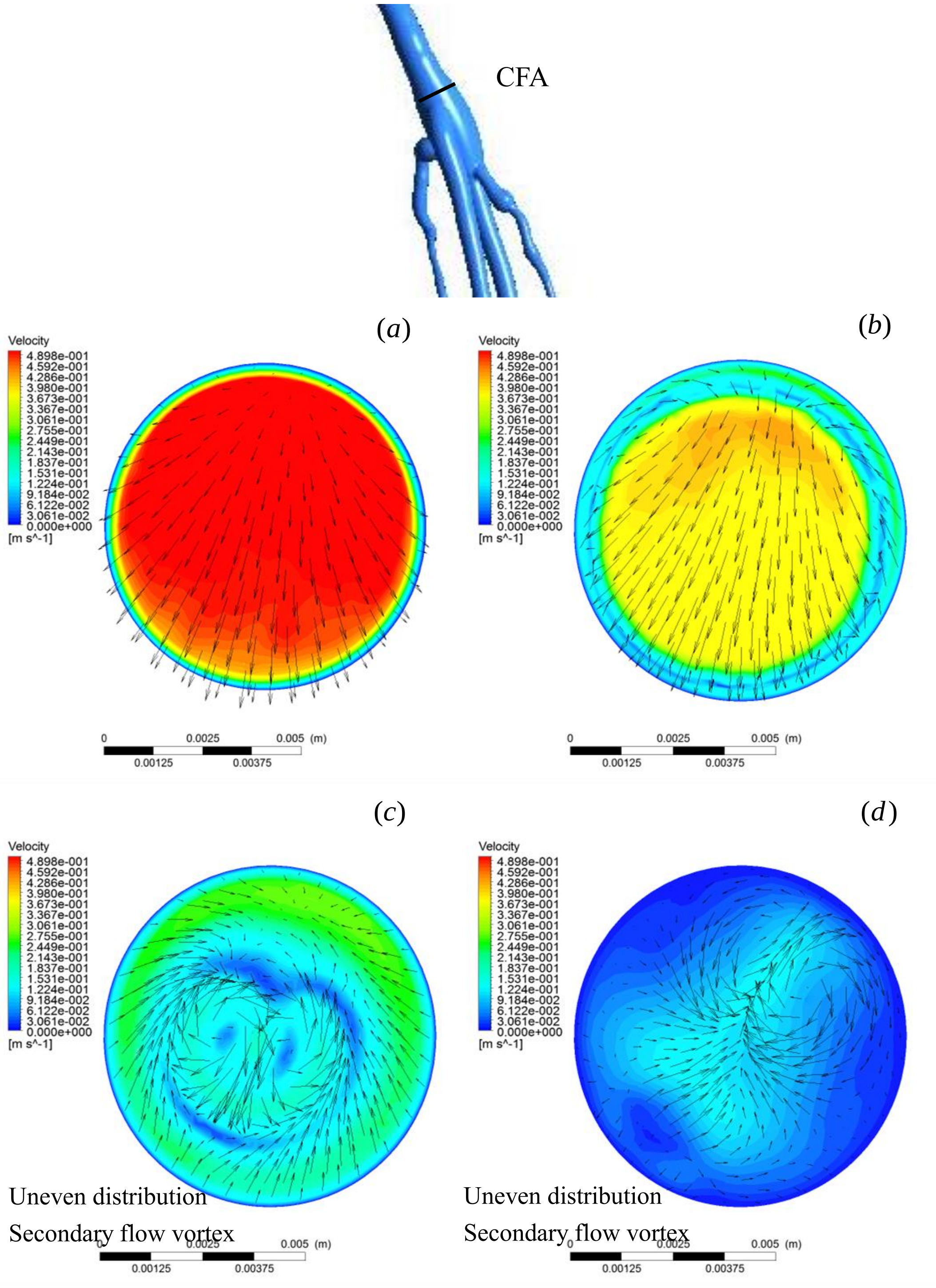

Figure 7.27 The velocity vector on CFA cross section of the 3D-WK coupling model in Case-1's RL. (a) t1; (b) t2; (c) t3; (d) t4.

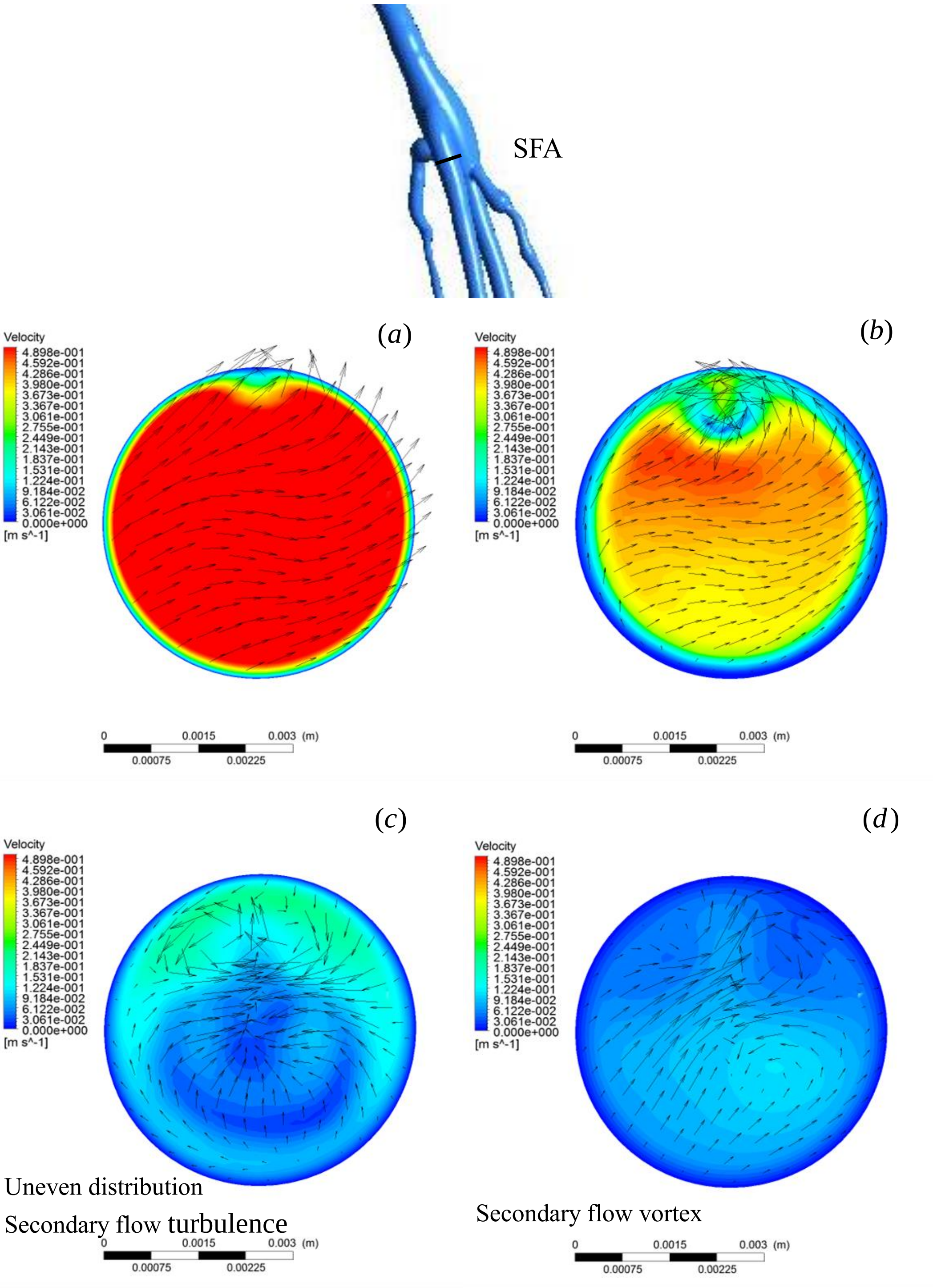

Figure 7.28 The velocity vector on SFA cross section of the 3D-WK coupling model in Case-1's RL. (a) t1; (b) t2; (c) t3; (d) t4.

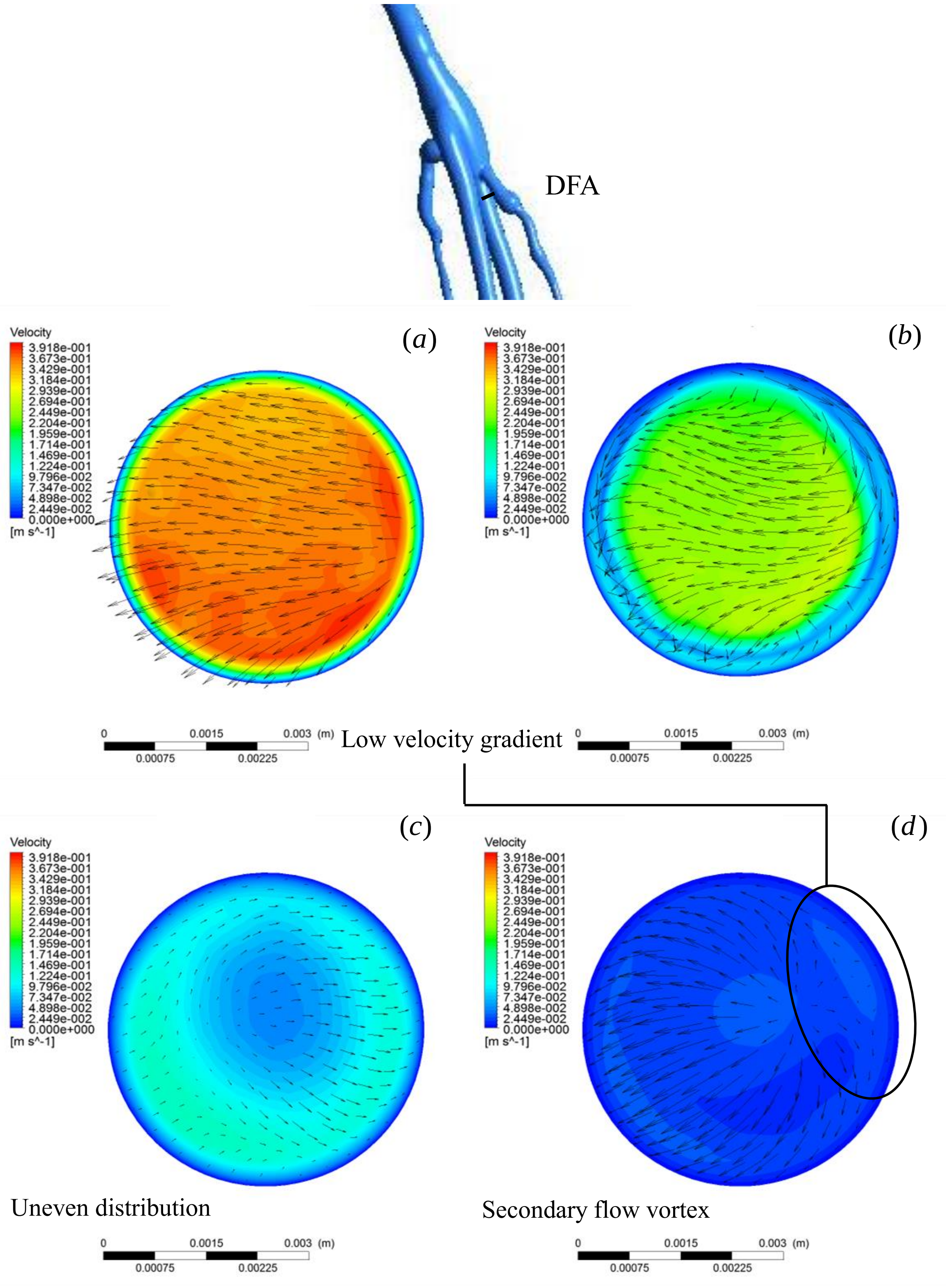

Figure 7.29 The velocity vector on DFA cross section of the 3D-WK coupling model in Case-1's RL. (a) t1; (b) t2; (c) t3; (d) t4.

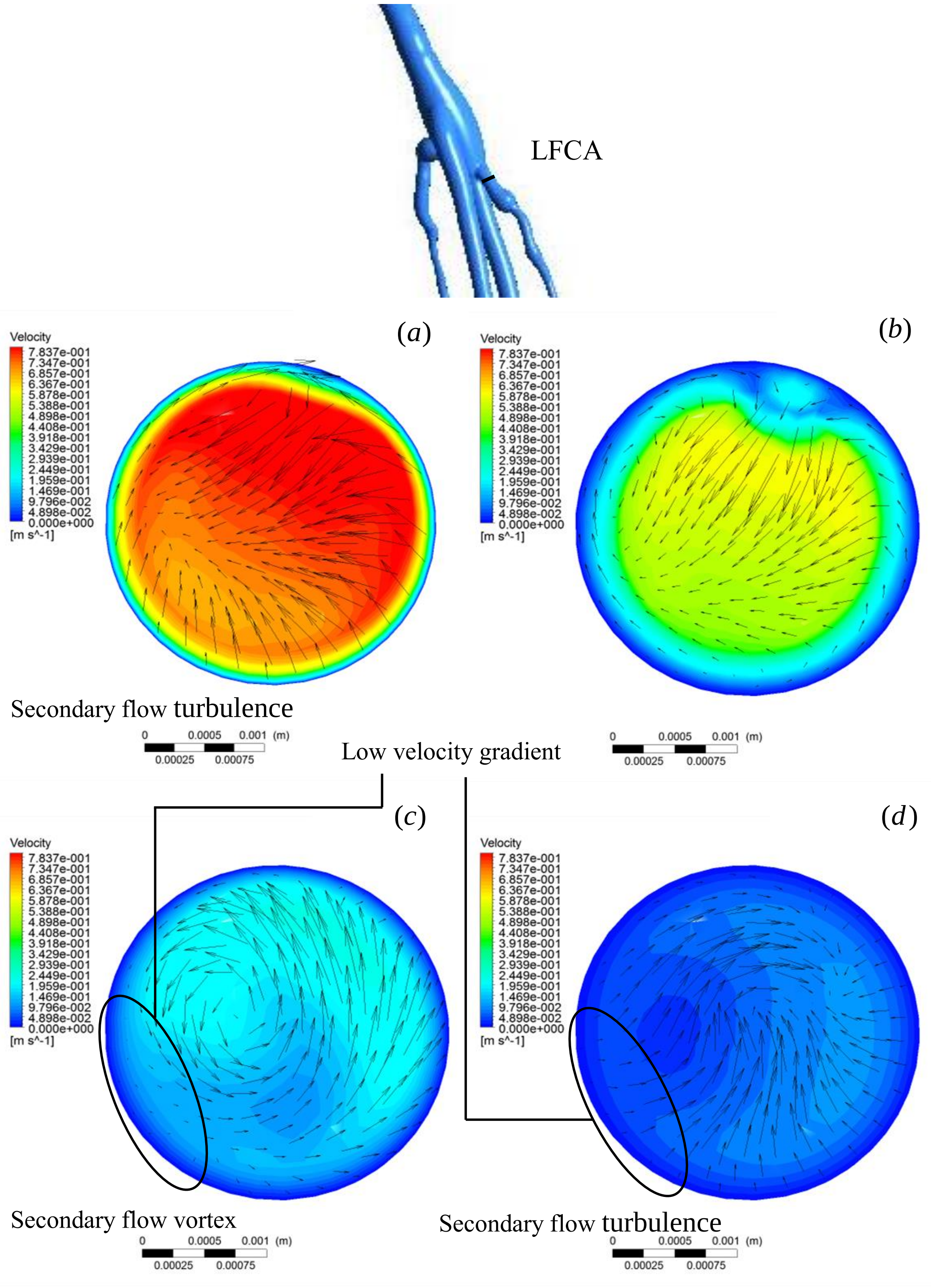

Figure 7.30 The velocity vector on LFCA cross section of the 3D-WK coupling model in Case-1's RL. (a) t1; (b) t2; (c) t3; (d) t4.

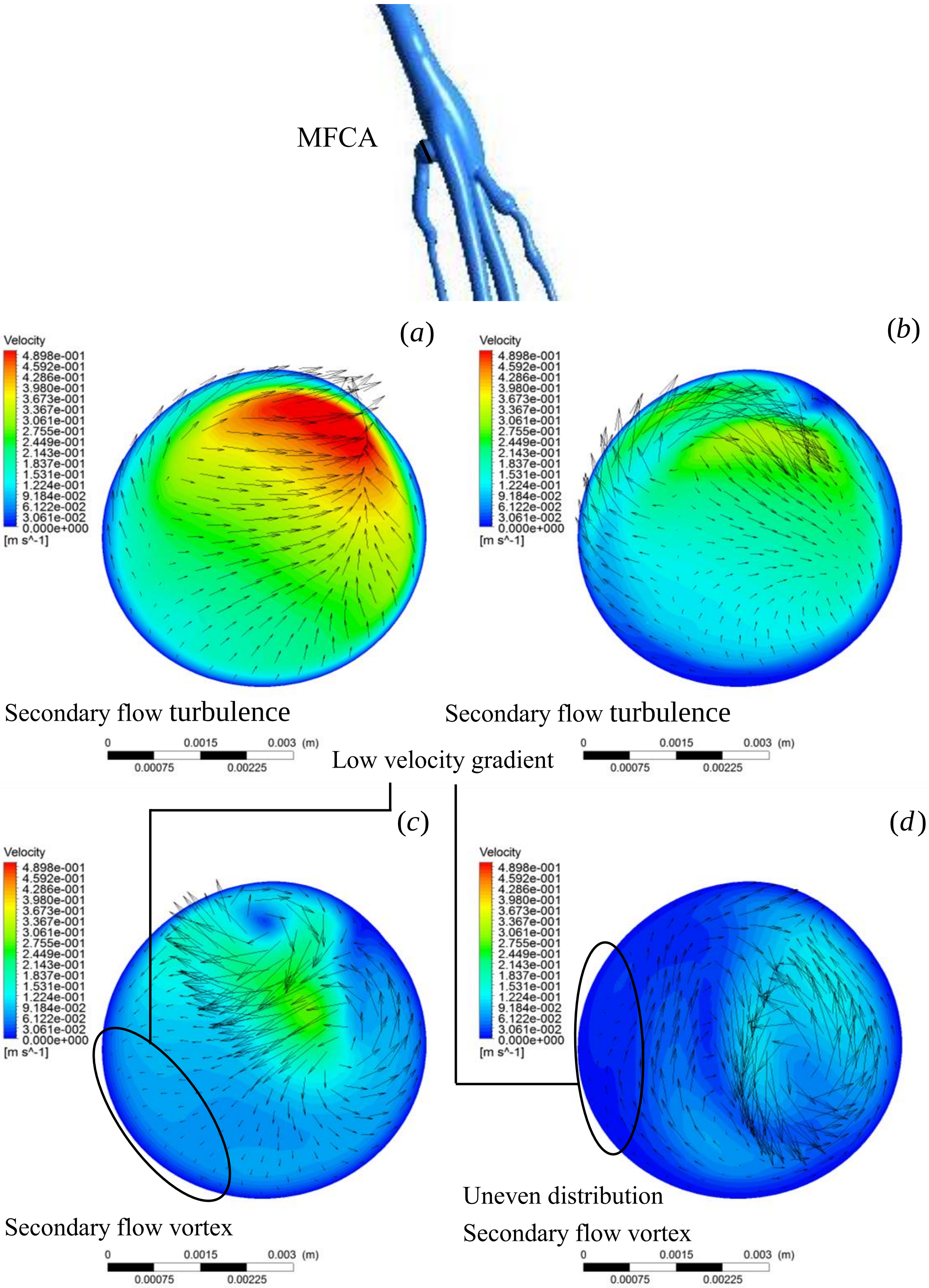

Figure 7.31 The velocity vector on MFCA cross section of the 3D-WK coupling model in Case-1's RL. (a) t1; (b) t2; (c) t3; (d) t4.

- ***Sound limb***

The wall pressure (WP), wall shear stress (WSS), low shear stress area (LSSA) and the flow velocity (FV) in bifurcation segment of the 3D-WK coupling model in Case-1's SL at the four moments t1, t2, t3, and t4 were successively shown in **Figure 7.32**, **Figure 7.33**, **Figure 7.34** and **Figure 7.35**.

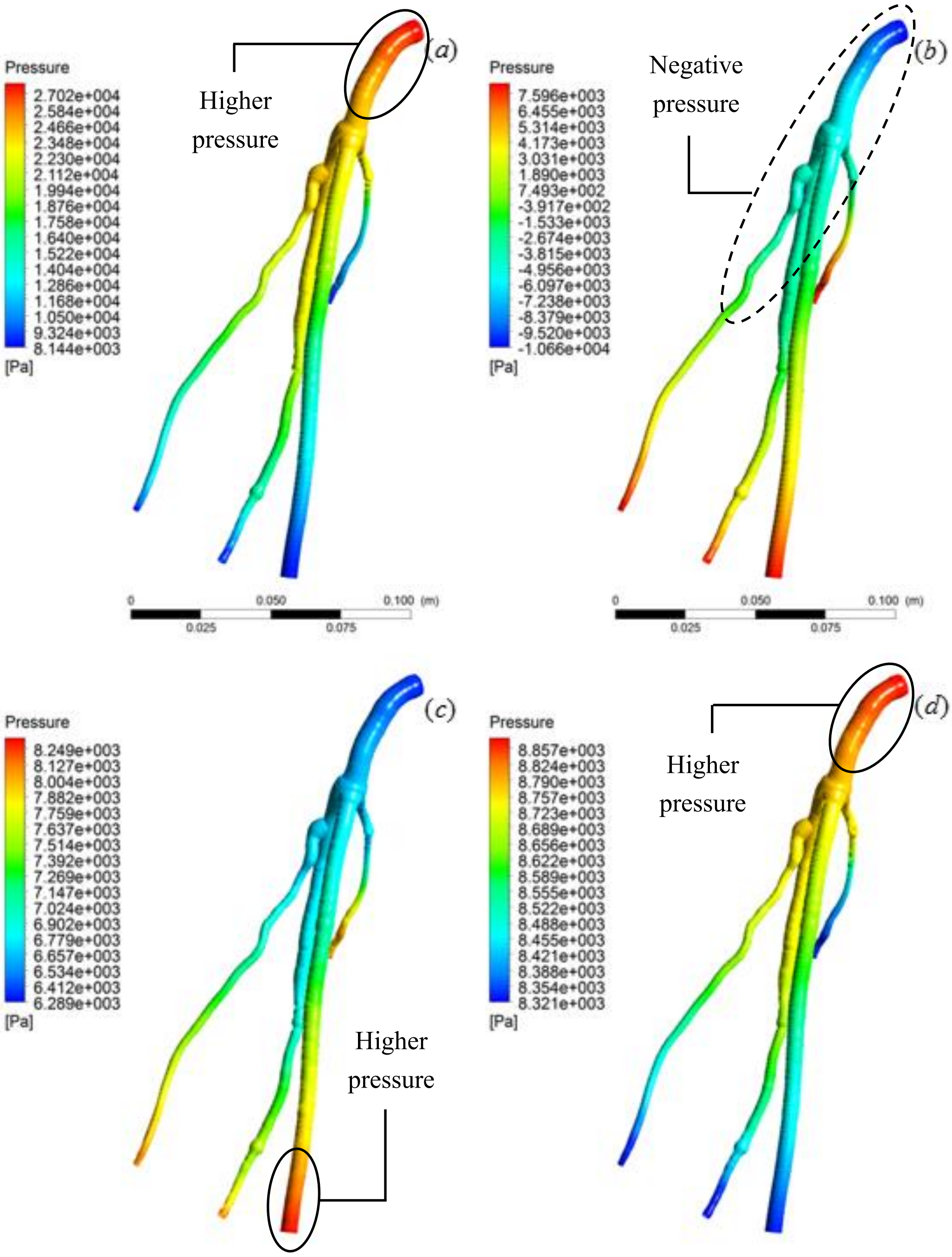

Figure 7.32 The wall pressure distribution contour of the 3D-WK coupling model in Case-1's SL. (a) t1; (b) t2; (c) t3; (d) t4.

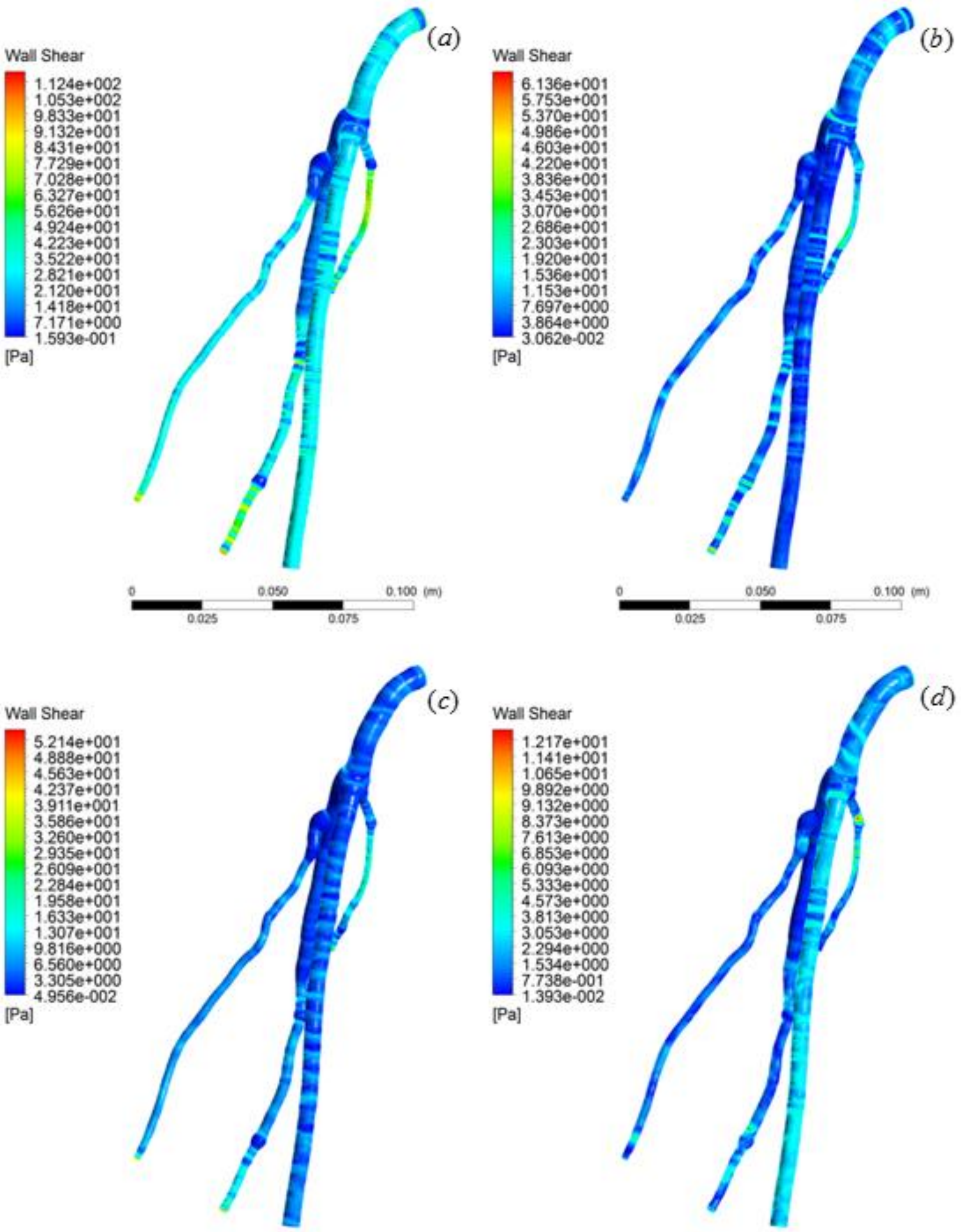

Figure 7.33 The wall shear stress distribution contour of the 3D-WK coupling model in Case-1's SL. (a) t1; (b) t2; (c) t3; (d) t4.

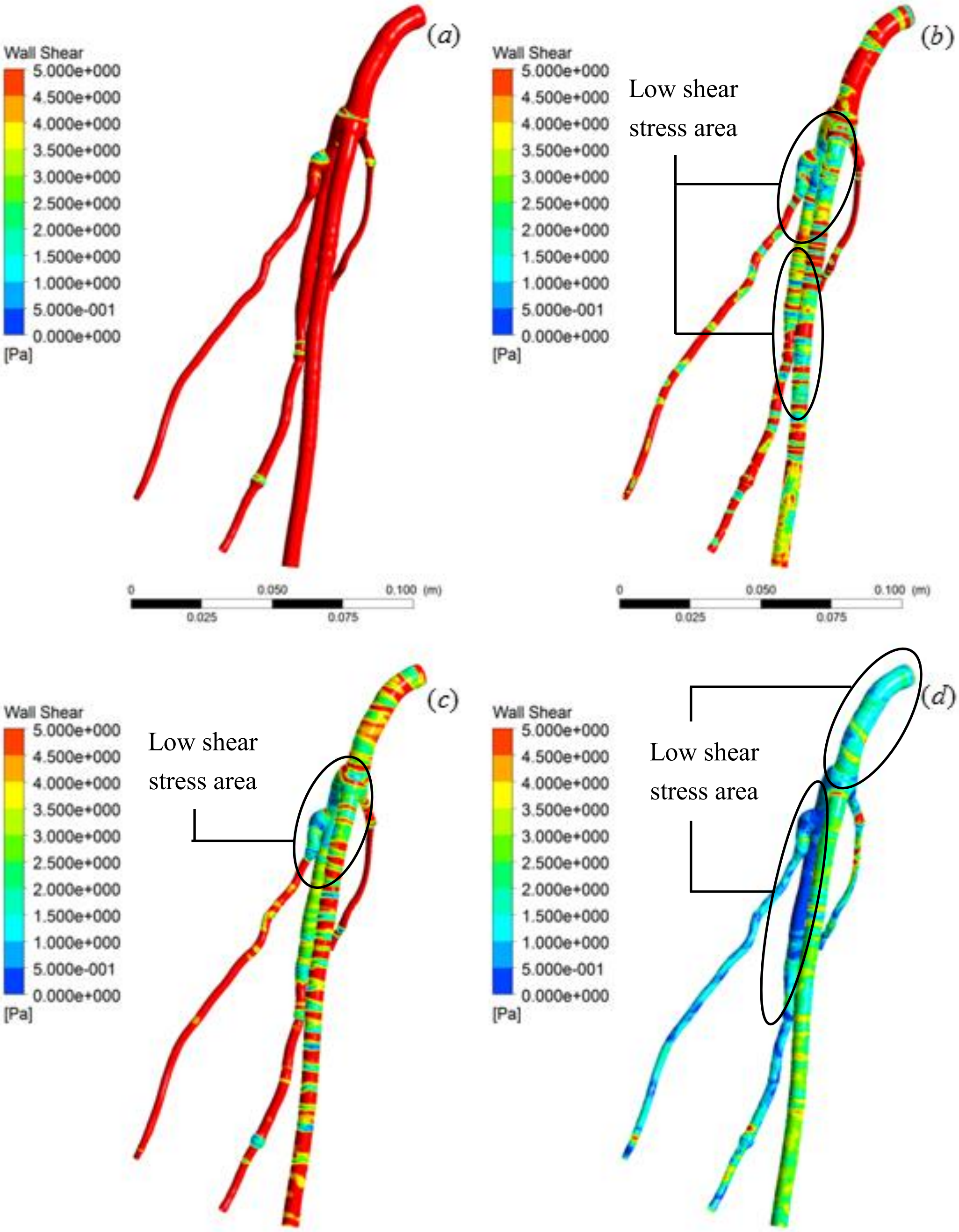

Figure 7.34 The low shear stress areas of the 3D-WK coupling model in Case-1's SL. (a) t1; (b) t2; (c) t3; (d) t4.

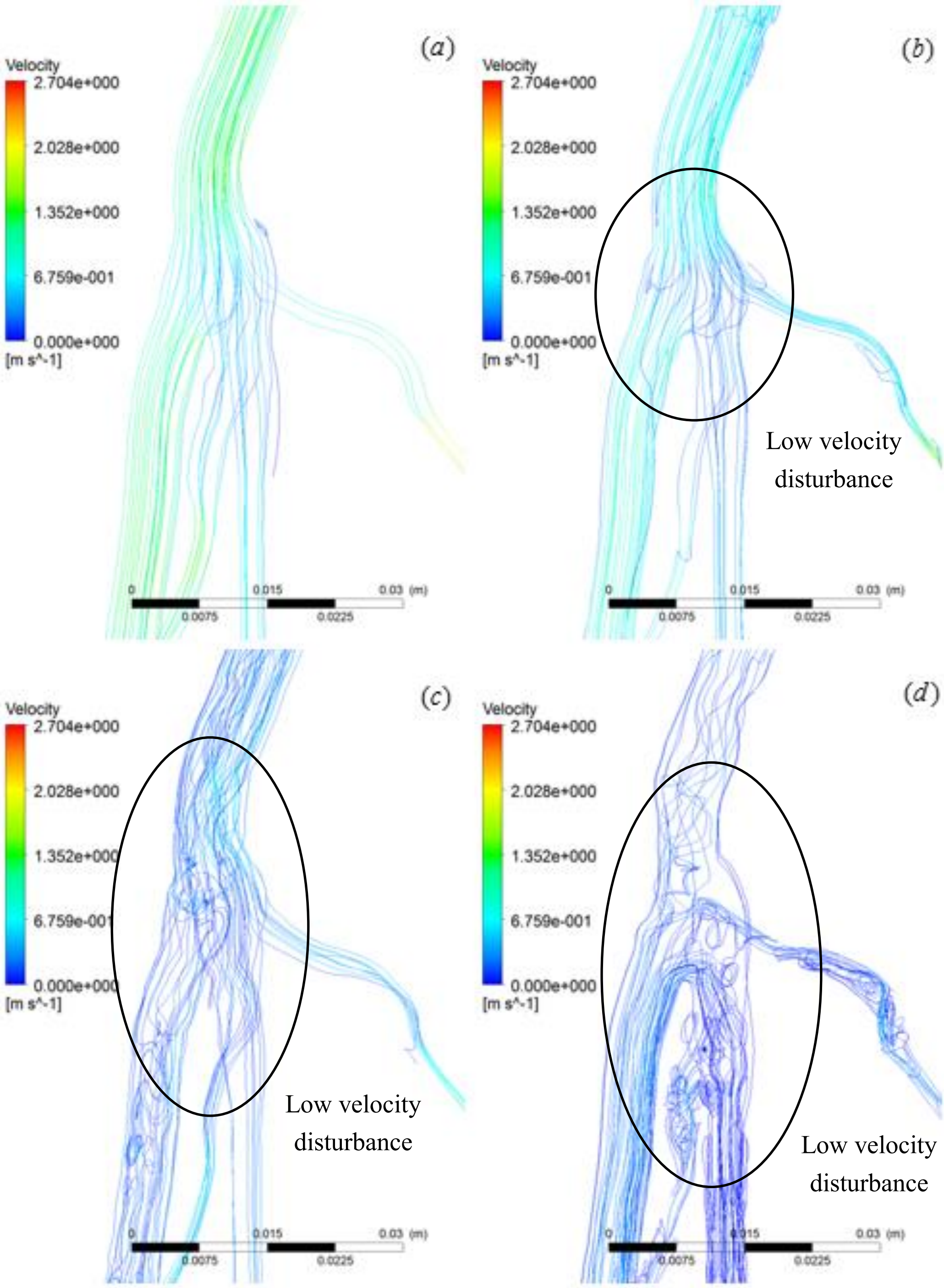

Figure 7.35 The flow velocity distribution streamline of the 3D-WK coupling model in Case-1's SL. (a) t1; (b) t2; (c) t3; (d) t4.

As can be seen in **Figure 7.32**, the WP ranges of the arterial tree in SL at four different moments were respectively 8143.6Pa--27811.1Pa at t1, -10661.4Pa--8356.5Pa at t2, 6289.4Pa--8330.9Pa at t3, 8321.0Pa--8879.3Pa at t4. The WP distributions were generally even at all moments with a gentle gradient along the flow direction. At four different moments, the overall situation was different from the SL result of 3D-CR model, but similar to the RL result of 3D-WK model. At t1, vessel walls bore the largest blood pressure; at t2, the upper half of whole arterial tree was in a negative pressure state and the lower half gradually changed to positive pressure; at t3, the WP value was the minimum; at t4, the value had a small rebound. At t1 and t4, WP decreased along the direction of blood flow, whereas from t2 to t3, it increased from negative to positive value.

WSS distributions were shown in **Figure 7.33**, and the differences between the four moments could be visually observed. The value ranges were respectively 0.1593Pa--117.02Pa at t1, 0.0306Pa--63.92Pa at t2, 0.0496Pa--54.31Pa at t3, 0.0131Pa--12.68Pa at t4, smaller than those of 3D-CR model. Specific observation on the WSS value of 0-5Pa was shown in **Figure 7.34**. The distribution of LSSAs at each moment was similar to the 3D-CR model. Except t1, the other three moments displayed remarkable wide ranges of LSSAs mainly in CFA, the bifurcation site, and the upper half of DFA. At t4, the high-risk areas <0.4Pa (the dark blue part) could be observed in the latter two sections. Comparison of the RL and SL results output from 3D-WK models illustrated that, the LSSAs in SL were smaller than those in RL, while the average values of those LSSAs were slightly larger in SL.

Figure 7.35 illustrated the velocity streamlines in the bifurcation segment. The velocity ranges of entire arterial tree were respectively 0--2.70m/s at t1, 0--1.69 m/s at t2, 0--1.29 m/s at t3, 0--0.57 m/s at t4, which were little smaller than those of RL and similar to the results of 3D-CR model. At t3 and t4, streamlines exhibited local concentration and the low velocity disturbances with relatively small amplitude. The velocity vector on each arterial cross section was shown in **Figure 7.36** to **Figure 7.40**.

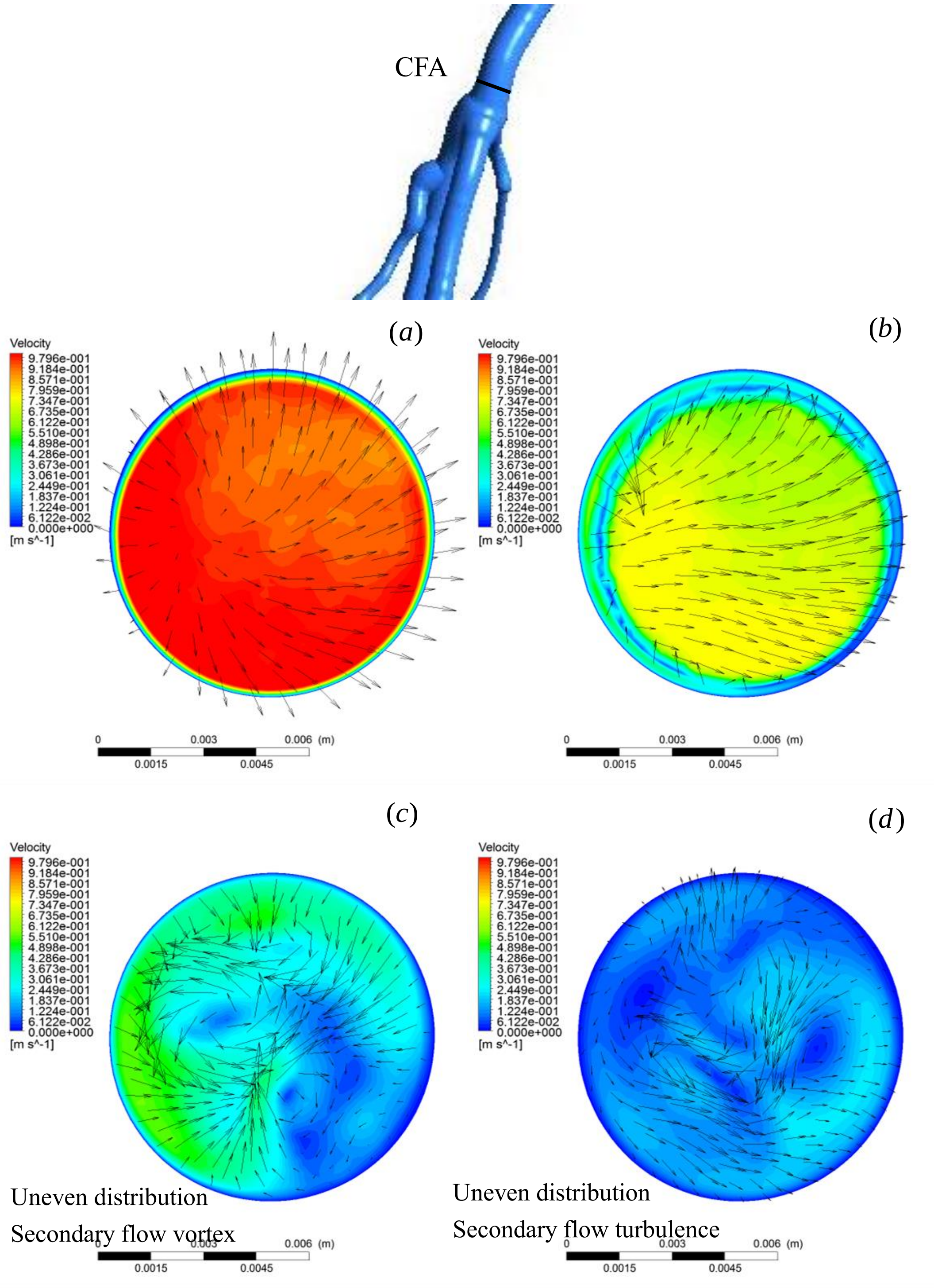

Figure 7.36 The velocity vector on CFA cross section of the 3D-WK coupling model in Case-1's SL. (a) t1; (b) t2; (c) t3; (d) t4.

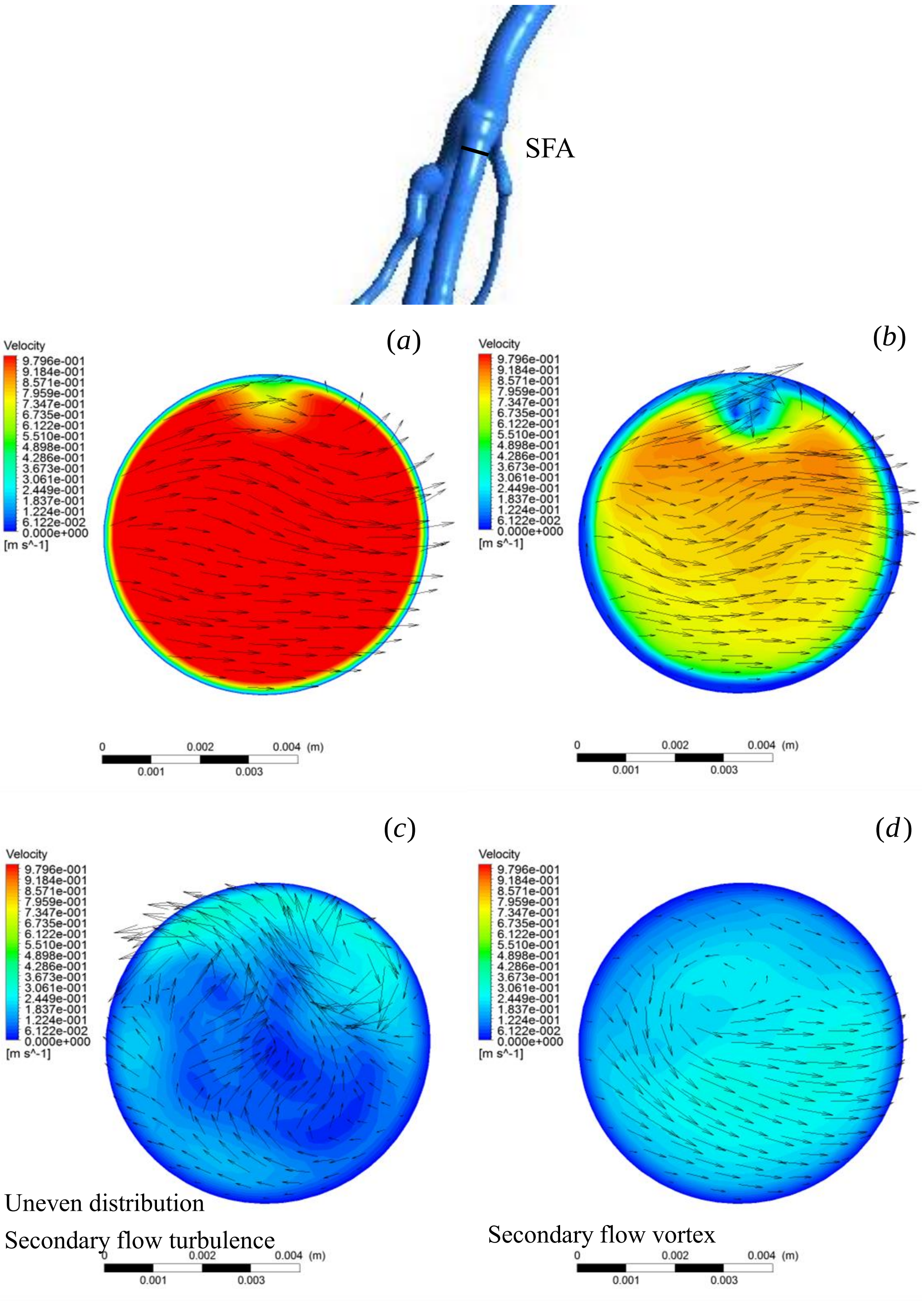

Figure 7.37 The velocity vector on SFA cross section of the 3D-WK coupling model in Case-1's SL. (a) t1; (b) t2; (c) t3; (d) t4.

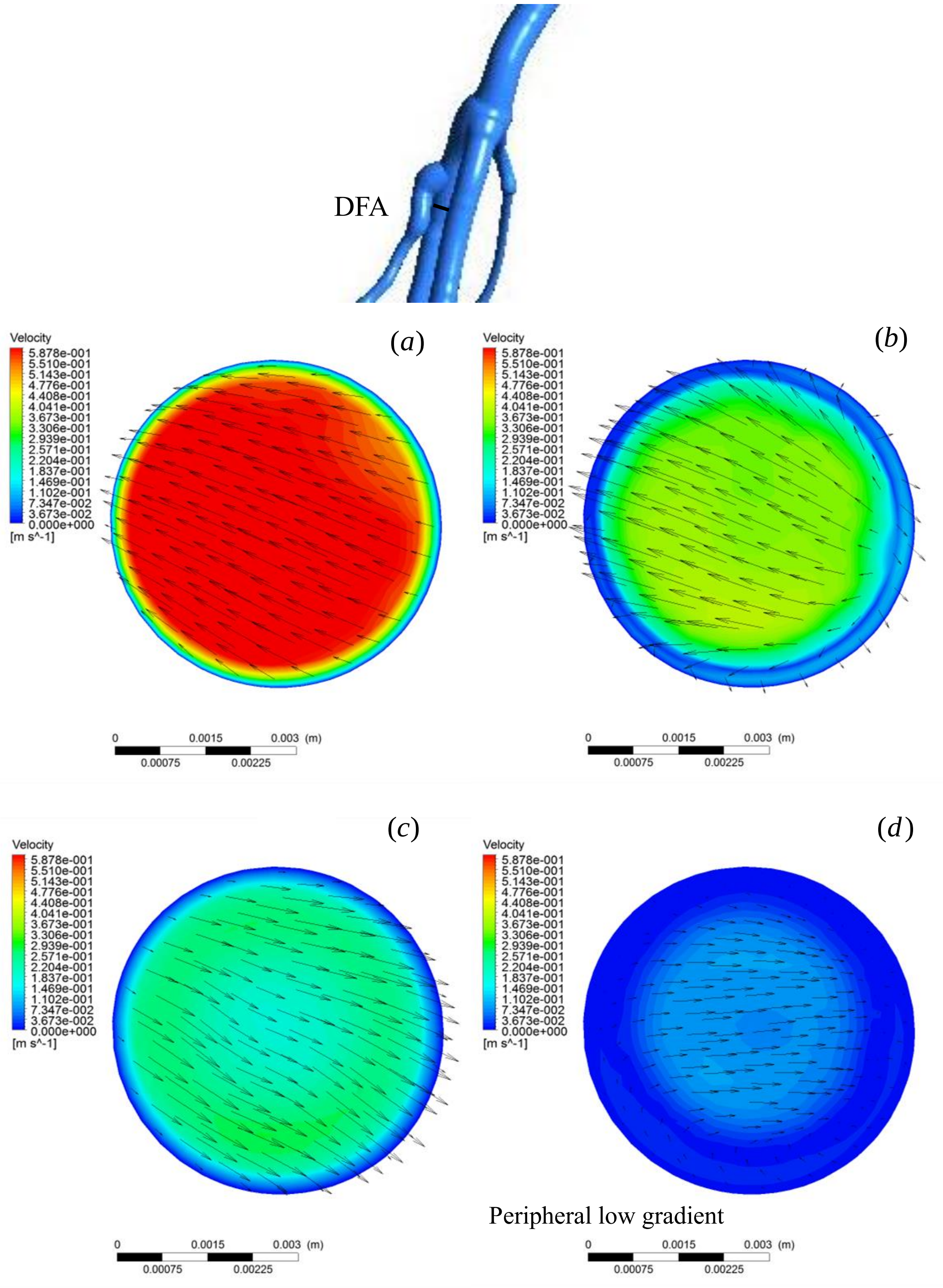

Figure 7.38 The velocity vector on DFA cross section of the 3D-WK coupling model in Case-1's SL. (a) t1; (b) t2; (c) t3; (d) t4.

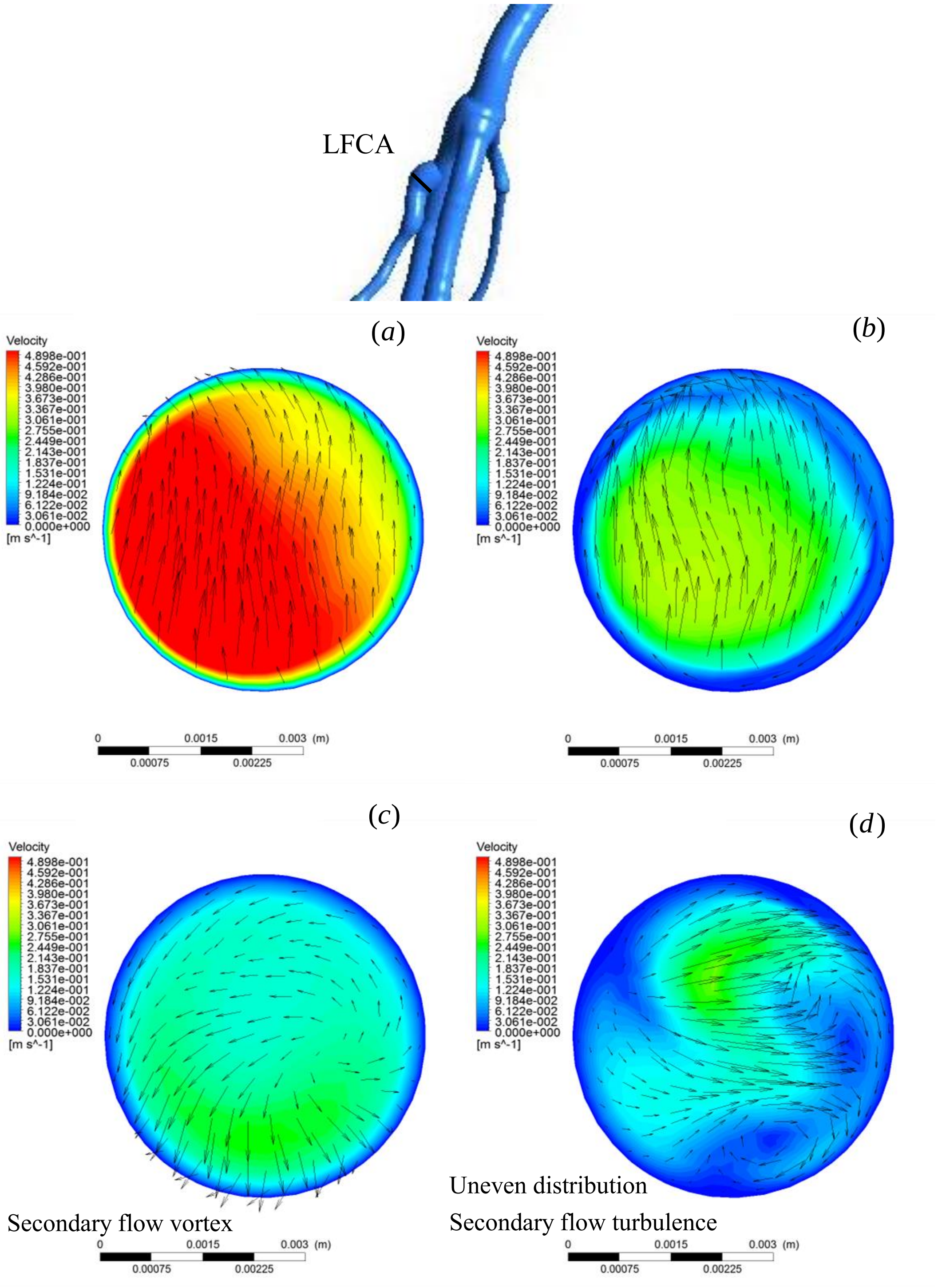

Figure 7.39 The velocity vector on LFCA cross section of the 3D-WK coupling model in Case-1's SL. (a) t1; (b) t2; (c) t3; (d) t4.

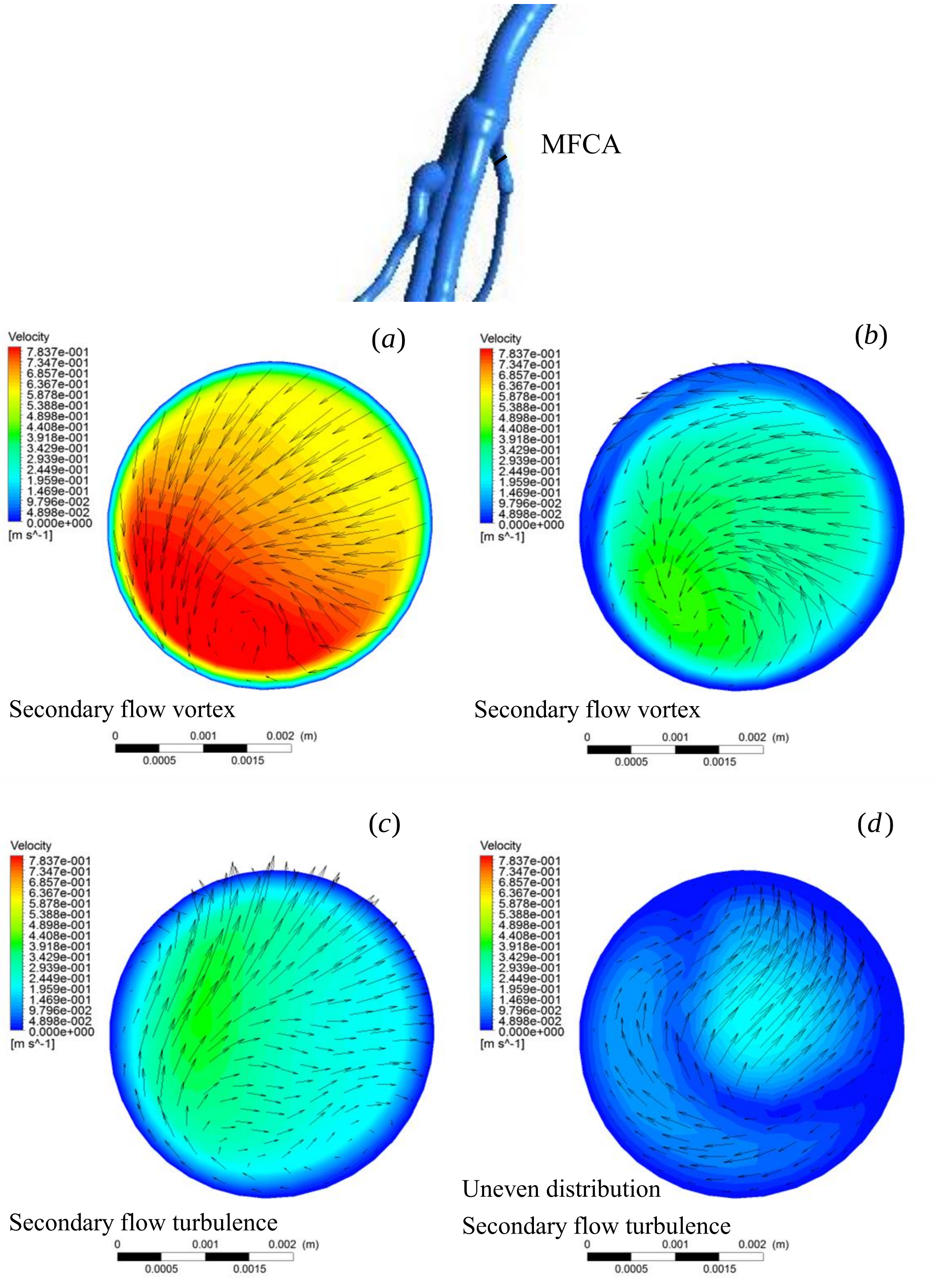

Figure 7.40 The velocity vector on MFCA cross section of the 3D-WK coupling model in Case-1's SL. (a) t1; (b) t2; (c) t3; (d) t4.

Figure 7.36 showed the velocity vector on CFA cross section. It could be seen that the FV distribution was similar to that of the 3D-CR model. At t1 and t2, high velocity zone (the red or yellow part) was larger and concentrated, and both velocity gradient and secondary flow direction were basically consistent on whole cross section. While at t3 and t4, FV value reduced with enlarged uneven low velocity zone and disordered multi-direction vortices or turbulences. As shown in **Figure 7.37**, the average FV value in SFA was higher. At four moments, the distributions, velocity gradients, and secondary flow directions were almost the same with those in CFA (**Figure 7.36**), yet the distribution nonuniformity at t3 and t4 in SFA was slighter. The FV distribution on DFA cross section was shown in **Figure 7.38**. The results of 3D-WK and 3D-CR models were basically consistent. At t4, overall low FV value (the dark or light blue part) and peripheral low gradient could be observed. The secondary flow directions at four moments were all single and consistent. The results of LFCA and MFCA were shown in **Figure 7.39** and **Figure 7.40**. Both of them had similar FV distribution and the change process from t1 to t4 with the other arteries. Like the 3D-CR model, MFCA displayed more disordered secondary flow directions, and there were vortices at t1 and t2.

7.2.3 Result verification and comparison between 3D-CR model and 3D-WK model

When CR model was used as lumped parameter (0D) model to be the outlet boundary condition of 3D model for coupling calculation, the results of the numerical simulation on Case-1 could be summarized as follows: in a complete cardiac cycle, the value ranges of WP and FV in the arterial tree of RL were far greater than those of SL and exhibited uneven distribution; after rapid ejection period, both limbs appeared obvious LSSAs which mainly located at CFA and the upper half of DFA, and the LSSAs in RL were less than those in SL; there was a wide extent of low velocity disturbance in the bifurcation segment of RL; each arterial cross section near the bifurcation site of RL showed uneven velocity distributions and turbulent flow fields, whereas the velocity distributions on those cross sections of SL were relatively uniform; the value ranges of FV in the bifurcation segment of SL varied with pulse wave, and there were slightly disordered flow fields in isovolumic relaxation period and slow filling period.

When three-element WK model was used as lumped parameter (0D) model to be the outlet boundary condition of 3D model for coupling calculation, the results of the numerical simulation on Case-1 could be summarized as follows: in a complete cardiac cycle, RL and SL had similar WP distributions and the maximum pressure drop occurred in rapid ejection period; from slow ejection period, both limbs appeared notable larger LSSAs which mainly located at CFA, bifurcation site and the upper half of DFA, while RL had more LSSAs with lower WSS values than SL; the value range of FV in RL was greater than that in SL, yet after rapid ejection period, bilateral sides showed small ranges of low velocity disturbance in the bifurcation segments; the velocity distribution on each cross section of both limbs was relatively uniform from lumen center to periphery; RL displayed more complex secondary flow directions; bilateral FV changed with pulse wave, and there were decreased peripheral velocity gradient and obviously disordered flow fields in both limbs during isovolumic relaxation period and slow filling period.

From the above summaries it can be seen, the two types of coupling model produced different results, especially in the RL. In order to intuitively reflect and identify the simulation effect and accuracy of the 3D-CR model and the 3D-WK model, the ultrasonic measured velocity waveforms in the DFA end in RL (**Figure 7.41**) and in the SFA end in SL (**Figure 7.42**) were compared with the calculated outlet waveforms exported by two coupling models (**Figure 7.43** and **Figure 7.44**).

Figure 7.41 The ultrasonic measured velocity waveform in the end of DFA in Case-1's residual limb.

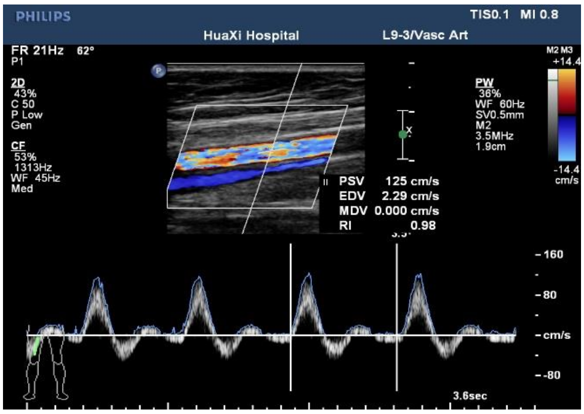

Figure 7.42 The ultrasonic measured velocity waveform in the end of SFA in Case-1's sound limb.

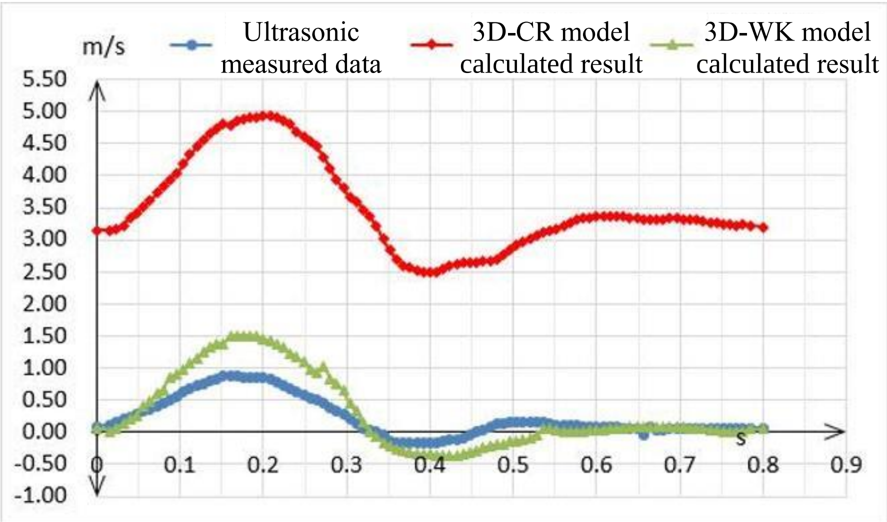

Figure 7.43 The DFA outlet velocity comparison between ultrasonic measured data and two calculated results in Case-1's residual limb.

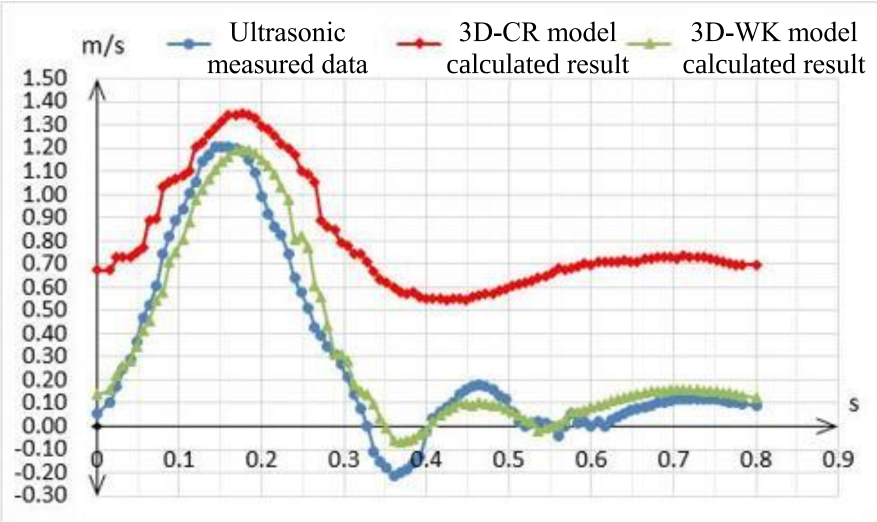

Figure 7.44 The SFA outlet velocity comparison between ultrasonic measured data and two calculated results in Case-1's sound limb.

As shown in **Figure 7.43** and **Figure 7.44**, the calculation result of the 3D-CR model had an approximate waveform with ultrasonic measured data, but the numerical difference was significant. In RL, the value output from 3D-CR model was almost 3-4 times larger than ultrasonic data, while in SL, the gap was 1-2 times except the middle phase of rapid ejection. In contrast, the calculation result of the 3D-WK model had approximate waveforms and numerical values with ultrasonic measured data in both limbs, especially in SL. That is to say, the simulation accuracy of 3D-CR model was inferior to that of 3D-WK model, and the former's numerical results were rough, even unreliable in RL. However, the good waveform fitting illustrated that, 3D-CR model had the validity to describe pulse wave, and the availability to qualitatively demonstrate the changes in hemodynamic parameters during a cardiac cycle. In addition, the waveform comparison in RL showed that CR model was not suitable to be the outlet boundary condition of the vessel with small diameter, because it would make the model error of pulse wave very large and would lead to deviated numerical results. In fact, some studies have proposed that, the smaller diameter of the arterial model truncation would produce the greater error of the coupling calculation results of lumped parameter model, especially the over simplified CR model [147]. Even though three element WK model could well simulate the pulse wave transmission in the arterial tree of RL, the accuracy of its numerical results still had some room for improvement due to the small outlet diameter problem. The simulation effects of these two types of 0D model in this study verified that conclusion.

In summary, taking the results provided by bilateral 3D-WK coupling models as the effective results of Case-1, it could be concluded that, the LSSAs which mainly located at the bifurcation site and the upper half of DFA in RL were more and larger than those in SL, and the disordered flow field in the bifurcation segment of RL was more serious than that of SL. Therefore, compared with SL, those locations in RL with LSSAs and turbulent secondary flow were the high risk areas of atherosclerosis and other lesions. This conclusion was consistent with the qualitative analysis result of the steady flow calculation on Case-1's bilateral 3D models.

7.3 RESULT ANALYSIS AND DISCUSSION OF CASE-2

7.3.1 3D-WK coupling model

The previous section 7.2 demonstrated the advantage of 3D-WK model in numerical accuracy due to the consideration of vascular compliance. So this section directly performed the analysis, comparison and verification on Case-2's 3D-WK model coupling calculation results.

- ***Residual limb***

The wall pressure (WP), wall shear stress (WSS), low shear stress area (LSSA) and the flow velocity (FV) in bifurcation segment of the 3D-WK coupling model in Case-2's RL at the four moments t1, t2, t3, and t4 were successively shown in **Figure 7.45**, **Figure 7.46**, **Figure 7.47** and **Figure 7.48**.

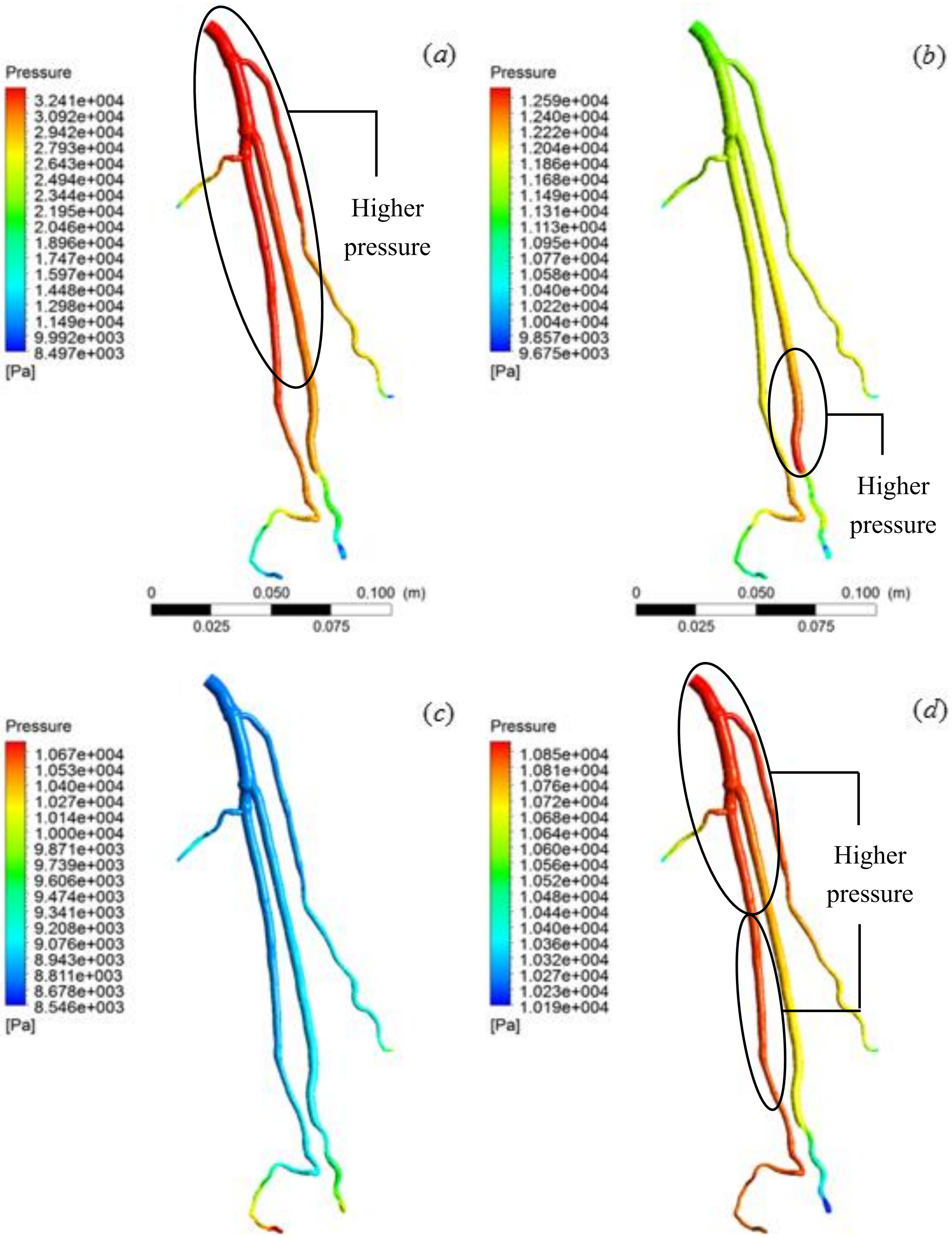

Figure 7.45 The wall pressure distribution contour of the 3D-WK coupling model in Case-2's RL. (a) t1; (b) t2; (c) t3; (d) t4.

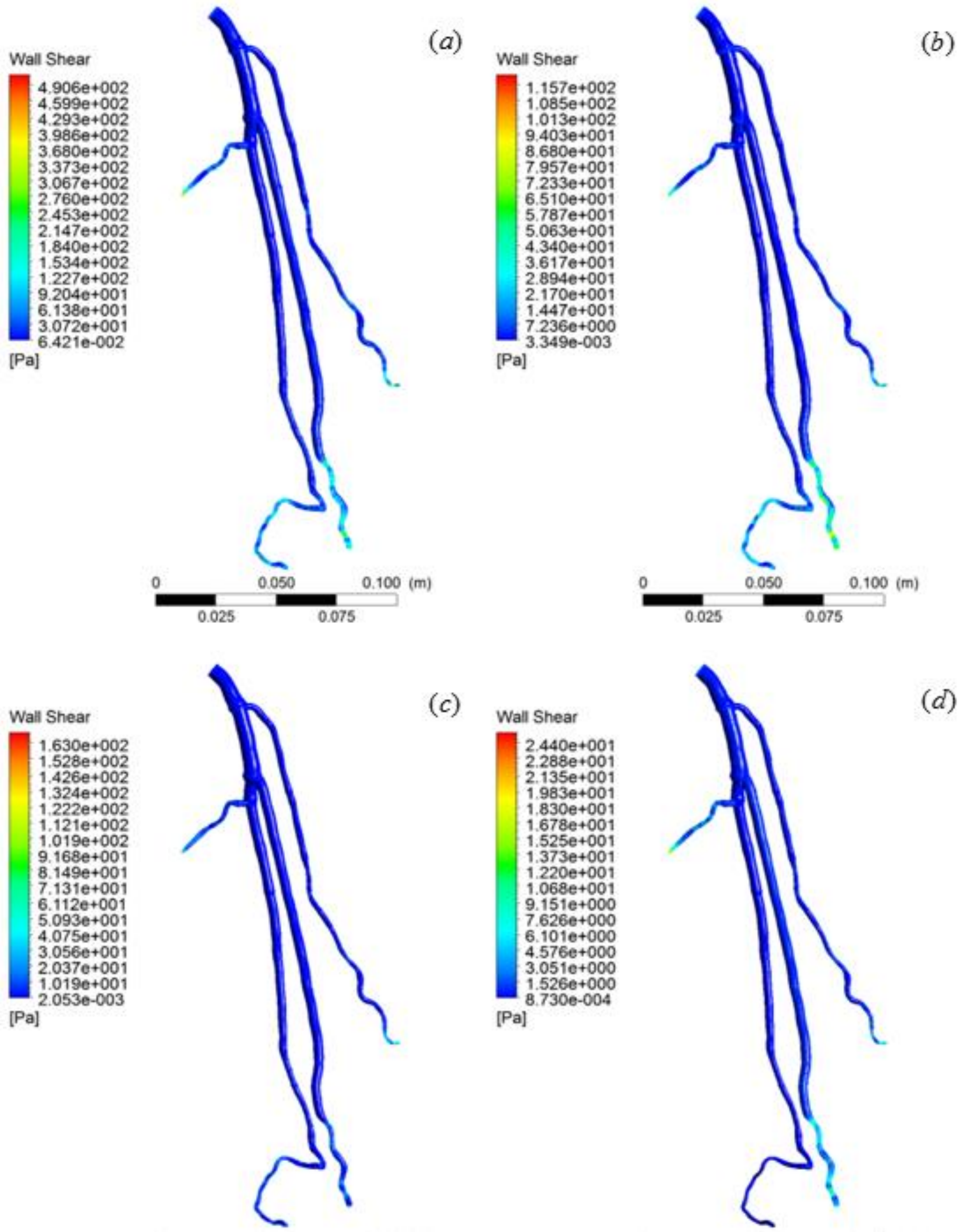

Figure 7.46 The wall shear stress distribution contour of the 3D-WK coupling model in Case-2's RL. (a) t1; (b) t2; (c) t3; (d) t4.

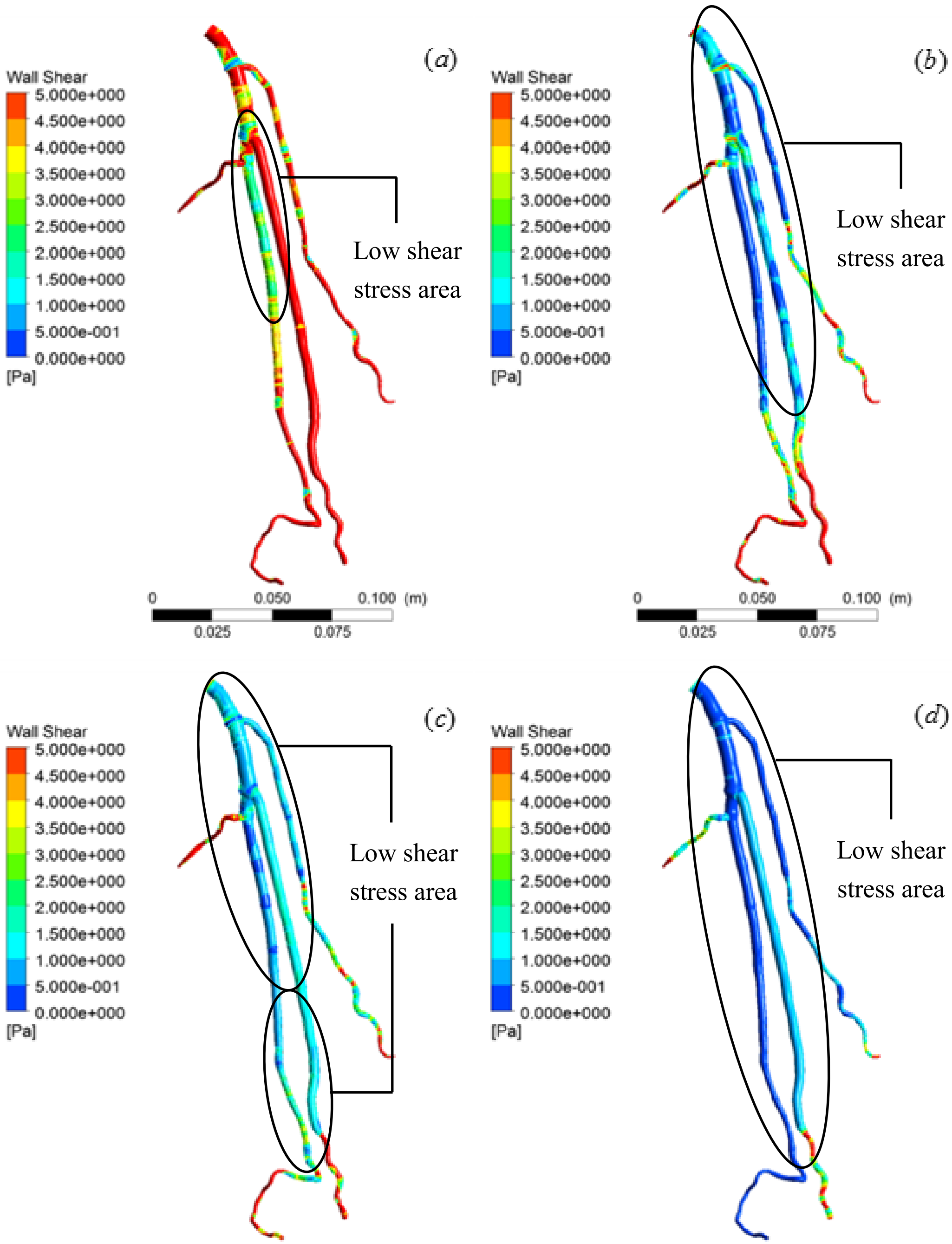

Figure 7.47 The low shear stress areas of the 3D-WK coupling model in Case-2's RL. (a) t1; (b) t2; (c) t3; (d) t4.

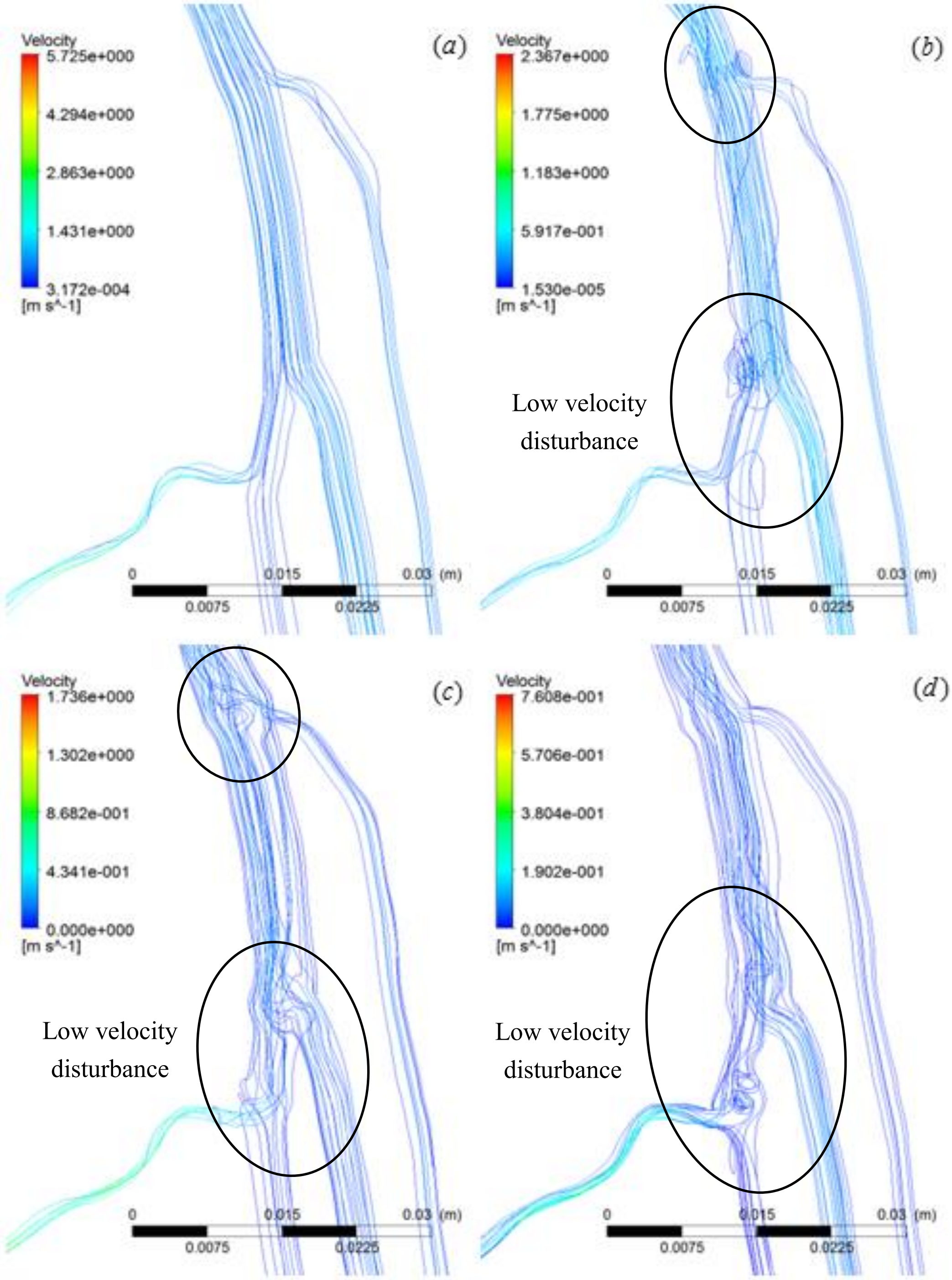

Figure 7.48 The flow velocity distribution streamline of the 3D-WK coupling model in Case-2's RL. (a) t1; (b) t2; (c) t3; (d) t4.

As can be seen in **Figure 7.45**, the WP ranges of the arterial tree in RL at four different moments were respectively 8497.4Pa--33409.9Pa at t1, 9674.7Pa--

12707.8Pa at t2, 8545.6Pa--10755.3Pa at t3, 10193.1Pa--10873.4Pa at t4, slightly larger than those of Case-1 at all moments, and there was no negative pressure area. Similar to Case-1, at t1 vessel walls bore the largest blood pressure, whereas at t3, the WP was the minimum. From t2 to t4, WP ranges were close but with different distributions. At t1 and t4, the upper half of entire arterial tree and almost whole DFA were in a relatively higher pressure state, while t2 and t3 showed local small areas of the higher WP at the lower SFA and the outlets. Comparatively speaking, WP gradient in the tail section of each artery was obviously greater.

WSS distributions were shown in **Figure 7.46**. The value ranges with great difference were respectively 0.0642Pa--511.05Pa at t1, 0.0033Pa--120.55Pa at t2, 0.0021Pa--169.78Pa at t3, 0.0009Pa--25.42Pa at t4. Compared with Case-1, Case-2 had notale larger WSS ranges and smaller low values. Near the outlets, WSS increased with the reduce of lumen diameters, but high shear stress areas were too small to be observed in this figure, implying that the uneven distribution of WSS at different locations in Case-2 was more severe than that in Case-1. Specific observation on the WSS value of 0-5Pa was shown in **Figure 7.47**. At t1, CFA and the bifurcation site already exhibited small LSSAs, while the WSS value of the upper half of DFA was generally lower than 2Pa. The other three moments showed notable great extent of LSSAs covering almost all walls except the four outlet segments. Especially at t2 and t4, there were large high-risk areas <0.4Pa (the dark blue part) in the bifurcation segment, DFA, and the upper half of LFCA. Overall, Case-2 displayed larger LSSAs with lower values and longer duration than Case-1.

Figure 7.48 illustrated the velocity streamlines in the bifurcation segment. The velocity ranges of entire arterial tree were respectively 0--5.72m/s at t1, 0--2.35m/s at t2, 0--1.74m/s at t3, 0--0.76m/s at t4. Similar to Case-1, the high FV areas were very small and just in the four outlets as well as some segments with smaller diameter, indicating that the variation of FV distribution with vessel size made it uneven. At t1, the isovelocity streamlines in bifurcation site were smooth-going and uniform. The other three moments exhibited local low velocity disturbance in bifurcation sites between different arteries. For detailed observation of the lumen flow field, the velocity vector on each arterial cross section 2mm away from the bifurcation site was shown in **Figure 7.49** to **Figure 7.53**.

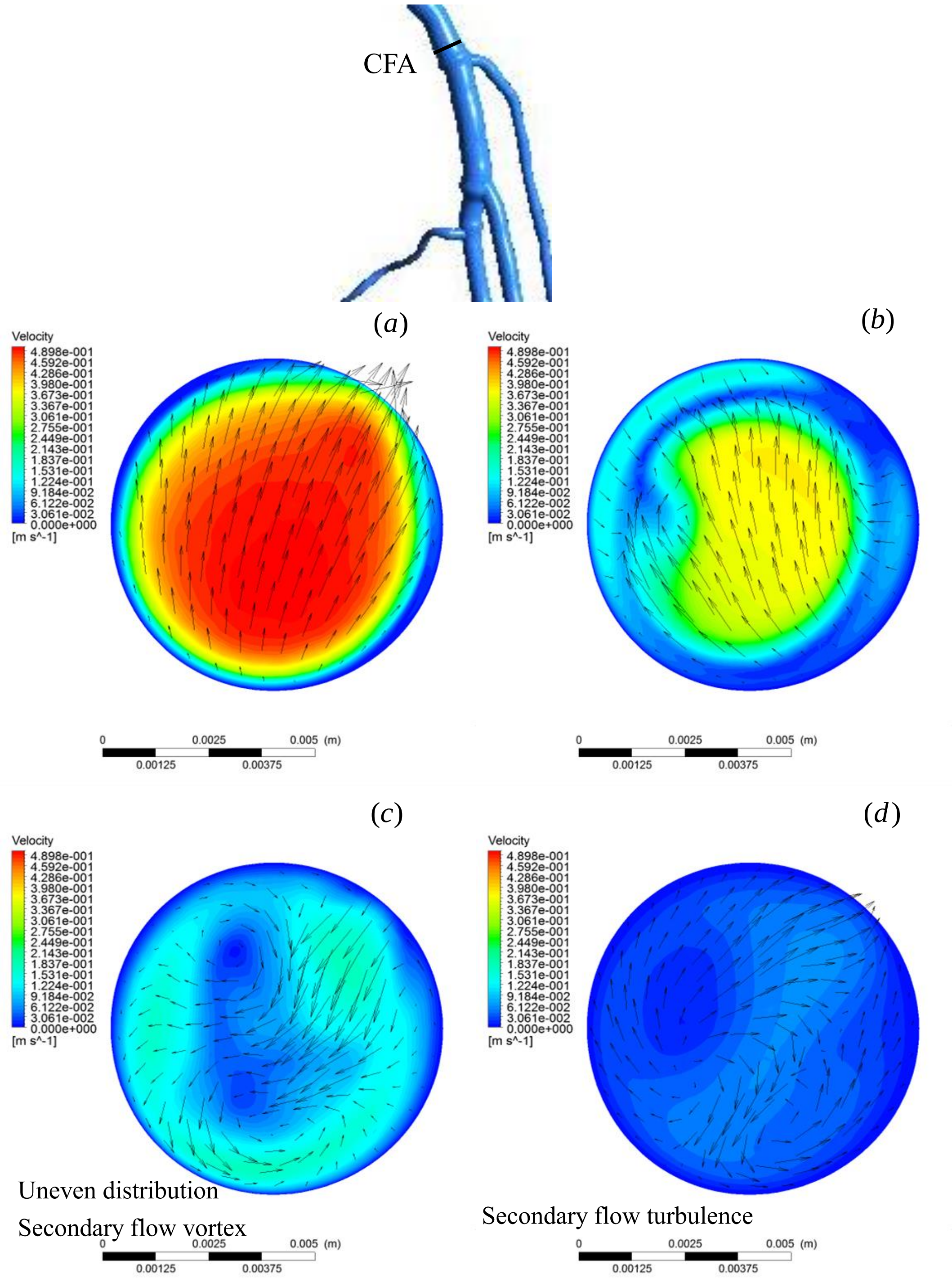

Figure 7.49 The velocity vector on CFA cross section of the 3D-WK coupling model in Case-2's RL. (a) t1; (b) t2; (c) t3; (d) t4.

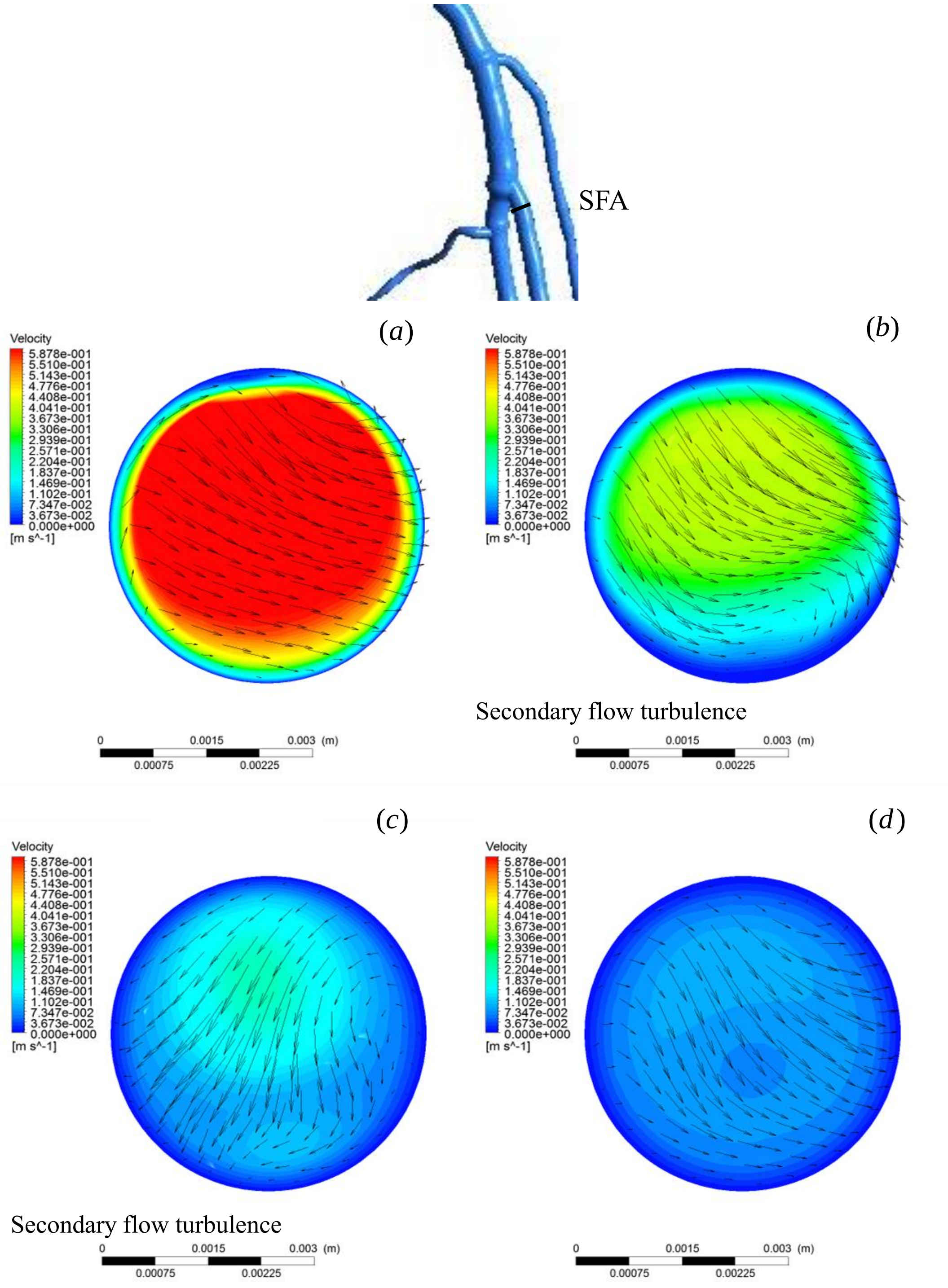

Figure 7.50 The velocity vector on SFA cross section of the 3D-WK coupling model in Case-2's RL. (a) t1; (b) t2; (c) t3; (d) t4.

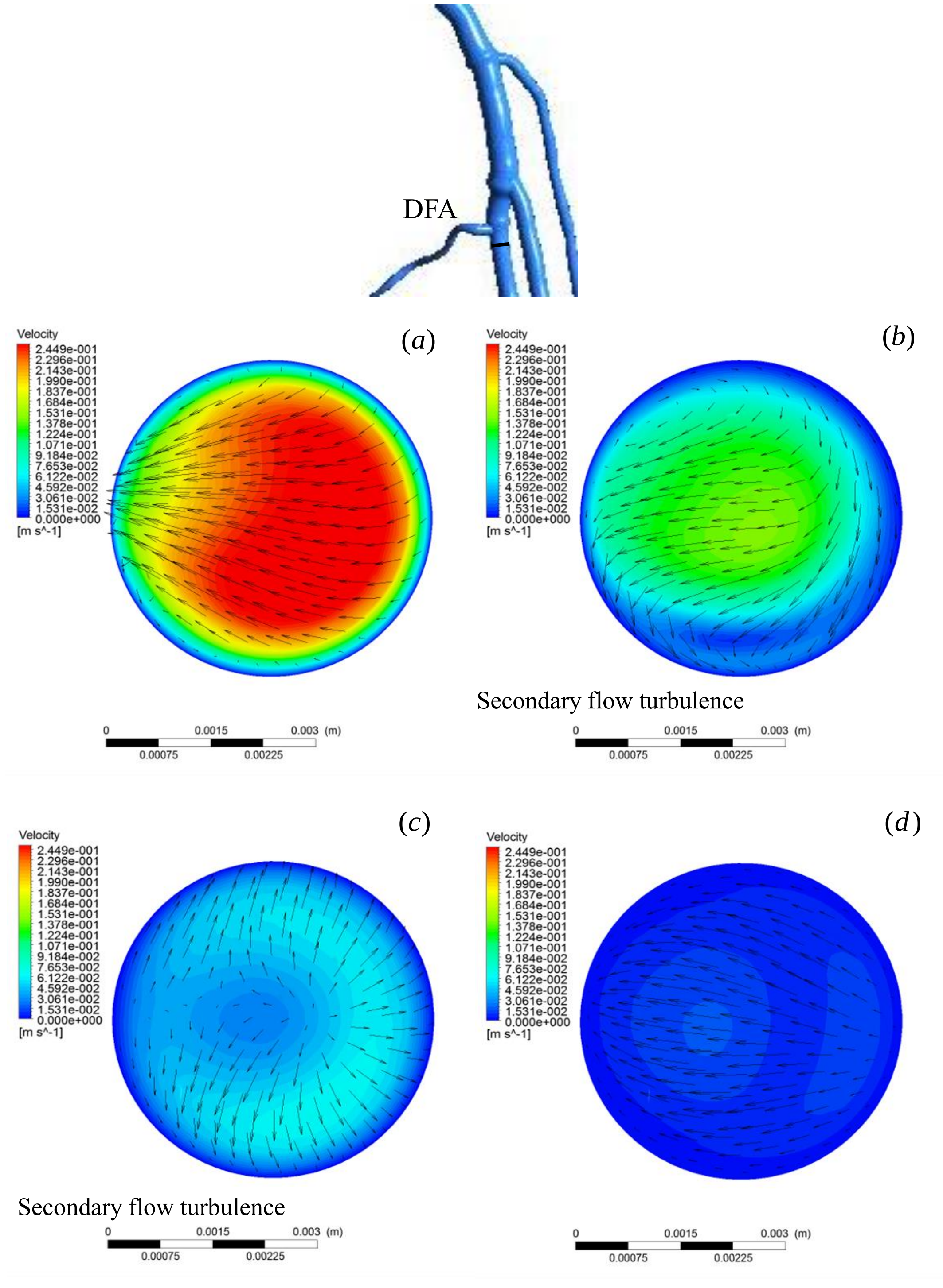

Figure 7.51 The velocity vector on DFA cross section of the 3D-WK coupling model in Case-2's RL. (a) t1; (b) t2; (c) t3; (d) t4.

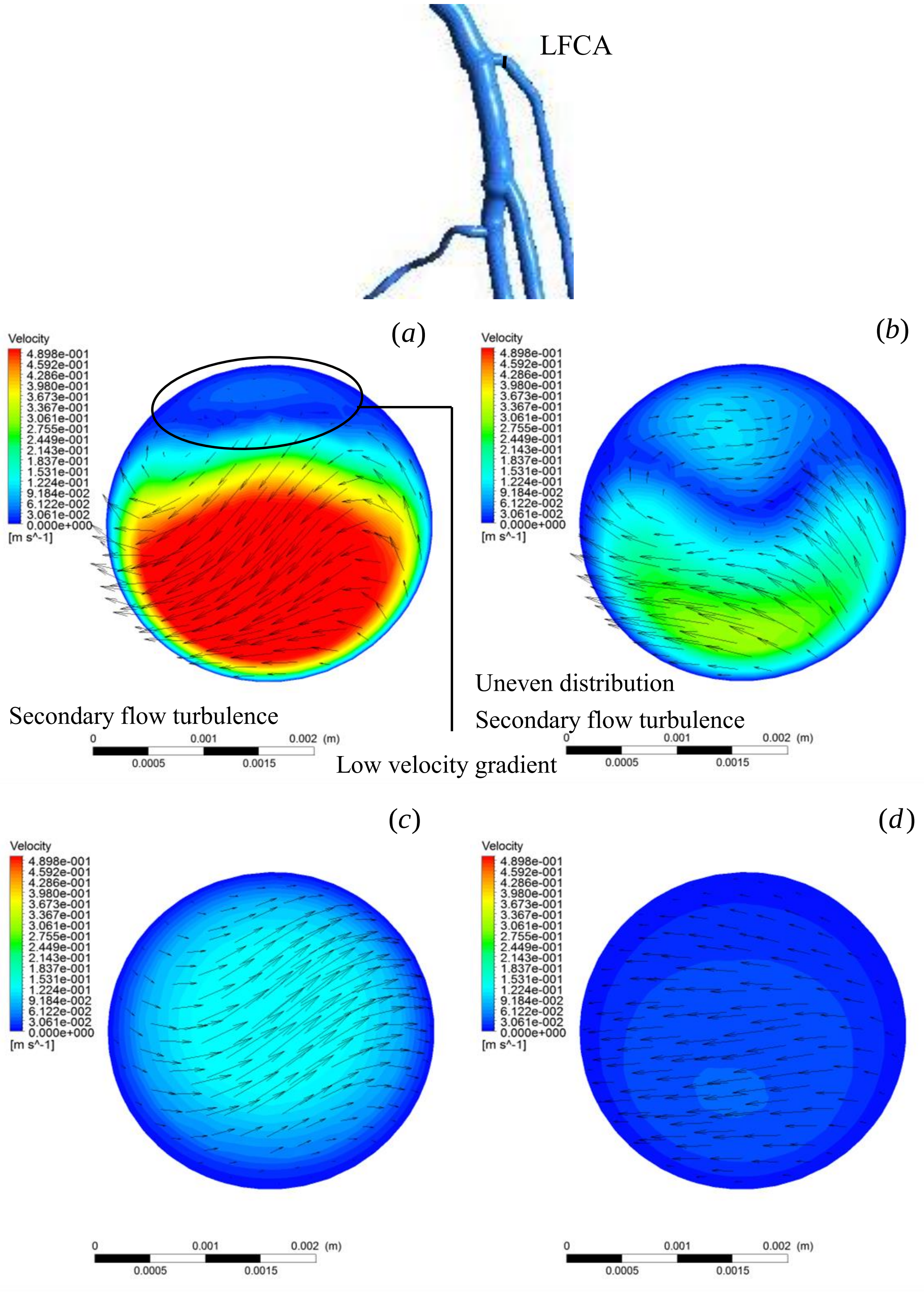

Figure 7.52 The velocity vector on LFCA cross section of the 3D-WK coupling model in Case-2's RL. (a) t1; (b) t2; (c) t3; (d) t4.

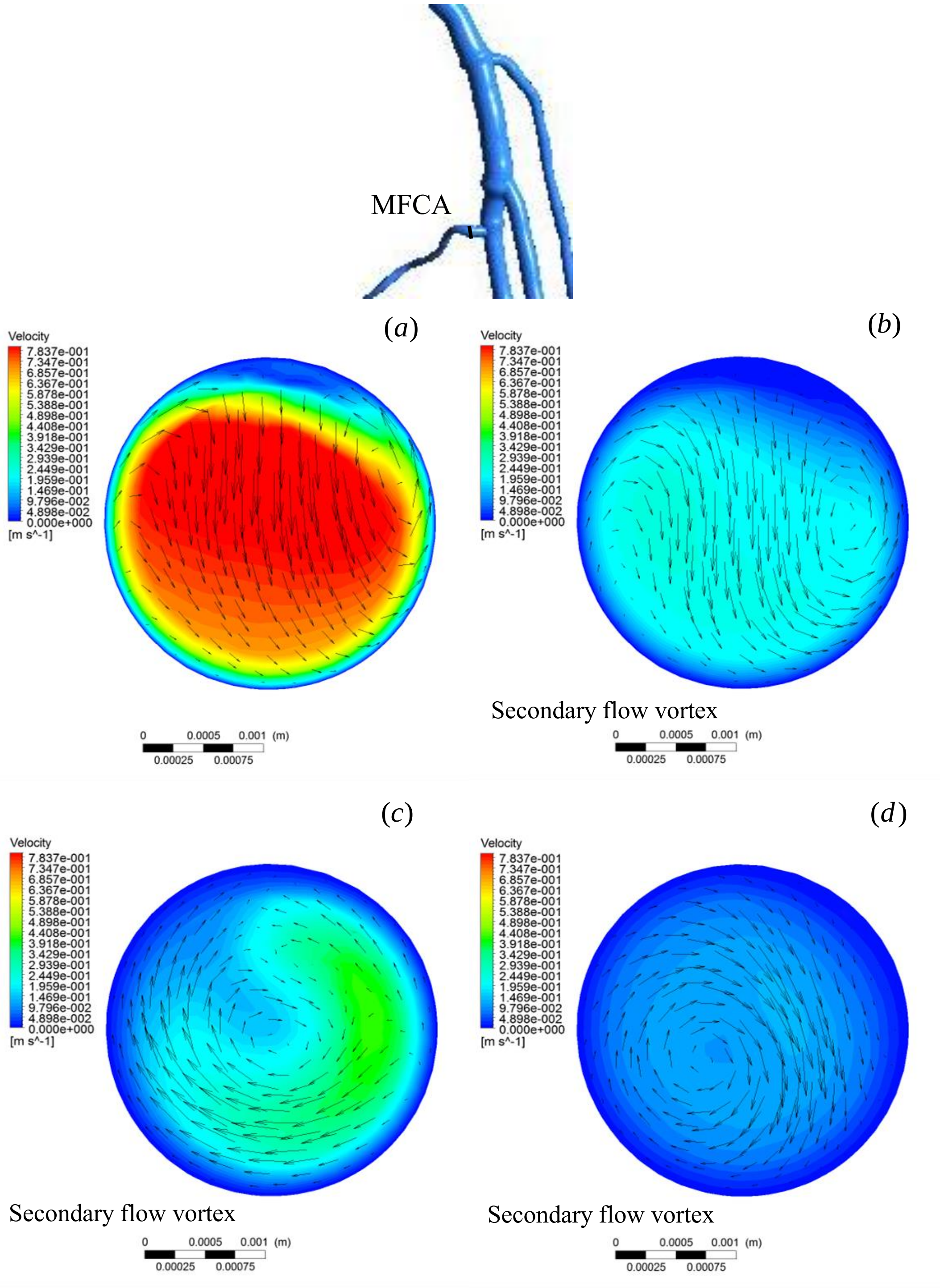

Figure 7.53 The velocity vector on MFCA cross section of the 3D-WK coupling model in Case-2's RL. (a) t1; (b) t2; (c) t3; (d) t4.

Since LFCA originated from the higher position of CFA, the inlet cross section in CFA was intercepted at the plane 2mm above the LFCA bifurcation site. **Figure 7.49** showed the velocity vector on CFA cross section. It could be seen that at t1 and t2, the thickness of peripheral low velocity area (the blue part) was greater than that of Case-1. The high velocity zone (the red or yellow part) was concentrated and the velocity gradient was basically consistent on whole cross section. While at t3 and t4, FV value reduced with enlarged uneven low velocity zone and multi-direction secondary flow vortices. As shown in **Figure 7.50** and **Figure 7.51**, the FV distributions, velocity gradients, and secondary flow directions were very similar between SFA and DFA. Their high velocity zone (the red or yellow part) was concentrated at t1 and t2, and the transition from high to low velocity was moderate. All four moments exhibited relatively uniform secondary flow directions and gradients. There were slight turbulences at t2 and t3. The results of LFCA and MFCA were shown in **Figure 7.52** and **Figure 7.53**. Both of them displayed smaller high velocity zone at t1 and t2, yet the overall FV value in MFCA was larger than that of LFCA. LFCA exhibited much greater peripheral low velocity regions (the dark blue part) and secondary flow turbulences at t1 and t2. While MFCA displayed wide ranges of secondary flow vortex at t2, t3 and t4.

- ***Sound limb***

The wall pressure (WP), wall shear stress (WSS), low shear stress area (LSSA) and the flow velocity (FV) in bifurcation segment of the 3D-WK coupling model in Case-2's SL at the four moments t1, t2, t3, and t4 were successively shown in **Figure 7.54**, **Figure 7.55**, **Figure 7.56** and **Figure 7.57**.

As can be seen in **Figure 7.54**, the WP ranges of the arterial tree in SL at four different moments were respectively 10324.5Pa--22545.9Pa at t1, 8999.1Pa--11082.1Pa at t2, 10026.1Pa--11054.4Pa at t3, 10325.5Pa--11647.8Pa at t4, close to those of RL and slightly larger than those of Case-1. Except t1, the WP ranges had little difference at the other three moments with no negative value. WP distribution and gradient of each vessel were relatively uniform. Consistent with RL, the upper half of DFA was in a relatively higher pressure state, while t2 and t3 showed local small areas of the higher WP at the end of SFA.

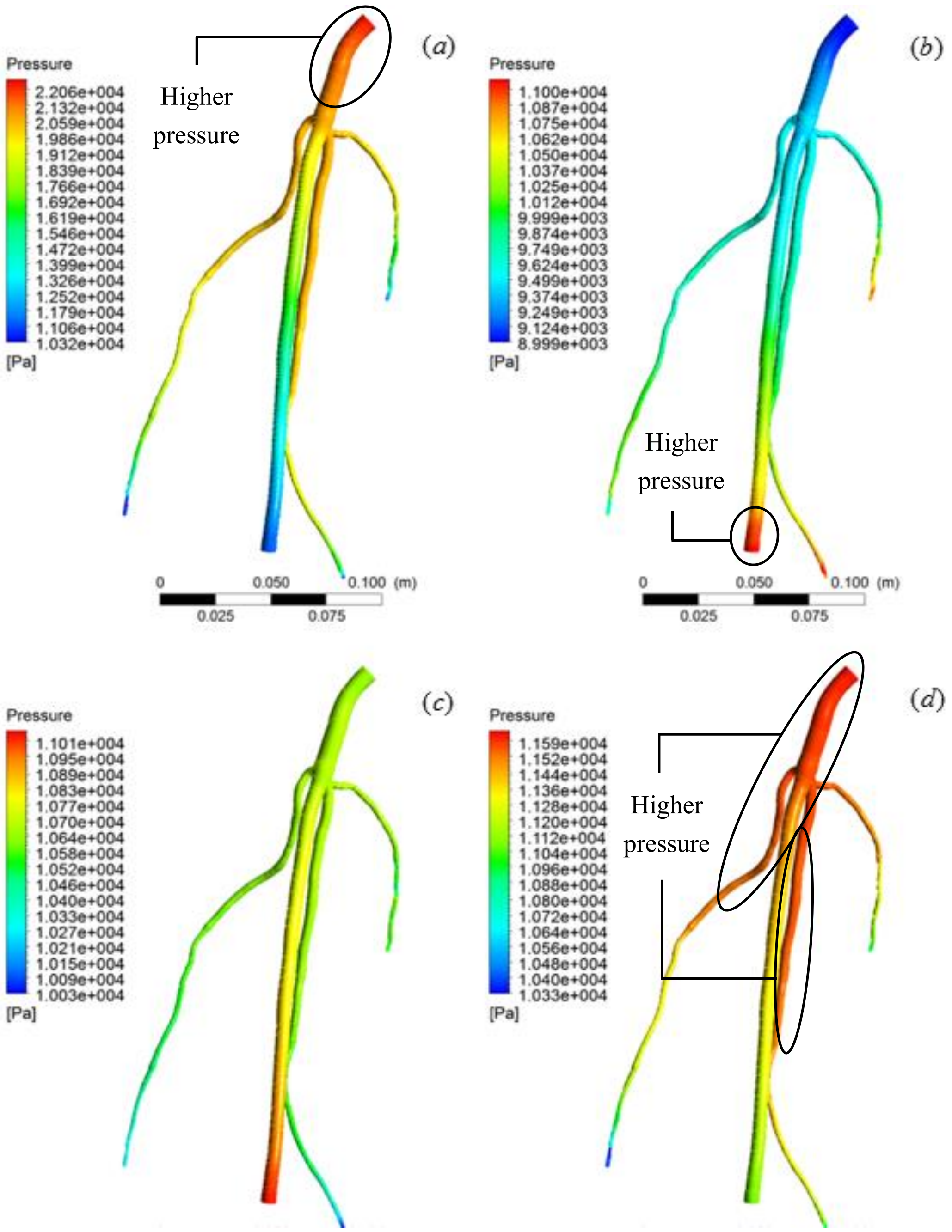

Figure 7.54 The wall pressure distribution contour of the 3D-WK coupling model in Case-2's SL. (a) t1; (b) t2; (c) t3; (d) t4.

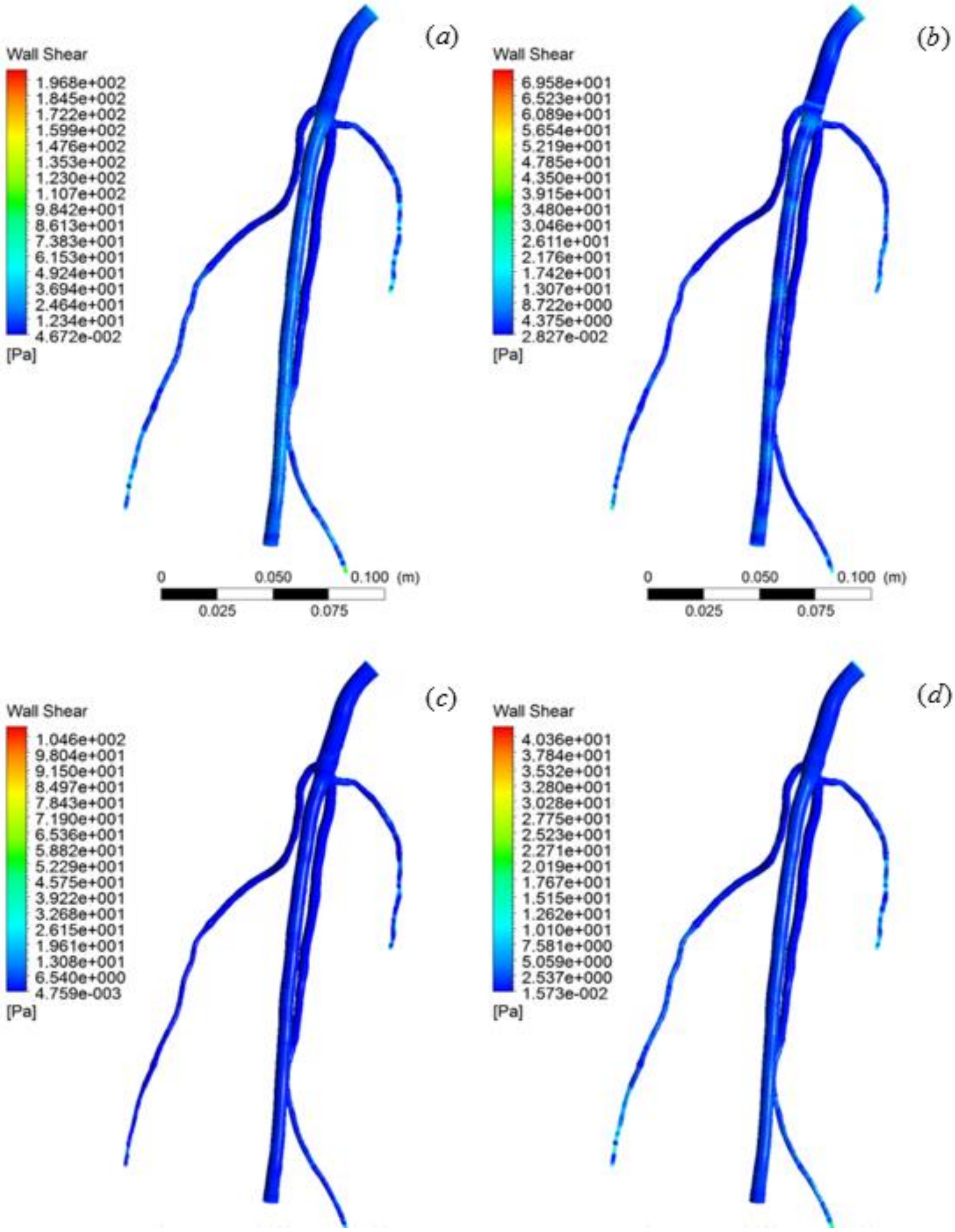

Figure 7.55 The wall shear stress distribution contour of the 3D-WK coupling model in Case-2's SL. (a) t1; (b) t2; (c) t3; (d) t4.

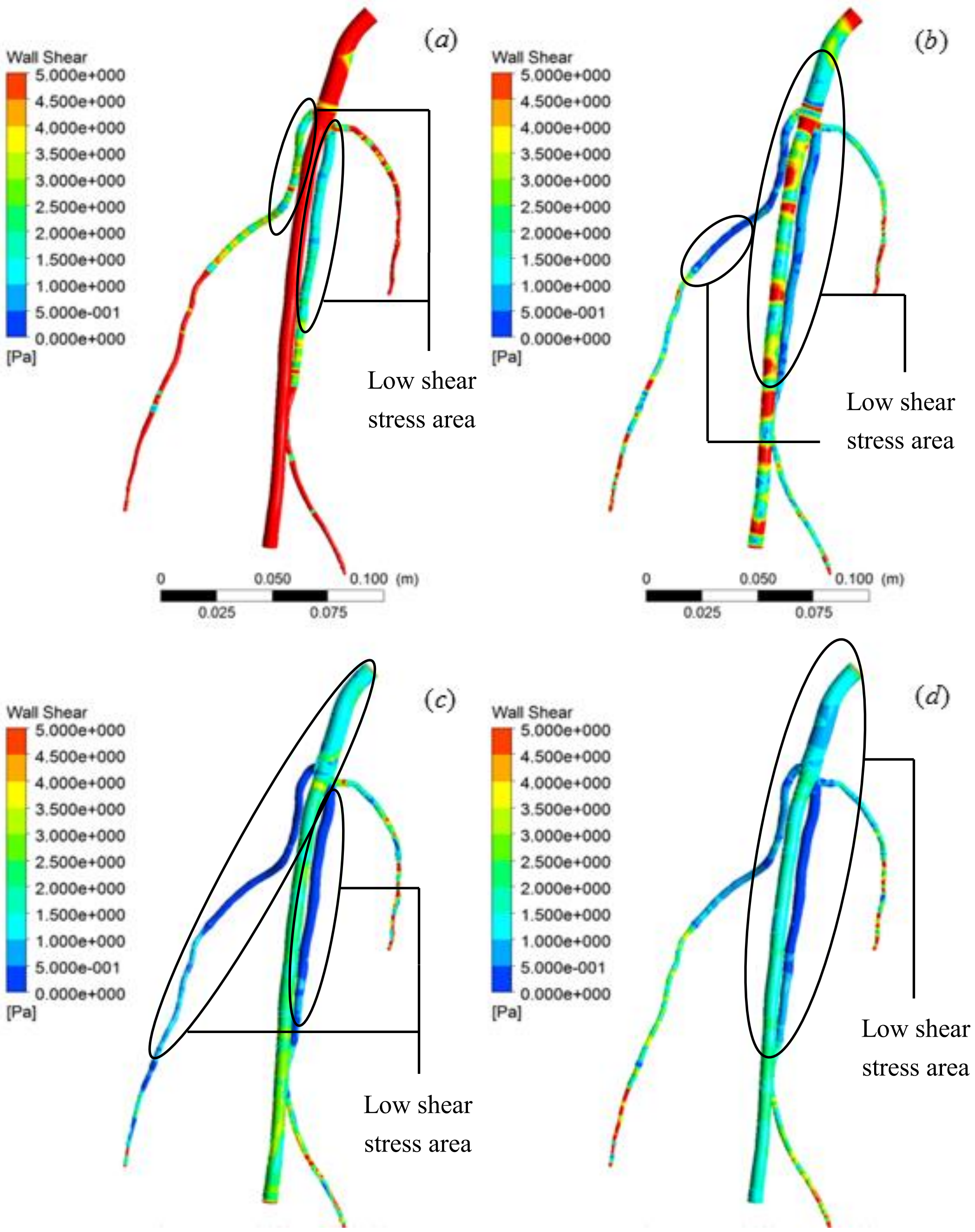

Figure 7.56 The low shear stress areas of the 3D-WK coupling model in Case-2's SL. (a) t1; (b) t2; (c) t3; (d) t4.

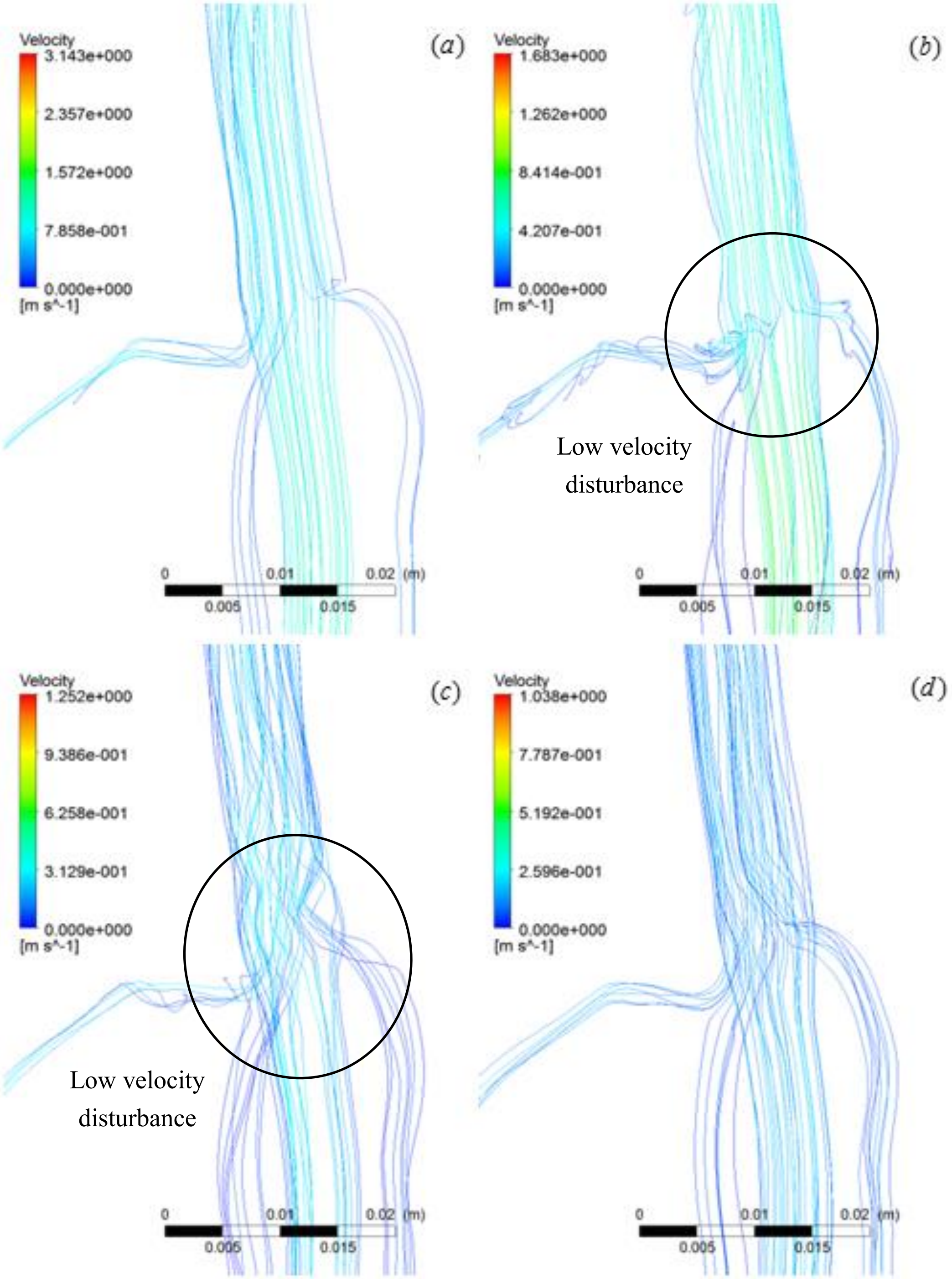

Figure 7.57 The flow velocity distribution streamline of the 3D-WK coupling model in Case-2's SL. (a) t1; (b) t2; (c) t3; (d) t4.

The results of WSS were shown in **Figure 7.55**. At different moments, there were notable differences of the value ranges: 0.0467Pa--205.01Pa at t1, 0.2827Pa--72.48Pa at t2, 0.0048Pa--108.93Pa at t3, 0.0157Pa--42.04Pa at t4, which were slightly smaller than those of RL. Bilateral limbs had almost the same overall distributions. Specific observation on the WSS value of 0-5Pa was shown in **Figure 7.56**. Similar to RL, there were WSS<2Pa areas in the upper half of DFA and LFCA at t1, wherein the value was minimum in DFA. While the other three moments displayed remarkable wide ranges of high-risk LSSAs (<0.4Pa) also mainly in the upper half of DFA and LFCA. Compared with RL, the LSSAs were smaller in SL.

Figure 7.57 illustrated the velocity streamlines in the bifurcation segment. The velocity ranges of entire arterial tree were respectively 0--3.18m/s at t1, 0--1.68 m/s at t2, 0--1.25m/s at t3, 0--0.96m/s at t4. At all four moments, the isovelocity streamlines in bifurcation site were smooth-going and uniform except local slight low velocity disturbances with small amplitude at t2 and t3, indicating that the bifurcation segment of SL had more orderly and stable flow field than that of RL. The velocity vector on each arterial cross section was shown in **Figure 7.58** to **Figure 7.62**.

As shown in **Figure 7.58** to **Figure 7.60**, the FV distributions, velocity gradients, and secondary flow directions of CFA, SFA and DFA in SL were basically the same situation as those in RL, thus no more detailed description. The only difference was that SL exhibited lighter degrees of low velocity distribution nonuniformity and secondaty flow disturbances than RL, especially in CFA. The results of LFCA and MFCA were shown in **Figure 7.61** and **Figure 7.62**. Compared to the above three arteries, both of them displayed uneven velocity distributions and gradients at t1 and t2, and decreased gradients in the peripheral low velocity regions at t3 and t4. Different from RL, the overall FV value in LFCA was larger than that of MFCA. Similar to RL, secondary flow turbulences or vortices could be observed at four moments.

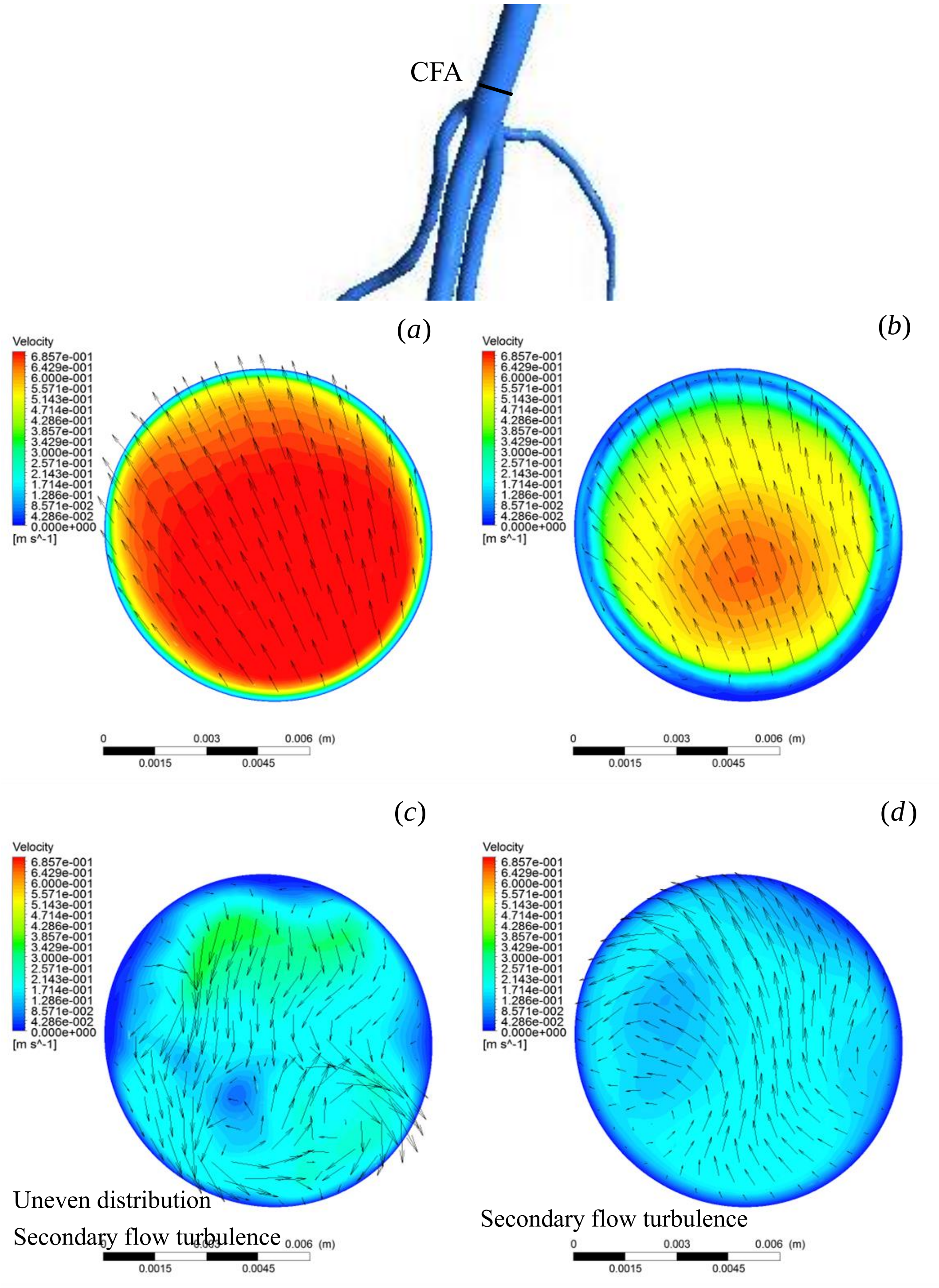

Figure 7.58 The velocity vector on CFA cross section of the 3D-WK coupling model in Case-2's SL. (a) t1; (b) t2; (c) t3; (d) t4.

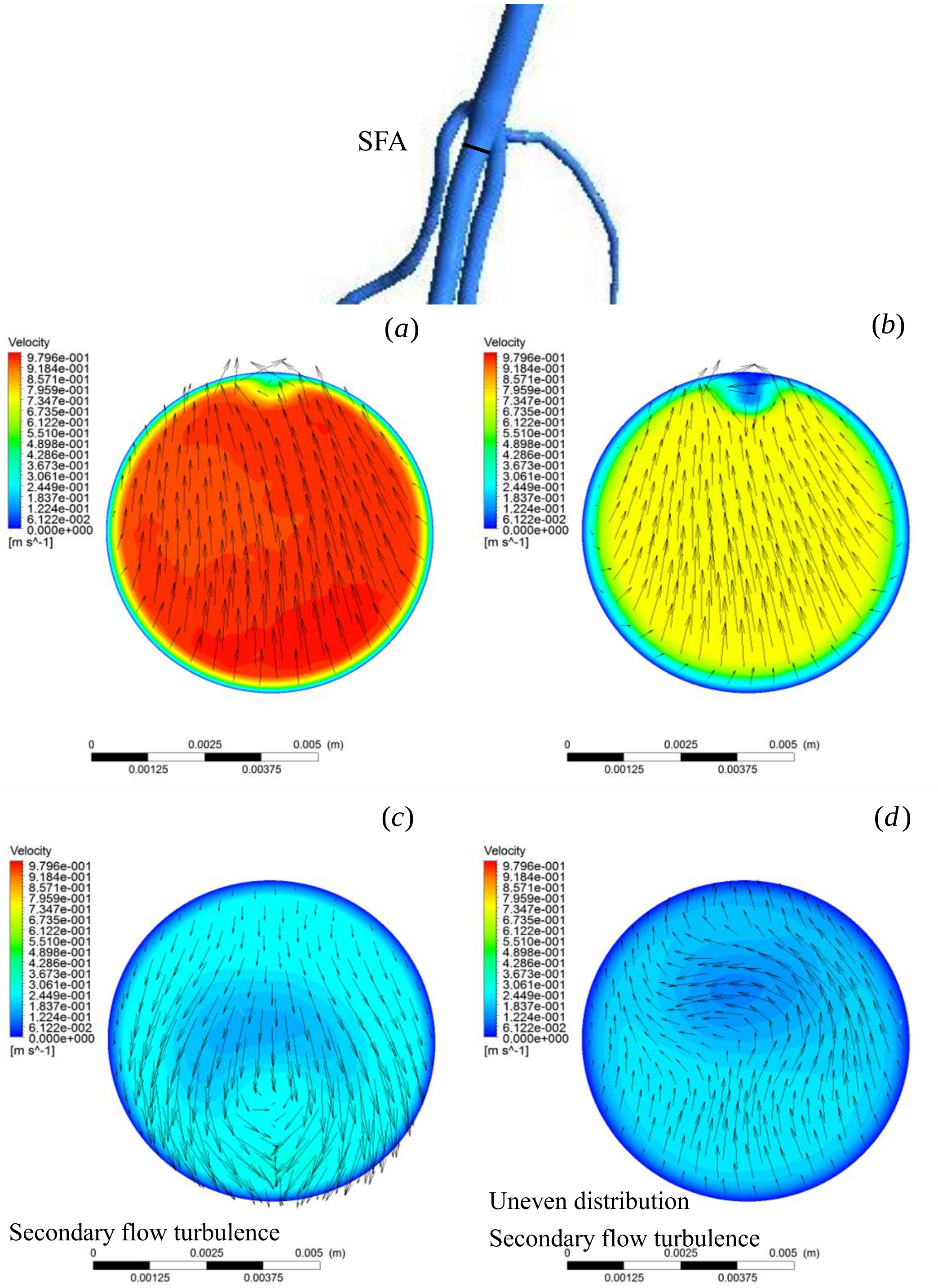

Figure 7.59 The velocity vector on SFA cross section of the 3D-WK coupling model in Case-2's SL. (a) t1; (b) t2; (c) t3; (d) t4.

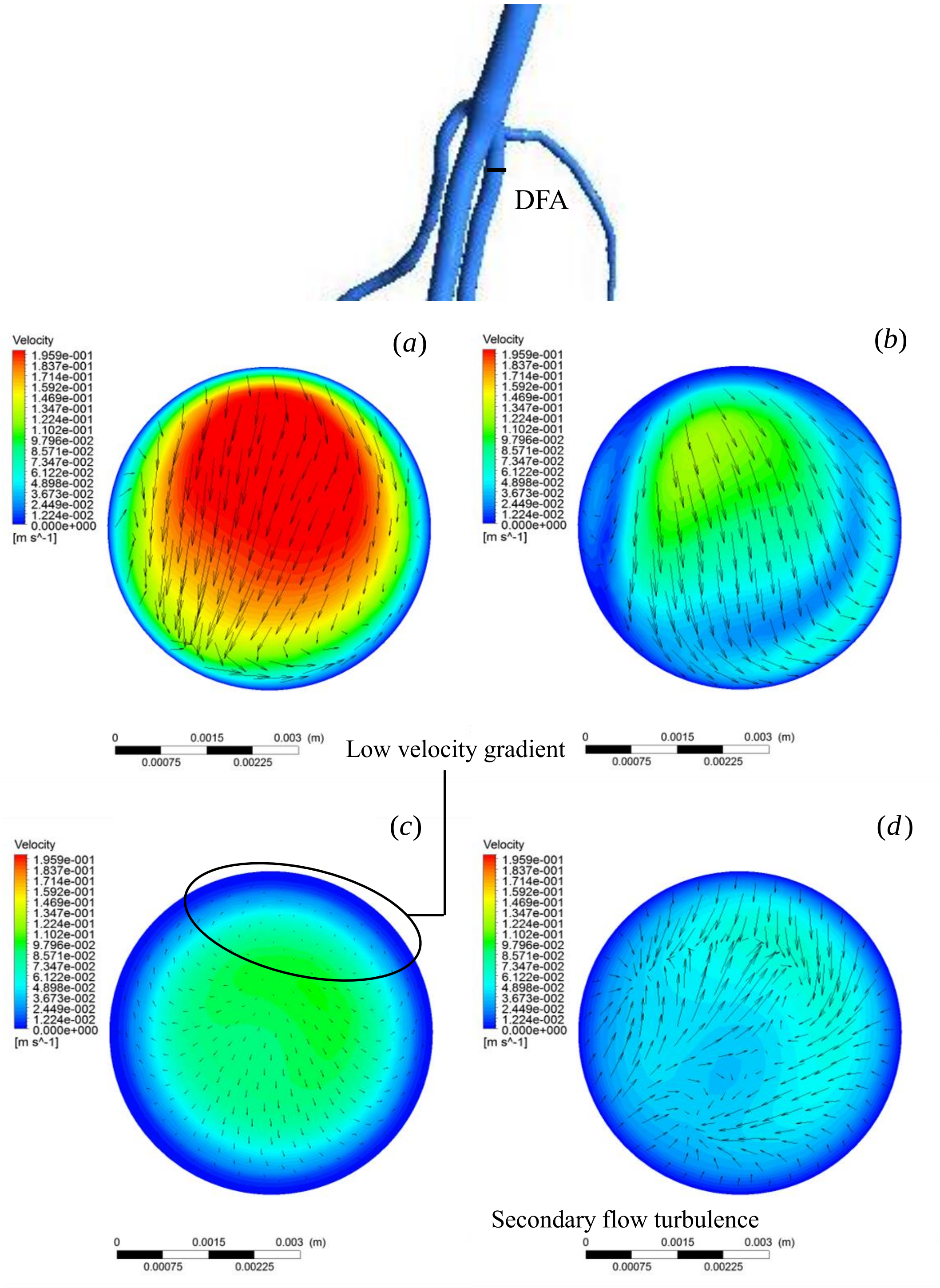

Figure 7.60 The velocity vector on DFA cross section of the 3D-WK coupling model in Case-2's SL. (a) t1; (b) t2; (c) t3; (d) t4.

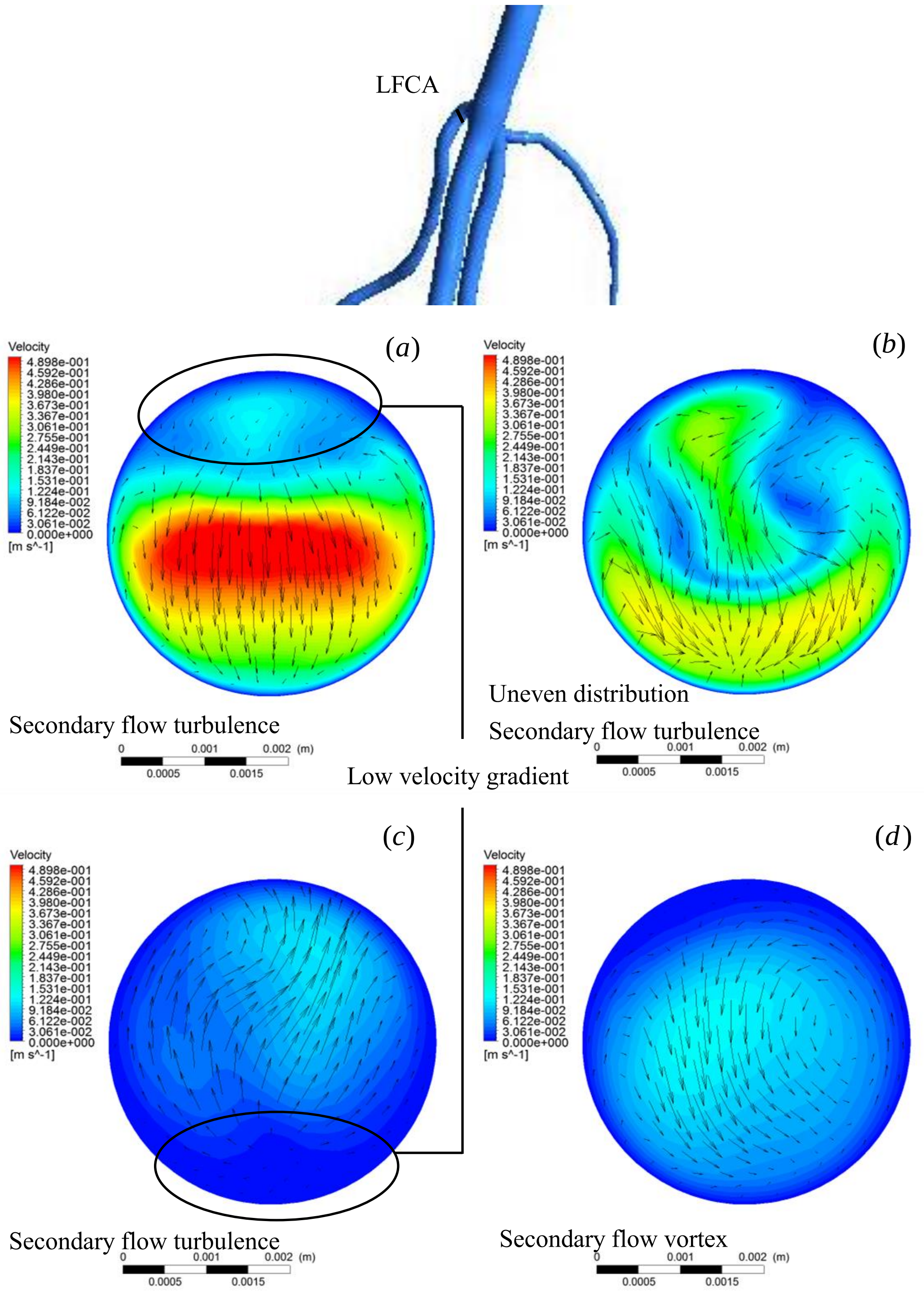

Figure 7.61 The velocity vector on LFCA cross section of the 3D-WK coupling model in Case-2's SL. (a) t1; (b) t2; (c) t3; (d) t4.

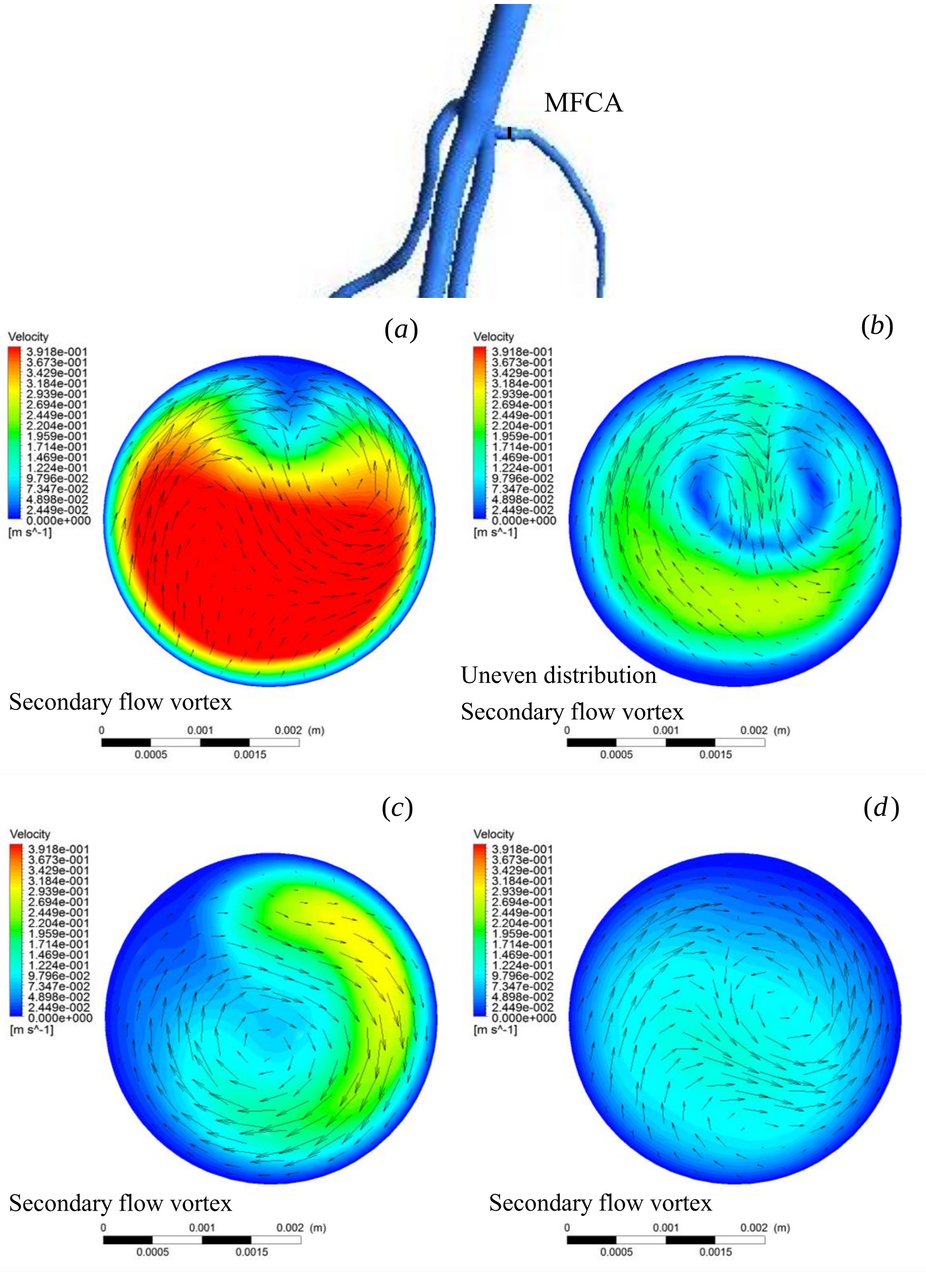

Figure 7.62 The velocity vector on MFCA cross section of the 3D-WK coupling model in Case-2's SL. (a) t1; (b) t2; (c) t3; (d) t4.

7.3.2 Result verification and summary of 3D-WK model

In order to verify the simulation effect and numerical accuracy of the 3D-WK coupling model of Case-2, the ultrasonic measured velocity waveforms in the DFA end in RL (**Figure 7.63**) and in the SFA end in SL (**Figure 7.64**) were compared with the calculated outlet waveforms (**Figure 7.65** and **Figure 7.66**).

Figure 7.63 The ultrasonic measured velocity waveform in the end of DFA in Case-2's residual limb.

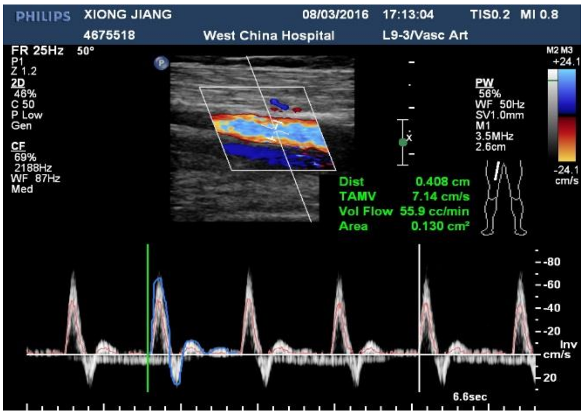

Figure 7.64 The ultrasonic measured velocity waveform in the end of SFA in Case-2's sound limb.

Figure 7.65 and **Figure 7.66** illustrated that, when three-element WK model was used as lumped parameter (0D) model to be the outlet boundary condition of Case-2's 3D model for coupling calculation, the exported results had approximate waveforms and numerical values with ultrasonic measured data in both limbs, except a little time lag. This indicated the propagation of pulse wave in lower limb arteries was well simulated. Combining the result verification of Case-1 and Case-2, it could draw the conclusion that, the coupling calculation of local 3D arterial model and outlet three-element WK model is advisable for the quantitative numerical analysis of arterial hemodynamics in both lower limbs after amputation.

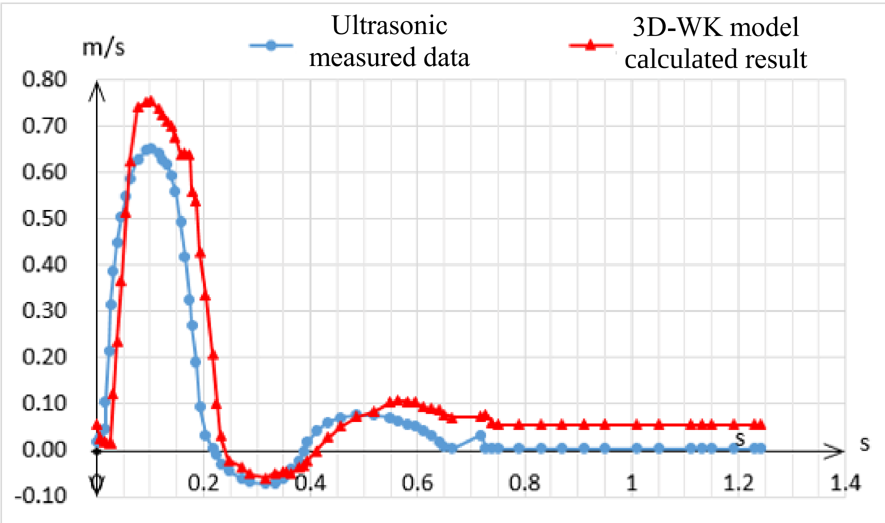

Figure 7.65 The DFA outlet velocity comparison between ultrasonic measured data and 3D-WK model calculated result in Case-2's residual limb.

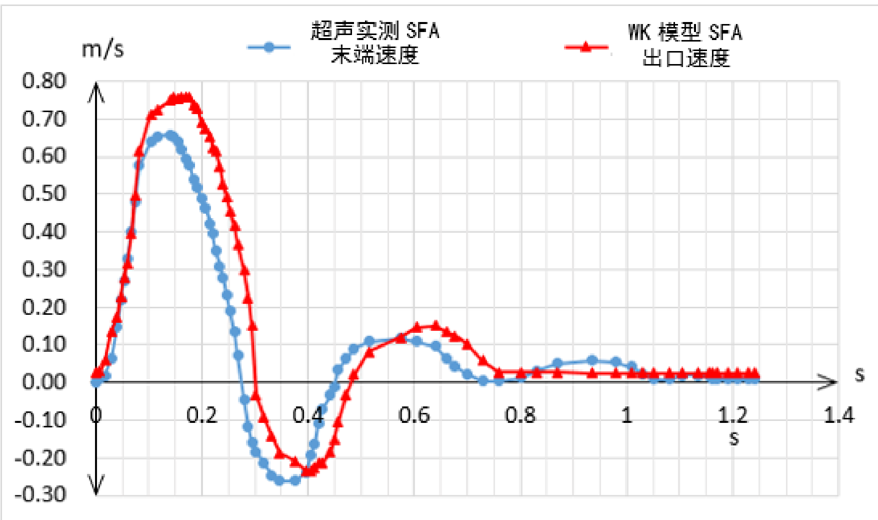

Figure 7.66 The SFA outlet velocity comparison between ultrasonic measured data and 3D-WK model calculated result in Case-2's sound limb.

The results of the numerical simulation on Case-2 could be summarized as follows: in a complete cardiac cycle, RL and SL had similar WP distributions and the maximum pressure drop occurred in rapid ejection period; from slow ejection period, both limbs appeared notable larger LSSAs which mainly located at the upper half of DFA and of LFCA, while RL had more LSSAs with lower WSS values than SL; the value range of FV in RL was greater than that in SL, and after rapid ejection period, RL showed small ranges of low velocity disturbance in the bifurcation segments; the velocity distribution on each cross section of both limbs was relatively uniform in ejection period; RL displayed more complex secondary flow directions; bilateral FV changed with pulse wave, and there were decreased peripheral velocity gradient and obviously disordered flow fields in both limbs during isovolumic relaxation period and slow filling period.

Comparing the 3D-WK coupling calculation results of Case-1 and Case-2 in their own cardiac cycle, the two cases had similar WP situation; Case-2 showed greater bilateral LSSAs with lower WSS values than Case-1; in addition to the same high-risk area of arterial diseases with Case-1 --- the upper half of DFA in RL, the upper half of LFCA in Case-2's both limbs were also susceptible areas; Case-1 exhibited larger range of unevenly distributed bilateral isovelocity streamlines in the bifurcation segment than Case-2; both of them had more complicated velocity distribution and more disordered secondary flow direction at the cross sections near the bifurcation site in RL than in SL.

7.4 SUMMARY

This chapter discussed the numerical calculation results of multi-scale coupling model in detail, and described the construction principle and the coupling method with 3D model of the two types of lumped parameter model --- CR model and three-element WK model. Through the comparison between ultrasonic measured data and the results calculated by the two types of coupling model of Case-1, it found that, although 3D-CR model had the validity to describe pulse wave and the availability to qualitatively demonstrate the changes in hemodynamic parameters, its numerical accuracy was inferior to that of 3D-WK model, especially in RL. Combining the 3D-WK model results analysis of Case-1 and Case-2, conclusions could be drawn as follow: the chance of atherosclerosis and other arterial lesions in RL was greater than in SL, and the high-risk areas with WSS lower than 0.4Pa mainly located at the arterial tree bifurcation site and the upper half of DFA. The differences between two cases were that, the WSS situation in SL of Case-1 was better than that of Case-2, while Case-2 showed similar bilateral WSS with larger LSSAs and lower WSS values than Case-1. In addition, Case-2 also exhibited a high occurrence likelihood of arterial diseases in the upper half of LFCA.

This study first performed numerical study on the hemodynamic state of bilateral lower limbs after amputation, and through the comparison between RL and SL illustrated their differences of various hemodynamic parameters. That implied the hemodynamic state of RL deserves in-depth and meticulous targeted investigation with a large quantity of samples. Meanwhile, compared with SL, the local high-risk areas in RL with relatively high pressure, flow field disturbance and low shear stress represented by the upper half of DFA were prone to arterial lesions. Once atherosclerosis plaque is induced, the narrowed vessel would further occur luminal stenosis slowing down flow velocity or blocking flow rate to form the stagnant zone. The resulting ischemia, hypoxia and malnutrition would greatly increase the probability of a vicious cycle with the common RL problems such as muscle atrophy (detailed discussion in Chapter 3). When these problems jointly develop to a serious stage, amputees will likely face the second amputation. Therefore, it is very necessary to attach importance to the hemodynamic state of RL in various research directions, including surgery techniques, follow-up observation, rehabilitation treatment and training methods, and prosthetic socket design etc., to avoid multiple amputations and promote comprehensive rehabilitation.

CHAPTER 8: CONCLUSION AND OUTLOOK

8.1 CONCLUSIONS

This thesis from both clinical and biomechanical points of view, performed the morphological measurements on bilateral thigh muscles and main arteries, and the multi-scale numerical simulation on bilateral hemodynamic states of unilateral trans-femoral amputees. Through the residual/sound limb comparison the quantitative analysis of each case was achieved, and the following conclusions were drawn:

(1) After trans-femoral amputation, the atrophy degree of each muscle of RL was different: the quadriceps were larger and the hamstrings were smaller. The atrophy degree gaps in prosthesis users were less than those cases without using prosthesis. The narrowness extent of each main artery of RL was also different: SFA was the largest, while DFA or MFCA was the smallest. The prosthesis users showed lighter overall narrowness degree but greater differences between each artery. Based on the blood nourishing relationship, the subjects using prostheses exhibited a certain extent of positive correlation between muscle atrophy and the narrowness of its main blood-supply artery. However, this kind of positive correlation was not clear in the subjects who did not use prostheses.

(2) According to the spatial structure changes of bilateral arterial systems during the follow-up period, Case-1 wearing prosthesis showed greater arterial tree deformation in the RL than in the SL, and her bilateral deformation degree gap decreased over time. While Case-2 without using prosthesis presented greater arterial tree deformation in the SL and there was little change in his bilateral gap. These results suggested that using prosthesis not only can achieve the functional compensation for RL, but also could promote the joint physiological state adjustment of both lower limbs to accommodate a new bipedal gait pattern, in order to reduce the disuse of RL and the overwork of SL.

(3) The steady flow calculation of 3D models showed that, the results of Case-1

and Case-2 exhibited notable differences, especially in the value ranges of WP and WSS. However, there were also some similarities: the upper half of DFA in RL was in a state of relative high WP; the LSSAs of both limbs mainly located at the bifurcation site and the upper half of DFA, and the LSSAs of SL was slightly bigger; the average blood FV of RL was lower than that of SL; there was a wide range of medium/low velocity disturbance in the bifurcation site of RL; the cross sections of RL showed more complex secondary flow direction and more disordered flow field. Therefore, the originating segment of DFA in RL was the high-risk area of the occurrence of peripheral vascular diseases.

(4) The unsteady flow calculation of multi-scale model which coupled the 3D model of main arteries and the lumped parameter model of outlet terminal impedance was achieved by 3D-CR model and 3D-WK model. In Case-1, the numerical result produced by 3D-CR model differed from that exported by 3D-WK model. The comparison between Case-1's calculated results by two types of coupling model and the ultrasonic measured data illustrated that, 3D-CR model had the validity to describe pulse wave, and the availability to qualitatively demonstrate the changes in hemodynamic parameters during a cardiac cycle, but its numerical accuracy was much inferior to that of 3D-WK model, especially in RL.

(5) Combining the 3D-WK model results analysis of Case-1 and Case-2, conclusions could be drawn as follow: the WP of bilateral arterial trees were highest during rapid ejection period; from slow ejection period, larger LSSAs appeared in RL with lower WSS value compared with SL; the velocity field disturbance in the bifurcation segment of RL was more severe than that of SL, and RL displayed more disordered secondary flow directions at the cross sections near the bifurcation site. These phenomena demonstrated that the chance of atherosclerosis and other arterial lesions in RL was greater than in SL, and the high-risk areas with WSS lower than 0.4Pa mainly located at the arterial tree bifurcation site and the upper half of DFA. The differences between two

cases were that, Case-1's WSS state in SL was better than that in RL, while Case-2 had similar bilateral WSS situations; Case-2 exhibited larger bilateral LSSAs with lower WSS values than Case-1; in addition to the same high-risk sites with Case-1, the upper half of LFCA in Case-2's both limbs were also susceptible to vascular diseases.

Based on the above conclusions, the main contributions and innovations of this thesis are as follows:

- *Correlation between arterial system and muscular issues in RL*

This study performed the detailed indices comparison between the atrophy degree of muscles and the narrowness degree of their main feeding arteries, and then analyzed their correlation based on the biggest reason of the differences of external stress source and distribution---prosthesis usage. That prospectively introduced the consideration of blood-supply relationship into RL problem research. Meanwhile, a topological concept Hausdorff distance was innovatively employed to quantify the overall spatial deformation of unilateral thigh artery tree during the follow-up period. Through case analysis, it found that the mobility pattern after amputation namely prosthesis usage is a key factor affecting the states of RL muscles and arteries.

The description of these phenomena presented in this study made up for the lack of concerns about vessels and blood flow after amputation, meanwhile illustrated that the overall characteristics of arterial system and its correlations with muscle, skin and other issues are worthy of being observed and discussed in detail in the clinical or biomechanical investigations of lower RL. The combined consideration of various physiological factors and the comprehensive analysis of their mutual interaction and mechanism could conduce to explain the occurrence and development of RL problems, so as to promote the multi-aspect integration of solution which means to break the limitation of single treatment for single problem. For example, in order to alleviate muscle atrophy, neuromuscular electrical stimulation [27], intermittent electrical stimulation [103], medication (e.g. deferoxamine [92]), and standard living habits could be used to increase muscular blood flow and tissue oxygenation, and to avoid arterial stenosis and decreased blood supply caused by hypertension and hyperlipidemia. In order to reduce the occurrence or deterioration risk of peripheral vascular diseases, the external pressure on the skin/socket interface could be controlled by the improvement of prosthesis design, to avoid the microcirculatory disturbance or local blood flow obstruction due to the extrusion and internal stress changes of muscles.

- *Bilateral difference of hemodynamic state and arterial disease high-risk areas*

According to the numerical calculation results of multi-scale coupling model, the value ranges, distributions and changes in a cardiac cycle of various hemodynamic parameters were different between RL and SL. RL has greater possibility of inducing arterial lesions than SL, and the high-risk areas located at bifurcation segment and the upper half of DFA. These results have not been reported before.

The contrastive analysis of bilateral hemodynamic states demonstrated the possibility of repeated surgery. No matter the amputation reason is peripheral vascular disease or not, arteries in RL narrowed significantly with severe spatial deformation, thus affecting blood flow field and the distribution of hemodynamic parameters. Those variations of hemodynamic state in RL make it different from that in SL and before amputation, and pose the high-risk of triggering atherosclerotic plaque. Therefore, the previous studies about blood flow in lower limb before amputation are not applicable to RL. Based on various conditions (amputation reason, RL length, mobility pattern, etc.) to quantify hemodynamic state and to classify the risk degree, in follow-up examination to emphatically observe the high-risk local regions of RL, to control and reduce the probability of RL arterial disease from clinical and rehabilitative treatment fields, all these measures to be tried are very necessary. The vascular endothelial growth factor gene-carrying plasmid by intramuscular administration [64], the hypertensive extracorporeal limb perfusion [65], the endovascular stent implantation [68], and even the cell transplantation for neovascularization [110], such multi-effect treatment programs which are beneficial to both local blood perfusion improvement and muscle atrophy remission deserve more attention and further development.

- *Methodology of multi-scale coupling model for lower limb arteries*

According to the target arteries (in thigh), the research purpose, and the original data conditions, this study set the inlet boundary condition as the measured ultrasonic velocity waveform, and then carried out three kinds of numerical simulation method: the steady flow calculation on arterial tree 3D model, the unsteady flow coupling calculation on 3D-CR model, and the unsteady flow coupling calculation on 3D-WK model. Their results were basically consistent in qualitative terms, but the numerical accuracy had clear gaps.

There were not many studies on the numerical simulation of hemodynamics for lower limb in the past, and in these a few studies a single scale model (mainly 0D or 1D model) was often applied. The hemodynamic numerical study specifically aiming at lower RL has not been reported so far. In this thesis, through the model effect analysis, we suggested that, the qualitative observation for single hemodynamic parameter could employ the characteristic velocity in different phases of a cardiac cycle as the inlet boundary condition to perform relatively simple steady flow calculation on 3D model. For example, to observe the distribution of high WP and pressure drop could select the peak velocity in rapid ejection period as the inlet data; to observe the location of LSSAs and the disordered degree of velocity field in bifurcation site could select the maximum velocity in diastole or filling period. In the absence of ultrasonic data and other setting conditions, or considering the computational scale and time cost, 3D-CR model could be used to perform the unsteady flow calculation in a cardiac cycle for lower limb arterial tree. But it is much more reliable in the limb without being amputated, which means RL has better not adopt this type of model. When the ultrasonic data, the boundary and computational conditions are satisfied, the unsteady flow calculation of 3D-WK model could achieve quantitative results with higher numerical accuracy, even in RL.

In summary, this thesis launched a quantitative study combining the muscle, arterial vessel and hemodynamic state in the lower RL after unilateral trans-femoral amputation. The consideration of blood-supply relationship was prospectively introduced into RL problem research. The muscle atrophy---arterial narrowness correlation, and the high-risk areas of vessel diseases were discussed and described in detail. Meanwhile the numerical simulation gave methodological suggestions for subsequent lower limb hemodynamic studies. These results and conclusions would provide reference data and theoretical support for various future lower limb amputation researches involving muscle or blood flow situations.

In addition, the idea of the morphological study could be applied to upper limb, based on the corresponding blood supply relationship between muscles and arteries. Although upper limb rarely suffers from peripheral vascular diseases, we also could investigate the hemodynamic state by numerical simulation to figure out some issues, such as the effect of blood oxygen saturation on nerves. That means as a research tool, numerical model and its computational system can be applied to the study of blood flow (blood oxygen) states in various parts of the human body.

8.2 LIMITATION AND OUTLOOK

Studies on various diseases and the physiological changes of lower RL would be a main topic in the fields of rehabilitation medicine and biomechanics in the future. In recent years, as a relatively new research direction, lower limb hemodynamics has attracted more and more attention. As a prospective study, the limitations of this thesis and the expectation for future research are as follows:

(1) The sample size was 8 subjects including 2 follow-up cases. Based on this, we did case study, so the results were not statistically significant. In subsequent work, the cooperation latitude for clinical data collection should be further expanded to increase the number of samples and to group them according to the

control variables (age, amputation reason, amputation level, and postoperative time, etc.), in order to conduct more detailed large sample analysis.

(2) From the comparison between the calculated results and the measured ultrasonic waveform, it can be seen that the numerical accuracy of lumped parameter model (even the three-element WK model) still has room for improvement. That is to say the simulations of terminal impedance and vascular wall compliance could be closer to the true physiological state. If not considering computation amount and time consumption, a more perfect multi-scale coupling model for RL could be further developed.

(3) This study assumed vessel wall as no-slip, no-leakage rigid wall, which means the 3D model was reasonably simplified. In future work, the fluid-structure interaction which are characterized by complex solution and large computation could be applied to describe the interaction between blood and vessels. Thus the true physiological state of arterial blood flow would be approximated to the greatest extent and the most accurate numerical simulation results could be obtained.

Appendix Ⅰ Ethics approval letter

THE HONG KONG POLYTECHNIC UNIVERSITY
香港理工大學

To	Wong Man Sang (Interdisciplinary Division of Biomedical Engineering)		
From	MAN Hau Chung, Chair, Faculty Research Committee		
Email	mfhcman@	Date	28-Aug-2013

Application for Ethical Review for Teaching/Research Involving Human Subjects

I write to inform you that approval has been given to your application for human subjects ethics review of the following project for a period from 03-Sep-2012 to 31-Dec-2015:

Project Title:	Numerical Study on the Hemodynamic State of Trans-femoral Residual Limb with Muscle Atrophy
Department:	Interdisciplinary Division of Biomedical Engineering
Principal Investigator:	Wong Man Sang

Please note that you will be held responsible for the ethical approval granted for the project and the ethical conduct of the personnel involved in the project. In the case of the Co-PI, if any, has also obtained ethical approval for the project, the Co-PI will also assume the responsibility in respect of the ethical approval (in relation to the areas of expertise of respective Co-PI in accordance with the stipulations given by the approving authority).

You are responsible for informing the Faculty Research Committee in advance of any changes in the proposal or procedures which may affect the validity of this ethical approval.

You will receive separate email notification should you be required to obtain fresh approval.

MAN Hau Chung

Chair

Faculty Research Committee

Appendix Ⅱ Information sheet

THE HONG KONG
POLYTECHNIC UNIVERSITY
香港理工大學

INFORMATION SHEET

Numerical Study on the Hemodynamic State of Trans-femoral Residual Limb with Muscle Atrophy

You are invited to participate on a study conducted by DONG Ruiqi, who is a post-graduate student of the Department of BME in The Hong Kong Polytechnic University. The project has been approved by the Human Subjects Ethics Sub-committee (HSESC) (or its Delegate) of The Hong Kong Polytechnic University (HSESC Reference Number:).

The aim of this study is to provide theoretical guidance for clarifying the occurrence and development mechanism of residual limb muscle atrophy and to promote early adaptation of definitive prosthetic and infrequent prosthetic replacement. The study will consult your case to know your personal information and basic condition. You will then be asked to take part in a procedure to investigate the muscles image information and hemodynamic parameters of residual limb. Measurements will be taken by 3D digital subtraction angiography instrument (or MRA), Doppler ultrasonic diagnostic apparatus and MRI spectrometer. It is hoped that this information will help to understand the relationship between residual limb muscle atrophy and hemodynamic parameter variations in order to develop better treatments.

The testing should not result in any undue discomfort, but you will need to be recorded some clinical information. All information related to you will remain confidential, and will be identifiable by codes only known to the researcher. You have every right to withdrawn from the study before or during the measurement without penalty of any kind. The whole investigation will take about 3 hours per time.

If you would like to get more information about this study, please contact Dr. MS Wong on tel. no.27667680 or Ms. Ruiqi Dong on tel. no. 6099 ; mailing address Department of BME, the Hong Kong PolyU, Hung Hom and email address: 1290

If you have any complaints about the conduct of this research study, please do not hesitate to contact Ms Kath Lui, Secretary of the Human Subjects Ethics Sub-Committee of The Hong Kong Polytechnic University in writing (c/o Research Office of the University) stating clearly the responsible person and department of this study.

Thank you for your interest in participating in this study.

Dr. MS Wong
Principal Investigator/Chief Investigator

Hung Hom Kowloon Hong Kong 香港 九龍 紅磡
Tel 電話 (852) 2766 5111 Fax 傳真 (852) 2784 3374
Email 電郵 polyu@polyu.edu.hk
Website 網址 www.polyu.edu.hk

THE HONG KONG
POLYTECHNIC UNIVERSITY
香港理工大學

研究信息表

膝上截肢患者肌肉萎缩残肢血流动力学研究

您被邀請參與由香港理工大學生物醫學工程跨領域學部的博士研究生董瑞琪進行的一項研究。該項目已被香港理工大學的人類受試者倫理小組委員會（HSESC或其代表）批准（HSESC編號：　　　　）。

這項研究的目的是為闡明殘肢肌肉萎縮的發生和發展機制提供理論指導，并降低假肢更換頻率及促進患者早日適應最終假肢。本研究將查閱您的病例以瞭解您的個人信息和基本病情。隨後您將被邀請參與檢測殘肢的肌肉圖像信息和血流動力學參數。測量方法分別是三維數字減影血管造影（或MRA），多普勒超聲診斷和核磁共振成像。

我們希望這些信息將有助於研究和瞭解殘肢肌肉萎縮和殘肢血流動力學參數變化之間的關係，以此發展更好的康復治療。

這些檢測不會導致任何不必要的不適，但您會被記錄一些臨床數據和資料。所有與您有關的信息將保持機密，并將用只有研究員知曉的代碼來進行識別。

你有權利在檢測開始前或進行中退出該項研究，并且沒有任何形式的處罰。所有檢測每次將需要大約3小時。

如果您想獲得更多關於這項研究的信息，請電話聯繫黃文生博士，號碼是27667680；或者董瑞琪女士，號碼是6099　　。郵件地址：BME，香港理工大學，紅磡。
電子郵件：1290　　　　　　　　.

如果您有任何關於此項研究行為的投訴，請不要猶豫，以書面形式清楚寫明這項研究的負責人與部門并聯繫香港理工大學人類受試者倫理小組委員會秘書Kath Lui女士（c/o 研究院辦公室）。

感謝您有興趣參與這項研究。

黃文生博士
首席研究員

Hung Hom Kowloon Hong Kong 香港 九龍 紅磡
Tel 電話 (852) 2766 5111 Fax 傳真 (852) 2784 3374
Email 電郵 polyu@polyu.edu.hk
Website 網址 www.polyu.edu.hk

Appendix Ⅲ Consent form

THE HONG KONG
POLYTECHNIC UNIVERSITY
香港理工大學

CONSENT TO PARTICIPATE IN RESEARCH

Numerical Study on the Hemodynamic State of Trans-femoral Residual Limb with Muscle Atrophy

I ________________________ hereby consent to participate in the captioned research conducted by ____DONG Ruiqi______________.

I understand that information obtained from this research may be used in future research and published. However, my right to privacy will be retained, i.e. my personal details will not be revealed.

The procedure as set out in the attached information sheet has been fully explained. I understand the benefit and risks involved. My participation in the project is voluntary.

I acknowledge that I have the right to question any part of the procedure and can withdraw at any time without penalty of any kind.

Name of participant ____

Signature of participant ____

Name of researcher ______董瑞琪 DONG Ruiqi______________________

Signature of researcher ____

Date ________27/08/2013________________________________

Hung Hom Kowloon Hong Kong 香港 九龍 紅磡
Tel 電話 (852) 2766 5111 Fax 傳真 (852) 2784 3374
Email 電郵 polyu@polyu.edu.hk
Website 網址 www.polyu.edu.hk

THE HONG KONG POLYTECHNIC UNIVERSITY
香港理工大學

參與研究同意書

膝上截肢患者肌肉萎缩残肢血流动力学研究

本人____________________同意參與由__________董瑞琪__________開展的上述研究。

本人知悉此研究所得的資料可能被用作日後的研究及發表，但本人的私隱權利將得以保留，即本人的個人資料不會被公開。

研究人員已向本人清楚解釋列在所附資料卡上的研究程序，本人明瞭當中涉及的利益及風險；本人自願參與研究項目。

本人知悉本人有權就程序的任何部分提出疑問，並有權隨時退出而不受任何懲處。

參與者姓名 ____

參與者簽署 ____

研究人員姓名 ____董瑞琪 DONG Ruiqi________________

研究人員簽署 ____

日期 _______2013年8月27日__________________________

Hung Hom Kowloon Hong Kong 香港 九龍 紅磡
Tel 電話 (852) 2766 5111 Fax 傳真 (852) 2784 3374
Email 電郵 polyu@polyu.edu.hk
Website 網址 www.polyu.edu.hk

Reference

1. Wang, M., et al., *MicroRNA-21 regulates vascular smooth muscle cell function via targeting tropomyosin 1 in arteriosclerosis obliterans of lower extremities.* Arterioscler Thromb Vasc Biol, 2011. **31**(9): p. 2044-53.
2. Piazza, G. and M.A. Creager, *Thromboangiitis obliterans.* Circulation, 2010. **121**(16): p. 1858-61.
3. Blevins, W.A., Jr. and P.A. Schneider, *Endovascular management of critical limb ischemia.* Eur J Vasc Endovasc Surg, 2010. **39**(6): p. 756-61.
4. Shapiro, L.T. and M.E. Huang, *Inpatient rehabilitation of survivors of purpura fulminans with multiple limb amputations: a case series.* Arch Phys Med Rehabil, 2009. **90**(4): p. 696-700.
5. Belmont, P.J., Jr., et al., *Risk factors for 30-day postoperative complications and mortality after below-knee amputation: a study of 2,911 patients from the national surgical quality improvement program.* J Am Coll Surg, 2011. **213**(3): p. 370-8.
6. Lyon, C.C., et al., *Skin disorders in amputees.* J Am Acad Dermatol, 2000. **42**(3): p. 501-7.
7. Sanders, J.E., et al., *A bidirectional load applicator for the investigation of skin response to mechanical stress.* IEEE Trans Biomed Eng, 1997. **44**(4): p. 290-6.
8. Portnoy, S., et al., *Patient-specific analyses of deep tissue loads post transtibial amputation in residual limbs of multiple prosthetic users.* J Biomech, 2009. **42**(16): p. 2686-93.
9. Fraisse, N., et al., *[Muscles of the below-knee amputees].* Ann Readapt Med Phys, 2008. **51**(3): p. 218-27.
10. Schmalz, T., S. Blumentritt, and C.D. Reimers, *Selective thigh muscle atrophy in trans-tibial amputees: an ultrasonographic study.* Arch Orthop Trauma Surg, 2001. **121**(6): p. 307-12.
11. Boonyarom, O., et al., *Effect of electrical stimulation to prevent muscle atrophy on morphologic and histologic properties of hindlimb suspended rat hindlimb muscles.* Am J Phys Med Rehabil, 2009. **88**(9): p. 719-26.
12. Tugcu, I., et al., *Muscle strength and bone mineral density in mine victims with transtibial amputation.* Prosthet Orthot Int, 2009. **33**(4): p. 299-306.
13. Dou, P., et al., *Pressure distribution at the stump/socket interface in transtibial amputees during walking on stairs, slope and non-flat road.* Clinical Biomechanics, 2006. **21**(10): p. 1067-1073.
14. Lee, W.C.C., et al., *Finite element modeling of the contact interface between trans-tibial residual limb and prosthetic socket.* Medical Engineering & Physics, 2004. **26**(8): p. 655-662.
15. Sanders, J.E., et al., *Changes in interface pressures and shear stresses over time on trans-tibial amputee subjects ambulating with prosthetic limbs: comparison of diurnal and six-month differences.* J Biomech, 2005. **38**(8): p. 1566-73.
16. Wolf, S.I., et al., *Pressure characteristics at the stump/socket interface in transtibial amputees using an adaptive prosthetic foot.* Clin Biomech (Bristol, Avon), 2009. **24**(10): p. 860-5.
17. Mak, A.F., M. Zhang, and D.A. Boone, *State-of-the-art research in lower-limb prosthetic biomechanics-socket interface: a review.* J Rehabil Res Dev, 2001. **38**(2): p. 161-74.

18. Sanders, J.E., et al., *Changes in interface pressure and stump shape over time: preliminary results from a trans-tibial amputee subject.* Prosthet Orthot Int, 2000. **24**(2): p. 163-8.
19. Sherk, V.D., M.G. Bemben, and D.A. Bemben, *Interlimb muscle and fat comparisons in persons with lower-limb amputation.* Arch Phys Med Rehabil, 2010. **91**(7): p. 1077-81.
20. Isakov, E., et al., *Stump length as related to atrophy and strength of the thigh muscles in trans-tibial amputees.* Prosthet Orthot Int, 1996. **20**(2): p. 96-100.
21. Glass, D.J., *IGF-1 Regulation of Skeletal Muscle Hypertrophy and Atrophy.* Igfs: Local Repair and Survival Factors Throughout Life Span, 2010: p. 85-96.
22. Stratos, I., et al., *Inhibition of caspase mediated apoptosis restores muscle function after crush injury in rat skeletal muscle.* Apoptosis, 2012. **17**(3): p. 269-77.
23. Goldberg, T., *Postoperative management of lower extremity amputations.* Phys Med Rehabil Clin N Am, 2006. **17**(1): p. 173-80, vii.
24. Hase, K., et al., *Effects of Therapeutic Gait Training Using prosthesis and a Treadmill for Ambulatory Patients With Hemiparesis.* Arch Phys Med Rehabil, 2011. **92**(12): p. 1961-1966.
25. Yeung, L.F., et al., *Long-distance walking effects on trans-tibial amputees compensatory gait patterns and implications on prosthetic designs and training.* Gait & Posture, 2012. **35**(2): p. 328-333.
26. Guo, B.S., et al., *Electrical stimulation influences satellite cell proliferation and apoptosis in unloading-induced muscle atrophy in mice.* PLoS One, 2012. **7**(1): p. e30348.
27. Dirks, M.L., et al., *Neuromuscular electrical stimulation prevents muscle disuse atrophy during leg immobilization in humans.* Acta Physiol (Oxf), 2014. **210**(3): p. 628-41.
28. Brooks, N., et al., *Resistance training and timed essential amino acids protect against the loss of muscle mass and strength during 28 days of bed rest and energy deficit.* J Appl Physiol (1985), 2008. **105**(1): p. 241-8.
29. Pyle, A.L. and P.P. Young, *Atheromas feel the pressure: biomechanical stress and atherosclerosis.* Am J Pathol, 2010. **177**(1): p. 4-9.
30. Ochi, M., et al., *Arterial stiffness is associated with low thigh muscle mass in middle-aged to elderly men.* Atherosclerosis, 2010. **212**(1): p. 327-332.
31. Liao, F.Y., D.W. Garrison, and Y.K. Jan, *Relationship between nonlinear properties of sacral skin blood flow oscillations and vasodilatory function in people at risk for pressure ulcers.* Microvascular Research, 2010. **80**(1): p. 44-53.
32. Netter, F.H., *Atlas of human anatomy*, 2011, Saunders/Elsevier,: Philadelphia, Pa.
33. Boonyarom, O. and K. Inui, *Atrophy and hypertrophy of skeletal muscles: structural and functional aspects.* Acta Physiol (Oxf), 2006. **188**(2): p. 77-89.
34. Alzghoul, M.B., et al., *Ectopic expression of IGF-I and Shh by skeletal muscle inhibits disuse-mediated skeletal muscle atrophy and bone osteopenia in vivo.* FASEB J, 2004. **18**(1): p. 221-3.
35. Sanders, J.E. and S. Fatone, *Residual limb volume change: systematic review of measurement and management.* J Rehabil Res Dev, 2011. **48**(8): p. 949-86.
36. Sanders, J.E., et al., *Clinical utility of in-socket residual limb volume change measurement: Case study results.* Prosthet Orthot Int, 2009. **33**(4): p. 378-390.
37. Lilja, M., P. Hoffmann, and T. Oberg, *Morphological changes during early trans-tibial prosthetic fitting.* Prosthet Orthot Int, 1998. **22**(2): p. 115-22.

38. Schmalbruch, H., *Natural killer cells and macrophages in immature denervated rat muscles.* J Neuropathol Exp Neurol, 1996. **55**(3): p. 310-9.
39. Glass, D.J., *Skeletal muscle hypertrophy and atrophy signaling pathways.* Int J Biochem Cell Biol, 2005. **37**(10): p. 1974-84.
40. Ferreira, R., et al., *Evidences of apoptosis during the early phases of soleus muscle atrophy in hindlimb suspended mice.* Physiol Res, 2008. **57**(4): p. 601-11.
41. Isakov, E., et al., *Isokinetic and isometric strength of the thigh muscles in below-knee amputees.* Clin Biomech (Bristol, Avon), 1996. **11**(4): p. 232-235.
42. Bruusgaard, J.C. and K. Gundersen, *In vivo time-lapse microscopy reveals no loss of murine myonuclei during weeks of muscle atrophy.* J Clin Invest, 2008. **118**(4): p. 1450-7.
43. Tews, D.S., *Muscle-fiber apoptosis in neuromuscular diseases.* Muscle Nerve, 2005. **32**(4): p. 443-58.
44. Powers, S.K., A.J. Smuder, and A.R. Judge, *Oxidative stress and disuse muscle atrophy: cause or consequence?* Curr Opin Clin Nutr Metab Care, 2012. **15**(3): p. 240-5.
45. Schakman, O., et al., *Glucocorticoid-induced skeletal muscle atrophy.* Int J Biochem Cell Biol, 2013. **45**(10): p. 2163-72.
46. Vandenburgh, H., et al., *Attenuation of skeletal muscle wasting with recombinant human growth hormone secreted from a tissue-engineered bioartificial muscle.* Hum Gene Ther, 1998. **9**(17): p. 2555-64.
47. Rennie, M.J., *Exercise- and nutrient-controlled mechanisms involved in maintenance of the musculoskeletal mass.* Biochem Soc Trans, 2007. **35**(Pt 5): p. 1302-5.
48. Fergason, J., J.J. Keeling, and E.M. Bluman, *Recent advances in lower extremity amputations and prosthetics for the combat injured patient.* Foot Ankle Clin, 2010. **15**(1): p. 151-74.
49. Brown, B.J., et al., *Outcomes after 294 transtibial amputations with the posterior myocutaneous flap.* Int J Low Extrem Wounds, 2014. **13**(1): p. 33-40.
50. Coupland, R.M., *Amputation for antipersonnel mine injuries of the leg: preservation of the tibial stump using a medial gastrocnemius myoplasty.* Ann R Coll Surg Engl, 1989. **71**(6): p. 405-8.
51. Gottschalk, F., *Transfemoral amputation. Biomechanics and surgery.* Clin Orthop Relat Res, 1999(361): p. 15-22.
52. Portnoy, S., et al., *Internal mechanical conditions in the soft tissues of a residual limb of a trans-tibial amputee.* J Biomech, 2008. **41**(9): p. 1897-909.
53. Moo, E.K., et al., *Interface pressure profile analysis for patellar tendon-bearing socket and hydrostatic socket.* Acta Bioeng Biomech, 2009. **11**(4): p. 37-43.
54. Darter, B.J., et al., *Home-based treadmill training to improve gait performance in persons with a chronic transfemoral amputation.* Arch Phys Med Rehabil, 2013. **94**(12): p. 2440-7.
55. Kubota, A., et al., *Prevention of disuse muscular weakness by restriction of blood flow.* Med Sci Sports Exerc, 2008. **40**(3): p. 529-34.
56. Staresinic, M., et al., *Effective therapy of transected quadriceps muscle in rat: Gastric pentadecapeptide BPC 157.* J Orthop Res, 2006. **24**(5): p. 1109-17.
57. Bhargava, J.S., et al., *Pedicled omental transfer for ischaemic limbs--a 5-year experience.* J Indian Med Assoc, 1997. **95**(4): p. 100-2.
58. Santilli, J.D. and S.M. Santilli, *Chronic critical limb ischemia: diagnosis, treatment and*

prognosis. Am Fam Physician, 1999. **59**(7): p. 1899-908.

59. Ubbink, D.T., et al., *The usefulness of capillary microscopy, transcutaneous oximetry and laser Doppler fluxmetry in the assessment of the severity of lower limb ischaemia.* Int J Microcirc Clin Exp, 1994. **14**(1-2): p. 34-44.
60. Kalani, M., et al., *Transcutaneous oxygen tension and toe blood pressure as predictors for outcome of diabetic foot ulcers.* Diabetes Care, 1999. **22**(1): p. 147-51.
61. Zioupos, P., et al., *Foot microcirculation and blood rheology in diabetes.* J Biomed Eng, 1993. **15**(2): p. 155-8.
62. Demiroglu, H., A. Gurlek, and I. Barista, *Enhanced erythrocyte aggregation in type 2 diabetes with late complications.* Exp Clin Endocrinol Diabetes, 1999. **107**(1): p. 35-9.
63. Khodabandehlou, T. and C. Le Devehat, *Hemorheological disturbances as a marker of diabetic foot syndrome deterioration.* Clin Hemorheol Microcirc, 2004. **30**(3-4): p. 219-23.
64. Kusumanto, Y.H., et al., *Treatment with intramuscular vascular endothelial growth factor gene compared with placebo for patients with diabetes mellitus and critical limb ischemia: a double-blind randomized trial.* Hum Gene Ther, 2006. **17**(6): p. 683-91.
65. Lane, R.J., et al., *Hypertensive extracorporeal limb perfusion (HELP): a new technique for managing critical lower limb ischemia.* J Vasc Surg, 2008. **48**(5): p. 1156-65; discussion 1165.
66. Schillinger, M., et al., *Sustained benefit at 2 years of primary femoropopliteal stenting compared with balloon angioplasty with optional stenting.* Circulation, 2007. **115**(21): p. 2745-9.
67. Krankenberg, H., et al., *Nitinol stent implantation versus percutaneous transluminal angioplasty in superficial femoral artery lesions up to 10 cm in length: the femoral artery stenting trial (FAST).* Circulation, 2007. **116**(3): p. 285-92.
68. Falkowski, A., et al., *The evaluation of primary stenting of sirolimus-eluting versus bare-metal stents in the treatment of atherosclerotic lesions of crural arteries.* Eur Radiol, 2009. **19**(4): p. 966-74.
69. Karimi, A., et al., *Randomized trial of Legflow((R)) paclitaxel eluting balloon and stenting versus standard percutaneous transluminal angioplasty and stenting for the treatment of intermediate and long lesions of the superficial femoral artery (RAPID trial): study protocol for a randomized controlled trial.* Trials, 2013. **14**: p. 87.
70. Lee, B.Y., et al., *Noninvasive hemodynamic evaluation in selection of amputation level.* Surg Gynecol Obstet, 1979. **149**(2): p. 241-4.
71. Cheng, E.Y., *Lower extremity amputation level: selection using noninvasive hemodynamic methods of evaluation.* Arch Phys Med Rehabil, 1982. **63**(10): p. 475-9.
72. Wang, C.L., M. Wang, and T.K. Liu, *Predictors for wound healing in ischemic lower limb amputation.* J Formos Med Assoc, 1994. **93**(10): p. 849-54.
73. Sarin, S., et al., *Selection of amputation level: a review.* Eur J Vasc Surg, 1991. **5**(6): p. 611-20.
74. Adera, H.M., et al., *Prediction of amputation wound healing with skin perfusion pressure.* J Vasc Surg, 1995. **21**(5): p. 823-8; discussion 828-9.
75. Wutschert, R. and H. Bounameaux, *Determination of amputation level in ischemic limbs. Reappraisal of the measurement of TcPo2.* Diabetes Care, 1997. **20**(8): p. 1315-8.
76. Misuri, A., et al., *Predictive value of transcutaneous oximetry for selection of the*

amputation level. J Cardiovasc Surg (Torino), 2000. **41**(1): p. 83-7.

77. Figoni, S.F., et al., *Preamputation evaluation of limb perfusion with laser Doppler imaging and transcutaneous gases.* J Rehabil Res Dev, 2006. **43**(7): p. 891-904.

78. Scremin, O.U., et al., *Preamputation evaluation of lower-limb skeletal muscle perfusion with H(2) (15)O positron emission tomography.* Am J Phys Med Rehabil, 2010. **89**(6): p. 473-86.

79. Mavroforou, A., et al., *The evolution of lower limb amputation through the ages. Historical note.* International Angiology, 2007. **26**(4): p. 385-9.

80. Bruce, A.S., C.J. Getty, and J.D. Beard, *The effect of the ankle brachial pressure index and the use of a tourniquet upon the outcome of total knee replacement.* J Arthroplasty, 2002. **17**(3): p. 312-4.

81. Wolthuis, A.M., et al., *Use of a pneumatic tourniquet improves outcome following trans-tibial amputation.* Eur J Vasc Endovasc Surg, 2006. **31**(6): p. 642-5.

82. Choksy, S.A., et al., *A randomised controlled trial of the use of a tourniquet to reduce blood loss during transtibial amputation for peripheral arterial disease.* Eur J Vasc Endovasc Surg, 2006. **31**(6): p. 646-50.

83. Welling, D.R., et al., *A balanced approach to tourniquet use: lessons learned and relearned.* J Am Coll Surg, 2006. **203**(1): p. 106-15.

84. Navein, J., R. Coupland, and R. Dunn, *The tourniquet controversy.* J Trauma, 2003. **54**(5 Suppl): p. S219-20.

85. Husum, H., et al., *Prehospital tourniquets: there should be no controversy.* J Trauma, 2004. **56**(1): p. 214-5.

86. Taylor, G.I. and J.H. Palmer, *The vascular territories (angiosomes) of the body: experimental study and clinical applications.* Br J Plast Surg, 1987. **40**(2): p. 113-41.

87. Taylor, G.I. and W.R. Pan, *Angiosomes of the leg: anatomic study and clinical implications.* Plast Reconstr Surg, 1998. **102**(3): p. 599-616; discussion 617-8.

88. Serra, R., et al., *Angiosome-targeted revascularisation in diabetic foot ulcers.* Int Wound J, 2013.

89. Biancari, F. and T. Juvonen, *Angiosome-targeted lower limb revascularization for ischemic foot wounds: systematic review and meta-analysis.* Eur J Vasc Endovasc Surg, 2014. **47**(5): p. 517-22.

90. Sacks, A.H., *Theoretical prediction of a time-at-pressure curve for avoiding pressure sores.* J Rehabil Res Dev, 1989. **26**(3): p. 27-34.

91. Barnett, R.I. and J.A. Ablarde, *Skin vascular reaction to standard patient positioning on a hospital mattress.* Adv Wound Care, 1994. **7**(1): p. 58-65.

92. Sundin, B.M., et al., *The role of allopurinol and deferoxamine in preventing pressure ulcers in pigs.* Plast Reconstr Surg, 2000. **105**(4): p. 1408-21.

93. Tsuji, S., et al., *Analysis of ischemia-reperfusion injury in a microcirculatory model of pressure ulcers.* Wound Repair Regen, 2005. **13**(2): p. 209-15.

94. Bergstrand, S., et al., *Blood flow measurements at different depths using photoplethysmography and laser Doppler techniques.* Skin Res Technol, 2009. **15**(2): p. 139-47.

95. Pinzur, M.S. and H. Osterman, *Tips of the trade #26. Treatment of amputation residual limb ulcers with a hydroactive dressing and continued weight bearing.* Orthop Rev, 1990.

19(7): p. 638-40.
96. Traballesi, M., et al., *Residual limb wounds or ulcers heal in transtibial amputees using an active suction socket system. A randomized controlled study.* Eur J Phys Rehabil Med, 2012. **48**(4): p. 613-23.
97. Daniel, R.K., D.L. Priest, and D.C. Wheatley, *Etiologic factors in pressure sores: an experimental model.* Arch Phys Med Rehabil, 1981. **62**(10): p. 492-8.
98. Salcido, R., et al., *Histopathology of pressure ulcers as a result of sequential computer-controlled pressure sessions in a fuzzy rat model.* Adv Wound Care, 1994. **7**(5): p. 23-4, 26, 28 passim.
99. Bouten, C.V., et al., *The etiology of pressure ulcers: skin deep or muscle bound?* Arch Phys Med Rehabil, 2003. **84**(4): p. 616-9.
100. Levine, S.P., et al., *Blood flow in the gluteus maximus of seated individuals during electrical muscle stimulation.* Arch Phys Med Rehabil, 1990. **71**(9): p. 682-6.
101. Bogie, K.M., et al., *Electrical stimulation for pressure sore prevention and wound healing.* Assist Technol, 2000. **12**(1): p. 50-66.
102. Bogie, K.M., X. Wang, and R.J. Triolo, *Long-term prevention of pressure ulcers in high-risk patients: a single case study of the use of gluteal neuromuscular electric stimulation.* Arch Phys Med Rehabil, 2006. **87**(4): p. 585-91.
103. Solis, L.R., et al., *Prevention of pressure-induced deep tissue injury using intermittent electrical stimulation.* J Appl Physiol (1985), 2007. **102**(5): p. 1992-2001.
104. Solis, L.R., et al., *Effects of intermittent electrical stimulation on superficial pressure, tissue oxygenation, and discomfort levels for the prevention of deep tissue injury.* Ann Biomed Eng, 2011. **39**(2): p. 649-63.
105. Tyml, K., O. Mathieu-Costello, and E. Noble, *Microvascular response to ischemia, and endothelial ultrastructure, in disused skeletal muscle.* Microvascular Research, 1995. **49**(1): p. 17-32.
106. Brevetti, L.S., et al., *Exercise-induced hyperemia unmasks regional blood flow deficit in experimental hindlimb ischemia.* J Surg Res, 2001. **98**(1): p. 21-6.
107. Wang, Q., et al., *DNA degradation in nuclei of muscle cells followed by ischemic injury in a rabbit amputation model.* Microsurgery, 2006. **26**(5): p. 391-5.
108. Liu, Q., et al., *Intra-arterial transplantation of adult bone marrow cells restores blood flow and regenerates skeletal muscle in ischemic limbs.* Vasc Endovascular Surg, 2009. **43**(5): p. 433-43.
109. Caron, M.A., et al., *Hypoxia alters contractile protein homeostasis in L6 myotubes.* Febs Letters, 2009. **583**(9): p. 1528-1534.
110. Huang, C.C., et al., *Hypoxia-induced therapeutic neovascularization in a mouse model of an ischemic limb using cell aggregates composed of HUVECs and cbMSCs.* Biomaterials, 2013. **34**(37): p. 9441-50.
111. Wang, J.J., et al., *Systemic venous circulation. Waves propagating on a windkessel: relation of arterial and venous windkessels to systemic vascular resistance.* Am J Physiol Heart Circ Physiol, 2006. **290**(1): p. H154-62.
112. Alastruey, J., et al., *Pulse wave propagation in a model human arterial network: Assessment of 1-D visco-elastic simulations against in vitro measurements.* J Biomech, 2011. **44**(12): p. 2250-8.

113. LaCourse, J.R., G. Mohanakrishnan, and K. Sivaprasad, *Simulations of arterial pressure pulses using a transmission line model.* J Biomech, 1986. **19**(9): p. 771-80.
114. Shi, Y., P. Lawford, and R. Hose, *Review of zero-D and 1-D models of blood flow in the cardiovascular system.* Biomed Eng Online, 2011. **10**: p. 33.
115. Noordergraaf, A., D. Verdouw, and H.B. Boom, *The use of an analog computer in a circulation model.* Prog Cardiovasc Dis, 1963. **5**: p. 419-39.
116. Westerhof, N., et al., *Analog studies of the human systemic arterial tree.* J Biomech, 1969. **2**(2): p. 121-43.
117. Westerhof, N. and A. Noordergraaf, *Arterial viscoelasticity: a generalized model. Effect on input impedance and wave travel in the systematic tree.* J Biomech, 1970. **3**(3): p. 357-79.
118. Pietrabissa, R., et al., *A lumped parameter model to evaluate the fluid dynamics of different coronary bypasses.* Medical Engineering & Physics, 1996. **18**(6): p. 477-84.
119. Taylor, M.G., *Wave transmission through an assembly of randomly branching elastic tubes.* Biophysical Journal, 1966. **6**(6): p. 697-716.
120. Taylor, M.G., *The elastic properties of arteries in relation to the physiological functions of the arterial system.* Gastroenterology, 1967. **52**(2): p. 358-63.
121. Schaaf, B.W. and P.H. Abbrecht, *Digital computer simulation of human systemic arterial pulse wave transmission: a nonlinear model.* J Biomech, 1972. **5**(4): p. 345-64.
122. Reymond, P., et al., *Validation of a one-dimensional model of the systemic arterial tree.* Am J Physiol Heart Circ Physiol, 2009. **297**(1): p. H208-22.
123. Raghu, R., et al., *Comparative study of viscoelastic arterial wall models in nonlinear one-dimensional finite element simulations of blood flow.* J Biomech Eng, 2011. **133**(8): p. 081003.
124. Balakrishnan, B., et al., *Strut position, blood flow, and drug deposition: implications for single and overlapping drug-eluting stents.* Circulation, 2005. **111**(22): p. 2958-65.
125. Boutsianis, E., et al., *Computational simulation of intracoronary flow based on real coronary geometry.* Eur J Cardiothorac Surg, 2004. **26**(2): p. 248-56.
126. Pivkin, I.V., et al., *Combined effects of pulsatile flow and dynamic curvature on wall shear stress in a coronary artery bifurcation model.* J Biomech, 2005. **38**(6): p. 1283-90.
127. Perktold, K. and G. Rappitsch, *Computer simulation of local blood flow and vessel mechanics in a compliant carotid artery bifurcation model.* J Biomech, 1995. **28**(7): p. 845-56.
128. Gijsen, F.J., F.N. van de Vosse, and J.D. Janssen, *The influence of the non-Newtonian properties of blood on the flow in large arteries: steady flow in a carotid bifurcation model.* J Biomech, 1999. **32**(6): p. 601-8.
129. Zhao, S.Z., et al., *Blood flow and vessel mechanics in a physiologically realistic model of a human carotid arterial bifurcation.* J Biomech, 2000. **33**(8): p. 975-84.
130. Kim, T., A.Y. Cheer, and H.A. Dwyer, *A simulated dye method for flow visualization with a computational model for blood flow.* J Biomech, 2004. **37**(8): p. 1125-36.
131. Hsia, T.Y., et al., *Computational fluid dynamic study of flow optimization in realistic models of the total cavopulmonary connections.* J Surg Res, 2004. **116**(2): p. 305-13.
132. Quarteroni, A. and A. Valli, *Domain decomposition methods for partial differential equations*. Numerical mathematics and scientific computation1999, Oxford

New York: Clarendon Press ;

Oxford University Press. xv, 360 p.

133. Lagana, K., et al., *Multiscale modeling of the cardiovascular system: application to the study of pulmonary and coronary perfusions in the univentricular circulation.* J Biomech, 2005. **38**(5): p. 1129-41.

134. Liang, F., et al., *Multi-scale modeling of the human cardiovascular system with applications to aortic valvular and arterial stenoses.* Med Biol Eng Comput, 2009. **47**(7): p. 743-55.

135. Raines, J.K., M.Y. Jaffrin, and A.H. Shapiro, *A computer simulation of arterial dynamics in the human leg.* J Biomech, 1974. **7**(1): p. 77-91.

136. Law, Y.F. and V.C. Roberts, *Per-operative haemodynamic assessment of lower limb arterial surgery. Part 2: Modelling of the arterial system.* J Biomed Eng, 1983. **5**(3): p. 194-200.

137. Porenta, G., D.F. Young, and T.R. Rogge, *A finite-element model of blood flow in arteries including taper, branches, and obstructions.* J Biomech Eng, 1986. **108**(2): p. 161-7.

138. Willemet, M., V. Lacroix, and E. Marchandise, *Inlet boundary conditions for blood flow simulations in truncated arterial networks.* J Biomech, 2011. **44**(5): p. 897-903.

139. Zhang, B., L. Zhang, and F. Karray, *Retinal vessel extraction by matched filter with first-order derivative of Gaussian.* Comput Biol Med, 2010. **40**(4): p. 438-45.

140. Conversano, F., et al., *Hepatic vessel segmentation for 3D planning of liver surgery experimental evaluation of a new fully automatic algorithm.* Acad Radiol, 2011. **18**(4): p. 461-70.

141. Flasque, N., et al., *Acquisition, segmentation and tracking of the cerebral vascular tree on 3D magnetic resonance angiography images.* Med Image Anal, 2001. **5**(3): p. 173-83.

142. Belavy, D.L., et al., *Differential atrophy of the lower-limb musculature during prolonged bed-rest.* Eur J Appl Physiol, 2009. **107**(4): p. 489-99.

143. Azer, K. and C.S. Peskin, *A one-dimensional model of blood flow in arteries with friction and convection based on the Womersley velocity profile.* Cardiovasc Eng, 2007. **7**(2): p. 51-73.

144. Hyun, S., C. Kleinstreuer, and J.P. Archie, Jr., *Hemodynamics analyses of arterial expansions with implications to thrombosis and restenosis.* Medical Engineering & Physics, 2000. **22**(1): p. 13-27.

145. Davies, P.F., et al., *A spatial approach to transcriptional profiling: mechanotransduction and the focal origin of atherosclerosis.* Trends Biotechnol, 1999. **17**(9): p. 347-51.

146. Palumbo, R., et al., *Different effects of high and low shear stress on platelet-derived growth factor isoform release by endothelial cells: consequences for smooth muscle cell migration.* Arterioscler Thromb Vasc Biol, 2002. **22**(3): p. 405-11.

147. Du, T., D. Hu, and D. Cai, *Outflow boundary conditions for blood flow in arterial trees.* PLoS One, 2015. **10**(5): p. e0128597.

148. Stergiopulos, N., D.F. Young, and T.R. Rogge, *Computer simulation of arterial flow with applications to arterial and aortic stenoses.* J Biomech, 1992. **25**(12): p. 1477-88.

149. Simon, A.C., et al., *An evaluation of large arteries compliance in man.* Am J Physiol, 1979. **237**(5): p. H550-4.